An Electron and Ion Scattering Spectroscopic Study of Interfaces for Organic Photovoltaic Applications

Natalya Schmerl

Thesis submitted to Flinders University
For the degree of

Doctor of Philosophy

College of Science and Engineering
Flinders University

7th November 2018

“Nature isn’t classical . . . and if you want to make a simulation of Nature, you’d better make it quantum mechanical, and by golly it’s a wonderful problem, because it doesn’t look so easy”

- *Richard P. Feynman, 1981*

Contents

Abstract

The importance of interfacial phenomena in nanoelectronics device performance has become increasingly apparent in recent years. Organic photovoltaics is a field in nanoelectronics with the potential to provide cheaper, flexible alternatives to silicon based cells if their interfaces can be better understood and controlled, as this is where most issues with degradation or charge transport occur. As such, this dissertation has been dedicated to researching a range of materials, modifications and interfacial phenomena which have organic photovoltaic applications. In particular a focus has been on comparing the electronic structure at the outermost layer to the near surface area of each selected interface, as at this stage there are very few studies of this type in this field. Depth profiling was also performed in most instances to check for diffusion at the interface.

One chapter has also been dedicated to valence band spectral acquisition for insulating polymers. Insulating polymers can be embedded with conductors or semiconductors to create specific properties or morphology, and to properly characterize the electronic structure composite films the constituent film characterization is desirable. Three methods for charge compensation were compared, the most successful of these was embedding the polymer surface with nanotubes which had a rather featureless valence band spectrum. In this way the valence band features of the polymer were able to be successfully identified and compared to theoretical calculations in the literature.

Cleaning processes such as sputtering, plasma, and heating are common film treatments, all of which influence the electronic structure at the surface. As such, a comparative study was performed using ZnO as the case study. A range of Al doped films were likewise investigated and the band gap was also measured. The doping process was shown to incorporate AlO_x into the ZnO lattice, increase the band gap, lower the conduction band and induce band bending in the valence band. Sputter cleaning with UHV heating was most effective for removing contamination, and plasma cleaning resulted in extra oxygen at the surface and surface dipole formation, this dipole was removed with UHV heating. When UHV heating was applied to both the sputter cleaned and plasma cleaned samples a surface conduction channel was exposed which could improve charge conduction in devices.

An interfacial layer inserted between the PCBM/P3HT photoactive layer and high workfunction electrode improves device performance but the mechanisms are not fully understood. LiF and NaF are two such interfacial materials, so a study was performed to gain insight into the differences in surface electronic structure induced by each salt on each organic material. Both salts induced a redistribution of electrons in the organics. NaF had a stronger influence which, with sufficient thickness fluorinated both PCBM and P3HT. Both salts induced an interfacial dipole on PCBM and

P3HT, and it was found that altering the deposition method of salt from a single layer to sequential thinner depositions had an influence on the effect the dipole had on the valence band. The ability to alter the dipole via deposition method could be beneficial for OPV devices.

Declaration

I certify that this thesis does not incorporate without acknowledgment any material previously submitted for a degree or diploma in any university; and that to the best of my knowledge and belief it does not contain any material previously published or written by another person except where due reference is made in the text.

Signed..

Date...

Acknowledgements

The experience of undergoing and completing a PhD is not something which can be easily expressed in words. It is a process of gaining competence as an independent researcher, the obvious result of which is given in the form of the thesis. However, I have found that it is the trials and tribulations that occur along the way both externally and internally, and the process of learning how to overcome them which truly makes the PhD experience what it is rather than the specific experiments or techniques.

I have to begin my acknowledgements with my family, without whom I never would have managed to achieve my goals. The gratitude and love I have for my parents is endless, and I have wondered many times how you've handled dealing with both of your children doing PhDs simultaneously. Eric and Vicki you are both so encouraging, tolerant and supportive it's unbelievable. Thank you. As for my brother Brett, well, it's pretty hard to take life too seriously when you live with your sibling who happens to be your best friend. It's been an amazing experience to share this time in our lives together. Also, given I finished my PhD first I'm clearly the superior sibling (Ha!). Love you Brettdstar.

On a professional level I unquestionably have to start with acknowledging Professor Jamie S. Quinton. It was your passion for science, unforgettable physics introduction lecture and highly approachable and communicative personality that gave me the confidence and inspiration to transfer from my initial subject choices in first year to instead pursue my career as a physicist, despite having not seen any serious mathematics since completing high school 7 years prior. Thank you so much. Throughout undergraduate you continued to inspire with your fantastic, intelligent and often humorous lecturing style. I would like to thank you for being my co-supervisor in my PhD, and although we have not had regular meetings, our occasional discussions have been once again, immensely helpful for me as a student.

Naturally, I must next acknowledge my primary supervisor Professor Gunther G. Andersson who supervised me in my Honours year as well as PhD. Being one of your first PhD students gave me certain opportunities and challenges which have, in the end, made me a stronger scientist. Throughout the duration of my candidature we had to work together to further understand the capabilities and limits of both the MIES technique and analysis methods, but also with issues that arose with the instrument. You gave me the opportunity to be a laboratory manager for over three years, and although I probably should have stopped much earlier to prioritize my candidature I thoroughly enjoyed my time managing the laboratory and instrument. There were also a range of issues that arose during my candidature which you always did your best to assist with, and you are one of the hardest working academics I've ever seen. The experience I received in my candidature has been an enormous opportunity for growth and learning, and I feel that I have completed my PhD with a far better understanding of UHV instruments as well as time management and critical thinking as a result. Thank you for all your hard work and for always doing the best you could to help.

I also cannot extend my gratitude enough to the former mechanical and electronic workshops at the university. The assistance that Gunther and I received from them was amazing, and they were always happy to help when I'd inevitably, once again, rock up at the door with a rig in crisis. Chris Price, Bob Northeast, Wayne Peacock, Bill Drury and Andrew Dunn, you have been an absolute pleasure to work with, thank you for always providing such amazing service with a smile. The MIES couldn't have functioned without you in those years.

The two others who have been my greatest pleasure to work with have been my office mates Alex Sibley and Ben Chambers. We have had countless discussions assisting each other on a professional as well as highly unprofessional level and kept each other sane. I will dearly miss our office, it has been a wonderful and crazy place. I love you both and hope to collaborate with you in the future. Anders Barlow, Anirudh Sharma, Daniel Mangos and Chris Ridings absolutely require a mention here also. It has been wonderful to have you as my colleagues and friends, and I sincerely hope to work with you again.

I would also like to thank Andrew Stapleton for many interesting and useful conversations whilst we were collaborating in the Transparent Electrode Cluster project together, as well as thank Chris Gibson for training me on the AFM. My thanks are also extended to Dr. Cameron Shearer for making some samples used as controls in my final results chapters. My thanks also need to be extended to Amanda Ellis and Dmitriy Khodakov, The project we attempted did not go as planned, but I must acknowledge all the efforts made and the time we spent working together. Jennie Brand and the (former) school office also requires a mention, you all work so hard and Jennie in particular has been of assistance to me many times.

I gratefully acknowledge the funding sources which have made this research and my candidature possible. This includes the Australian Government Research Training Program Scholarship I gained through Flinders University for three and a half years, and the Australian Nanotechnology Network (ANN) for a travel grant towards an international conference. I would also like to acknowledge the collaboration in which I was involved, the Transparent Electrode Cluster, which resulted in a chapter of this thesis as well as paid interstate visits for meetings and laboratory tours.

Finally, I must express my overwhelming gratitude to Professor Tara Brabazon and all of the hardworking people in the office of graduate research. I met Tara in the final year of my candidature. Her support, enthusiasm, encouragement, and incredible professional conduct which she blended perfectly with quirkiness and determination has absolutely blown me away. You’re an absolute inspiration Tara, thank you.

Publications

The following is a list of publications made during the author's candidature resulting from work directly related to the research herein.

Journal Articles:

Schmerl N., Khodakov D., Stapleton A., Ellis A., Andersson G., Valence Band Structure of PDMS Surface and a Blend with MWCNTs: A UPS and MIES Study of an Insulating Polymer, *Applied Surface Science*., 2015, **353**, 693-699

Schmerl N., Gentle A.R., Quinton J.S., Smith G.B., Andersson G.G., Surface and Near Surface Area Density of States for Magnetron- Sputtered ZnO and Al-ZnO: A MIES, UPS, and VBXPS Study Investigating Ultra-High Vacuum Sputter Cleaning and UV Oxygen Plasma, *J. Phys. Chem. C,* 2016, **120**, 15772-15784

Schmerl N., Quinton J.S., Andersson G., On the Growth of Evaporated LiF on P3HT and PCBM, *J. Phys. Chem. C*, 2018, **122**, 41, 23420-23431

Presentations:

[Poster prize] Schmerl N., Quintson J.S., Andersson G.G., On the Growth of LiF on P3HT and PCBM, Flinders Centre for Nano Scale Science and Technology Conference 2017, Bedford Park, Australia

[Poster] Schmerl N., Quinton J.S., Lewis D., Andersson G.G., Electron Spectroscopic Studies on the Monolayer Formation of Phosphonic Acid on Titania, 20th Inelastic Ion-Surface Collisions conference (IISC-20) 2014, Wirrina Cove, Australia

[Poster] Schmerl N., Gentle A., Quinton J.S., Smith J., Lewis D., Andersson G.G., Investigation of the Electronic Structure of Modified Zinc Oxide for Transparent Electrodes, Nanostructures for Sensors, Electronics, Energy and the Environment (Nano S-E3) conference 2013, Airlie Beach, Australia

[Poster] Schmerl N., Andersson G.G., Polymeric Surface Modifications: An Investigation with Ion Scattering and Photoelectron Spectroscopy, 28th Australian Colloid and Surface Science Student Conference (ACSSSC) 2011, Newcastle, Australia

Abbreviations

AD	Auger de-excitation
AFM	Atomic force microscopy
AN	Auger neutralization
ARXPS	Angle resolved X-ray photoelectron spectroscopy
AZO	Aluminium doped zinc oxide
BHJ	Bulk heterojunction
CB	Conduction band
CBM	Conduction band minimum
CNT	Carbon nanotube
CVD	Chemical vapor deposition
DOS	Density of occupied states
ETL	Electron transport layer
FWHM	Full width at half maximum
HEISS	High energy ion scattering spectroscopy
HOMO	Highest occupied molecular orbital
HTL	Hole transport layer
HWE	High workfunction electrode
IBM	International business machines
ICISS	Impact collision ion scattering spectroscopy
IEA	International energy agency
IP	Ionization potential

ISS	Ion scattering spectroscopy
ITO	Indium tin oxide
LED	Light emitting diode
LUMO	Lowest unoccupied molecular orbital
LWE	Low workfunction electrode
MCS	Multichannel systems
MIES	Metastable induced electron spectroscopy
MIM	Metal – insulator – metal
MO	Molecular orbital
MWCNT	Multi-walled carbon nanotube
NICISS	Neutral impact collision ion scattering spectroscopy
NREL	National renewable energy laboratory
OLED	Organic light emitting diode
OPV	Organic photovoltaic
P3HT	Poly(3-hexylthiophene)
PCBM	Phenyl-C61-butyric acid methyl ester
PDMS	Poly(dimethylsiloxane)
PEDOT:PSS	Poly(3,4-ethylenedioxythiophene) poly(styrene sulfonate)
PES	Photoelectron spectroscopy
PIES	Penning ionization electron spectroscopy
PPV	Poly(p-phenylene vinylene)
PV	Photovoltaic

PVD	Physical vapor deposition
RI	Resonance ionization
SAM	Self assembling monolayer
SEM	Scanning electron microscopy
SIMS	Secondary ion mass spectroscopy
SVD	Singular value decomposition
TCO	Transparent conductive oxide
ToF	Time of flight
UHV	Ultra high vacuum
UPS	Ultraviolet photoelectron spectroscopy
UV	Ultraviolet
UV-Vis	Ultraviolet-visible
VB	Valence band
VBM	Valence band maximum
VBXPS	Valence band X-ray photoelectron spectroscopy
VL	Vacuum level
XPS	X-ray photoelectron spectroscopy

List of Figures

List of Tables

1. Introduction

1.1) Nanotechnology: From its Origins to Nanoelectronics

Nanotechnology is the development of technology on the atomic and molecular scale. The nanoscale itself is 10^{-9}m (0.000000001m), and the term nanotechnology is used to describe the measurement of materials at a nanoscale resolution, and also the development and/or manipulation of materials with at least one dimension of less than 1000nm (1µm, micron) and typically <100nm. The development of nanotechnology was a gradual process throughout the 20th century, with its origins in the theoretical study of atomic structure. There is no singular discovery which facilitated this field, however there are several notable moments which deserve a mention and have led science to its current position.

Quantum theory was born in 1900 with Max Planck's law of black body radiation[1]. In 1911 the nuclear model of the atom was proposed by Ernest Rutherford, and then modified a few years later to a model still in use today known as the Rutherford-Bohr model[2] By the 1930's the electron microscope had been developed, allowing scientists to observe structures smaller than the resolutions obtainable with optical lensing techniques for the first time[3], sparking further interest that would lead to the development of many other surface sensitive techniques.

The contributions of Richard Feynman also require a mention in even the briefest of summaries on nanotechnology history. His famous 1959 lecture "There's plenty of room at the bottom" helped reorient the scientific paradigm on how to progress via a 'bottom up' approach with – as he so eloquently put – the 'building blocks of the universe', and atomic manipulation[4].

The term nanotechnology was first used by the Japanese scientist Norio Taniguchi in 1974 to describe production methods for creating structures with control at the nanoscale[5]. By the 1980's nanotechnology had become a field in its own right. Chemistry was evolving as fast as physics, with notable discoveries such as fullerenes in 1985[6], and the beginning of defined goals published in 'Engines of Creation' by Drexler in 1986[7] which was then further discussed in his 1991 book 'Nanosystems: Molecular machinery, manufacturing and computation'[8] in which he points out that the developments of nanotechnology could even create change akin to that of another industrial revolution.

In 1989, International Business Machines Corp. (IBM) scientists Don Eigler and Erhard Schweizer demonstrated the ability to arrange individual atoms by creating the IBM logo at the nanoscale using 35 Xenon atoms on a single crystal nickel substrate at 4K[9], a moment in scientific history clearly demonstrating control at the atomic scale.

Since then research has expanded in multiple directions and the use or development of nano-based technologies is now a facet in most scientific fields. Having the capability to manipulate at such a small scale has allowed new structures to be fabricated, as well as incorporate various materials that were previously unsuitable for use in many applications.

The miniaturization and reduced cost of electronic devices is one of these. The need to reduce data storage in computing systems was one of the initial drives for this particular field (and also mentioned in Feynman's 1959 lecture), and very recently IBM had a press release stating that once again they had made another pioneering step – this time by storing data on a single atom[10].

Naturally, other electronic devices such as those which either generate light (light emitting diodes, LEDs) or convert it to electricity (photovoltaic (PV) devices) have been under intensive research as well. As quoted by Nobel Laureate Professor Stephen Chu (Princeton University) in a 2014 interview: "New nanotechnology can change the rules of the ways we manipulate light. We can use this to make devices with unprecedented performance"[11]. Some of the changes in performance of LED and PV devices can be attributed to appropriate or novel material selection and overall design, but the other highly significant factor which affects performance is the ability for charge to transfer between the various layers/materials of the device thereby creating the current. These regions where various materials are in contact with each other are known as interfaces.

1.2) Surfaces and Modifications: The Formation and Importance of the Interfaces

To discuss interfaces effectively a material's surface must first be defined. In this dissertation the focus is on solid materials (as opposed to liquids or gases), and for any solid the surface is unique as it experiences a different environment to the rest of the material. The majority of the solid is denoted as the bulk, with a (largely) well-defined, static local physical and chemical environment. The surface is the small fraction of the material exposed to the external environment and thus is the region which may undergo chemical or physical interactions with the environment itself, but also any other deposited material(s). This interaction can be purely at the outermost layer of a surface but can also extend a few nanometers into the surface as well. An interface is defined as the region in which two dissimilar surfaces or phases come together. Thus, a surface is actually an interface, in this general case it is with the local environment. As such, a surface or interface in solid state physics is the region of highest interest for many applications.

A surface modification is the change brought about in a surface due to a chemical or physical interaction which alters the surface structure. A classic example of this is rust, the oxidative corrosion that occurs at the surface of metals in particular. In nanotechnology these modifications can be as simple as cleaning a surface or inducing a surface rearrangement via thermal annealing which can alter the location of desired functional groups to a specific orientation or packing structure. Modifications can also be complex and involve a series of chemical and/or physical interactions which results in an entirely new outermost surface composition or structure. Surface modifications are constantly utilized in nanoelectronics to enhance surfaces with poorly matched properties to form better, functional interfaces that are tailored for use and capable of chemically bonding and transferring charge into other layers of the device. This opens the range of potential applications for many emerging materials, as well as maximize the function of devices for any particular combination of selected materials. Creating and controlling interfaces in nanoelectronics is thus one of the most critical aspects of the technology[12-13] .

1.3) The Physics of The Interface: An Overview

Nanoelectronic devices all rely on the electronic properties and thus electronic structure of the constituent materials. To understand organic photovoltaics (OPVs) and the surfaces/ interfaces that are the focus of this work an introduction to the electronic structure of the atom and solid materials is given here, followed by an introduction to the relevant solid state physics.

1.3.1) Intra-Atomic Physics: Electronic Structure of Atoms

Most would be at least vaguely familiar with the aforementioned Rutherford-Bohr atomic model in which electrons surround the nucleus in a series of orbits of different radii known as shells. To understand electronic structure however, the quantum selection rules must be taken into account[14]. The rules can be explained through the use of four quantum numbers. The first is the principal quantum number ‘n’ (n = 1,2,3,4…) which refers to the shell in which an electron is located and in spectroscopic notation (which becomes relevant in Chapter 2) is denoted K,LM,N. The angular quantum number ‘l’ (l = 0,1.2.. (n-1)) describes the subshell or orbital, and in spectroscopy this is denoted s,p,d,f respectively. The electron spin momentum is denoted as ‘s’ = ± ½, and lastly the total angular momentum is given by ‘j’ = l + s. Together these selection rules describe the electron configuration of atoms and thus the range of energies permitted for electron occupation and can be depicted graphically, see Figure 1.1. This range of energies is known as the binding energy which is measured in electron volts (eV), and the point just beyond the highest possible permitted energy level for the atom is defined as the vacuum level (VL). The electron occupation at any given binding energy is referred to as the density of occupied states, or DOS. Furthermore, electrons can be placed into two categories: those which are in the outermost shells of the atom and can participate in chemical bonding, and those which are situated closer to the nucleus and are not affected by chemical interactions. The former are valence electrons and the latter are core electrons.

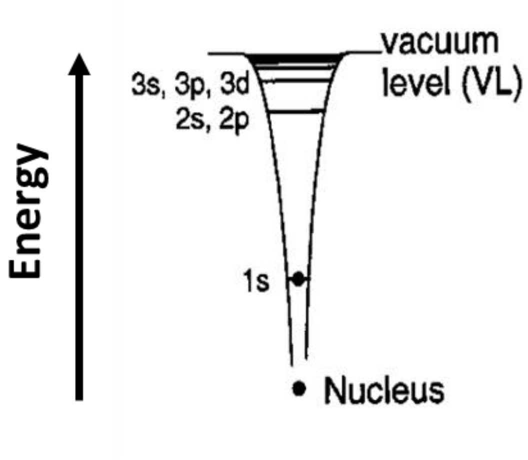

Figure 1.1: Energy level diagram for hydrogen showing electronic occupation in the 1s state. Modified image from Ishii *et.al*[15].

1.3.2) Inter-Atomic Physics: Electronic Structure of Solids and Relevant Phenomena

To introduce the reader to the relevant solid state physics for this dissertation molecular orbital theory and band theory will be introduced first (section 1.3.2.1). Then the following phenomena and terms shall be introduced: workfunction and ionization potential (section 1.3.2.2), dipoles (section 1.3.2.3), electronic excitations (section 1.3.2.4), exciton formation (section 1.3.2.5), quantum tunneling (section 1.3.2.6) and finally, doping (section 1.3.2.7).

1.3.2.1) Molecular Orbital and Band Theory

When working with materials other than free atoms the electron energy levels are discussed differently. This is due to the changes in the overall valence electron structure induced by the bonding of the constituent atoms which form new types of energy levels. Core electrons are not discussed in the following theories as they do not participate in the chemical bonding and are therefore not relevant.

For molecules the energy levels are discussed in terms of molecular orbitals (MOs). This is known as molecular orbital (or MO) theory. Just like atomic energy levels some of these orbitals are occupied, and some are not. The main points of reference are the highest occupied molecular orbital which is known as the HOMO, and the lowest unoccupied molecular orbital which is known as the LUMO, see Figure 1.2. These energy levels are of high significance in organic nanoelectronics applications as they define the conduction properties of the material.

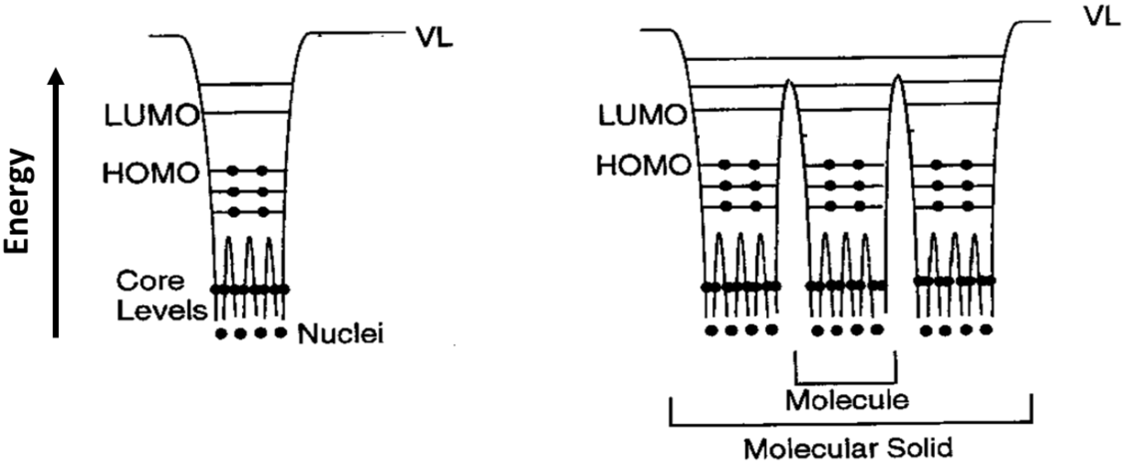

Figure 1.2: Energy level diagram for a molecule (left) and molecular solid (right). Modified image from Ishii *et.al*[15].

For materials with long range order (as opposed to discrete molecules) another theory is used to define the electronic structure. When the energy levels of the constituent atoms merge in this instance it induces bands of electron density, and as such this is known as band theory. An important reference point for energy bands is the Fermi level, which is the top of the occupied energy levels at temperatures close to absolute zero. Bands are placed into two categories with respect to the Fermi level. The valence band (VB) is located below the Fermi level and the highest occupied energy level in the VB is the valence band maximum (VBM), this is the equivalent of the HOMO in organic molecules. The conduction band (CB) is located above the Fermi level, and the lowest energy level within it is the conduction band minimum (CBM) which is the equivalent of the LUMO in organic molecules. The electrical conductivity is determined by the position of the CB relative to the Fermi level, see Figure 1.3. The difference between the VB and CB is known as the band gap. Electrically conducting materials have an overlap between the VB and CB. Insulators have a large band gap and semiconductors lie between the two extremes.

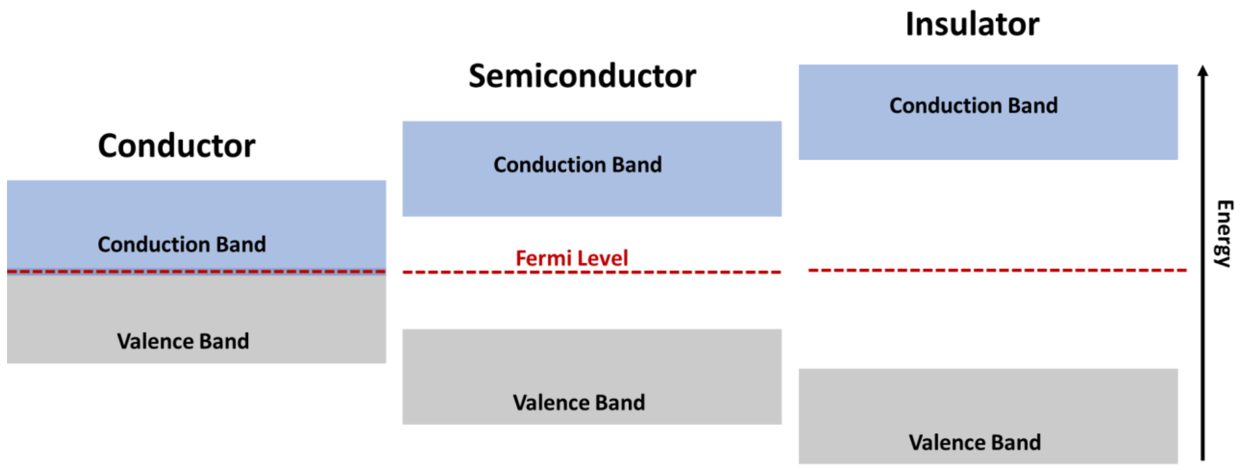

Figure 1.3: Difference in the band structure and band gap between conductors, semiconductors and insulators.

When interfaces are created between organic materials and either metals or inorganic semiconductors the energy levels align provided the organic material has sufficient charge carriers. This alignment occurs due to the flow of charge from the material with the higher Fermi energy to the material with the lower Fermi energy. In the instance of organic substances with higher electron mobility than the pure material (due to impurities), band bending occurs. It is common to find references to band gaps and Fermi levels for organic material interfaces in the literature, and these interfaces are one of the significant topics undergoing research in nanoelectronic devices due to the implications of the energy level alignment[15-19]. Energy level alignments also occur between organic-organic interfaces provided the materials have sufficient charge carriers[18], and again if the interface is produced with organic materials with sufficient charge carrier impurities band bending can occur.

1.3.2.2) Workfunction and Ionization Potential

Workfunction (Φ) and ionization potential (IP) (or ionization energy) are terms used to describe the minimum energy required to remove the most loosely bound electron from a material. The workfunction by definition is the difference between the Fermi level and VL. The ionization energy is the minimum required energy to remove an electron from an atom or molecule in the gas state, thus from the HOMO. For the case of a metal solid the workfunction and ionization energy are effectively equivalent terms due to the population of states at the Fermi level. For semiconductor materials however, the situation is more complex. For cases where the Fermi level lies within a partially filled band, the workfunction is what is measured. This state can be induced in materials by adding impurities to enhance charge carrier states (which is realistically the general case, as it is rare that materials are completely pure). For other semiconductor materials (and insulators) where the Fermi level is situated within the band gap, energetic states are forbidden in this region. Thus there is a difference between the workfunction and ionization energy in these cases, see Figure 1.4.

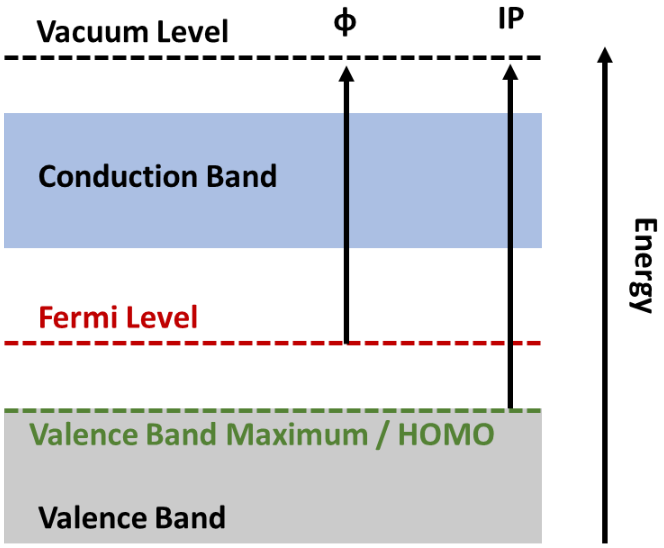

Figure 1.4: Energy level diagram of a semiconductor showing the difference between workfunction (Φ) and ionization potential (IP).

For organic semiconductors it is the IP which is reported in literature and it relates to the position of the HOMO. For inorganic semiconductors it is workfunction which is reported. This situation is more complex due to factors such as band bending, carrier concentration and surface dipoles, and the exact validity of workfunction in these instances has been considered as both variable and debatable[20], however, inorganic semiconductors generally have sufficient states such that they can align along the Fermi level and thus workfunction has been taken as the appropriate measure for these materials. The workfunction or IP of a material holds particular relevance for nanoelectronic devices as they are generally comprised of sequential layers of different materials (known as films), and for charge conduction to be facilitated in a particular direction the materials must be selected in a manner such that their workfunctions or IPs allow it [15, 21]. Also, any modifications made to a surface which includes even a slight amount of contamination can alter the workfunction of the material in question, a paper was recently published by Kahn which specifically focusses on some of the factors and mechanisms behind changes in workfunction[22]. Workfunction and IP will be further discussed in Chapter 2.

1.3.2.3) Dipoles

A surface phenomenon which is strongly influenced by the conductivity of the material is the formation of a surface dipole. Dipoles are regions of separated charge distribution or polarity in a material, and they play a strong role in charge transfer at an interface, influence surface properties and also influence workfunction[23-25]. Dipoles naturally form on pristine (perfectly clean) metal and many semiconductor surfaces as a result of the change in electron density toward the surface which forms in order to keep electrons within the solid[13]. Dipoles can also form at solid film interfaces, such as the semiconductor/ metal interfaces encountered in nanoelectronic devices[15, 26]. Dipoles have such a strong influence on charge transfer properties of interfaces that some materials in nanoelectronics are specifically engineered toward inducing dipole formation[27-28].

1.3.2.4) Electronic Excitations

Inducing electron movement is known as an electronic excitation and it can be induced by photon absorption or electrical excitation. When electron movement is induced by photon absorption the resulting effect is dependent upon the photon energy. When the photon energy matches the energy difference between an occupied and unoccupied electronic state in the material the electron is excited into this state, but still bound within the material. This can be into (for example) the LUMO in a molecule as discussed below in exciton generation, or into the CB in an inorganic semiconductor. If the incident photon energy is sufficiently high the electron can be removed from the atom entirely. This forms the basis for photoelectron spectroscopy discussed in Chapter 2.

1.3.2.5) Exciton Formation

When an electron is excited from the VB to the CB in a crystalline semiconductor or from the HOMO to the LUMO for organic semiconductors it may form an electron-hole pair called an exciton. The exciton is then capable of diffusing within the material. If an exciton reaches an energetically favourable interface within its lifetime the respective charge carriers can separate. If not, then it will relax back to the initial (also known as ground) state, this is known as recombination. The binding energy and radius of an exciton is dependent upon the dielectric constant (the ability to store electrical energy in the presence of an electric field). For inorganic semiconductors the exciton can have long range delocalization, with a low binding energy of ~10meV and a large radius in the order of ~100Å. For organic semiconductors and some inorganic semiconductors which are relatively less polarizable, the exciton has short range delocalization, with a binding energy typically much higher at ~1eV and radius much smaller ~10Å[29] see Figure 1.5. The diffusion lengths in organic materials are also significantly smaller than in inorganic crystalline materials, due to the reduced lifetime of the state which is typically less than 1ns[30].

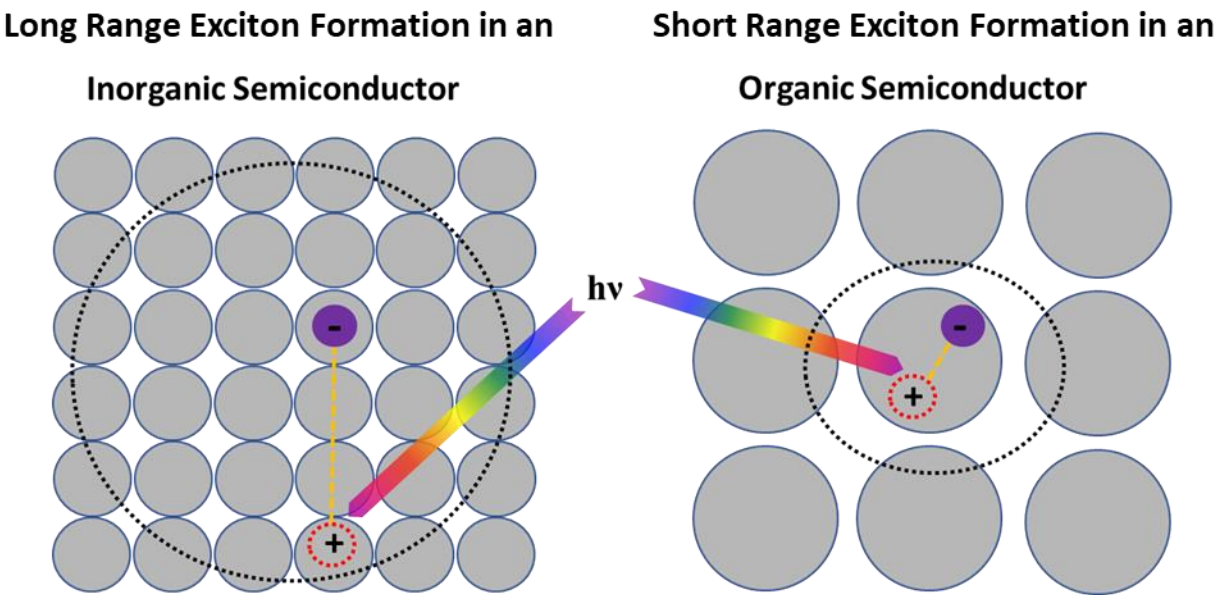

Figure 1.5: Excitons in an inorganic semiconductor (left) and organic semiconductor (right).

The difference comes from the structure within the semiconductor. Inorganic semiconductor films in nanoelectronics are of a crystalline type structure with a high degree of order which forms long range energy bands in which the exciton can readily diffuse through. For organic semiconductors the films are packed molecular structures, each of which having their own energy bands. As such, the charge carriers are required to 'hop' between these localized energy states. A consequence of this hopping mechanism is that there is generally a reduced charge carrier mobility in organic semiconductors compared to their inorganic counterparts. For a nanoelectronic device utilizing organic materials the need to match the electronic properties of constituent materials and optimize interfaces is therefore even higher, as the likelihood of exciton recombination is much higher in these materials. For further details on excitons in organic materials the reader is referred to a review on the electronic excitation energy transfer in organic materials by Laquai *et.al*[31].

1.3.2.6) Quantum Tunneling

Charge transport in metals and crystalline inorganic semiconductors occurs through the long range energy bands previously described, and for organic semiconductors via the hopping mechanism. It is also possible however for charge transport to occur through insulators if the insulating layer is sufficiently thin. This occurs via a process known as quantum tunneling[32]. Essentially, it is the ability of an electron to move through a barrier (insulator) which would be forbidden in classical mechanics. As electrons have wave like properties the resulting phenomenon is an exponentially decreasing probability function which occurs through the barrier thickness. Thus if the barrier or insulating material is sufficiently thin conduction can occur. This becomes relevant for composite material fabrication as it means insulators can be embedded with conductors or semiconductors and the distribution and contact does not necessarily have to be continuous for charge transport to occur.

1.3.2.7) Doping

One method that is employed to modify materials to alter their electronic properties is the process of doping. Doping involves adding a material to a semiconductor which changes the band gap by adding energy levels either at the bottom of the CB or at the top of the VB. These energy levels contain added charge carriers which thus alter the electronic properties including the workfunction. When the added charge carriers are electrons it's negatively doped and thus labelled as N-type doping. When the added charge carriers are the positive equivalent known as holes it's called P-type doping, see Figure 1.6.

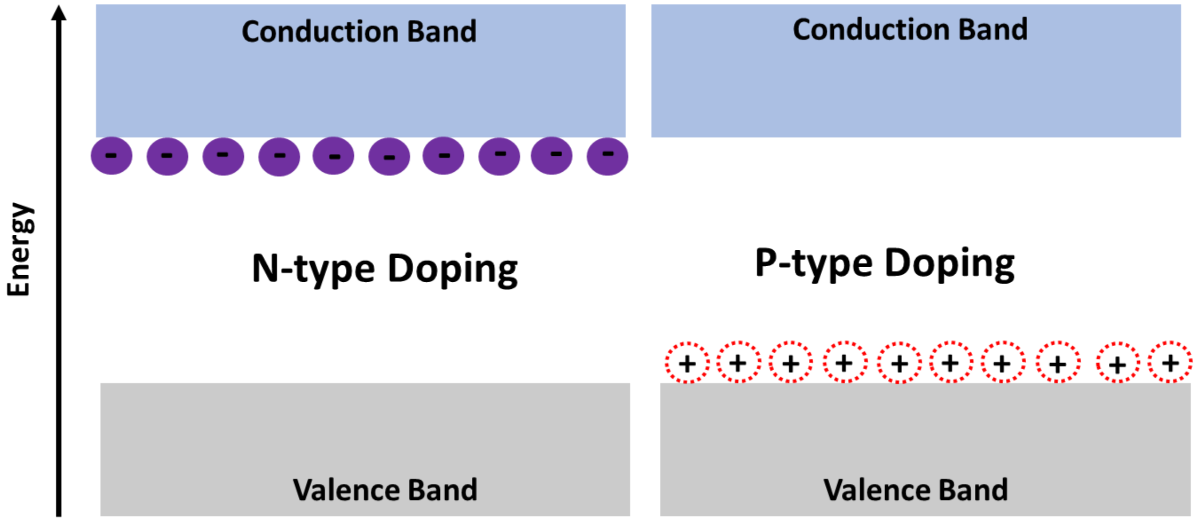

Figure 1.6: N-type and P-type doping in a semiconductor material.

Doping is a process which has been utilized in inorganic semiconductors for decades and is commonplace in nanoelectronic devices. Doping is often deliberate but can also be an inadvertent phenomenon that occurs at some interfaces due to impurities, contaminants or diffusion and segregation. Doping can also be induced in organic molecules, but this is a more recent phenomenon and is more akin to adding MOs, although the referencing of P and N type is still used[33].

1.4) The Energy Crisis and the Need for Alternatives to Fossil Fuels

The incredible developments of technology which have facilitated the ability to develop concepts and devices only few even dreamed of 100 years ago has come at a price. The industrial revolution has undoubtedly improved life for humans but has thus far required a sacrifice of overall planetary health. Despite the overwhelming scientific evidence regarding climate change, many still debate the issue, but none can debate the damage caused by the use of fossil fuels. One only needs to travel to a city such as Hong Kong or Delhi to observe the pollution levels, and there are countless images available of the damage to ecosystems caused by mining. The key world energy statistics show an average annual energy consumption of ~500 Exajoules as of 2014, with most of this still coming from fossil fuels, and it is predicted that by 2050 the energy requirements will be between 600-700 Exajoules depending upon global energy policies[34]. In the *World Energy Outlook 2017* by the International Energy Agency (IEA)[35] it was stated that the primary rising factor in worldwide energy use is electricity, with its use predicted to be 40% of the increase in energy consumption to 2040 -which is an equivalent to the rise in oil over the last 25 years, see Figure 1.7.

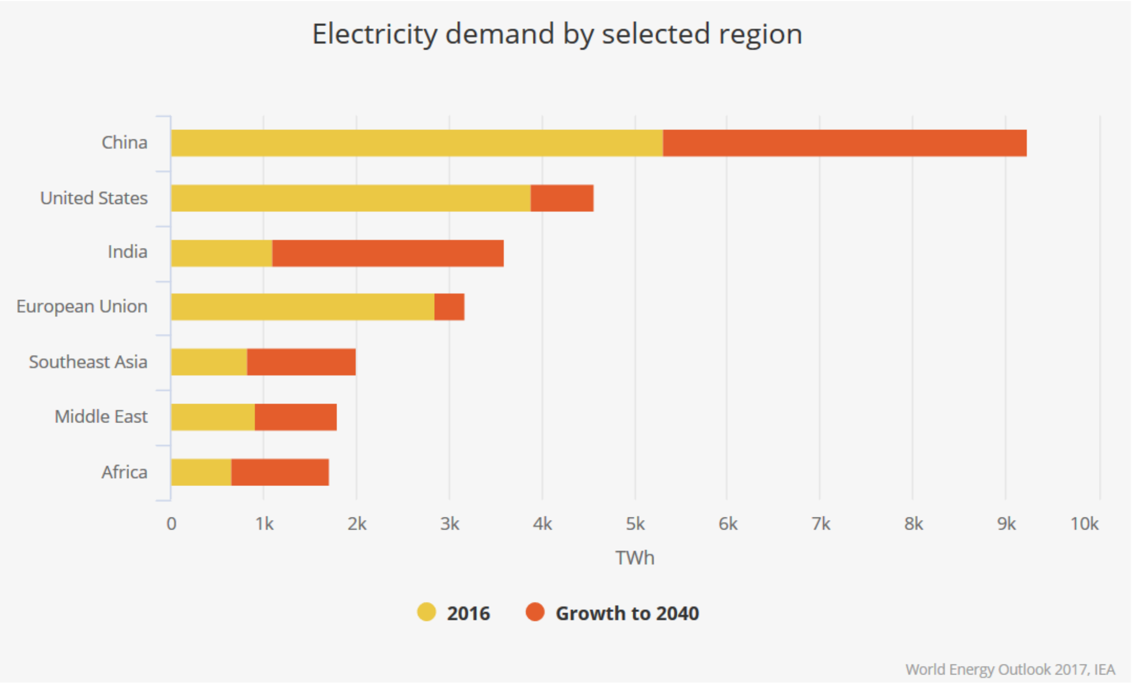

Figure 1.7: Excerpt from the IEA's World Energy Outlook 2017 showing the predicted rise in electricity demand globally[35].

New methods for energy capture and transformation into current which are highly efficient and not reliant upon fossil fuels are imperative and changes are already being implemented. In fact, renewable resources accounted for nearly two thirds of the net global new power capacity in 2016, which was partially due to the strong solar cell market[35]. Sunlight is the most prominent and readily available renewable energy source see Figure 1.8, so it is logical to continue making solar technology one of the priorities for research and development[36].

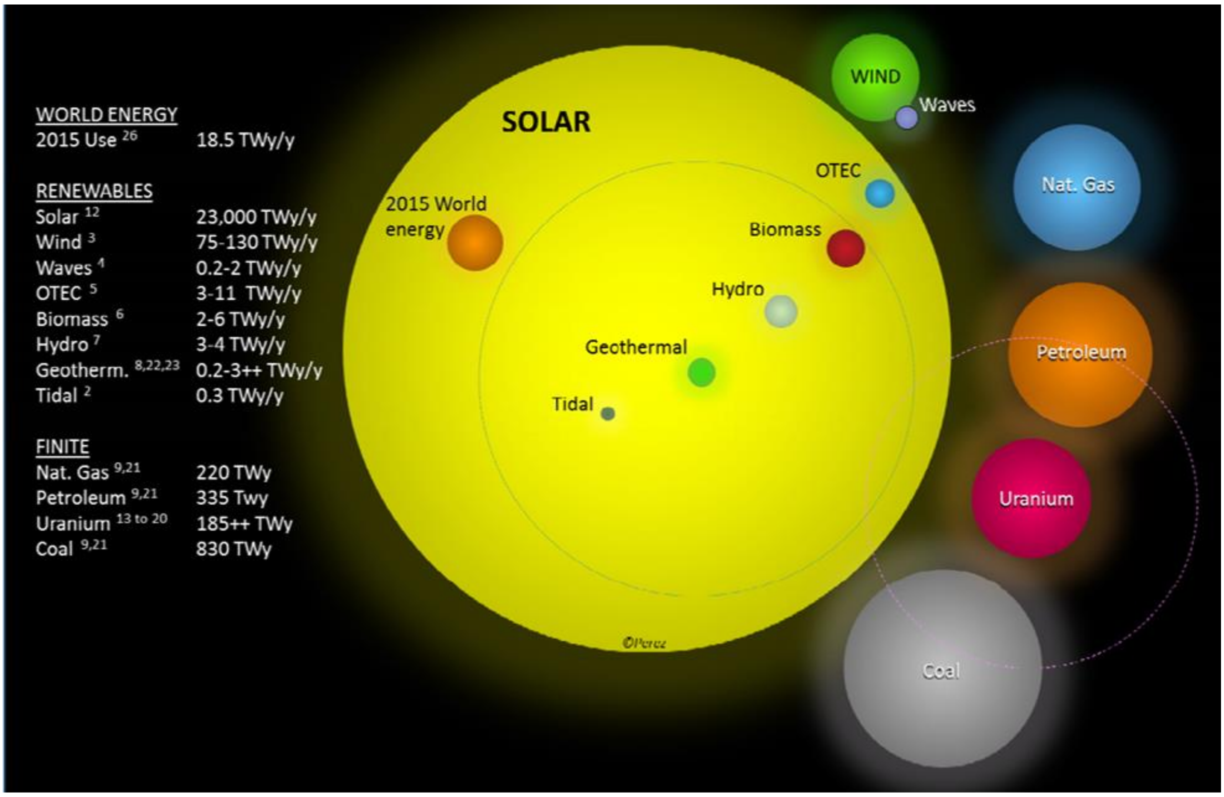

Figure 1.8: Comparing finite and renewable planetary energy reserves (Terawatt-years) in 2015. Total recoverable reserves are shown for the finite resources. Yearly potential is shown for the renewables. Reproduced from Perez *et.al*[37].

Solar panels can also be easily transported or created in different sizes so that even small towns and individual households could manufacture their own power, thus giving them a versatility that is not possible with many other ‘clean’ sources. Solar cells have such versatility that the first solar road has been installed in the Netherlands[38] and since then also in France, and applications are considered in many other areas as well including for water pumping and space applications[39-41]. However, continuing research into different cell types and ways of improving their efficiencies is still important despite the advances which we’ve already made globally so that the role of solar cells may become even more diverse and hopefully become a global primary resource.

1.5) Solar cells

Solar cells are the common name for PV cells which utilize light emitted from the sun to extract energy. The PV effect is a phenomenon which can occur when an incident photon is absorbed into a material with sufficiently high charge carrier concentration. The process is as follows: photon absorption excites a charge carrier to a higher energy state within the material which is then transported (via diffusion or an internal electric field) to an interface. When charges accumulate at the interface a photovoltage is produced, and the extraction of these accumulated charges to an external circuit allows work to be done in the circuit. PV cells are devices which utilize this effect to then extract the separated charge carriers to an external circuit. This is facilitated by combining materials with appropriate P-N differences in charge carrier properties. The interface(s) where the materials meet is called a junction.

The history of these cells began in 1839 when Alexandre Becquerel discovered that a current was induced when he illuminated an electrochemical cell comprised of platinum electrodes and an acidic silver chloride solution[42]. In the 1870's the concept that photon absorption can induce current (known as photoconductivity) was firmly established with experiments using selenium[43]. The first single junction solid state PV cell was created by Charles Fritts in 1883 using selenium on a layer of gold which had an efficiency of <2%[44] . Since then a myriad of devices have been created, which will now be discussed in order of discovery. A detailed summary of devices and recorded efficiencies is available online and updated each year through the National Renewable Energy Laboratory (NREL)[45].

1.5.1) First Generation Solar Cells

In the 1950's the use of silicon was discovered to be far more efficient than selenium and cells with ~6% efficiency were produced by the physicists at Bell laboratories[46]. This gave rise to the first generation of solar cells available on the commercial market. This cell type is denoted as a homojunction cell, as the materials creating the junction are only different in their dopants. In this instance it is created via the doping of silicon, some to become P-type, the other N-type, so the junction is also called a P-N junction. Silicon based cells have evolved greatly since their discovery and are the most predominant cell type in mainstream production with efficiencies now as high as 26.7% as of 2017[47]. The downside to this cell design is that production is expensive both financially but also energetically. The silicon must be purified, crystallized into wafers and diced before placement in the cell, which uses up large amounts of energy and materials[48]. These solar cells are also relatively heavy and inflexible which limits their range of placement.

1.5.2) Second Generation Solar Cells

Second generation cells began with the use of thin film technology to replace the use of crystallized silicon (Si) wafers and thus reduce material consumption. The use of thin films means that the cells are less fragile than the first generation and can have some level of flexibility. The downside to these cells is that they generally contain scarce elements and production involves high temperatures and vacuum conditions due to the reactive nature of the films. These cells typically include thin films such as CdS, CdTe, $CuInSe_2$ and amorphous Si[49].

1.5.3) Multijunction Cells

The use of thin films has also facilitated the ability to create multijunction cells. Multijunction or 'tandem' cells have been placed in both the second[50] or third[51] generation solar cells categories. These cells are the most successful as far as efficiencies are concerned, devices have been fabricated in the laboratory with efficiencies as high as 46% using a GaInP/GaAs; GaInAsP/GaInAs structure[47] yet the issue with scarce material use and cost is still a problem.

1.5.4) Third Generation Solar Cells

Third generation cells remain focused on thin film technology, the difference is that these cells incorporate nanostructured semiconductors in the device structure. This has created two tangents of researched cells called group A and group B. The target of group A is toward fabricating devices which utilize quantum effects such as hot carrier injection and multiple electron-hole pair production. These devices have theoretical efficiencies much higher than that of single junction cells but these approaches are yet to produce highly efficient devices[50, 52]. Group B are instead focused on achieving low cost devices with moderate efficiencies. Both the group A and group B ventures show promise, and these third generation cells have potential to become the lowest financial and energetic cost devices produced if efficiencies can be sufficiently increased see Figure 1.9.

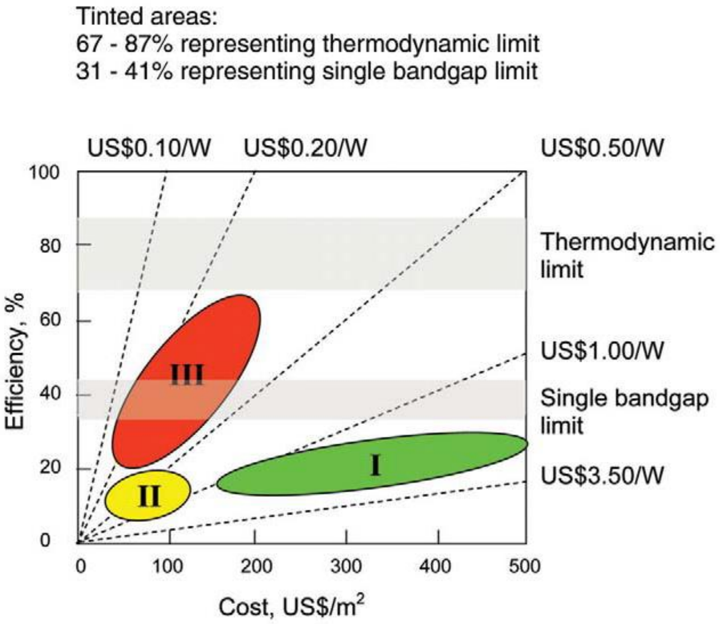

Figure 1.9: Efficiency and cost projections for first- (I), second- (II), and third generation (III) PV technologies (wafer-based, thin films, and advanced thin films, respectively). Figure reproduced from[53], originally published by Green[54].

1.6) Organic Photovoltaics (OPVs)

OPVs are the subcategory of third generation, group B solar cells which utilize organic materials (predominantly conjugated polymers and fullerene derivatives) to create the photoactive layer. This use of organic materials in thin film technology gives these cells beneficial properties such as flexibility, reduced mass, and transparency to many of the wavelengths not absorbed by the cell itself. These cells also have the benefit of cheaper fabrication via solution processing methods[55-56].

1.6.1) OPV Development: Basic Structures and Principles of Operation

The first OPVs were produced in 1983 and were a simple design consisting of a single photoactive layer material between two electrodes[57]. The greater the workfunction difference between the electrodes, the greater the overall voltage difference between them (which is the cell potential, ΔV_{cell} shown in Figure 1.10), as described by the metal – insulator – metal (MIM) model[58].

This basic structure of an OPV is relatively simple (see Figure 1.10) and involves three materials and therefore two interfaces and consists of the organic photoactive layer and two electrodes. One electrode is the low workfunction electrode (LWE) which is metallic, and the other is the high workfunction electrode (HWE), which needs to be transparent to allow light into the photoactive layer. Electrode selection is ultimately dependent upon the energy levels of the active layers. If the energy level difference between the materials is too large then charge separation will not be energetically favourable. As such, the LWE needs to match the LUMO, and the HWE match the HOMO, both as closely as possible.

The basic overview of the mechanisms behind cell function is as follows and is numerically labelled in Figure 1.10 and Figure 1.11: 1) Photon absorption in the active layer induces exciton generation, 2) random diffusion of the exciton occurs through the layer, 3) charge separation occurs 4) once the charges are separated the cell potential induces diffusion of the charges to the respective electrodes for collection at the electrodes. Further discussion on OPV charge generation and functioning principles can be found in the literature[59-60].

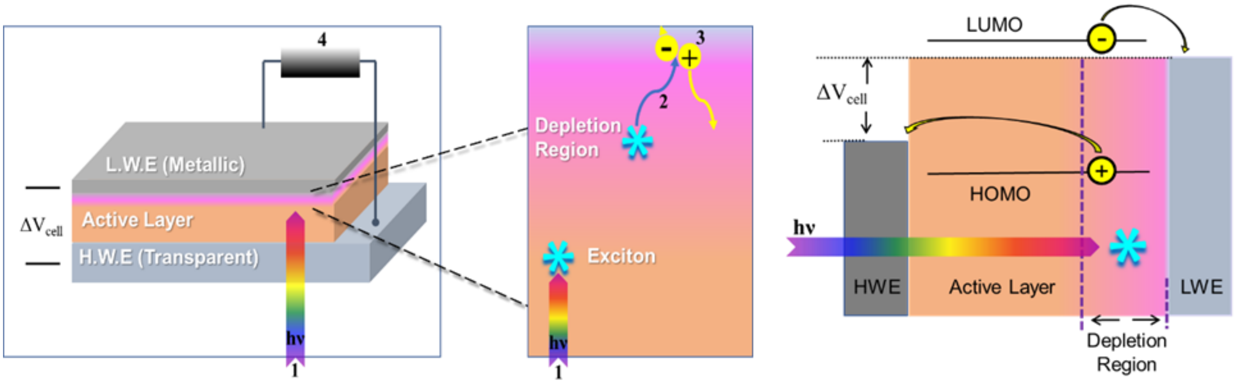

Figure 1.10: General structure of the first OPV (left), with corresponding energy levels (right). The four main mechanisms of cell function are labelled 1-4 and described in the text.

Although this cell worked, the efficiency was exceptionally low. The only region in which exciton dissociation could occur is in the depletion region which is at the active layer/ LWE interface. The separation is there facilitated by the potential difference between the organic material and the metal[15] allowing circuit completion to occur. Excitons have no net charge until dissociated, so the diffusion through the active layer is random. As the typical lifetime and thus diffusion length is so short in organic materials the chances of recombination prior to reaching the appropriate interface is high for this cell structure.

It was in 1986 that the first bilayer heterojunction cell was introduced by Tang *et.*al[61], so named due to the use of two layers of organic materials in the active layer. One of which being a P-type polymer denoted a ‘donor’ (due to the electron donation), and the other an N-type organic material, denoted an ‘acceptor’. The role of the acceptor is to create an energetically favourable situation for the exciton to split into the electron/ hole pair, which minimizes the chances of recombination and enables the cell potential to draw the charges to the respective electrodes. This cell structure was more successful than the mono-active layer cell, this was attributed to improved electron/hole separation occurring at the interface between the two active layer materials. The presence of an extra material (and thus extra interface) in the cell permitted more ‘steps’ in the cell, thus reducing the difference in energy levels at each interface.

In 1995 another improvement to OPV active layer structure was developed independently by several research groups: Heeger *et.al*[62], Hiramoto[63-64] and Yoshino[65] and is known as a bulk heterojunction (BHJ) OPV, see Figure 1.11. The difference in this cell structure is that the active layer materials are blended such that they have phase separation and a nanoscale morphology, which results in a significantly larger interfacial area within the layer. This significantly increased the interfacial region between the donor and acceptor throughout the active layer which allows for a much larger portion of the generated excitons to reach an interface prior to recombination. However, despite further improving the overall cell efficiency, the theoretical limits of the cell still could not be reached using just this structure.

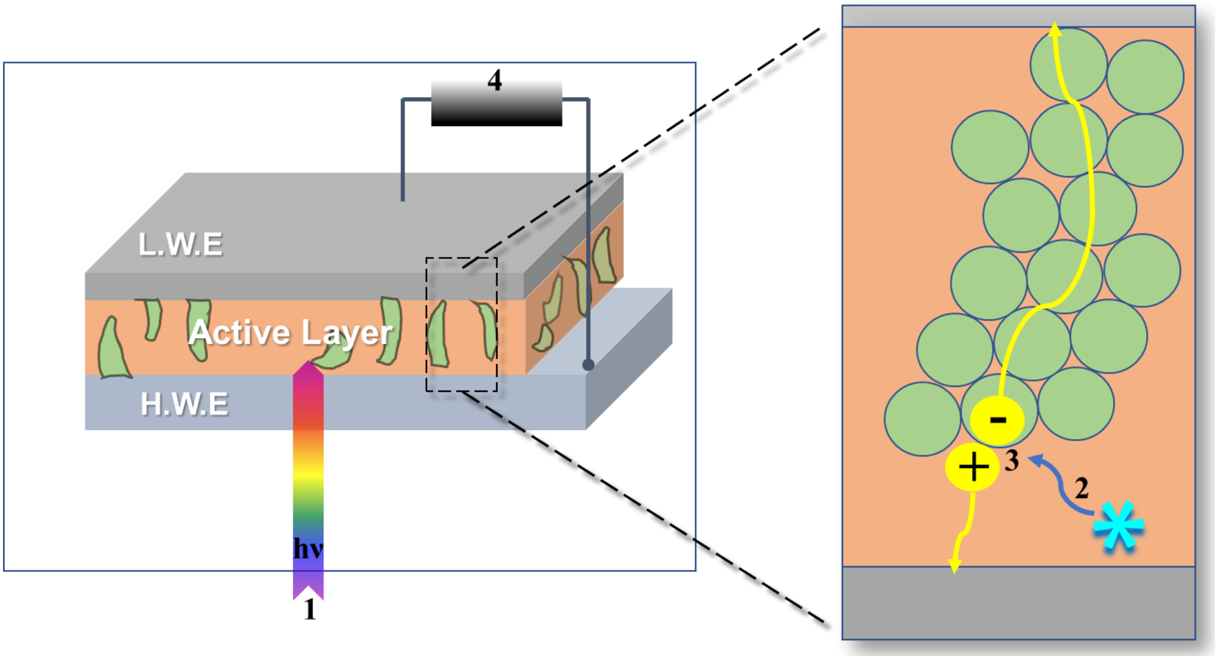

Figure 1.11: General schematic of a BHJ OPV. In this image the active layer has been enhanced, displaying the nanophase morphology of the active layer. The donor polymer is shown in beige, the acceptor molecule (generally a fullerene derivative) is shown as green balls. The four basic mechanisms of cell function previously described in the text are also displayed in this figure.

This cell structure is known as the conventional structure, other cell structures have also been developed. These include inverted cell structures where the function of the electrodes has is opposite to that in a conventional cell, and tandem cell structures which are effectively two cells built into one which absorb at different frequencies of the electromagnetic spectrum. Each cell structure has their own advantages and disadvantages, however the mechanisms behind charge transfer and various interfacial phenomena are universal to all OPV structures. A comprehensive discussion on different cell designs can be found in the literature[66].

1.6.2) Interfacial Buffer Layers and their Influence on Performance

It is clearly possible to fabricate an OPV cell using only the active layer and electrodes, but despite advances in the BHJ style of active layer, cell performance remains below the theoretical limits of the cell as well as having a short working lifetime. This is largely due to issues with active layer/ electrode interfaces[67-70]. Upon deposition, inter-diffusion of the electrode materials into the active layer can occur. This process creates creates charge ‘traps’ that accept the charge carrier prior to collection at the electrode and thus reduce the efficiency of the cell[71]. The evaporation process for the LWE is known to induce chemical interactions which occur between the hot metal atoms and organic materials which is known as bonding induced degradation[15]. Reactions at the electrode/ organic interface reducing charge transport are another known degradation mechanism acting in a cell[67]. Delamination of the electrodes can also occur due to poor adhesion or worse, corrosion between the interfaces[69].

The use of interlayers between the active layer and respective electrodes (see Figure 1.12, left) has been shown to clearly assist with these issues by preventing diffusion and also protecting the active layer upon electrode deposition, and they significantly enhance device performance. For the HWE/active layer interface the interfacial layer is commonly referred to as the hole transporting layer (HTL), and for the LWE/ active layer interface the interfacial layer is referred to as the electron transporting layer (ETL). The use of these interlayers assists in bridging the energy level gap between the active layer and respective electrode, thus making charge transfer more energetically favourable[72] (Figure 1.12, right), the aim is to achieve ohmic contact[73]. The interlayers can also improve the charge transfer selectivity at the electrode by blocking unwanted charge carriers (holes at the LWE, electrons at the HWE)[74]. Interfacial buffer layers have become the most effective method for interfacial engineering in OPVs and are an inherent part of modern device architecture which are no longer considered as optional[75-76].

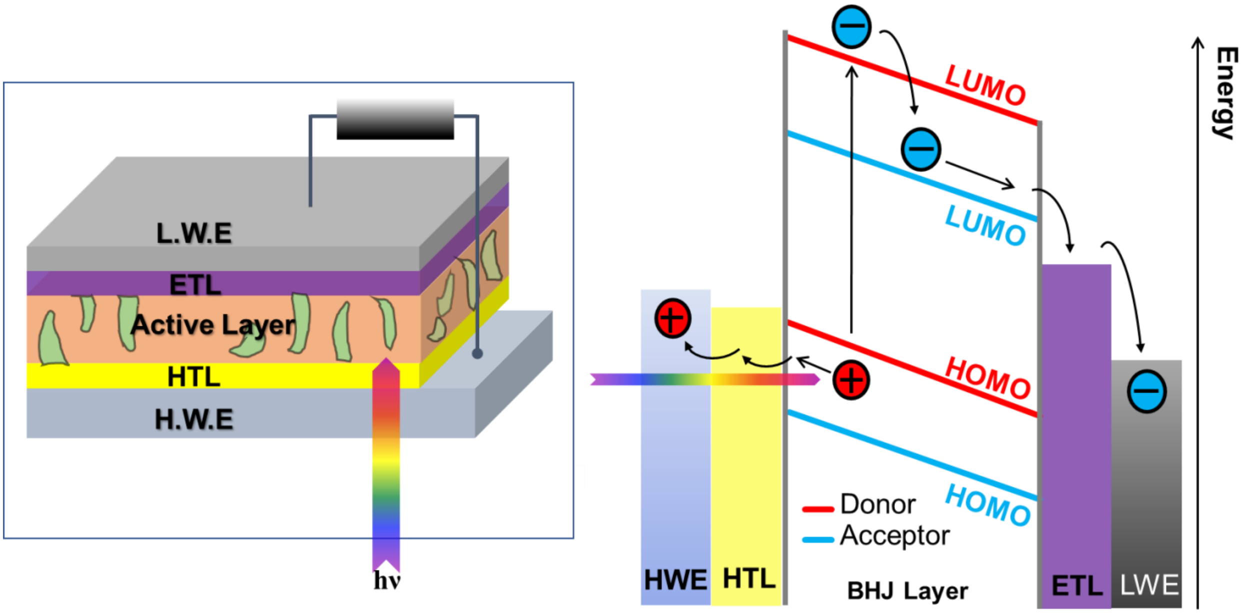

Figure 1.12: BHJ OPV structure including the use of interfacial buffer layers (left), with corresponding energy level diagram (right) displaying the extra energy ‘steps’ facilitated by the buffer layers.

1.7) OPV Materials and Fabrication

For charge transport to be successful the correct combination of materials must be selected as it has a critical effect on the cell efficiency. Careful material selection can also assist in the prevention of degradation in the cell[77]. In a review by Scharber in 2006[58] it was presented that the cell efficiency potential for BHJ OPVs is not the difference in workfunction of the electrodes (MIM model) but in fact is dictated by the molecular energy levels of the constituent active layer materials, as such the correct materials selection is imperative. The electrode materials then need to be selected so that there is a sufficient difference in workfunction between them, and one electrode along with its interfacial layer must be transparent to allow sunlight into the cell itself. The purity of each layer within the cell is also crucial to device performance, as impurities potentially alter the charge transport and/or incite degradation within the cell. The following materials discussion is focused on the conventional OPV structure, they can be used in the other cell structures although they may be used in a different manner to that stated here.

1.7.1) Electrodes

The choice of electrode materials is largely dependent upon the choice of the active layer materials. Electrodes have traditionally been made from metals, as their conductivity and work functions are well known, allowing voltage gradients to be easily created across the cell. For the LWE in a traditional OPV device structure the use of a metal is still commonplace, as the electrode does not require transparency for cell operation. The use of aluminium as the LWE has been widely accepted and is used in many devices[78-80]. Other metals can also be used depending on the desired electrode workfunction.

There are issues with the HWE material selection. The electrode needs to be transparent so that light can enter the cell and induce the PV effect in the active layer, and as such, a metal film is not appropriate for use. The most common material choice is indium tin oxide (ITO)[81-83]. ITO fits the requirements of optical transparency and conductivity and has had much success in the laboratory, however the ability to upscale to industrial purposes is limited as indium is a scarce material. Most of the global indium consumption is caused by ITO production and it is generally a by-product of zinc mining rather than specifically sourced[84]. ITO is mechanically brittle, there are transparency issues in the near infra-red region, large energy requirements for processing, and there are contamination issues with ITO-OPVs due to diffusion[85]. As such, a range of ITO free alternatives for the HWE which can be placed into three general categories: alternative metal oxides, carbonaceous electrodes, and hybrid/ composite materials. Each of these have their own advantages and disadvantages, so research continues on each. An introduction to the use of ZnO as one of these alternative materials will be given in Chapter 5. As alternative electrode materials is a lengthy discussion in its own right the reader is also referred to the literature[86-89].

1.7.2) Active Layer

1.7.2.1) Donor Materials

It is well accepted that a large contributing factor towards cell efficiency is the ability of generated excitons within the donor material to effectively separate[82]. This is an inherent issue with using polymeric semiconductors as active materials, as the charges are required to utilize a hopping mechanism to move between the delocalised π states which are the charge carrier regions of the molecular chains (as opposed to moving though the bands present in materials such as silicon). As such, there is a large range of conjugated polymers researched for use as electron donor materials, with novel polymers and conductive polymer nanocomposites continually under development[90-91]. Thiophenes are one the prevalent classes of polymers used as donor materials[92], with Poly (3-hexylthiophene) (P3HT) being a predominant choice[73] (see Figure 1.13) due to its stability, scalability and processability in fabrication. A recent development is the fabrication of a cell using P3HT and environmentally friendly solvents was seen to achieve efficiencies of 11.7% [93].

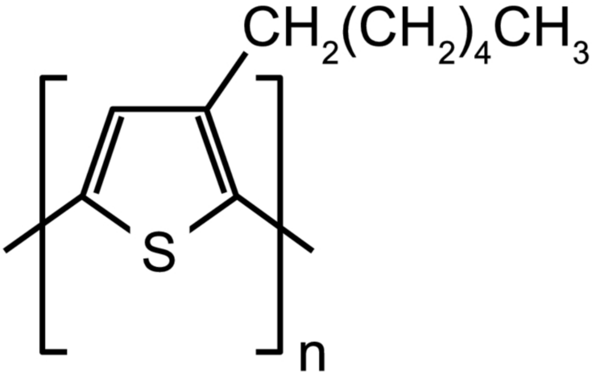

Figure 1.13: Molecular structure of P3HT, image reproduced from Researchgate[94] .

An alternative to thiophene based polymers as donor materials is the use of small molecules. Cells utilizing small molecule donors have had efficiencies of over 8%[91], however the optimization of these cell types typically relies on post processing techniques to improve the morphology of the BHJ layer, and like with other OPVs it is again reported that a deeper understanding of device physics is required[95].

1.7.2.2) Acceptor Materials

The predominant choice for electron acceptors are C_{60} and C_{70} fullerenes and their derivatives[91, 96-97]. Fullerenes were first recognised as highly suitable electron acceptor molecules in 1988[98] with gas phase experiments. The fullerene structure is predominantly sp^2 hybridization, however due to the curvature of molecule it technically lies between sp^2 and sp^3, and found to be $sp^{2.28}$ for theoretical calculations[98]. The hybridization is also variable depending on how the structure is modified. As a result, many different fullerene derivatives have been researched and tested. A common choice for OPVs is [6,6]-phenyl-C_{61}-butyric acid methyl ester (PCBM) which was developed in 1995[99], see Figure 1.14. PCBM has been seen to stabilize the active layer by reducing the degradation rate under different conditions[100], but for some choices of donor polymer it is suspected that the PCBM enhances the degradation, which highlights the need for careful material selection and testing[77].

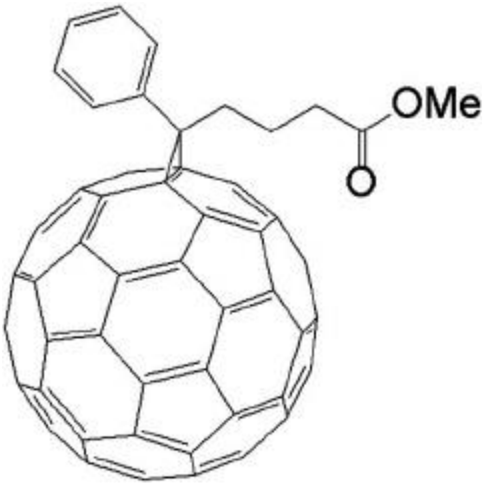

Figure 1.14: Molecular structure of PCBM, image reproduced from Researchgate[101] **.**

Other organic electron acceptor alternatives are also under investigation for use in OPVs. The first bilayer OPV previously mentioned used a perylene based small molecule, and since then other rylene diimides[102] and other small molecules have also been used[103]. Other alternatives include carbon nanotubes (CNTs), graphene based acceptors, poly(phenelene vinylene (PPV) and its derivatives, and alternative symmetric molecules to fullerenes which are electron acceptors. All of which are discussed in reviews in the literature[104-105], as is a discussion on the physics of small molecule electron acceptors as fullerene replacements[106].

1.7.3) Interfacial Buffer Layers

As discussed, the HTL and ETL interfacial layers have several roles in a device and different materials are required to meet the needs at each active layer/ electrode interface. For the HTL the most predominant interlayer choice for devices which still utilize ITO as an electrode is poly(3,4-ethylenedioxythiophene) poly(styrenesulfonate) (PEDOT:PSS). However PEDOT:PSS is rather acidic and can corrode the electrode, so alternatives have been developed, these include metal oxides, graphene oxide, organic polymers and self assembled monolayers (SAMs)[107].

For the ETL the material selection is as large as that for the HTL, with novel materials and combinations constantly under development[108]. One of the predominant choices for the ETL has been the use of alkali halide salts, with lithium fluoride (LiF) being a common choice, this will be discussed further in Chapter 6. The use of a bilayer metal electrode has also seen some success. A low workfunction metal layer which does not require high temperatures for deposition is deposited prior to the Al or Ag electrode layer, which acts as a protective barrier for the organic materials from the hot metal atoms upon their deposition[108]. Metal oxides are an option for this interlayer as well, with popular choices being ZnO or TiO_2[107]. The large range of properties available with the various metal oxides (which includes ternary metal oxides), and the ability to use doping to convert many metal oxides between n or p type materials means they can be utilized in several ways in an OPV. Several polymers, small molecules and SAMs also have been synthesized which can be used for this interlayer. The range of materials used for interlayers in an OPV is clearly extensive, and novel materials and combinations are continually being developed[109-110].

1.8) Film preparation and Morphology: Impact on the Interface

As well as material selection the film preparation/ deposition method plays an imperative role in its final properties. The OPV niche in the PV industry is for inexpensive fast processing and manufacturing with the aim of roll to roll processing for full device fabrication[111]. Achieving this is not trivial, and in most instances there is still a range of techniques utilized in device fabrication, especially whilst still working on material or device optimization in the laboratory. Here fabrication methods are discussed with a focus on individual layer preparation and modification rather than complete device fabrication methods, as this dissertation is on the investigation of various thin films.

1.8.1) Common Film Preparation Methods

Film preparation can be loosely grouped into two categories. One is the use of wet chemical methods (solution processing). Wet chemical methods include spin coating, sol-gel, lithography, spray pyrolysis, and printing methods such as screen or inkjet printing amongst others[112]. These processes fit the OPV aim in that they are inexpensive, however they have the disadvantage in that the resulting film morphology can be imprecise. The other category for film preparation is the use of vacuum environments. This is broken down into chemical vapor deposition techniques (CVD) which can include the use of aerosols, plasmas or precursor reactants, or physical vapor deposition (PVD) techniques which are predominantly evaporation or magnetron sputter deposition. These techniques have a high degree of precision and the resulting film morphology is more guaranteed. However, the infrastructure required can make it a costly process. These methods are highly advantageous in the laboratory in that films deposited with these techniques are highly precise and thus allow certain parameters or phenomena to be more accurately measured, enabling a ‘bottom up’ approach for OPV research.

1.8.2) Influences on the Interface

A critical aspect of working with solid surfaces is that the surface structure or composition is not necessarily the same as the bulk of the material, and in reality, is usually different. As such, many materials which are considered to have appropriate properties for use in an OPV device may not perform in the manner expected, and as a result the films require detailed investigations into the electronic structure and physical profile of the created surface(s). Some films may then require modification(s) during the manufacturing process for a device to efficiently function. The difference between a surface and the bulk of a film is due to the fact that chemical/ intermolecular bonds at the surface are under larger strain than the bulk because of the difference in local environment. This difference between the bulk energy of the material and its surface is known as the surface energy. Surfaces will always conform to the lowest surface energy possible which has a number of implications.

For films which have been produced via wet chemical methods such as the curing of polymers the formation of the outermost layer during the curing process will naturally be to the lowest surface energy conformation. For neat (single material) films this can mean that certain function groups may be all facing in a particular orientation (which may or may not be favourable), and for composite films (two or more materials in the final product) this can mean a significantly different composition between the surface and the bulk, as polymeric creep can occur during the curing process as well as diffusion. A prime example of this is the morphology of the highly popular solution processed P3HT/PCBM active layer blend. As a part of this Author's Honours dissertation an investigation of a spin coated 1:1 P3HT:PCBM blend was performed to study the vertical molecular distribution of the film via concentration depth profiles, and also investigated the electronic properties of the outermost layer and near surface area of the film[113]. The results showed that the outermost layer of the film was predominantly P3HT with a PCBM rich phase just below the surface. The PCBM rich phase near the surface would be desirable for OPVs, but the P3HT outermost layer may affect charge transport through to the LWE. These findings have also been reported by others[114-116]. Diffusion is a phenomenon which can also occur irrespective of polymer curing processes and was noted as one cause of degradation in section 1.6.2, however diffusion can also be beneficial to device function, but still requires mapping to understand the device fully[117].

The deposition method can greatly affect both the morphology of a film and also its electronic properties[110, 118-120]. Films produced in vacuum conditions may have a more controlled morphology compared to solution processing, but deposited layers often still differ in electronic structure and or morphology depending on the reaction conditions and substrate/film upon which it is deposited, as the resulting interfaces can have different chemical reactions or electronic affinity.

Surface cleanliness is another factor which will affect a fabricated surface or interface. Unless a perfectly controlled atmosphere (such as a glovebox with an inert atmosphere such as argon) is adopted amorphous hydrocarbons and oxygen are usually present on the surface of films prepared in air and they will possess non-ideal electronic properties. For films fabricated under vacuum conditions exposure to atmosphere can completely alter the surface structure as the films often have a high surface energy which attracts contamination very quickly. Thus, surface modifications can very easily occur and do so unintentionally. There are many surface cleaning procedures used for thin films and these include heating, plasma, sputter cleaning and solvent use. All of these have different influences on the film’s surface. Heating can also be used as an annealing process which can increase the crystallinity of some films and is a standard approach for the case of P3HT/PCBM cells[121-123], but even this can reduce rather than enhance the cell efficiency if an inappropriate electrode/ buffer layer is selected[124].

There are clearly many factors able to influence interfacial phenomena and hence affect the mechanisms acting to enhance (or reduce) charge carrier mobility at the interfaces within an OPV which are clearly material dependent and no unique solutions exist. The impact of interfaces and associated phenomena on electronic structure and properties of materials is so great that entire books have been dedicated to it[13, 125-127] and research remains ongoing.

1.9) References

1. Planck, M., On the Law of Distribution of Energy in the Normal Spectrum. *Annalen der Physik* **1901**, *4*, 1-11.

2. Bohr, N., Lxxiii. On the Constitution of Atoms and Molecules. *The London, Edinburgh, and Dublin Philosophical Magazine and Journal of Science* **1913**, *26*, 857-875.

3. Young, J., The Early Development of Electron Lenses and Electron Microscopy, *Microscopica Acta. Supplement,* **1981**; Vol. 32, p 214-214.

4. Feynman, R. P., There's Plenty of Room at the Bottom. *Engineering and Science* **1960**, *23*, 22-36.

5. Taniguchi, N., On the Basic Concept of Nano-Technology. *Proc. Intl. Conf. Prod. London, 1974* **1974**.

6. Kroto, H. W., Heath, J.R, O'Brien, S.C, Curl, R.F, Smalley, R.E, C60: Buckminsterfullerene. *Nature* **1985**, *318*, 162-163.

7. Drexler, E., Engines of Creation; Anchor Books: New York, **1986**.

8. Drexler, E., Nanosystems: Molecular Machinery, Manufacturing and Computation; Wiley-Interscience: New York, **1991**.

9. Eigler, D. M.; Schweizer, E. K., Positioning Single Atoms with a Scanning Tunneling Microscope. *Nature* **1990**, *344,* 524.

10. Natterer, F. D.; Yang, K.; Paul, W.; Willke, P.; Choi, T.; Greber, T.; Heinrich, A. J.; Lutz, C. P., Reading and Writing Single-Atom Magnets. *Nature* **2017**, *543,* 226.

11. Sullivan, J., https://www.Princeton.Edu/News/2014/09/24/Nanotechnology-Leads-Better-Cheaper-Leds-Phones-and-Lighting. **2014**, news article.

12. Iwamoto M., Kaneto K., Mashiko S., Nanotechnology and Nano-Interface Controlled Electronic Devices; Elsevier, **2003**.

13. Brillson, L. J., Surface and Interfaces of Electronic Materials; Wiley-VCH: Weinheim, **2010**.

14. Eisberg R., R. R., Quantum Physics of Atoms, Molecules, Solids, Nuclei and Particles; Hamilton Printing Co.: USA, **1985**.

15. Ishii H., Sugiyama K., Ito E., Seki K., Energy Level Alignment and Interfacial Electronic Structures at Organic/Metal and Organic/Organic Interfaces, *Advanced Materials,* **1999**; Vol. 11, pp 605-625.

16. Oehzelt, M.; Koch, N.; Heimel, G., Organic Semiconductor Density of States Controls the Energy Level Alignment at Electrode Interfaces. *Nature Communications* **2014**, *5*, 4174.

17. Hill, I. G.; Milliron, D.; Schwartz, J.; Kahn, A., Organic Semiconductor Interfaces: Electronic Structure and Transport Properties. *Applied Surface Science* **2000**, *166*, 354-362.

18. Vázquez, H.; Gao, W.; Flores, F.; Kahn, A., Energy Level Alignment at Organic Heterojunctions: Role of the Charge Neutrality Level. *Physical Review B* **2005**, *71*, 041306.

19. Elumalai, N. K.; Uddin, A., Open Circuit Voltage of Organic Solar Cells: An In-Depth Review. *Energy & Environmental Science* **2016**, *9*, 391-410.

20. Walsh, A.; Butler, K. T., Prediction of Electron Energies in Metal Oxides. *Accounts of Chemical Research* **2014**, *47*, 364-372.

21. Zhang, Z.; Yates, J. T., Band Bending in Semiconductors: Chemical and Physical Consequences at Surfaces and Interfaces. *Chemical Reviews* **2012**, *112*, 5520-5551.

22. Kahn, A., Fermi Level, Work Function and Vacuum Level. *Materials Horizons* **2016**, *3*, 7-10.

23. Leung, T. C.; Kao, C. L.; Su, W. S.; Feng, Y. J.; Chan, C. T., Relationship between Surface Dipole, Work Function and Charge Transfer: Some Exceptions to an Established Rule. *Physical Review B* **2003**, *68*, 195408.

24. Lee, H. J.; Jamison, A. C.; Lee, T. R., Surface Dipoles: A Growing Body of Evidence Supports Their Impact and Importance. *Accounts of Chemical Research* **2015**, *48*, 3007-3015.

25. Good, R. J., Surface Free Energy of Solids and Liquids: Thermodynamics, Molecular Forces and Structure. *Journal of Colloid and Interface Science* **1977**, *59*, 398-419.

26. Hu, Z.; Zhong, Z.; Zhang, K.; Hu, Z.; Song, C.; Huang, F.; Peng, J.; Wang, J.; Cao, Y., Dipole Formation at Organic/Metal Interfaces with Pre-Deposited and Post-Deposited Metal. *NPG Asia Materials* **2017**, *9*, e379.

27. Ma, H.; Yip, H.-L.; Huang, F.; Jen, A. K. Y., Interface Engineering for Organic Electronics. *Advanced Functional Materials* **2010**, *20*, 1371-1388.

28. Shu, A. L.; McClain, W. E.; Schwartz, J.; Kahn, A., Interface Dipole Engineering at Buried Organic–Organic Semiconductor Heterojunctions. *Organic Electronics* **2014**, *15*, 2360-2366.

29. Pope, M., Swenberg, C.E, *Electronic Processes in Organic Crystals and Polymers*; Oxford University Press: Oxford, **1999**, p 1328.

30. Tamai, Y.; Ohkita, H.; Benten, H.; Ito, S., Exciton Diffusion in Conjugated Polymers: From Fundamental Understanding to Improvement in Photovoltaic Conversion Efficiency. *The Journal of Physical Chemistry Letters* **2015**, *6*, 3417-3428.

31. Laquai, F.; Park, Y.-S.; Kim, J.-J.; Basché, T., Excitation Energy Transfer in Organic Materials: From Fundamentals to Optoelectronic Devices. *Macromolecular Rapid Communications* **2009**, *30*, 1203-1231.

32. Grifoni, M.; Hänggi, P., Driven Quantum Tunneling. *Physics Reports* **1998**, *304*, 229-354.

33. Lüssem, B.; Riede, M.; Leo, K., Doping of Organic Semiconductors. *Physica Status Solidi (A)* **2013**, *210*, 9-43.

34. Key World Energy Statistics by the International Energy Agency (IEA); Paris, France **2017**.

35. IEA, World Energy Outlook 2017; OECD Publishing/IEA, **2017**.

36. Branker, K.; Pathak, M. J. M.; Pearce, J. M., A Review of Solar Photovoltaic Levelized Cost of Electricity. *Renewable and Sustainable Energy Reviews* **2011**, *15*, 4470-4482.

37. Perez M., P. R., Update 2015 - A Fundamental Look at Supply Side Energy Reserves for the Planet. *IEA-SHCP Newsletter* **2015**, *62*.

38. Shekhar, A. K., S. Bauer, P. Prasanth, V., Solar Road Operating Efficiency and Energy Yield - an Integrated Approach Towards Inductive Power Transfer. *Proceedings of the 31st European Photovoltaic Solar Energy Conference and Exhibition, Hamburg 14-18 Sept.* **2015**.

39. Parida, B.; Iniyan, S.; Goic, R., A Review of Solar Photovoltaic Technologies. *Renewable and Sustainable Energy Reviews* **2011**, *15*, 1625-1636.

40. Pandey, A. K.; Tyagi, V. V.; Selvaraj, J. A. L.; Rahim, N. A.; Tyagi, S. K., Recent Advances in Solar Photovoltaic Systems for Emerging Trends and Advanced Applications. *Renewable and Sustainable Energy Reviews* **2016**, *53*, 859-884.

41. Khan, J.; Arsalan, M. H., Solar Power Technologies for Sustainable Electricity Generation – a Review. *Renewable and Sustainable Energy Reviews* **2016**, *55*, 414-425.

42. Becquerel, Research on the Effects of Chemical Radiation from Solar Light by Means of Electric Currents. *Compt. Rend. Acad. Sci* **1839**, *9*, 145-149.

43. Adams, W. G.; Day, R. E., Ix. The Action of Light on Selenium. *Philosophical Transactions of the Royal Society of London* **1877**, *167*, 313-349.

44. Fritts, C. E., On a New Form of Selenium Photocell. *American Journal of Science* **1883**, *26*.

45. Website: NREL. https://www.nrel.gov/pv/

46. Kazmerski, L. L., The Bell Telephone Laboratories Discovery: Ushering in Our Modern Age of Solar Photovoltaics. In *Photovoltaics for Sustainable Electricity and Buildings*, Sayigh, A., Ed. Springer International Publishing: Cham, **2017**; pp 15-23.

47. Green, M. A.; Hishikawa, Y.; Warta, W.; Dunlop, E. D.; Levi, D. H.; Hohl-Ebinger, J.; Ho-Baillie, A. W. H., Solar Cell Efficiency Tables (Version 50). *Progress in Photovoltaics: Research and Applications* **2017**, *25*, 668-676.

48. Shah, A.; Torres, P.; Tscharner, R.; Wyrsch, N.; Keppner, H., Photovoltaic Technology: The Case for Thin-Film Solar Cells. *Science* **1999**, *285*, 692-8.

49. Green, M., Third Generation Photovoltaics: Solar Cells for 2020 and Beyond, *Physica E,* **2002**; *14*, 65-70.

50. Shaheen, S. E.; Ginley, D. S.; Jabbour, G. E., Organic-Based Photovoltaics: Toward Low-Cost Power Generation. *MRS Bulletin* **2005**, *30*, 10-19.

51. Yamaguchi, M.; Takamoto, T.; Araki, K.; Ekins-Daukes, N., Multi-Junction Iii–V Solar Cells: Current Status and Future Potential. *Solar Energy* **2005**, *79*, 78-85.

52. Brongersma, M. L.; Halas, N. J.; Nordlander, P., Plasmon-Induced Hot Carrier Science and Technology. *Nature Nanotechnology* **2015**, *10*, 25.

53. Conibeer, G., Third-Generation Photovoltaics. *Materials Today* **2007**, *10*, 42-50.

54. Green, M. A., Third Generation Photovoltaics: Ultra-High Conversion Efficiency at Low Cost. *Progress in Photovoltaics: Research and Applications* **2001**, *9*, 123-135.

55. Li, G.; Zhu, R.; Yang, Y., Polymer Solar Cells. *Nature Photonics* **2012**, *6*, 153.

56. Youn, H.; Park, H. J.; Guo, L. J., Organic Photovoltaic Cells: From Performance Improvement to Manufacturing Processes. *Small* **2015**, *11*, 2228-2246.

57. Chamberlain, G., Chamberlain, G.A.: Organic Solar Cells: A Review. *Sol. Cells 8,* **1983**; *8,* p 47-83.

58. Scharber, M. C.; Mühlbacher, D.; Koppe, M.; Denk, P.; Waldauf, C.; Heeger, A. J.; Brabec, C. J., Design Rules for Donors in Bulk-Heterojunction Solar Cells—Towards 10 % Energy-Conversion Efficiency. *Advanced Materials* **2006**, *18*, 789-794.

59. Pelzer, K. M.; Darling, S. B., Charge Generation in Organic Photovoltaics: A Review of Theory and Computation. *Molecular Systems Design & Engineering* **2016**, *1*, 10-24.

60. Girtan, M., Future Solar Energy Devices: Chapter 3: New Trends in Solar Cells Research; Springer, **2018**.

61. Tang, C. W., Two-Layer Organic Photovoltaic Cell. *Applied Physics Letters* **1986**, *48*, 183-185.

62. Yu, G.; Gao, J.; Hummelen, J. C.; Wudl, F.; Heeger, A. J., Polymer Photovoltaic Cells: Enhanced Efficiencies Via a Network of Internal Donor-Acceptor Heterojunctions. *Science* **1995**, *270*, 1789-1791.

63. Hiramoto, M.; Fujiwara, H.; Yokoyama, M., Three-Layered Organic Solar Cell with a Photoactive Interlayer of Co-Deposited Pigments. *Applied Physics Letters* **1991**, *58*, 1062-1064.

64. Hiramoto, M.; Fujiwara, H.; Yokoyama, M., P-I-N Like Behavior in Three-Layered Organic Solar Cells Having a Co-Deposited Interlayer of Pigments. *Journal of Applied Physics* **1992**, *72*, 3781-3787.

65. Yoshino, K.; Morita, S.; Kawai, T.; Araki, H.; Yin, X. H.; Zakhidov, A. A., Characteristics of Buckminsterfullerene Doped Conducting Polymer. *Synthetic Metals* **1993**, *56*, 2991-2996.

66. Cao, W.; Xue, J., Recent Progress in Organic Photovoltaics: Device Architecture and Optical Design. *Energy & Environmental Science* **2014**, *7*, 2123-2144.

67. Reese, M. O.; Morfa, A. J.; White, M. S.; Kopidakis, N.; Shaheen, S. E.; Rumbles, G.; Ginley, D. S., Pathways for the Degradation of Organic Photovoltaic P3HT:PCBM Based Devices. *Solar Energy Materials and Solar Cells* **2008**, *92*, 746-752.

68. Jørgensen, M.; Norrman, K.; Krebs, F. C., Stability/Degradation of Polymer Solar Cells. *Solar Energy Materials and Solar Cells* **2008**, *92*, 686-714.

69. Grossiord, N.; Kroon, J. M.; Andriessen, R.; Blom, P. W. M., Degradation Mechanisms in Organic Photovoltaic Devices. *Organic Electronics* **2012**, *13*, 432-456.

70. Voroshazi, E.; Verreet, B.; Aernouts, T.; Heremans, P., Long-Term Operational Lifetime and Degradation Analysis of P3HT:PCBM Photovoltaic Cells. *Solar Energy Materials and Solar Cells* **2011**, *95*, 1303-1307.

71. Krebs, F. C.; Norrman, K., Analysis of the Failure Mechanism for a Stable Organic Photovoltaic During 10000 H of Testing. *Progress in Photovoltaics: Research and Applications* **2007**, *15*, 697-712.

72. Wang, H.; Amsalem, P.; Heimel, G.; Salzmann, I.; Koch, N.; Oehzelt, M., Band-Bending in Organic Semiconductors: The Role of Alkali-Halide Interlayers. *Advanced Materials* **2014**, *26*, 925-930.

73. Etxebarria, I.; Ajuria, J.; Pacios, R., Solution-Processable Polymeric Solar Cells: A Review on Materials, Strategies and Cell Architectures to Overcome 10%. *Organic Electronics* **2015**, *19*, 34-60.

74. Park, J. H.; Lee, T.-W.; Chin, B.-D.; Wang, D. H.; Park, O. O., Roles of Interlayers in Efficient Organic Photovoltaic Devices. *Macromolecular Rapid Communications* **2010**, *31*, 2095-2108.

75. Po, R.; Carbonera, C.; Bernardi, A.; Camaioni, N., The Role of Buffer Layers in Polymer Solar Cells. *Energy & Environmental Science* **2011**, *4*, 285-310.

76. Chen, L.-M.; Xu, Z.; Hong, Z.; Yang, Y., Interface Investigation and Engineering - Achieving High Performance Polymer Photovoltaic Devices. *Journal of Materials Chemistry* **2010**, *20*, 2575-2598.

77. Madogni, V. I.; Kounouhéwa, B.; Akpo, A.; Agbomahéna, M.; Hounkpatin, S. A.; Awanou, C. N., Comparison of Degradation Mechanisms in Organic Photovoltaic Devices Upon Exposure to a Temperate and a Subequatorial Climate. *Chemical Physics Letters* **2015**, *640*, 201-214.

78. Torabi, S.; Liu, J.; Gordiichuk, P.; Herrmann, A.; Qiu, L.; Jahani, F.; Hummelen, J. C.; Koster, L. J. A., Deposition of LiF onto Films of Fullerene Derivatives Leads to Bulk Doping. *ACS Applied Materials & Interfaces* **2016**, *8*, 22623-22628.

79. Jin, Y. D.; Ding, X. B.; Reynaert, J.; Arkhipov, V. I.; Borghs, G.; Heremans, P. L.; Van der Auweraer, M., Role of LiF in Polymer Light-Emitting Diodes with LiF-Modified Cathodes. *Organic Electronics* **2004**, *5*, 271-281.

80. Paul, S.; Rajbongshi, B.; Bora, B.; Nair, R. G.; Samdarshi, S. K., Organic Photovoltaic Cells Using MWCNTs. *New Carbon Materials* **2017**, *32*, 27-34.

81. Busby, Y.; List-Kratochvil, E. J. W.; Pireaux, J.-J., Chemical Analysis of the Interface in Bulk-Heterojunction Solar Cells by X-Ray Photoelectron Spectroscopy Depth Profiling. *ACS Applied Materials & Interfaces* **2017**, *9*, 3842-3848.

82. Chizu, S.; Yoshiaki, T.; Takeshi, Y.; Makoto, K.; Shuji, D., Recent Progress of High Performance Polymer OLED and OPV Materials for Organic Printed Electronics. *Science and Technology of Advanced Materials* **2014**, *15*, 034203.

83. Girtan, M., Comparison of ITO/Metal/ITO and ZnO/Metal/ZnO Characteristics as Transparent Electrodes for Third Generation Solar Cells. *Solar Energy Materials and Solar Cells* **2012**, *100*, 153-161.

84. Lokanc M., E. R., Redlinger M, *The Availability of Indium: The Present, Medium Term and Long Term*; National Renewable Energy Laboratory (NREL): Colorado, **2015**.

85. Sharma, A.; Watkins, S. E.; Lewis, D. A.; Andersson, G., Effect of Indium and Tin Contamination on the Efficiency and Electronic Properties of Organic Bulk Hetero-Junction Solar Cells. *Solar Energy Materials and Solar Cells* **2011**, *95*, 3251-3255.

86. Soukoulis, C. M.; Wegener, M., Past Achievements and Future Challenges in the Development of Three-Dimensional Photonic Metamaterials. *Nature Photonics* **2011**, *5*, 523.

87. Emmott, C. J. M.; Urbina, A.; Nelson, J., Environmental and Economic Assessment of ITO-Free Electrodes for Organic Solar Cells. *Solar Energy Materials and Solar Cells* **2012**, *97*, 14-21.

88. Sannicolo, T.; Lagrange, M.; Cabos, A.; Celle, C.; Simonato, J.-P.; Bellet, D., Metallic Nanowire-Based Transparent Electrodes for Next Generation Flexible Devices: A Review. *Small* **2016**, *12*, 6052-6075.

89. Cao, W.; Li, J.; Chen, H.; Xue, J. In Transparent Electrodes for Organic Optoelectronic Devices: A Review, *SPIE*: **2014**; p 28.

90. Zhan, C.; Yu, G.; Lu, Y.; Wang, L.; Wujcik, E.; Wei, S., Conductive Polymer Nanocomposites: A Critical Review of Modern Advanced Devices. *Journal of Materials Chemistry C* **2017**, *5*, 1569-1585.

91. Vogelbaum, H. S.; Sauvé, G., Recently Developed High-Efficiency Organic Photoactive Materials for Printable Photovoltaic Cells: A Mini Review. *Synthetic Metals* **2017**, *223*, 107-121.

92. Mazzio, K. A.; Luscombe, C. K., The Future of Organic Photovoltaics. *Chemical Society Reviews* **2015**, *44*, 78-90.

93. Zhao, J.; Li, Y.; Yang, G.; Jiang, K.; Lin, H.; Ade, H.; Ma, W.; Yan, H., Efficient Organic Solar Cells Processed from Hydrocarbon Solvents. *Nature Energy* **2016**, *1*, 15027.

94. P3HT Structure. https://www.researchgate.net/figure/264645031_fig1_The-molecular-structure-of-Poly3-hexylthiophene-25-diyl-P3HT

95. Collins, S. D.; Ran, N. A.; Heiber, M. C.; Nguyen, T.-Q., Small Is Powerful: Recent Progress in Solution-Processed Small Molecule Solar Cells. *Advanced Energy Materials* **2017**, *7*, 1602242-n/a.

96. Nelson, J., Polymer: Fullerene Bulk Heterojunction Solar Cells. *Materials Today* **2011**, *14*, 462-470.

97. Vandewal, K.; Tvingstedt, K.; Gadisa, A.; Inganäs, O.; Manca, J. V., On the Origin of the Open-Circuit Voltage of Polymer–Fullerene Solar Cells. *Nature Materials* **2009**, *8*, 904.

98. Haddon, R. C., The Fullerenes: Powerful Carbon-Based Electron Acceptors. *Philosophical Transactions of the Royal Society of London. Series A: Physical and Engineering Sciences* **1993**, *343*, 53.

99. Hummelen, J. C.; Knight, B. W.; LePeq, F.; Wudl, F.; Yao, J.; Wilkins, C. L., Preparation and Characterization of Fulleroid and Methanofullerene Derivatives. *The Journal of Organic Chemistry* **1995**, *60*, 532-538.

100. Tournebize, A.; Bussière, P.-O.; Rivaton, A.; Gardette, J.-L.; Medlej, H.; Hiorns, R. C.; Dagron-Lartigau, C.; Krebs, F. C.; Norrman, K., New Insights into the Mechanisms of Photodegradation/Stabilization of P3HT:PCBM Active Layers Using Poly(3-Hexyl-D13-Thiophene). *Chemistry of Materials* **2013**, *25*, 4522-4528.

101. PCBM Structure. https://www.researchgate.net/figure/224443832_Molecular-structure-of-PCBM.

102. Wu, Q.; Zhao, D.; Schneider, A. M.; Chen, W.; Yu, L., Covalently Bound Clusters of Alpha-Substituted Pdi—Rival Electron Acceptors to Fullerene for Organic Solar Cells. *Journal of the American Chemical Society* **2016**, *138*, 7248-7251.

103. Bin, H., et al., 9.73% Efficiency Non Fullerene All Organic Small Molecule Solar Cells with Absorption-Complementary Donor and Acceptor. *Journal of the American Chemical Society* **2017**, *139*, 5085-5094.

104. Sonar, P.; Fong Lim, J. P.; Chan, K. L., Organic Non-Fullerene Acceptors for Organic Photovoltaics. *Energy & Environmental Science* **2011**, *4*, 1558-1574.

105. Nielsen, C. B.; Holliday, S.; Chen, H.-Y.; Cryer, S. J.; McCulloch, I., Non-Fullerene Electron Acceptors for Use in Organic Solar Cells. *Accounts of Chemical Research* **2015**, *48*, 2803-2812.

106. Gasparini, N.; Wadsworth, A.; Moser, M.; Baran, D.; McCulloch, I.; Brabec, C. J., The Physics of Small Molecule Acceptors for Efficient and Stable Bulk Heterojunction Solar Cells. *Advanced Energy Materials*, **2018**,1703298.

107. Lattante, S., Electron and Hole Transport Layers: Their Use in Inverted Bulk Heterojunction Polymer Solar Cells. *Electronics* **2014**, *3*, 132.

108. Yi, C.; Hu, X.; Gong, X.; Elzatahry, A., Interfacial Engineering for High Performance Organic Photovoltaics. *Materials Today* **2016**, *19*, 169-177.

109. Steim, R.; Kogler, F. R.; Brabec, C. J., Interface Materials for Organic Solar Cells. *Journal of Materials Chemistry* **2010**, *20*, 2499-2512.

110. Yin, Z.; Wei, J.; Zheng, Q., Interfacial Materials for Organic Solar Cells: Recent Advances and Perspectives. *Advanced Science* **2016**, *3*, 1500362.

111. Roth B., Søndergaard. R. R., Krebs F.C, Handbook of Flexible Organic Electronics, Chapter 7; Elsevier, Woodhead Publishing: Oxford, UK, **2015**.

112. Hoth C.N, S. P., Choulis S.A, Balasubramanian S., Brabec C.J, Applications of Organic and Printed Electronics: A Technology-Enabled Revolution Chapter 2, Solution Processed Organic Photovoltaics; Springer: Netherlands, **2013**.

113. Schmerl, N.; Andersson, G., A Layered Structure at the Surface of P3HT/PCBM Blends. *Physical Chemistry Chemical Physics* **2011**, *13*, 14993-15002.

114. Clark, M. D.; Jespersen, M. L.; Patel, R. J.; Leever, B. J., Predicting Vertical Phase Segregation in Polymer-Fullerene Bulk Heterojunction Solar Cells by Free Energy Analysis. *ACS Applied Materials & Interfaces* **2013**, *5*, 4799-4807.

115. Guan, Z.-L.; Kim, J. B.; Wang, H.; Jaye, C.; Fischer, D. A.; Loo, Y.-L.; Kahn, A., Direct Determination of the Electronic Structure of the Poly(3-Hexylthiophene):Phenyl-[6,6]-C61 Butyric Acid Methyl Ester Blend. *Organic Electronics* **2010**, *11*, 1779-1785.

116. Xue, B.; Vaughan, B.; Poh, C.-H.; Burke, K. B.; Thomsen, L.; Stapleton, A.; Zhou, X.; Bryant, G. W.; Belcher, W.; Dastoor, P. C., Vertical Stratification and Interfacial Structure in P3HT:PCBM Organic Solar Cells. *The Journal of Physical Chemistry C* **2010**, *114*, 15797-15805.

117. Tseng, W.-H.; Lo, H.; Chang, J.-K.; Liu, I. H.; Chen, M.-H.; Wu, C.-I., Metal-Induced Molecular Diffusion in [6,6]-Phenyl-C61-Butyric Acid Methyl Ester Poly(3-Hexylthiophene) Based Bulk-Heterojunction Solar Cells. *Applied Physics Letters* **2013**, *103*, 183506.

118. Ramm, M.; Ata, M.; Gross, T.; Unger, W., X-Ray Photoelectron Spectroscopy and near-Edge X-Ray-Absorption Fine Structure of C60 Polymer Films. *Appl. Phys. A* **2000**, *70*, 387-390.

119. Diao, Y.; Shaw, L.; Bao, Z.; Mannsfeld, S. C. B., Morphology Control Strategies for Solution-Processed Organic Semiconductor Thin Films. *Energy & Environmental Science* **2014**, *7*, 2145-2159.

120. Pivrikas, A.; Neugebauer, H.; Sariciftci, N. S., Influence of Processing Additives to Nano-Morphology and Efficiency of Bulk-Heterojunction Solar Cells: A Comparative Review. *Solar Energy* **2011**, *85*, 1226-1237.

121. Clarke, T. M.; Ballantyne, A. M.; Nelson, J.; Bradley, D. D. C.; Durrant, J. R., Free Energy Control of Charge Photogeneration in Polythiophene/Fullerene Solar Cells: The Influence of Thermal Annealing on P3HT/PCBM Blends. *Advanced Functional Materials* **2008**, *18*, 4029-4035.

122. Ibrahim, M. M.; Ghazy, O. A.; Abouelfadl, F. I.; Hosni, H. M.; Shehata, E. M.; Balboul, M. R., Thermal Annealing Effects on the Fine Structure and Performance of P3HT: PCBM Based Organic Solar Cells Fabricated in Air. *Molecular Crystals and Liquid Crystals* **2014**, *599*, 23-29.

123. Verploegen, E.; Mondal, R.; Bettinger, C. J.; Sok, S.; Toney, M. F.; Bao, Z., Effects of Thermal Annealing Upon the Morphology of Polymer–Fullerene Blends. *Advanced Functional Materials* **2010**, *20*, 3519-3529.

124. Zhao, Y.; Xie, Z.; Qu, Y.; Geng, Y.; Wang, L., Effects of Thermal Annealing on Polymer Photovoltaic Cells with Buffer Layers and in Situ Formation of Interfacial Layer for Enhancing Power Conversion Efficiency. *Synthetic Metals* **2008**, *158*, 908-911.

125. Steim, R., *T*he Impact of Interfaces on the Performance of Organic Photovoltaic Cells; KIT Scientific Publishing: Karlsruhe, Germany, **2010**, p 133.

126. Brillson, L. J., An Essential Guide to Electronic Material Surfaces and Interfaces; Wiley: West Sussex, UK, **2016**.

127. Margaritondo, G., Electronic Structure of Semiconductor Heterojunctions; Kluwer Academic Publishers: Milano, **1988**.

2. Experimental

Here the primary techniques utilised in this work shall be introduced along with the standard analysis methods applied throughout this thesis and the specifications of the instruments at Flinders University. Analysis procedures used in only a single chapter of this thesis and techniques only contributing a minor role to this dissertation can be found in the relevant results chapter.

2.1) Ion Scattering Spectroscopy

2.1.1) Overview

Ion scattering spectroscopy (ISS) is a range of analytical techniques used to gain quantitative information about a sample's elemental composition. The use of ion scattering spectroscopy for measuring the bulk composition of materials was facilitated around 1950 with the invention of High Energy Ion Scattering Spectroscopy (HEISS), namely Secondary Ion Mass Spectroscopy (SIMS)[1] which works by targeting an ion beam at a surface to detach the top layers (by a process known as sputtering) whose mass is then measured for identification.

Other ISS techniques were then developed in the 1960's which do not rely on sputtering the sample surface to measure the mass of the detached particles but instead work by focusing a collimated beam of mono-energetic gas ions at the sample of interest, which then have one or more collisions with the target atoms of the top few layers and then backscatter as a result of the mutual coulombic repulsion between the atomic cores of the atoms involved beam[2], see Figure 2.1.

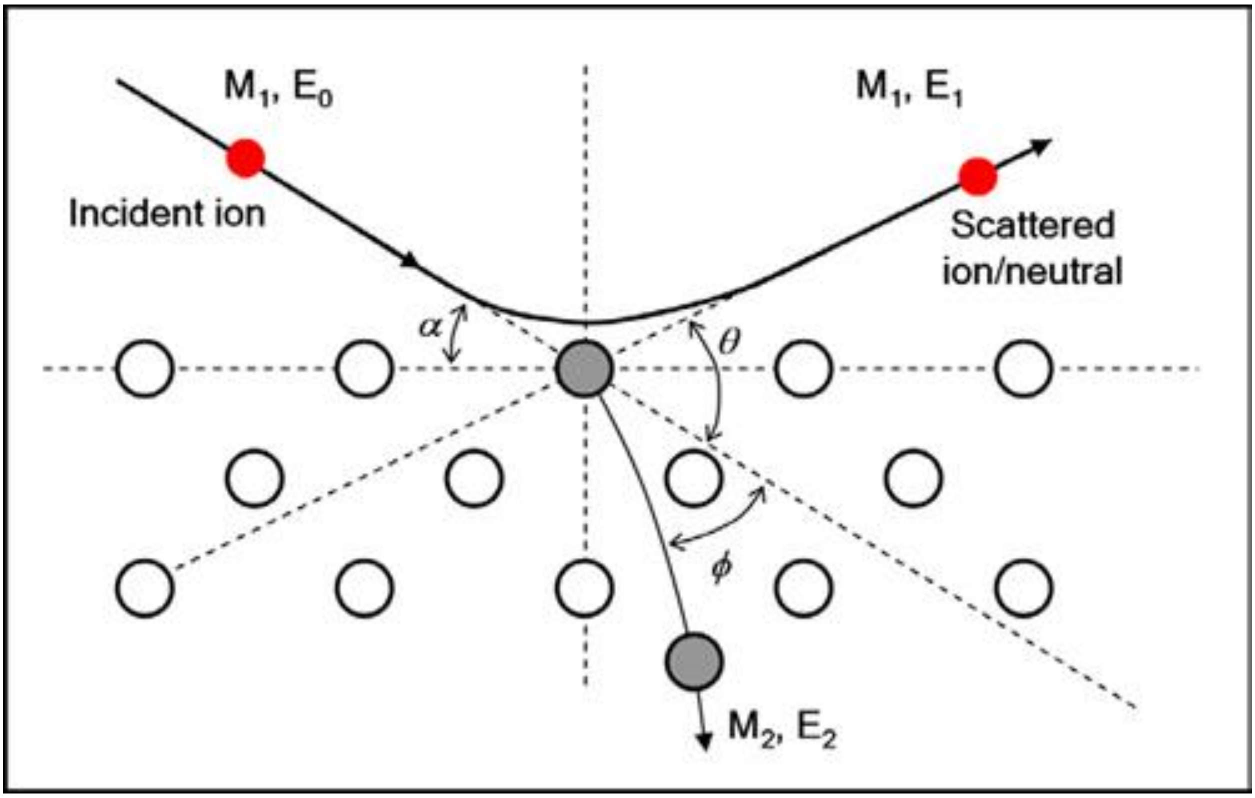

Figure 2.1: General schematic of an ion scattering experiment. Image reproduced from McConville *et.al*[3].

Techniques based on this concept utilise a binary collision model in which there are three assumptions. Firstly, each target atom is considered unbound or equivalent to a gas phase for the collision. Second, the target is considered to have a zero velocity prior to collision (cold lattice), and three, the collision itself is considered to be kinetic (electronic interactions can then be accounted for as seen in Equation 2.1). From this, with the conservation of momentum and energy in the backscattering process, the following relation between the mass of the target atom and energy of the backscattered neutral holds:

$$E_1 = E_o \frac{[\cos\theta + \sqrt{A^2 - \sin^2\theta}]^2}{(1+A)^2} - Q_{in} \quad , \quad A = \frac{M_2}{M_1}$$

---- **Equation 2.1**

Where E_1 and E_o are the respective final and initial projectile energies, θ the scattering angle, Q_{in} the inelastic energy loss from the collision, and M_1 *and* M_2 the mass of the projectile and target atom respectively. All components are known save for the mass of the target and E_1. By measuring E_1 the target mass can be calculated.

A time of flight (ToF) prior to the detector is utilized to separate the backscattered particles via their momentum, which is dependent upon the mass of the target atom involved in the collision. From this the mass of the target atom is able to be identified. This has the advantage of measuring individual atoms of the surface in question as opposed to the mass of detached 'chunks' of the surface, which often creates issues with surface rearrangements which are a natural surface response to sputtering[4], however this technique inherently had low resolution due to the large range of scattering angles and experimental conditions inducing neutralization of the incident ion beam.

This was refined in 1981 by Aono[5] by limiting the backscattered ion detection to head on collisions with the target *i.e.*180^{o} which thus removed much of the ambiguity and allowed for quantification of the backscattering process. This technique was called impact collision ion scattering spectroscopy (ICISS). The issue with backscattered ion neutralization was still an issue however and the technique subsequently still suffered with respect to detection and thus the signal to noise ratio was still low. The solution to this was facilitated by Niehus[6] in 1986, by altering the detection to that of backscattered neutrals rather than ions, thus significantly improving the statistic for detection of the backscattered particles. This marked the advent of Neutral impact collision ion scattering spectroscopy (NICISS).

2.1.2) Neutral Impact Collision Ion Scattering Spectroscopy (NICISS)

NICISS uses low energy He^{+} ions, the use of a low energy incident beam enhances the surface sensitivity of the technique[7]. The kinetic energy of the backscattered neutral is determined through the ToF system by channel plates which amplify the signal from the detected neutral collision. He^{+} is used as it is the only rare gas ion light enough to detect elements such as carbon and oxygen (heavier gases sputter these elements). The only elements that are thus undetectable are hydrogen and helium.

The trajectory of the projectiles within the sample consists of several small angle scattering events and one main backscattering process[8]. During the backscattering event, the He projectile loses kinetic energy in proportion to the mass of the target atom (via momentum conservation) in the order of a few hundred eV. Additional energy losses can occur along the trajectory of the projectile through the bulk (via multiple scattering events) and these losses are proportional to the penetration depth and known as the stopping power. This effect is minimised by using 180^{0} backscatter detection[9]. This additional energy loss is comprised of many small energy loss processes from various interactions within the sample surface, namely small angle scattering (nuclear stopping power) and nuclear and electronic excitations (electronic stopping power)[10], and is considered to be a continuous energy loss over the trajectory through the bulk in the order of a few eV per Å. For the case of organic molecules the energy loss (ΔE) is considered to be directly proportional to the depth (d) within the sample, as shown in Figure 2.2.

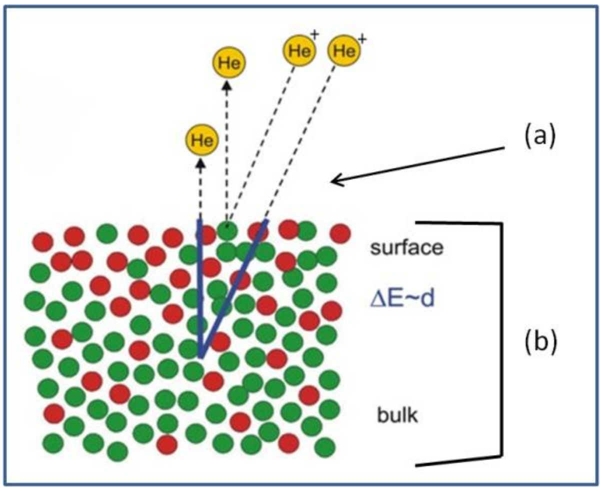

Figure 2.2: Trajectory of He^{2+} through target surface (a) backscattering event, (b) additional energy losses within target.

By combining the information gained through these energy loss processes, concentration depth profiles can be constructed to a depth of up to 30nm with a depth resolution of a few Å[11]. The high resolution of the technique is restricted though to a depth of about 30 nm due to the blurring of the backscattering angle of the helium projectiles caused by the low angle scattering. Surface roughness can also be an issue but is often resolved by rotating the sample or rastering the He^{+} beam whilst measuring. The data is thus an average over an area of investigation.

Experimentally the energy loss in inelastic scattering can determined via NICISS gas phase spectra[12]. This is performed by streaming a low density gas jet containing the desired element at the point in the NICISS chamber where the sample usually sits. In a gas phase spectrum the maxima depicts the ToF at the outermost layer of the target. This energy loss also has a spread which is caused by thermal broadening and energy straggling. Thermal broadening is a small effect and accounted for in most experiments when doing the gas phase calibration. Energy straggling is the statistical spread of stopping power energies which occurs due to the statistical probability of the events occurring. Energy straggling plays a role in the spectrum but is not important for most spectra unless the limits of depth resolution are required, in which case the gas phase experiments are again referenced to assist interpretation. In depth studies verifying this method have been performed[13-15]. Resolving the magnitude of the inelastic energy losses in the bulk can be difficult, as stopping powers for different materials can be hard to acquire. It can be theoretically calculated using the Bragg rule that states that the stopping power of a compound may be estimated by the linear combination of the stopping powers of individual elements[16]. The process and algorithm for determining the relation between energy and depth has been discussed in detail in a paper by Andersson[8] which also experimentally determined the energy loss in hydrocarbons at low energies.

2.1.3) NICISS Data Conversion

The NICISS spectrum is recorded as intensity (# backscattered neutrals) vs. ToF, usually measured in µs. The raw data of the spectrum shows a gradual incline interspersed with steps, which is shown in Figure 2.3 in black. This gradual incline is the backscattered hydrogen, from Equation 2.1 it can be seen that hydrogen is sputtered across a broad energy range ($A < 1$). This is accounted for in the data analysis process.

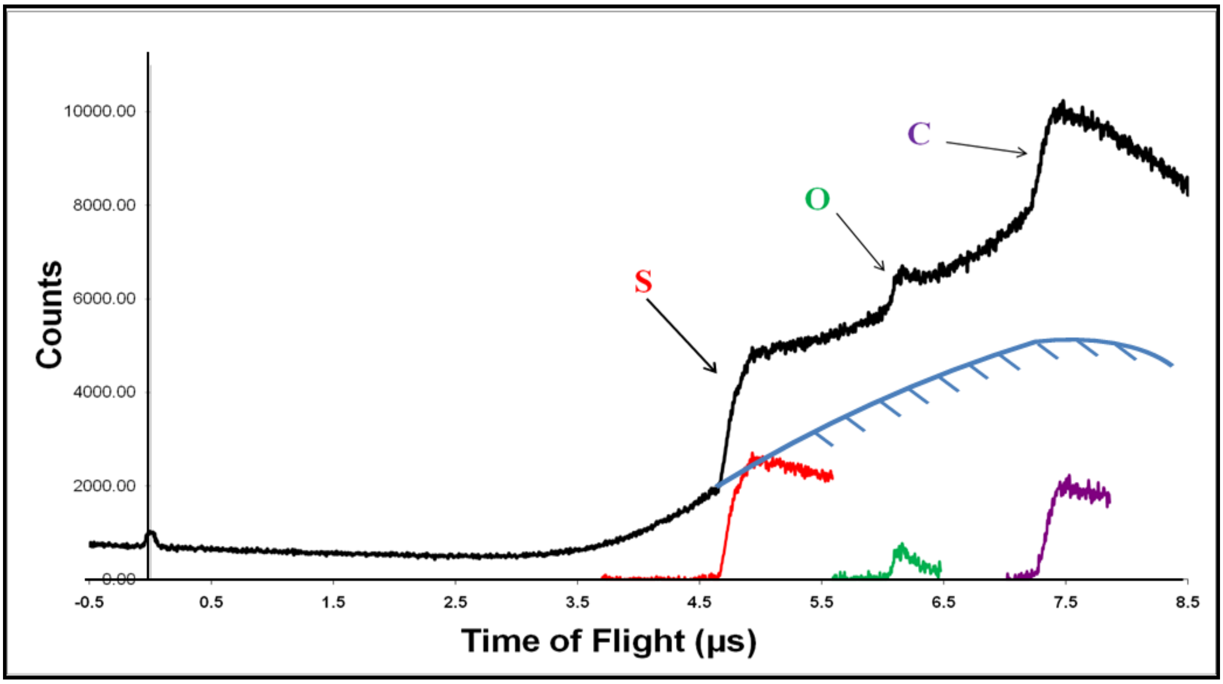

Figure 2.3: NICISS raw data spectrum for a blend sample of P3HT and PCBM. Raw data shown in black, note the photon peak at the zero mark for the ToF. Element profiles for sulfur, oxygen and carbon are also shown with the background removed.

Each step denotes the presence of a new element arriving at the ToF detector. The presence of sputtered hydrogen causes the background (blue in Figure 2.3), which is subtracted, leaving the element onsets (outermost layer) and tails which pertain to concentration in the bulk. A small percentage of the neutralization processes release a photon. This is the designated zero mark for the

ToF. NICISS has been able to also successfully measure interatomic distances on the surface plane, subsurface structure down to around 3 atomic layers and measure surface reconstructions[1].

The conversion from ToF spectra to energy spectra uses the following relation:

$$\mathrm{I(E)} = \mathrm{I(t)} \frac{\mathrm{dt}}{\mathrm{dE}} \frac{1}{d\sigma / \mathrm{d}\Omega(E)} \frac{1}{\mathrm{det}(E)}$$

------ Equation 2.2

Where *I(E)* is the energy loss spectrum, *I(t)* is the element contribution in the ToF spectrum, *dt/dE* is a factor which takes into account the non-linear relationship between ToF scale and the desired energy scale, *dσ/dΩ(E)* is the differential cross section and *det(E)* is the detector sensitivity. The energy spectrum is then converted to a concentration depth profile with the relation:

$$\mathrm{I}(x) = \mathrm{I(E)} \frac{\mathrm{dE}}{\mathrm{d}x} f$$

-------- Equation 2.3

Where x is depth within the target surface and f is the factor relating the backscattered projectiles to the concentration of the target element. It is calculated using the molecular weight [g/mol] and density [g/cm^3] to obtain the concentration as [mol/cm^3], and f is calibrated for each spectrum from concentrations in the bulk.

2.2) Electron Spectroscopy

2.2.1) Overview

Techniques based on photoelectron spectroscopy (PES) work via the photoelectric effect[17]. This phenomenon is the emission of electrons due to the absorption of energy by the sample from incident photons of high frequency (visible light or higher). Photons are able to ionize electrons from a molecule when the photon energy is larger than the binding energy of the electron. The difference in this energy is manifested as the kinetic energy of the outgoing electron. This kinetic energy is what is measured in electron spectroscopy via an analyzer. The fundamental equation relating the photon energy (hv) and the kinetic energy of the emitted photoelectron (E_k) is shown in Equation 2.4.

$E_k = h\nu - E_b - \Phi_{spec}$ ---- **Equation 2.4**

E_b is the ionization energy and refers to the binding energy of the electron with respect to the VL, and Φ_{spec} is the work function of the spectrometer. The actual value of Φ_{spec} can be experimentally determined by measuring a pure sample with well documented features such as Au or Ag.

PES measures ionization energies from different orbitals present within the sample, depending on which area of the electromagnetic spectrum is used. As photons are capable of penetrating into materials PES measures both the outermost layer and also into some depth of a sample surface. PES techniques are typically very surface sensitive, and the observed depth in the technique is dependent upon the incident photon energy and the electron mean free path in the material (λ). The limitations of the mean free path of electrons in solids results in an exponential decrease in measured intensity with depth. 3λ is taken as a general approximation for the observation depth, and information is acquired for (usually) the first 1~10nm depending upon the photon energy, see Figure 2.4. Photons of X-ray energies measure core electrons and those of the ultraviolet (UV) region measure valence electrons (Figure 2.5), providing different information about the measured sample.

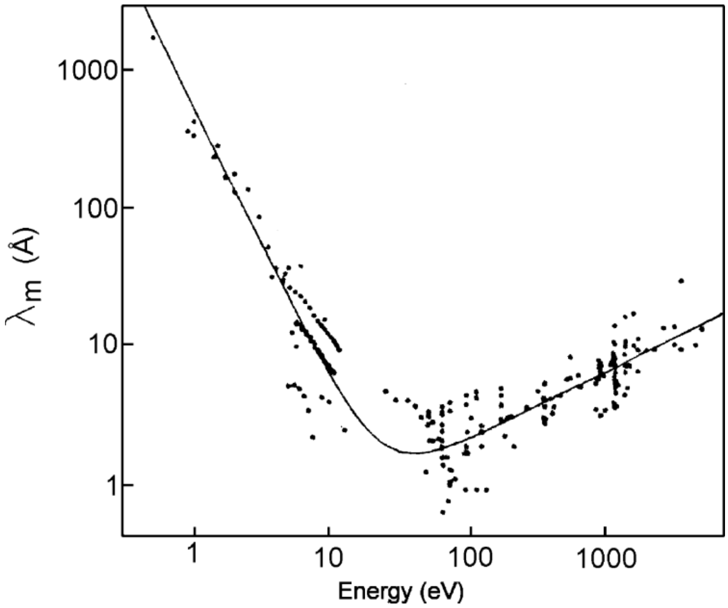

Figure 2.4: The Inelastic mean free path of various solids plotted against kinetic energy. Originally published by Seah[18] and reproduced by Westphal[19].

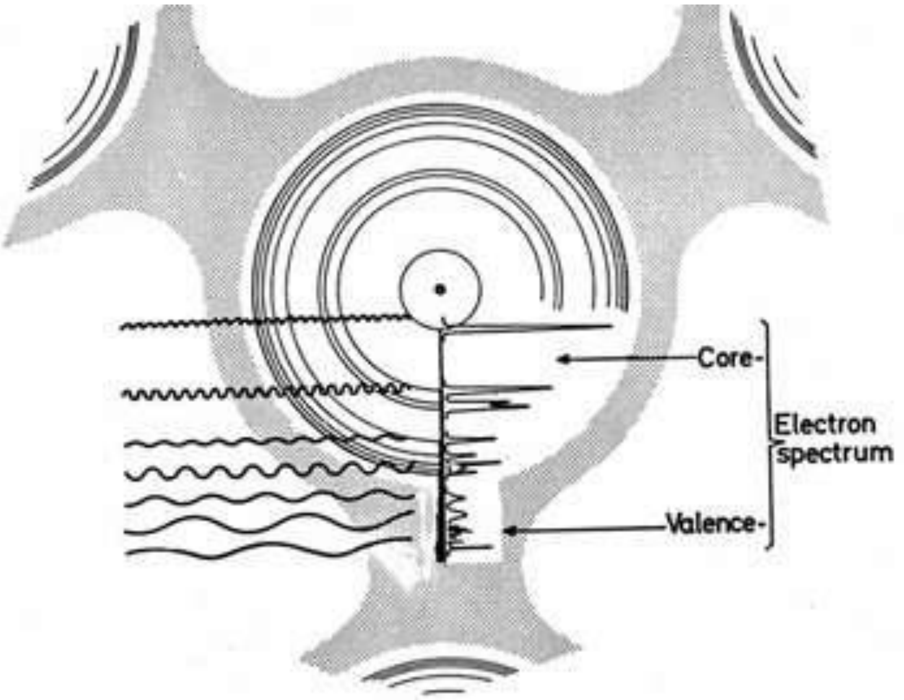

Figure 2.5: A schematic for photoemission spectroscopy from Nilsson[20]. In this example the photon energy is shown as differences in wavelength, and the corresponding observed electronic levels in the atom is displayed. The spectrum displayed vertically in the diagram is typical of an XPS spectrum, for UPS only the valence section is shown.

2.2.2) X-ray Photoelectron Spectroscopy (XPS)

2.2.2.1) General

The core electrons emitted in X-ray photoelectron spectroscopy (XPS) have different characteristic binding energies, primarily defined by the core electron energy levels specific to each element, but also subtly influenced by the bonding of the target atom with its neighbours in the solid. From this chemical specificity is obtained. The X-rays are generally produced within an x-ray tube under vacuum which contains either metallic aluminium or magnesium as an anode. High energy electrons (accelerated by a potential between 10kV to 150kV) are fired into the metal surface. The excitation that occurs within the metallic foil causes the emission of X-ray photons which have a characteristic energy. The corresponding X-ray lines and characteristic energies are Al K_α at 1486.6eV, and Mg K_α, at 1253.6eV, where K_α denotes the electronic transition occurring to produce the X-ray photons. For these photon energies the observation depth in the XP spectrum (from the IMFP, 3λ) is typically ~10nm.

There are two processes which can occur when electrons are ejected from the target surface (see Figure 2.6): photoelectrons and Auger electrons. Photoelectrons are the result of a direct transfer of energy from the X-ray photon into an electron on the target surface which results in its emission. The resulting peaks in the XP spectrum are quite sharp, as the binding energies are fixed. Photoelectrons are of primary interest in XPS and follow the relation described in Equation 2.4. This includes photoelectron peaks in the VB region of the spectrum and as such the VB can be measured with XPS, this is known as VBXPS and shall be discussed further in Chapter 5. Auger electrons follow a different process and are the result of relaxations within the core of the target atom. When a photoelectron is emitted, the resulting electron hole in the core is filled by a relaxation of an electron from a higher binding energy. The excess energy left over from this transition is emitted via a photon or is passed onto another electron which is ejected from the surface, this is the Auger electron. Transitions are labelled using quantum numbers but use K,L,M,N rather than n=1,2,3,4. They are of the form ‘KLL’ where firstly the primary vacancy is stated, secondly the shell for the Auger transition and thirdly the shell from which the Auger electron is ejected. Subshell information is generally included as a subscript.

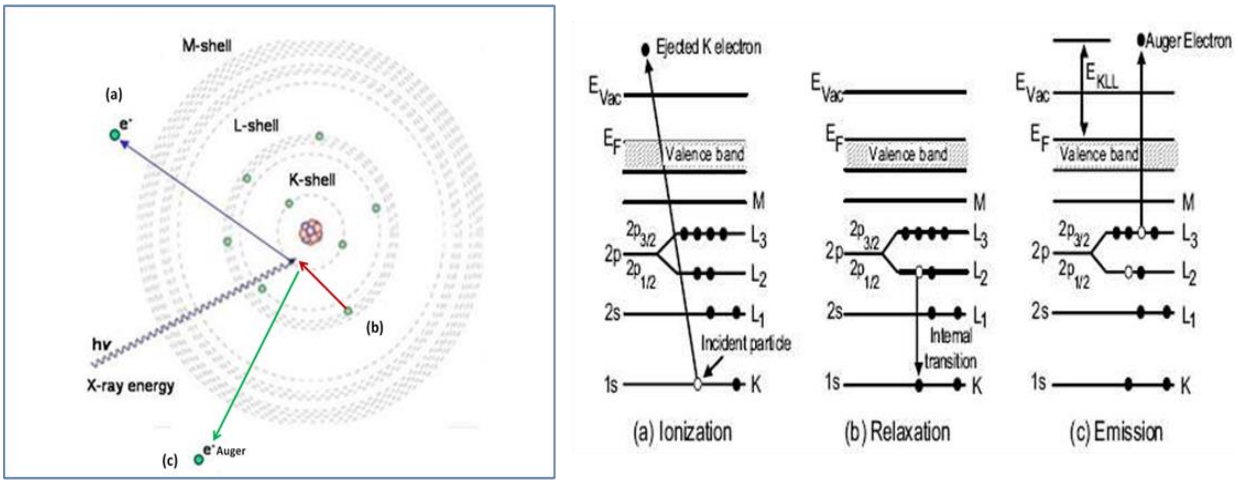

Figure 2.6: Example of (a) ionization, (b) relaxation and (c) Auger emission shown for a KLL transition. Shown as an atomic schematic (left) from Nilsson *et.al*[20] and as an energy level diagram (right) from Gunawardane *et.al*[21].

2.2.2.2) Depth Profiling with XPS

XPS can also be used as a depth profiling technique by changing the angle between the sample and analyzer which changes the probing depth, this is known as angle resolved XPS (ARXPS). It has the advantage over ion scattering techniques in that it measures any variance in chemical states of each element at the various depths as opposed to just the elemental composition, however the observed depth(s) can have a large margin of ambiguity when investigating multi-component profiles. A comparative study between ARXPS and NICISS can be found in the literature[22]. Another method for depth profiling with XPS involves the use of ion sputtering in between sequential XPS measurements to remove surface layers. The downside with this method is once again the potential surface disruption from ion beam damage. The most commonly used ion is Ar$^+$. Other ions can also be used such as C$_{60}^+$ but this has been shown to leave amorphous carbon on the surface post sputtering[23].

2.2.2.3) Analysis of XP Spectra

When quantitatively analysing the photoelectron peaks in an XP spectrum the first process which needs to be performed is the removal of the background. There are several background fitting methods available, but the most commonly accepted method is that of using the 'Shirley' background. This method is used as it attempts to use information about the spectrum to create a background which incorporates changes in the data as opposed to a linear background fit which will over or underestimate parts of the photoelectron peak whenever there is a change in background within the peak width. An example of a typical elemental region and of the Shirley vs. linear background fitting may be seen in Figure 2.7. It can be clearly seen that the background changes between the two ends of the measured region, and that the linear background would be overestimating the area of all components in the higher binding energy region of the spectrum.

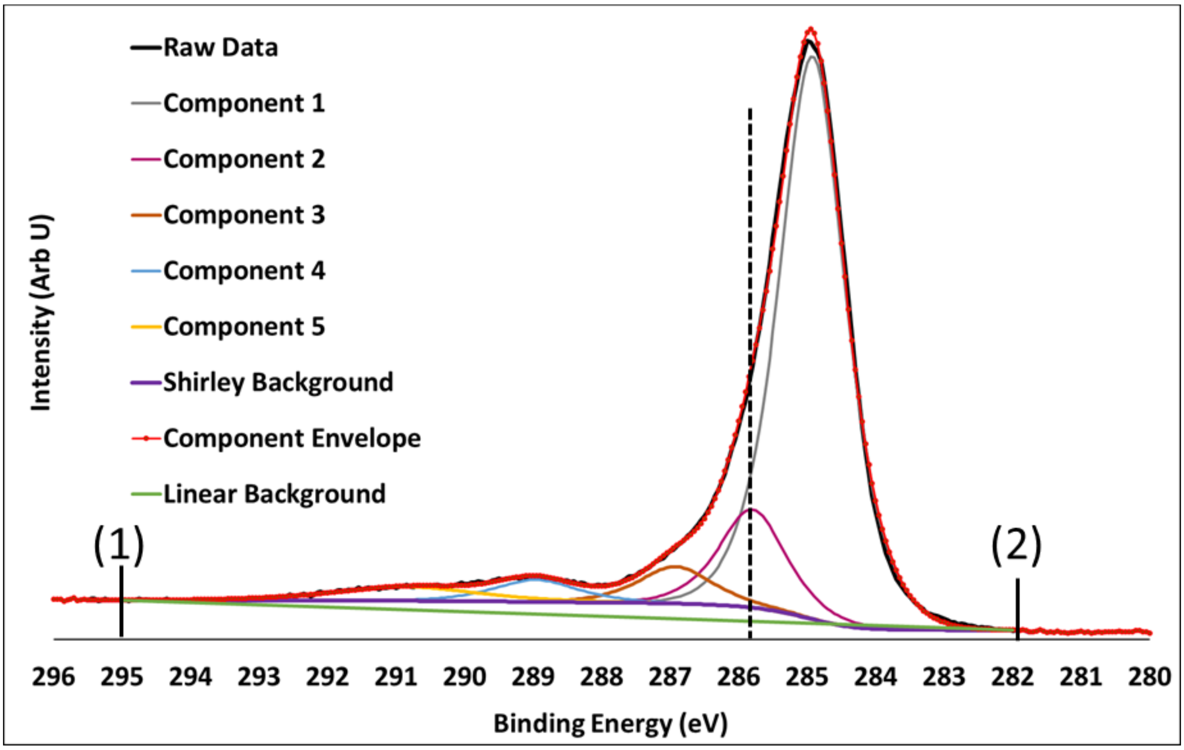

Figure 2.7: C1s XP spectrum of PCBM, showing the raw data, Shirley and linear background fits, fitted components and component envelope (sum of all fitted components). (1) and (2) are point 1 and 2 respectively for the Shirley background calculation, the dotted line marks the division point in the component areas which are denoted (A1) (component area left of dotted line) and (A2) (component area right of dotted line) in the calculation for the background subtraction.

The equation for the Shirley background is as follows:

$$S(E) = I_2 + k\frac{A2(E)}{(A1(E)+A2(E))}$$ -------- **Equation 2.5**

Where S(E) is the background, I_2 is the intensity at point 2, $A1$ and $A2$ are the photoelectron peak (component) areas respectively to the left and right of the dotted line shown in Figure 2.7, and k is defining the step in the background across the region of interest. Because the areas and S(E) are co-dependent the process is iterative, with the initial calculation based on a rough assumption of S(E).

Peak and subsequent component fitting for each of the elements and its chemical states is performed by adding Gaussian-Lorentz curves[24-25] within the raw data region so that the sum of the components (component envelope) equates to the raw data, however components cannot be added without consideration for their presence. Each specific chemical state has a known energy once the spectrum has been calibrated (*i.e* a C-C bond is generally taken as a standard of 285.0eV, seen as Component 1 in Figure 2.7, and one can use this along with the knowledge of the sample to roughly approximate the number of components required. Quite often the data indicates this as well, the C1s spectrum in Figure 2.7 for example clearly shows the presence of multiple states in the carbon peak. The total contribution of components within each element's photoelectron peak for analysis is then summed, the total is noted as the relative atomic percentage of the sample in question.

The error in peak intensities in XPS is induced by the peak and component fitting to the raw data. Each of the fitted peaks or components is, as stated only a best fit approximation and thus the error is in the area approximation for the peak. A procedure for calculating peak uncertainty was discussed in detail by Quinton in a PhD dissertation[26] and then verified by Barlow[27] which had the resulting relation between error in the area (ΔArea) and the measured area and peak width (known as the full width half maximum, FWHM):

$$\Delta Area \cong (\pi/ln2)^{1/4}(\sqrt{F}\mathrm{WHM}.Area)$$ ----- **Equation 2.6**

This error analysis procedure was performed for each data set using Microsoft Excel. The error in peak position has been taken as 0.2eV for the instrument at Flinders University. IMFPs for each element were accounted for via the Quases program[28] using the Powell and Penn algorithm and cross referenced to work done by Tanuma et.al[29]. Scofield relative sensitivity factors were used[30] [31] and the transmission function of the analyzer was also accounted for in the analysis process. Peak fitting was performed with CASA XPS software using the standard Shirley background model and Gaussian-Lorentzian component fitting.

Analysis of XP spectra can be, unfortunately, a slightly ambiguous process. The reason for this is twofold: firstly, the background present in an XP spectrum is entirely dependent upon the sample under investigation and thus changes each time, and secondly, because the subsequent component fitting which occurs for each elemental peak can easily be altered to show more or less binding states whilst still appearing to be valid. However, despite this it is still a highly quantitative method of analysis for most samples, and issues generally arise only when there are unknown numbers of binding states at very similar energies to each other within the sample.

2.2.3) Ultraviolet Photoelectron Spectroscopy (UPS)

2.2.3.1) General

For ultraviolet photoelectron spectroscopy (UPS) the incident radiation is within the UV region of the spectrum and the line source is typically created via a He discharge which produces photons with an energy of ~21.2eV, known as the He I line. For this photon energy the observed depth for the technique equates to approximately 3nm, again this is from the IMFP (3λ). UP spectra are capable of showing details of complex electronic structures and the molecular energy levels present in the valence region, see Figure 2.8. This includes shifts of the VL and workfunction that can occur at interfaces.

The occupation and density of states (DOS) is also shown in the spectrum. The DOS relates to the occupation of energy states which are available to an electron as a function of the binding energy, areas with higher occupation appear as peaks, these peaks can be fitted with Gaussians when comparing to theoretical calculations[32]. VBs present in the target are characterized by comparing the experimentally found MO energies to those found theoretically via quantum chemistry. In this way, and due to the high resolution present in the technique, fine structure is able to be observed due to the vibrational levels of the molecular ion. The information obtained with UPS indicates the conduction properties of the material in question via the VBM (the HOMO for organic materials) and shows any changes occurring in the valence region for different samples.

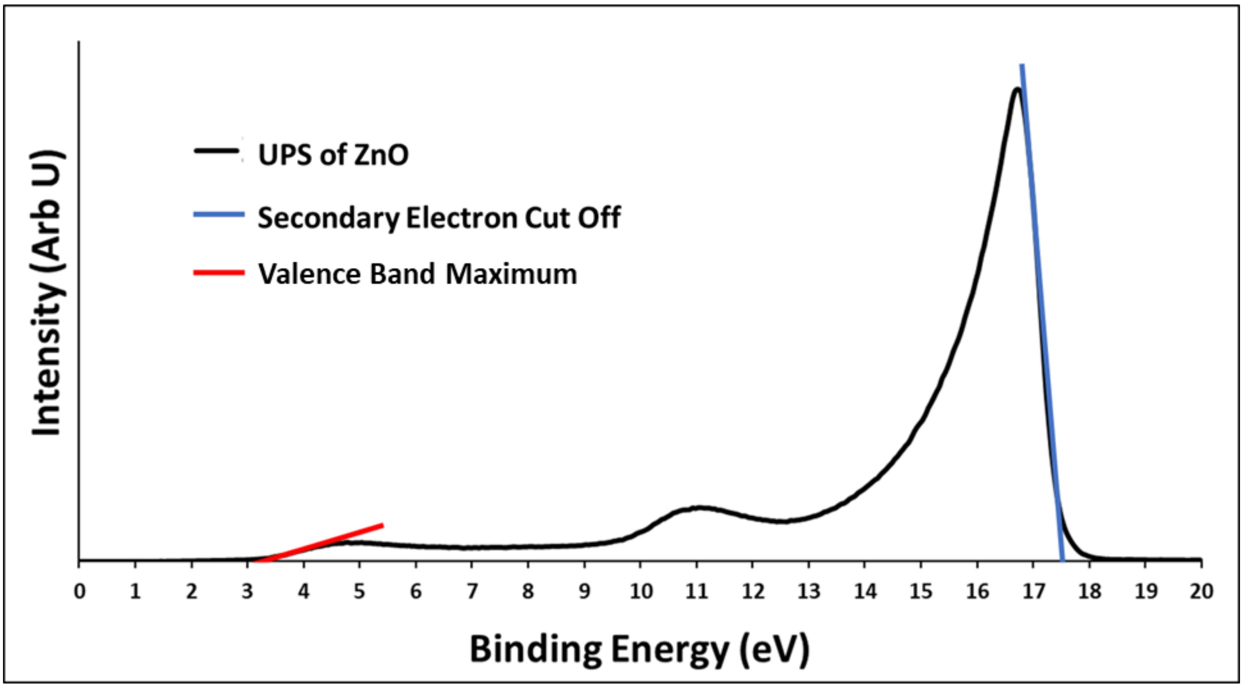

Figure 2.8: Typical UP spectrum, in this instance for ZnO. The valence band maximum is shown in red and in this instance has a value of 3.2eV, the secondary electron cut off point used for workfunction determination shown in blue, in this instance has a value of 17.5eV.

2.2.3.2) UPS Analysis

No analysis procedures are necessarily required for UPS data, as both the workfunction and position of the VBM can be read straight from the raw data as shown in Figure 2.8 by finding the point at which the line of best fit to both regions crosses the x-axis. The workfunction (Φ) is determined by the secondary electron cut off point. When working on the kinetic energy scale (which is how the raw data is collected) this is the point which has electrons of the lowest kinetic energy leaving the surface. It is general practice however to instead work with the binding energy scale as it is more relevant for the energy levels being measured. When using this scale the workfunction is measured by subtracting the secondary electron cut off (denoted SE in Equations 2.7 and 2.8) from the photon energy:

$\Phi = h\gamma - SE$ ------- **Equation 2.7**

Thus for the example shown in Figure 2.8 the workfunction is (21.2 – 17.5) = 3.7eV.

To measure the IP the VBM value also needs to be taken into account and is found by the following relation:

$IP = h\gamma - SE + VBM$ ------ **Equation 2.8**

The values of both the VBM and workfunction are still only an approximation however as they can only be as accurate as the resolution of the analyzer. One must be also careful when measuring workfunctions to ensure that the sample is perpendicular to the electron detector for the measurement to be correct[33]. DOS in the measured spectra can also be directly compared to values obtained via computational investigations. When a series of spectra are obtained to observe evolutions in the VB with changes in a desired sample parameter, a deconvolution algorithm can be utilized to discern the number of unique spectra contributing within the series. This will be discussed in section 2.2.5.

2.2.4) Metastable Induced Electron Spectroscopy (MIES)

2.2.4.1) General

Despite the success of PES techniques in surface studies, the problem of complete surface sensitivity still remains. The photons penetrate the surface so the resulting data is a convolution of orbital information from several nanometers, which is not ideal for interfacial studies where the changes in the outermost layer are of the highest interest as they are the orbitals which will be involved in charge transfer or further chemical bonding at the interface.

Another electron spectroscopy technique holds its roots in works by Hagstrum in the 1950's and 1960's in which rare gas ions were used to induce electron emission from surfaces[34-35]. This technique is known as metastable induced electron spectroscopy (MIES) or penning ionization electron spectroscopy (PIES). and is capable of specifically measuring only the outermost layer (or interfacial) orbitals in the VB[36]. MIES is able to obtain the same VB information as UPS, but for the outermost layer of the target surface only. This is facilitated via the use of excited (not ionized) helium atoms in the incident beam as opposed to photons. The helium atoms are excited to a meta-stable state and denoted He*. This is a low energy excited state which is neither capable of penetrating or sputtering the outermost layer and as such has complete surface sensitivity, only facilitating electron emission from the outermost facing orbitals of the surface. The meta-stable state is the He* 2s1s state which is acquired via the use of a carefully controlled electrical discharge and pressure gradient, and has an excitation energy of 19.8eV, which is sufficient energy to ionise the valence electrons. The lifetime of the state when under sufficient vacuum (~10^{-9}mbar) is ~4000s, as it is dipole forbidden for a transition back to the ground state due to quantum mechanical selection rules which state that dipole allowed transitions must have $\Delta l = \pm 1$ (where l is the orbital angular momentum). The transition required has $\Delta l = 0$. The He* relaxation occurs instead via a pathway provided by the target surface which occurs as soon as the atom is within a few Å of the surface, this occurs so readily due to the large cross section for the de-excitation processes[37]. The relation between the incident He* and electron emission is different to PES techniques as there are multiple de-excitation mechanisms which are possible see Figure 2.9. The de-excitation mechanism is entirely dependent upon the occupancy of the CB and the band gap of the material being investigated[38]. Organic substances and wide band gap semiconductors such as zinc oxide predominantly undergo Auger de-excitation (AD). In this process an electron from a state in the target surface tunnels into the He1s state in the He* once the He* is sufficiently close to the surface. The energy difference between this target surface state and the He1s is transferred to the He2s electron which is then emitted (provided the energy is sufficient to overcome the workfunction). This relaxation pathway results in a spectrum comparable to that of UPS, and the relation can be seen in Equation 2.9 where E_{e-} is the ejected electron energy, $E[\text{He}^*]$ the energy of the metastable, and E_{bind} the binding energy of the electron prior to ejection.

$E_{\text{e-}} = E[\text{He}^*] - E_{\text{bind}} - \Phi_{spec}$ ------- **Equation 2.9**

More conductive materials such as metals and narrow band gap semiconductors however also undergo a resonance ionization (RI) followed by Auger neutralization (AN). The RI occurs when the workfunction of the target surface is sufficiently low that the He* resonates with the target surface states inducing ionization of the helium (He^+). The ion is then neutralized by an electron from the target surface which is the AN step. Another electron is also ejected from the target surface due to the conservation of energy which thus has an energy equal to the difference between the state from which the AN electron originated in the sample and the He1s level, this is denoted as Φ_j in Figure 2.9. For AN a range of combinations of the kinetic energy of the emitted Auger electron and the binding energy of the electron tunnelling to the 1s orbital of the He atoms are possible which leads to far broader features in the resulting spectrum[39].

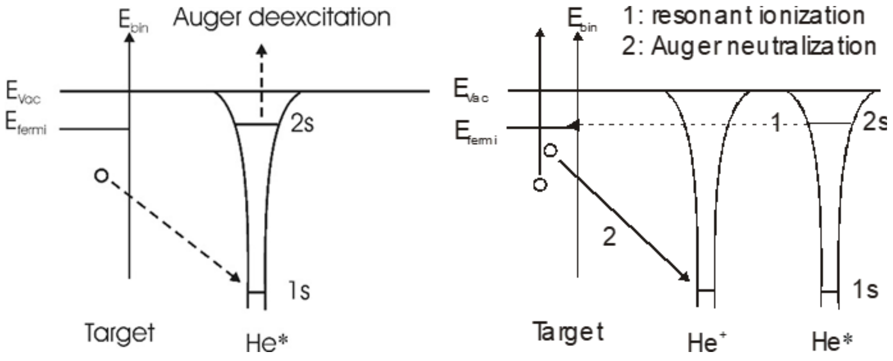

Figure 2.9: He* de-excitation mechanisms: Auger de-excitation (AD) mechanism shown on the left, resonance ionization (RI) followed by Auger neutralization (AN) shown on the right. Image courtesy of Chambers *et.al*[40]

The de-excitation process of the He* involves the emission of an electron from only the target surface, which is what is then measured via an analyzer in the same manner as other electron spectroscopy techniques, see Figure 2.10. This is how the outermost layer sensitivity is obtained, as only the atoms which come into direct contact with the impinging meta-stables emit electrons.

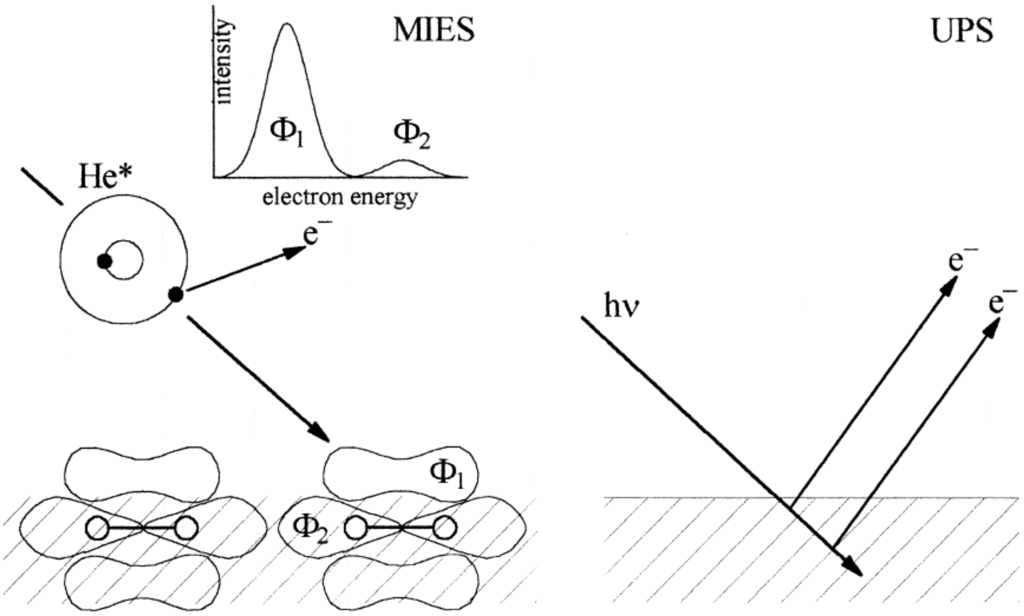

Figure 2.10: (left): Electron emission via MIES (left), note the presence of Φ$_1$ physically blocking most of Φ$_2$ from the outermost layer and thus incoming He*, resulting in a spectrum predominantly of Φ$_1$. Electron emission of UPS (right) which involves atoms from the outermost layer and near surface area. Image reproduced from Heinz *et.al*[41].

The resulting MIES spectrum is intensity/counts vs. kinetic or binding energy of the emitted electrons which shows the surface DOS. The kinetic energy scale can always be used, however the binding energy scale is only appropriate for instances where only the AD de-excitation mechanism is occurring. Most MIES instruments are capable of simultaneous UPS measurements due to the nature of the source. The advantage of this is that VB information can be obtained for both the outermost layer and also the near surface region in the same measurement. MIES is a very powerful tool when used in conjunction with UPS and can allow the deconvolution of the VB orbitals between the near surface area and that of the outermost layer, which can be significantly different. Naturally, this ability to observe the outermost orbitals and observe the impact of surface modifications on the outermost layer can give insights into subtle changes in surface rearrangements not discernible through other methods.

2.2.4.2) MIES Analysis

Similarly to UPS, MIE spectra do not inherently require analysis for the data to be useful. A spectrum can be compared to theoretical calculations of DOS in the literature (as long as one is aware of the de-excitation mechanisms occurring which can broaden the observed features depending on the sample), or if a series of measurements are performed the changes in DOS between spectra can be compared. When the spectra have been simultaneously acquired with UPS measurements the comparisons between the two can give insight into differences between the VB of the outermost layer and near surface area. Also, as stated for UPS, to gain further information from a series of spectra which have been obtained to observe evolutions in the VB with changes in a desired sample parameter, a deconvolution algorithm can be utilized to discern the number of unique spectra contributing within the series. This will now be discussed in section 2.2.5.

2.2.5) Valence Band Data Analysis: The Singular Value Decomposition

MIE/UP spectra are fitted in a very different manner to XPS. The background of the sample is generally more strongly dependent on the analyzer, however, it is common practise to leave the background in as it becomes of minor importance over the binding areas of interest. Component allocation is often far more difficult however, because the knowledge base from which to draw information from is far more restricted. As such a common method for data collection is to perform multiple scans whilst gradually altering the sample’s exposure to a changing parameter. Evaluation of this is then often based on the knowledge of the precise reaction conditions of each sample under investigation. If a sufficient number of spectra are measured in a series of valid experiments (for example heating a sample and measuring at various temperature intervals, or depositing increasing amounts of a material onto the initial substrate measured) a deconvolution procedure may be applied to obtain the number of unique spectra contributing to the series. This deconvolution procedure is known as singular value decomposition (SVD).

SVD is a linear algebra technique which extracts the base factors (eigenvectors and eigenvalues) of a matrix. For the application in VB spectroscopy a series of measured spectra is the initial matrix (A). The SVD then extracts the unique base spectra (eigenvectors) and their respective contributions (weighting factors/ eigenvalues) and reconstructs these as reference spectra. Thus each measured spectrum is some linear combination of these reference spectra[42-43]. This allows one to map the specific relative changes occurring in the measured data series.

The theory is as follows: Suppose matrix A is a real m x n matrix with a rank of r, and $m \geq n$. The SVD of A is:

$A = U.W.V^T$ -----**Equation 2.10**

Where U is an orthogonal m x n matrix, V is a square n x n matrix *i.e*: $U^TU = V^TV = VV^T = I_n$, and W is an r x r diagonal matrix whose elements contain the square roots of eigenvalues from U or V in descending order (positive or zero elements only). The elements on the diagonal of W are labelled σ_i and are the singular values of matrix A.

The practical application of this mathematical theory allows a deconvolution of data which is comprised of several constituent data sets. It is a method which allows correlated variables to be transformed into uncorrelated ones which is able to show relationships and substructure within the original data set. Once the points of maximum variation are found, the dimensions can be ordered according to the variation and an approximation of the original data with fewer dimensions is able to be created. In the instance of electron spectroscopy this effectively translates to the de-convolution of a measured spectrum into a linear combination of spectra [37]. Consider matrix A to be column vectors (columns are separate spectra, rows are electron energy channel) of the electron spectra to be analyzed such that:

$A_{ni} = S_i(E_n)$ -------- **Equation 2.11**

Where n =1,2...N denotes the number of energy channels in the spectra S_i are the spectra (i = 1,2...I), and E_n is the energy at channel n. The base spectra B_i can be obtained through SVD by defining them as:

$B_i(En) = U_i(En).w_i$ -------- **Equation 2.12**

These base spectra are orthogonal and as such contain negative values so are not meaningful spectra (counts ≥ 0 for all physical data), so only the linear combination is meaningful:

$S'_i(E_n) = \sum_{k=1}^{I'} B_k\,(E_n)v_{ki}^T$ with I' ≤ I -------- **Equation 2.13**

υ_{ki}^T are the sub vectors of V^T of Equation 2.10 and the basis spectra B_k (k = 1,2.....I'). The number of spectra required to reproduce S_i can then be calculated, with constraints that the weighting coefficients are ≥ 0, and the sum of which must equal unity. This method fails when $I' = I$, and physically means the spectrum is not a linear combination and that the sample has had electronic interactions/ rearrangements altering it from its known constituent components. Mathematically it is attempting to solve a vector space sum where the subspace equals the number of vectors in the series. The SVD was performed using a solver procedure in Microsoft Excel.

2.3) The Ultra High Vacuum Instruments at Flinders University: Technical Details

2.3.1) Electron Spectroscopy and *in situ* NICISS Instrument

The primary ultra high vacuum (UHV) instrument used for data acquisition in this dissertation has attached instrumentation for MIES/UPS, XPS and NICISS and was custom built by SPECS (Berlin, Germany). It is pictured in Figure 2.11 and a general schematic is shown in Figure 2.12.

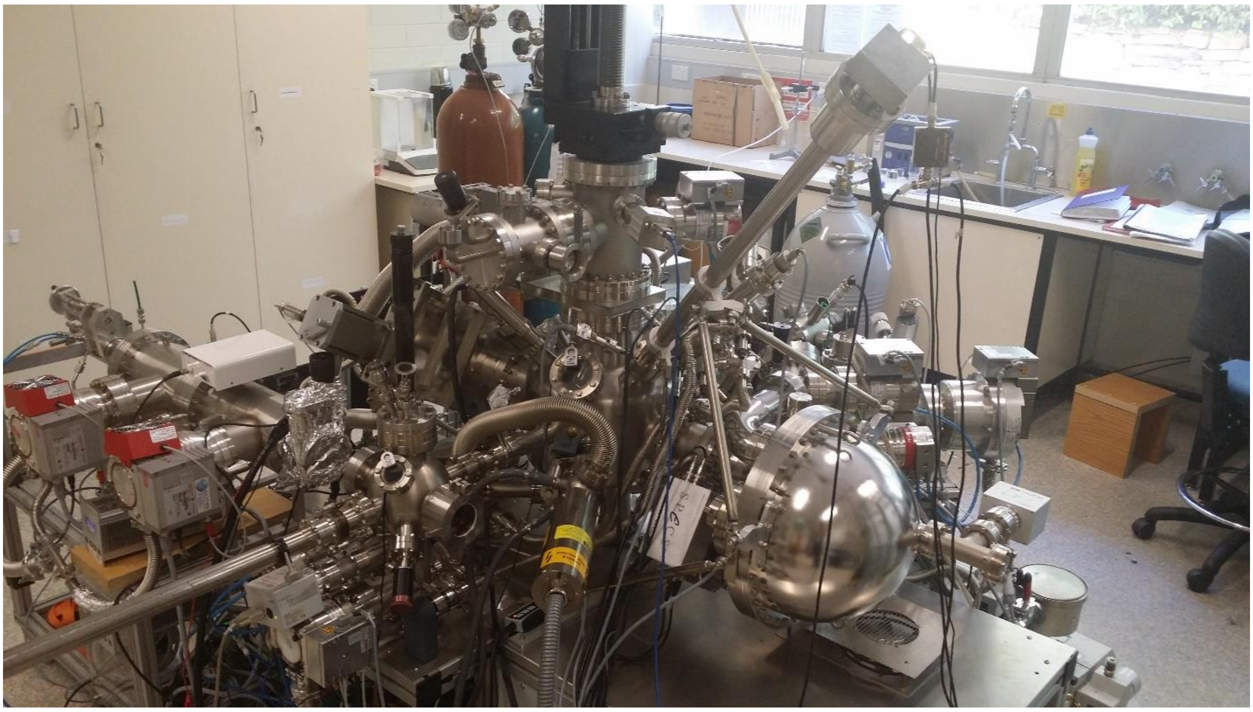

Figure 2.11: Image of the UHV apparatus at Flinders University containing equipment for XPS, MIES, UPS and NICISS experiments.

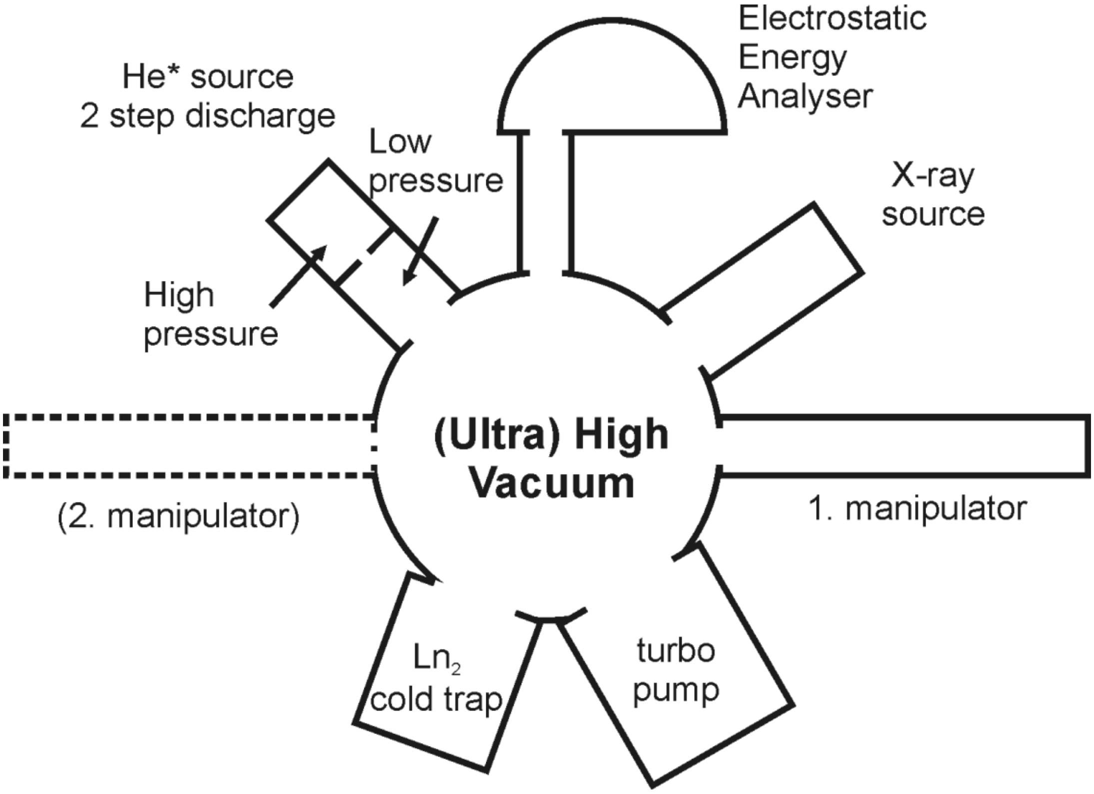

Figure 2.12: General schematic for the UHV instrument (top down view), in this image NICISS is not included, the ToF and detector setup is situated above the analyzer and can be seen in Figure 2.11.

The load lock contains a multi sample stacker, detachable evaporator unit (Createch) and detachable quartz crystal monitor for monitoring evaporated thickness rates (STM-100MF, Sycon Instruments). The temperature controller for the evaporator was the Invensys Eurotherm model 22116e with a control unit by Creaphys, model CU103. The base pressure during the evaporations (Chapters 6 and 7) was ~3x10^{-6}mbar, and for sample introduction in all instances to the main chamber ~7x10^{-7}mbar.

The main chamber holds a typical base pressure of ~5x10^{-10}mbar. The main chamber has a sample stage which is capable of manipulating on the X,Y and Z axes and has a SPECS sample heater power supply SH100 attached. For sample heating (Chapter 5) the temperature was monitored with both a Eurotherm 2208e and an Omega ir2 series temperature measurement control system. A mass spectrometer (LCD Dycor by Ametek Process Instruments) was run after each sample introduction to monitor contaminant levels. A hemispherical Phoibos 100 energy analyzer (also by SPECS) is used to record electron spectra. The acquisition software for all electron spectra is SPECS lab V2.0.

The X-ray source (XRC 1000M) contains magnesium and aluminium anodes for the generation of MgKα and AlKα photon beams, the source is non-monochromated. The typical chamber pressure during XP spectral acquisition was ~2x10^{-9}mbar. X-ray source was used with the Mg Kα anode and operated at 200W, 12kV (unless specified otherwise). MIES and UPS are facilitated with a two stage cold cathode gas discharge from MFS (Clausthal-Zellerfeld, Germany) which simultaneously generates the metastable helium atoms (He* $^3S_1$, 19.8eV) and UV light (He I line, 21.2eV). To separate the signal generated by the metastables and the photon beam a chopper (MFM Analytical Systems) is used and the signals are then de-convoluted by the software. The chopper frequency is 2kHz. Typical chamber pressure during spectral acquisition for MIES and UPS was around 8×10^{-10}mbar.

The angle between both the X-ray irradiation and analyzer and the He*/UV light irradiation and analyzer is 54°. This is the most commonly used angle for analysis due to the high cross section[24]. The angle between the analyzer and sample manipulator was parallel to the sample surface normal. All electron spectra were collected at a pass energy of 10eV with an energy resolution of 400meV as evaluated from the Fermi edge of polycrystalline silver[31].

The main chamber also has an ion source (SPECS Lab PU-IQE 12/38). This was used for sputter cleaning samples (Chapters 5,6,7). For sputter cleaning the accelerating voltage was set to 3kV with an ion current of about 250nA resulting in a total ion dose of about 2×10^{15} ions/cm^2, Ar^+ ions were used, and the settings were such that the beam was rastered across the sample. The ion source is also able to be used as an *in situ* NICISS (Chapters 6 and 7). For this the Wien filter (WMF-20 by SPECS) settings can be altered such that He^+ ions are selected instead. The detector was sourced from Scientific Instruments (SI, Germany) and the ToF analyzer is the P9888 from Fast ComTec (Germany). The analysis program used for data acquisition was the P7888, MCDWin from Fast ComTec (Germany). The general setup for a NICISS experiment is discussed in further detail below.

2.3.2) NICISS Instrument

As well as the NICISS described above there is a separate NICISS apparatus at Flinders University which was used for the experiments in Chapter 4. A schematic is shown in Figure 2.13 and pictured in Figure 2.14. In this instance the ion source was a Leybold-Heraeus 12/38, which included the ionization chamber, the first set of deflection plates (1) and focussing elements. The first set of deflection plates were used to create a pulse of the ion beam. Pulsing allowed for separation of the backscattered particles in the ToF unit by their velocities. The pulse width was ~20ns with a frequency of 56kHz. The Wien filter used for ion mass selection was from SPECS (Berlin). The extra deflection plates (2) were made by the electric and mechanical workshops at Flinders University. These facilitated the scanning of the ion beam across the target surface. The apparatus was also equipped with separate sample holders and a syringe input for liquid or foam film analysis, the use of this apparatus for these purposes was the focus of a PhD dissertation by Ridings in 2014[44]. The apparatus used 3kV He^+ ions, and the vacuum chamber pressure during NICISS acquisition was of the order of 10^{-7}mbar. Samples were mounted upon a rotating disc which was then also manually shifted to ensure ion dosing was kept below $5x10^{13}$ ions/cm^2. The ToF program was a multi-channel analyzer program from Multichannel Systems (MCS).

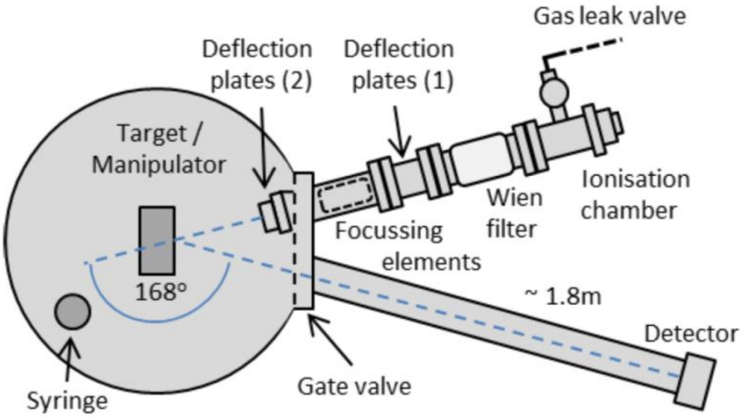

Figure 2.13: Top down schematic of the NICISS apparatus. Image courtesy of Ridings[44].

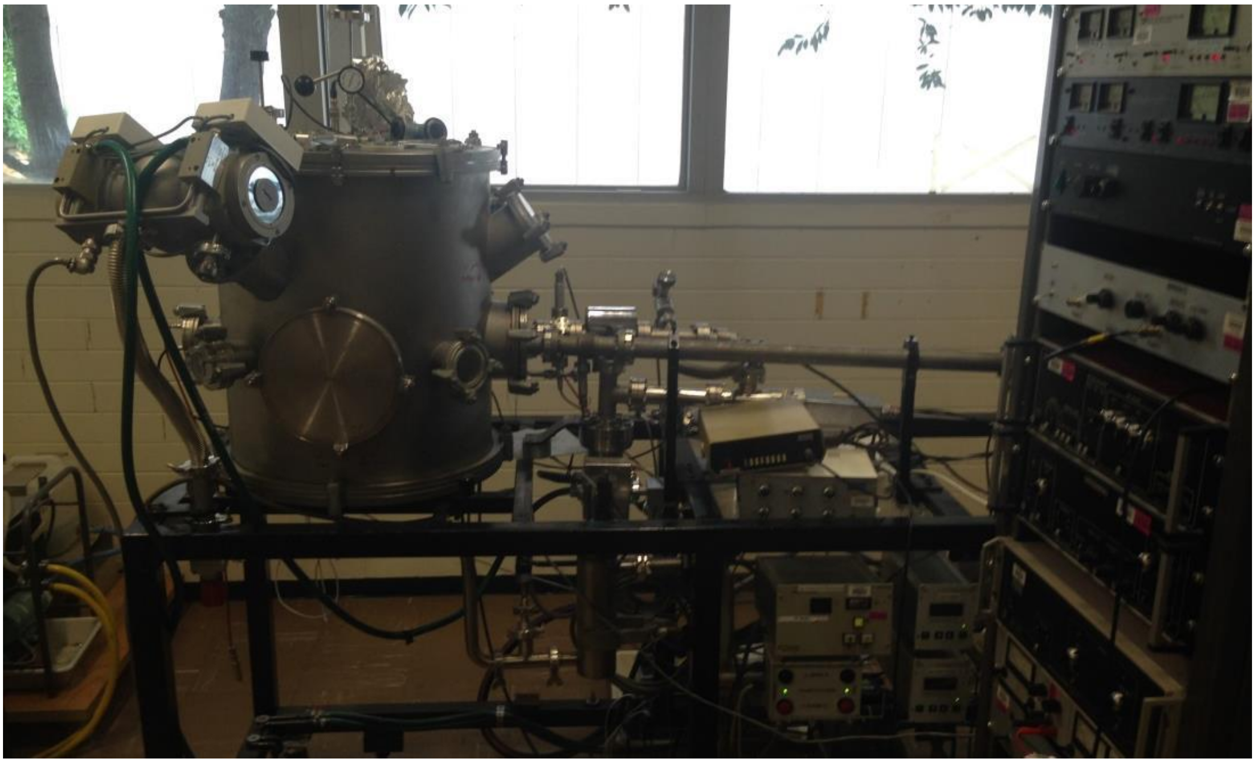

Figure 2.14: Image of the NICISS apparatus. Image courtesy of Ridings[44].

2.4) References

1. Briggs, D.; Seah, M. P., Practical Surface Analysis Second Edition Volume 2 Ion and Neutral Spectroscopy; John Wiley & Sons Ltd, **1992.**

2. Smith, D. P., Scattering of Low Energy Noble Gas Ions from Metal Surfaces. *J. App. Phys* **1967**, *38*, 340-347.

3. McConville C., W. M. Ion Scattering Schematic. http://www.caiciss.co.uk/caiciss.htm.

4. Grams, J., New Trends and Potentialities of ToF-SIMS in Surface Science; Nova Publishers, **2007**.

5. Aono, M.; Katayama, M.; Nomura, E.; Chassé, T.; Choi, D.; Kato, M., Recent Developments in Low-Energy Ion Scattering Spectroscopy (ISS) for Surface Structural Analysis. *Nuclear Instruments and Methods in Physics Research Section B: Beam Interactions with Materials and Atoms* **1989**, *37-38*, 264-269.

6. Niehus, H.; Comsa, G., Ion Scattering Spectroscopy in the Impact Collision Mode (ICISS): Surface Structure Information from Noble Gas and Alkali-Ion Scattering. *Nuclear Instruments and Methods in Physics Research Section B: Beam Interactions with Materials and Atoms* **1986**, *15*, 122-125.

7. Brongersma, H. H.; Gildenpfennig, A.; Denier van der Gon, A. W.; van de Grampel, R. D.; Jansen, W. P. A.; Knoester, A.; Laven, J.; Viitanen, M. M., Insight in the Outside: New Applications of Low-Energy Ion Scattering. *Nuclear Instruments and Methods in Physics Research Section B: Beam Interactions with Materials and Atoms* **2002**, *190*, 11-18.

8. Andersson, G.; Morgner, H., Impact Collision Ion Scattering Spectroscopy (ICISS) and Neutral Impact Collision Ion Scattering Spectroscopy (NICISS) at Surfaces of Organic Liquids. *Surface Science* **1998**, *405*, 138-151.

9. Aono.M, Quantitative Surface Atomic Geometry and Two-Dimensional Surface Electron-Distribution Analysis by a New Technique in Low-Energy Ion-Scattering. *Japanese Journal of Applied Physics* **1981**, *20*, L829-L832.

10. Rabalais, J. W., Principles of Ultraviolet Photoelectron Spectroscopy; Wiley: New York, **1977**, p 454.

11. Andersson, G.; Morgner, H., Investigations on Solutions of Tetrabutylonium Salts in Formamide with NICISS and ICISS: Concentration Depth Profiles and Composition of the Outermost Layer. *Surface Science* **2000**, *445*, 89-99.

12. Andersson, G.; Morgner, H.; Schulze, K. D., Surface Properties of Electrolyte Solutions Studied with Ion Beam Analysis. *Nuclear Instruments and Methods in Physics Research Section B: Beam Interactions with Materials and Atoms* **2002**, *190*, 222-225.

13. Briere, M. A.; Biersack, J. P., Energy Loss Straggling of MeV Ions in Thin Solid Films. *Nuclear Instruments and Methods in Physics Research Section B: Beam Interactions with Materials and Atoms* **1992**, *64*, 693-700.

14. Szilágyi, E., Energy Spread in Ion Beam Analysis. *Nuclear Instruments and Methods in Physics Research Section B: Beam Interactions with Materials and Atoms* **2000**, *161–163*, 37-47.

15. Andersson, G., Energy-Loss Straggling of Helium Projectiles at Low Kinetic Energies. *Physical Review A* **2007**, *75*, 032901.

16. Bragg, W. H.; Kleeman, R., On the A Particles of Radium, and Their Loss of Range in Passing through Various Atoms and Molecules. *Philosophical Magazine Series 6* **1905**, *10*, 318-340.

17. Einstein.A, On a Heuristic Point of View About the Creation and Conversion of Light. *Annalen der Physik* **1905**, *17*, 132-148.

18. Seah, M. P.; Dench, W. A., Quantitative Electron Spectroscopy of Surfaces: A Standard Data Base for Electron Inelastic Mean Free Paths in Solids. *Surface and Interface Analysis* **1979**, *1*, 2-11.

19. Westphal, C., The Study of the Local Atomic Structure by Means of X-Ray Photoelectron Diffraction. *Surface Science Reports* **2003**, *50*, 1-106.

20. Nilsson,A., Core Level Spectroscopy. http://ssrl.slac.stanford.edu/nilssongroup/corelevel.html.

21. Gunawardane R.P, A. C. R., Handbook of Applied Solid State Spectroscopy, Chapter 10, Auger Electron Spectroscopy; Springer: USA, **2006**.

22. Wang, C.; Andersson, G., Measuring Concentration Depth Profiles at Liquid Surfaces: Comparing Angle Resolved X-Ray Photoelectron Spectroscopy and Neutral Impact Collision Scattering Spectroscopy, *Surface Science*, **2011**; Vol. 605, p 889-897.

23. Chen, Y.-Y.; Yu, B.-Y.; Wang, W.-B.; Hsu, M.-F.; Lin, W.-C.; Lin, Y.-C.; Jou, J.-H.; Shyue, J.-J., X-Ray Photoelectron Spectrometry Depth Profiling of Organic Thin Films Using C60 Sputtering. *Analytical Chemistry* **2008**, *80,* 501-505.

24. Briggs, D.; Seah, M. P., Practical Surface Analysis Volume 1: Auger and X-Ray Photoelectron Spectroscopy 2nd ed.; Wiley ; Salle + Sauerlander: Chichester ; New York ; Aarau, **1990;** Vol. 1.

25. Grant, J. T., Methods for Quantitative Analysis in XPS and AES. *Surface and Interface Analysis* **1989**, *14*, 271-283.

26. Quinton, J. S. The Oscillatory Adsorption of Organofunctional Silanes on Metal Oxide Surfaces. PhD Dissertation, University of Newcastle, **2000**.

27. Barlow, A. J. Plasma Processing Studies with Application to Carbon Nanotube Fluorination. PhD dissertation, Flinders University, **2012**.

28. Quantitative Analysis of Surfaces by Electron Spectroscopy. http://www.quases.com/products/quases-imfp-tpp2m/.

29. Tanuma, S.; Powell, C. J.; Penn, D. R., Calculations of Electron Inelastic Mean Free Paths. Data for 41 Elemental Solids over the 50 eV to 30 keV Range. *Surface and Interface Analysis* **2011**, *43*, 689-713.

30. Scofield, J. H., Hartree-Slater Subshell Photoionization Cross-Sections at 1254 and 1487eV. *Journal of Electron Spectroscopy and Related Phenomena* **1976**, *8*, 129-137.

31. Schmerl, N.; Andersson, G., A Layered Structure at the Surface of P3HT/PCBM Blends. *Physical Chemistry Chemical Physics* **2011**, *13*, 14993-15002.

32. Horowitz, G., Validity of the Concept of Band Edge in Organic Semiconductors, *Journal of Applied Physics*, **2015**; Vol. 118, p 115502.

33. Helander, M. G.; Greiner, M. T.; Wang, Z. B.; Lu, Z. H., Pitfalls in Measuring Work Function Using Photoelectron Spectroscopy. *Applied Surface Science* **2010**, *256*, 2602-2605.

34. Hagstrum, H. D., Theory of Auger Ejection of Electrons from Metals by Ions. *Physical Review* **1954**, *96*, 336-365.

35. Hagstrum, H. D., Ion-Neutralization Spectroscopy of Solids and Solid Surfaces. *Physical Review* **1966**, *150*, 495-515.

36. Bell, K. L.; Dalgarno, A.; Kingston, A. E., Penning Ionization by Metastable Helium Atoms. *Journal of Physics B: Atomic and Molecular Physics* **1968**, *1*, 18.

37. Morgner, H., The Characterisation of Liquid and Solid Surfaces with Metastable Helium Atoms. *Advances in Atomic, Molecular and Optical Physics* **2000**, *42*, 387-488.

38. Harada, Y.; Masuda, S.; Ozaki, H., Electron Spectroscopy Using Metastable Atoms as Probes for Solid Surfaces. *Chemical Reviews* **1997**, *97*, 1897-1952.

39. van Emmichoven, P. A. Z.; Wouters, P. A. A. F.; Niehaus, A., Angle Resolved Electron Spectra from Grazing Incidence He2+/Cu(110) Collisions. *Surface Science* **1988**, *195*, 115-132.

40. Chambers, B. A.; Neumann, C.; Turchanin, A.; Gibson, C. T.; Andersson, G. G., The Direct Measurement of the Electronic Density of States of Graphene Using Metastable Induced Electron Spectroscopy. *2D Materials* **2017**, *4*, 025068.

41. Heinz, B.; Morgner, H., Surface Characterization by Means of Quantitative Evaluation of MIES Data. *Journal of Electron Spectroscopy and Related Phenomena* **1998**, *96*, 83-95.

42. Berlich, A.; Liu, Y. C.; Morgner, H., Evaporation of Ni and Carbon Containing Species onto NiO/Ni as Case Study for Metal Support Catalysts Investigated by Metastable Induced Electron Spectroscopy (MIES). *Radiation Physics and Chemistry* **2005**, *74*, 201-209.

43. Berlich, A.; Liu, Y.-C.; Morgner, H., Growth of Nickel Nanoparticles on NiO/Ni (001): Evidence of Adsorbed Oxygen on Metal Particles by Metastable Induced Electron Spectroscopy (MIES). *Surface Science* **2008**, *602*, 3737-3744.

44. Ridings, C. Investigating the Surface Structure of Liquids Containing Ionic Species. PhD Dissertation, Flinders University, Adelaide **2014**.

3. The Aims of This Work

There is clearly no single set of materials which has been found to create the optimal OPV cell with regards to efficiency as well as production cost and lifetime. This has driven the need for novel composite material fabrication and the ability to map and understand the precise nature of the created surfaces and interfaces formed with these various material combinations. There is also a range of requirements of the various thin films and interfaces comprising an OPV device which differs for each set of layers and their resulting interface. As such, the focus of this dissertation is not specifically geared towards the characterization of layers in one particular OPV cell, but instead toward a greater understanding of the electronic properties and film structure induced by some common film preparation or modification methods which can occur during fabrication, with a focus on the near surface area and in particular at the outermost layer of the film. The material selection here has been deliberately varied such that modifications to insulating materials, and both inorganic and organic semiconductors are all included in this work.

For electronic structure characterization UPS has been routinely used for measuring changes in workfunction and the electronic structure of the VB for many thin films, but thus far there have not been many studies which compare the electronic structure at various depths into the near surface area of a film. MIES in particular has not seen much use for OPV related thin film research despite it's obvious capacity to map changes in an interface which is not possible with other techniques. Naturally, electronic structure at the interface is not the only factor of importance, and the molecular distribution in the film will also play a role in the final properties. The combination of spectroscopic techniques available at Flinders University facilitates the ability to thoroughly map the electronic structure of thin films and also obtain concentration depth profiles, *in situ* if required. As such, the broad aim of this dissertation is the following:

To investigate the electronic properties and composition of thin films and modifications at various depths in the near surface area.

There is obviously an enormous range of materials and interfaces which could be studied in this manner, so a few common materials and modification methods have been selected for investigation with the hope that the insights gained here may assist other research methodologies. The researched interfaces are unique and as such the aims have been separated below.

3.1) Obtaining Valence Band Data for Insulating Materials

As already discussed, many of the films utilized in nano-based devices are composite materials. The constituents range through insulators, semiconductors and conductors depending on what the desired function of the film is. As discussed in Chapter 2, the principles of ES rely on the ejection of electrons from the surface in question. For insulating materials and some semiconductors surface charging can become an issue. Keeping an electronically neutral surface is imperative for a quantitative analysis of the surface because the data is a measurement of the electron energy. If a sample is charging, the resulting data is distorted. As such, methods for charge compensation need to be utilized to obtain useful data from these surfaces.

Although it may seem counterintuitive to require the VB of insulating materials when considering OPV devices, one of the points in forming composite materials or performing surface modifications in nanotechnology is the ability to change a material's properties into something which may then be useful in a nanoelectronic device, this can include modifying an electrically insulating material such that it has conductive properties. The ability to map the DOS for all constituent materials in a composite or modified film enables a deeper understanding of the created surface, and for the case of insulating polymers it may also facilitate a deeper understanding of mechanisms acting during the curing process. Thus one of the aims of this dissertation and the focus of Chapter 4 is to investigate multiple charge compensation mechanisms for VB spectral acquisition. These are:

1. Creating a very thin film such that the underlying substrate can replenish the surface electrons
2. The use of a gold mesh on top of the film
3. Embedding CNTs within the surface

The insulating polymer polydimethylsiloxane (PDMS) is gaining interest in the field of OPVs. As such it has been used in this work as the insulating material for which the VB spectra will be obtained. The VB spectra will be obtained for the near surface area with UPS and for the outermost layer with MIES. Chemical compositions will be mapped with XPS, and the diffusion (polymeric creep) of PDMS through the surface layer of CNTs during the curing process will be mapped in the form of concentration depth profiles with NICISS and also via the VB spectra.

3.2) Assessing the Impact of Doping and Surface Preparation/ Cleaning Methods on Transparent Conductive Oxides

Transparent conductive oxides (TCOs) are one of the choices for an electrode material in an OPV, and some of these a metal oxide which has been doped. These are generally fabricated via magnetron sputter deposition as this process is known to produce a uniform distribution of the dopant material. Different post fabrication surface treatments can be employed prior to depositing any further materials, however the impact on the electronic structure at the outermost layer has not yet been researched for a range of surface treatments. As discussed in detail already, the outermost layer holds great significance for the resulting interface when another material is deposited. As such, the aim of Chapter 5 is to investigate a range of surface treatment processes and the influences they have on the outermost layer and near surface area of a TCO film. The surface treatments are sputter cleaning with heating, plasma cleaning, and plasma cleaning with heating. This study also has the dual purpose of investigating any differences that a range of doping concentrations has on this region of the surface. The material selected for this investigation is zinc oxide along with a range of doping concentrations of aluminium which will be verified with XPS. MIES, UPS and also XPS of the VB will be employed to investigate changes in the electronic structure of various regions in the near surface area, and the band gap will be measured via ultraviolet-visible spectroscopy (UV-Vis).

3.3) Assessing the Impact of Alkali Fluoride Layer Thickness and Deposition Method on the Electronic Structure of PCBM and P3HT

Section 1.6.2 introduced the concept of using interlayers to assist in OPV performance. Although the use of interlayers is now rather universal, many fundamental studies on the influences of these interlayers on the active layer are still lacking. The aim of Chapters 6 and 7 is to perform a set of comparative studies between two alkali fluoride salts in an attempt to further the understanding of the influences that different salts have on the active layer materials prior to electrode deposition. For Chapter 6, lithium fluoride shall be deposited in various thicknesses on PCBM and P3HT films. The chemical composition and changes in chemical state will be mapped with XPS, the differences in the electronic structure between the outermost layer and near surface area will be investigated with MIES and UPS, and a concentration depth profile of one LiF layer will be obtained to check for diffusion of the LiF into the organic materials. A comparison will also be made between depositing the salt in a single exposure as compared to sequential exposures to investigate any changes in electronic structure that may come about from possible subtle changes in LiF layer formation.

In Chapter 7 this study will be repeated but with depositions of NaF instead of LiF. A discussion comparing the two salts will then be given.

4. Valence Band Structure of the PDMS Surface and a Blend with MWCNTs: a UPS and MIES Study of an Insulating Polymer

Natalya M. Schmerl, Dmitriy A. Khodakov, Andrew J. Stapleton, Amanda V. Ellis, Gunther G. Andersson*

Flinders Centre for NanoScale Science and Technology, Flinders University, Sturt Road, Bedford Park, Adelaide SA 5042, Australia

*Corresponding author email: gunther.andersson@flinders.edu.au

This work has been published and listed in the publications arising from this work section, alterations have been performed only in that any experimental methods and analysis procedures previously described in Chapter 2 have been removed, and supplementary information from the publication has been included in the text.

Author Contribution:

Natalya Schmerl: Designed and performed experiments, data analysis and interpretation, and prepared the manuscript for publication.

Gunther Andersson: Intellectual contribution in conceptualising experiments, data interpretation & revision of manuscript.

Amanda Ellis: Intellectual contribution in initial composite film design and revision of manuscript.

Dmitriy Khodakov: Sample preparation instruction for composite films.

Andrew Stapleton: Performed AFM measurements.

4.1) Abstract

The use of PDMS is increasing with new technologies working towards compact, flexible and transparent devices for use in nanoelectronics, medical and microfluidic systems. Electronic characterization of PDMS and other insulating materials is difficult due to charging, yet necessary for many applications where the interfacial structure is vital to device function or further modification. The outermost layer in particular is of importance as this is the area where chemical reactions such as surface functionalization will occur. Here, we investigate the VB structure of the outermost layer and near surface area of PDMS through the use of MIES paired with UPS. The chemical composition of the samples under investigation were measured via XPS, and the vertical distribution of the polymer was shown with NICISS. Three separate methods for charge compensation are used for the samples, and their effectiveness is compared.

4.2) Introduction

Technological developments are becoming increasingly precise with time, a larger variety of materials are being used and or modified for devices, and some of these materials are electronic insulators. Due to the highly precise nature of so many new developments there is an increasing need for the chemical structure and electronic properties of the various device interfaces to be known, as mismatched properties at these interfaces can impair or annihilate device function. Electron spectroscopy is one of the methods commonly used to determine the composition and electronic structure of surfaces. However, electron spectroscopy relies on electrons leaving the surface, so obtaining electron spectra for insulating materials is difficult and not common. Insulators build up charge when releasing the electrons in the measurement process which distorts the obtained spectra[1]. Here, we compare methods for measuring insulating surfaces with electron spectroscopic techniques. We have demonstrated these methods by investigating an insulating polymer surface along with a surface modification.

PDMS is a flexible, transparent polymer with a chemical formula of $[O\text{-}Si(CH_3)_2\text{-}]_n$ where *n* is the number of monomers. Also being hydrophobic it has a low surface energy in cured form (22.1 mN/m)[2], and is an important silicon-based polymer for industry [3-8]. It also has been gaining in popularity for flexible electronics and has been used as an encapsulation layer[9], and flexible substrate for an OPV[10]. It has even been used inside OPV devices as part of an active layer[11] and buffer layer[12] to assist the morphology. Modification of the surface of cured PDMS is difficult due to its propensity for hydrophobic recovery and its low surface energy[13]. As an alternative, PDMS could be mixed with other substances which allow for more permanent modification of the surface. Coupling PDMS with CNTs is one such example which could possibly be used as a transparent electrode in an OPV if sufficiently functionalized, or lead to other applications such as biosensors[14-16]. Multi-walled carbon nanotubes (MWCNTs) embedded into a PDMS layer need to form part of the surface for further chemical modification to occur. However, due to the low viscosity of the PDMS precursors they can migrate to the surface of the sample during preparation. In order to monitor the modification of a PDMS surface a surface sensitive method needs to be applied. Ideally, a method should be chosen which is sensitive exclusively to the outermost layer. MIES is an electron spectroscopic technique exclusively sensitive for the outermost layer and thus a method that can be used to monitor the modification of the PDMS surface via the VB. If the individual VB spectra of PDMS and MWCNTs are known, then features pertaining to PDMS in a composite sample can be identified. This is used in conjunction with UPS, which maps the VB for the near surface region, and XPS to give the chemical composition, providing an electronic energy level 'map' of the interface and surrounding region. This combination of techniques allows any creep of the PDMS through to the surface layers to be determined.

Insulating materials such as PDMS will charge when electron spectroscopy is performed, as the technique relies on the ejection of electrons from the surface and subsequent replenishment via electronic contact to the spectrometer. Insulating materials (materials with low conductivity) do not allow for sufficient charge transport and as a consequence causes charging of the sample while recording the spectra. Charge neutralization for insulators has been carried out previously and is somewhat common for XPS. The standard method is to use a charge compensating electron beam[17], however a grid of Au mesh can also be placed over the sample so the insulating surface charge is neutralized by electrons from the mesh. For VB electron spectroscopy the electron beam cannot be used as the beam energy is similar to the measured energies so it not only interferes with spectral acquisition but can also flood the analyzer with electrons and cause severe damage.

In this work, the authors used an Au mesh over the PDMS and MWCNT/PDMS surfaces to obtain XP, UP and MIE spectra. A 'standard' PDMS surface was created via drop casting onto a silicon wafer. The cured sample then had an Au mesh grid placed over the top prior to analysis. An ultrathin layer was also prepared to minimize charging taking note that this may have a different morphology to bulk material. For PDMS there is a critical transition which occurs at thicknesses <200 μm[18], so this method is not necessarily an accurate representation of bulk material so needs to be compared with other methods. An ultra-thin layer was created by diluting the PDMS pre-polymer in *n*-hexane and spin coating. This is referred to as 'thin PDMS' in the text. A third surface was prepared by adding MWCNTs, thus creating a surface with sufficient conductivity such that the samples do not charge. The purpose of this method is to create another method of measuring PDMS with electron spectroscopy, but also is an example composite film for potential nanoelectronic device applications. By comparing the spectra from these three methods, the UP and MIE spectra for PDMS was obtained and compared.

An elemental depth profile of the MWCNT/PDMS sample was obtained via NICISS to determine the distribution of PDMS through this samples surface.

4.3) Experimental

4.3.1) Materials and Sample Preparation

PDMS Sylgard 184 (Dow Corning Corporation, USA) was acquired in a two component form: pre-polymer base agent and a cross linking curing agent, used as a 10:1 ratio. Si wafers were As doped Si (n-type) $R < 5x10^{-3}$ Ω/cm (Materials Tech International, USA). The Si wafers were cleaned with Pyroneg solution (Johnson Diversey, Australia) then sonicated in absolute ethanol (Sigma-Aldrich, Australia) for 5 min, rinsed in ethanol and then dried under nitrogen. Au mesh was obtained from Goodfellow Cambridge LTD, UK with a nominal aperture of 0.25 mm, 99.9 % purity of the Au and 65 % open area. The mesh was cleaned with an oxygen plasma (Plasma Cleaner PDC-32G (Harrick Plasma)) with high purity oxygen (BOC LTD, Australia), operating at 200 mTorr for 2 min immediately prior to sample attachment and transfer into the UHV chamber of the electron spectrometer. Scanning electron microscopy (SEM) was performed on the Au mesh to ensure warping of the mesh had not occurred with various sample preparations. The microscopy was performed on a Camscan MX2500 at an accelerating voltage of 10 kV.

Thin PDMS films were produced by first diluting the 10:1 mix of pre-polymer PDMS/curing agent in *n*-hexane (HPLC grade >97 % Sigma-Aldrich, Australia) at 1:150 [19] and stirring for 24 h. A single layer was then spin coated (PWM32-PS-R790 spinner system, Headway Research) onto a cleaned Si wafer for 4 s at 1000 rpm (initial dispersion across surface), ii) 120 s at 5000 rpm (layer thickness reduction), and iii) 60 s at 300 rpm (initial settling of polymer). Subsequently each sample was cured on a hotplate for 1 h at approximately 80 ^{0}C. The layer thickness was determined by removing a local area of the PDMS layer with a scratch of a fresh scalpel blade and measuring the resulting average step height with an atomic force microscope (AFM). The AFM was acquired using a Bruker Multimode AFM with Nanoscope V controller using tapping mode. The average thickness of the PDMS layer was found to be approximately 86 nm. Thicker PDMS films were created via drop casting undiluted PDMS onto a Si wafer then cured, as described above.

MWCNTs with a purity of >99 %wt were obtained from www.cheaptubes.com and used as received. The MWCNT/PDMS layers were fabricated by initially dispersing 1 mg of MWCNTs in chloroform (HPLC grade >99.8 % Sigma-Aldrich, Australia) and sonicated until well dispersed. The solution was then filtered through a polyamide filter membrane (37 mm discs, 0.2 µm hole diameter, Sigma-Aldrich, Australia) using a Millipore filtration system creating a 25 mm diameter circular layer of MWCNTs. This was then fully dried by placing in an oven for 5 min at 60^0C. PDMS/Curing agent mix was then poured onto the MWCNT membrane with the use of a mold to create a 2 mm thick disc. This was then cured on a hotplate at 115^0C for 15 min. The mold was then removed and the polyamide filter membrane peeled off. The resulting MWCNT/PDMS disc was then baked for a further 5 min in an oven at 100^0C. The disc was then sonicated in ultra-high purity isopropanol (Sigma-Aldrich, Australia) for 5 min to remove any impurities then dried under nitrogen.

4.3.2) Methods

XPS, UPS and MIES were all performed in the standard manner with pass energies and resolution described in Chapter 2. For NICISS the separate rather than *in situ* apparatus was utilized as atmospheric exposure was not of concern to obtain the relevant data. The samples were mounted on a rotating disc. The surface of the samples was investigated in concentric circles with a total surface area of about 1 cm^2. The ion dose was kept below $5\cdot10^{13}$ ions/cm^2.

4.3.3) Analysis

4.3.3.1) XPS

Standard XPS analysis using CASA software was performed on all samples using the Shirley background subtraction method. Samples were calibrated to the C1s peak at 285 eV. For samples utilizing the Au mesh as charge compensation a further analysis was required so that the percentage of Au in the measured spectra could be known and subtracted from the MIES/UPS data. This is possible because the Au mesh does not chemically interact with the samples under investigation. The transparency of the mesh with respect to the analyzer must be known so that the contribution of the Au mesh to the spectra can be taken into account in the UPS and MIES analysis (see Equations 4.3 & 4.4). This can be done simply by comparing the elemental intensity in a control sample with that of a mesh covered sample. In this instance we have used a Si wafer for the calculation:

$$Transparency = {}^{I(Si+Au)}\!\big/_{I(Si)}$$ **--- Equation 4.1**

Where *I(Si+ Au)* is the intensity of Si in the Si + mesh sample and *I(Si)* is the intensity of Si in the Si control. It was found to be approximately 40% lower than the physical transparency due to shadowing effects of the analyzer. Results were reproducible. Shadowing effects are created from two phenomena occurring during measurements. Electrons emitted from the sample can collide with the mesh, and would be absorbed by the mesh. As a result, a lower percentage of the electrons emitted from the sample are seen in the resulting spectra. The mesh also creates areas on the sample surface which cannot be reached by the incident photons (physically shadowed). This is due to the angle between the X-ray source and the sample.

4.3.3.2) MIES/UPS

The procedure for extracting the PDMS spectrum from the Au mesh/PDMS sample is via simple subtraction methods, which have been used previously in UPS and MIES analysis[20-24]. This is only possible when the components are not chemically interacting, so the spectrum is a sum of the individual components such that:

$$S = \sum_{i=1}^{n} fiSi \qquad \text{--- } \textbf{Equation 4.2}$$

Where S is the spectrum of the sample, S_i the spectra of the pure components and f_i the weighting factors (α, β, γ etc). For MIE spectra f_i represents the fraction of the surface covered with the species i. In the case of UPS, f_i gives the fraction of the volume probed by UPS that is occupied by species i.

Following from Equation 4.2, for a PDMS sample with mesh:

$$S = \propto PDMS + \beta Au \qquad \text{--- } \textbf{Equation 4.3}$$

To be able to isolate the PDMS component of the MIE spectra the Au mesh spectrum must be known. To do this the control set of samples using Si wafers was used. The Au spectrum is extracted from the (Si + Au) spectrum by using the mesh transparency acquired via Equation 4.1 and weighting the Si component accordingly so that it may be subtracted:

$$S(Au) = S(Si + Au) - S(Si).(Mesh\ transparency) \qquad \text{--- } \textbf{Equation 4.4}$$

Then to extract the PDMS spectral component from the mesh covered PDMS sample:

$$S(PDMS) = S(PDMS + Au) - S(Au) \qquad \text{--- } \textbf{Equation 4.5}$$

From here the remaining PDMS spectrum can be plotted. It is worth noting here that this derivation method reduces the overall spectral intensity as the exponential background of the MIE/UP spectra and some of the occupied DOS common to both the Au and PDMS have been partially subtracted, but as it is being compared to other spectra qualitatively it is only the location of the features which is of primary interest. This spectrum will be denoted ‘derived PDMS’ in the results.

4.3.3.3) NICISS

A NICIS spectrum has a series of element steps which have a step height directly corresponding to the percentage of that element present within the sampling depth. Because of this, the amount of PDMS present within the sampling depth was able to be calculated. The silicon step is purely indicative of the presence of PDMS, whereas the carbon step has a contribution from both the PDMS and MWCNTs, see Equation 4.6. This again follows the principles of Equation 4.2, where in this instance the sum is the element step as a whole and the constituent parts are the intensities coming from the methyl groups of PDMS and the MWCNTs.

$$ICtot = IC(PDMS) + IC(MWCNTs)$$ --- **Equation 4.6**

Where *ICtot* is the total intensity of the measured carbon step in NICISS, IC*(PDMS)* is the contribution from the methyl groups of PDMS, and IC*(MWCNTs)* is that of the nanotubes. By using the intensity of the silicon step in the spectrum, the intensity of the PDMS related carbon *(IC(PDMS))* can be calculated by using the element ratios observed in XPS. Subsequently the remaining carbon intensity could then be attributed to the nanotubes, and the MWCNT content of the first 10nm can be discerned, see Equation 4.7. The limited depth of this calculation is due to the sampling depth of XPS.

$$IC(CNTs) = ICtot - I\ {}^{C}/_{Si}\, Si(PDMS)$$ --- **Equation 4.7**

Where $I\ {}^{C}/_{Si}\, Si(PDMS)$ is the height of the carbon step calculated via the known step height of silicon.

4.4) Results and Discussion

The discussion for each of the techniques is given with the results to allow the reader to follow the outcomes with more ease. XPS is discussed first (section 4.4.1). For MIES and UPS (section 4.4.2) the results of all PDMS containing samples is shown initially (section 4.4.2.1) and the MWCNT content of the MWCNT/PDMS sample was calculated in UPS. The MIE and UP spectra were fitted to Gaussian DOS components and compared with previous publications (section 4.4.2.2). The derivation of the thin PDMS spectra using Equations 4.4 and 4.5 is also shown for completion (section 4.4.2.3). The vertical MWCNT distribution of in the MWCNT/PDMS sample is then shown with NICISS (section 4.4.3).

4.4.1) XPS

XPS was performed on all samples, however, only the samples containing PDMS are shown below in Table 4.1. Peaks may be seen in Figures 4.1 and 4.2. The peak positions and the relative peak intensities for the thin film PDMS and the MWCNT/PDMS sample are shown in Table 4.1 and were reproducible. XP spectra taken using the Au mesh were only required for determining the transparency of the Au mesh in the electron spectroscopy measurements and thus are not discussed here. The MWCNT control sample was found to contain approximately 4.5% oxygen. The MWCNTs were not found to chemically react with the PDMS in the MWCNT/PDMS samples. Sample charging was not observed in XPS (peaks were not altered in shape or skewed toward higher binding energies).

The pristine thin PDMS was found to have a slightly higher oxygen component than the chemical formula (see Table 4.1). The peak positions were the same as reported previously in literature[25-28]. Higher O content than the stoichiometric ratio has been seen before in XPS[29].

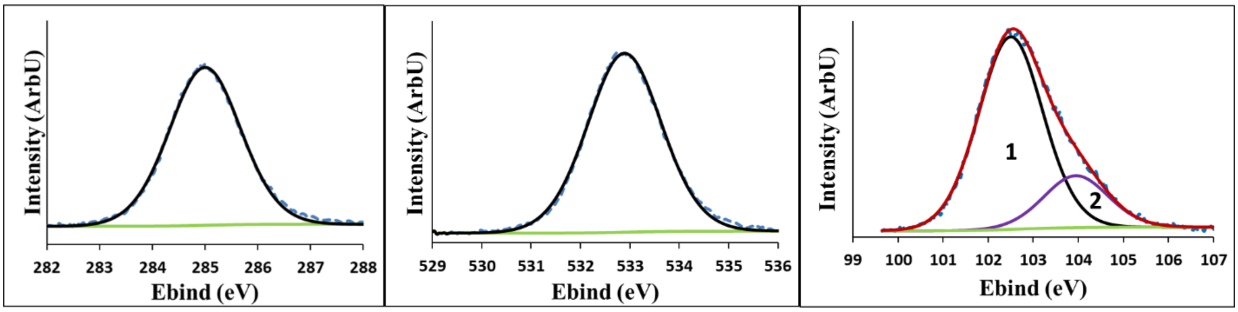

Figure 4.1: Primary (lef): C1s, (middle): O1s, and (right): Si2p photoelectron peaks for the thin PDMS sample.

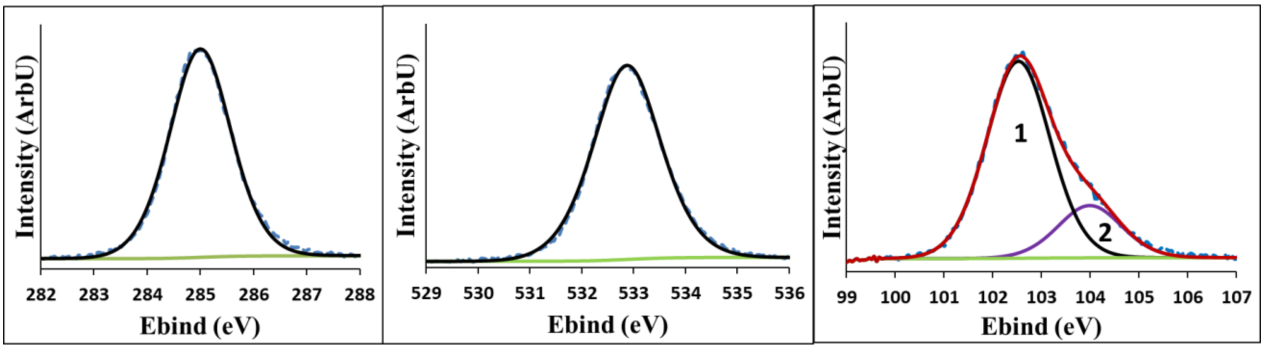

Figure 4.2: Primary (left): C1s, (middle): O1s, and (right): Si2p photoelectron peaks for the MWCNT/PDMS sample. A single peak was used to fit the Si2p doublet as the peak separation is small enough that the doublet could be appropriately approximated with a single component.

Sample	Peak	Composition % (theoretical)	Composition % (measured)	Position (eV)
Thin PDMS	Si 2p	25	21.8 ± 0.3	102.5, 104.0
	O 1s	25	34.5 ± 0.3	532.7
	C 1s	50	43.8 ± 0.4	285.0
MWCNT/PDMS	Si 2p	-	20.9 ± 0.3	102.5, 103.9
	O 1s	-	33.7 ± 0.4	532.9
	C 1s	-	45.5 ± 0.5	285.0

Table 4.1: XPS peak positions and composition of PDMS and MWCNT/PDMS samples.

The main silicon peak at 102.5 eV is from PDMS. The secondary component at 104.0 eV is possibly from slightly oxidized PDMS chains. This high binding energy peak in PDMS has been measured previously[24] and was attributed to oxidation of the backbone. Oxidized PDMS could also account for the extra oxygen in the sample. The contribution of the higher binding energy peak is 20% of the total silicon signal and does not change upon the addition of nanotubes. The addition of MWCNTs showed a 1.7% increase in C signal, a 0.9% decrease in Si and a 0.8% decrease in O compared to neat (thin) PDMS. This shows a high PDMS content still present in the first 10nm of the MWCNT/PDMS composite. By following the Si:O:C ratios it can be seen that there is roughly a 1:1 decrease in Si and O as would be expected if MWCNTs were replacing PDMS in the sample depth measured. According to the chemical formula for PDMS the carbon signal would decrease by a factor of 2 compared to silicon and oxygen, thus an overall decrease in signal of 1.8% in carbon from PDMS would have occurred (although this was masked in the observed intensities by the presence of new carbon in the form of MWCNTs). The total increase in MWCNTs was equal to the observed increased carbon signal plus any reduction in element intensity from PDMS (Si, O, C) = (0.9 + 0.8 + 1.8). The overall 1.7% increase in C peak with the addition of MWCNTs thus shows the addition of MWCNTs to be (0.9 + 0.8 + 1.8 +1.7) = 5.2% of the measured surface. For the purposes of this study a high concentration of PDMS is required at the surface to allow an accurate VB spectrum of PDMS to be shown, but for applied purposes it indicates that the applied method for producing the MWCNT/PDMS sample is not suitable for fabricating samples which require a strong presence of MWCNTs at the surface due to the PDMS ability to creep through the MWCNT layer. The exact percentage of PDMS present in the first 10nm cannot be determined from the XPS results however, as it is not possible to discern the MWCNTs from the PDMS in the component analysis. Also, the density of the MWCNTs and the distribution of the PDMS chains around the nanotubes is unknown and wrapping effects could be changing the density of the near surface area. The vertical PDMS distribution in the near surface area is thus shown with NICISS.

4.4.2) MIES/ UPS

4.4.2.1) Comparisons between charge compensation mechanisms

Figure and Figure show the MIE and UP spectra of neat (thin) PDMS, neat MWCNTs, derived PDMS and the MWCNT/PDMS composite, respectively. The derived PDMS spectrum is of a smaller intensity (as discussed in experimental) and has been plotted on a separate Y axis so that the peak maximum at 10eV in MIES and 11eV in UPS is matched to the spectral intensity of the MWCNT/PDMS composite at this point for easier comparison. The spectra used for the derivation process for the Au mesh and also the derived PDMS is then shown at the end of the VB results in section 4.4.2.3: Figures 4.7- 4.10.

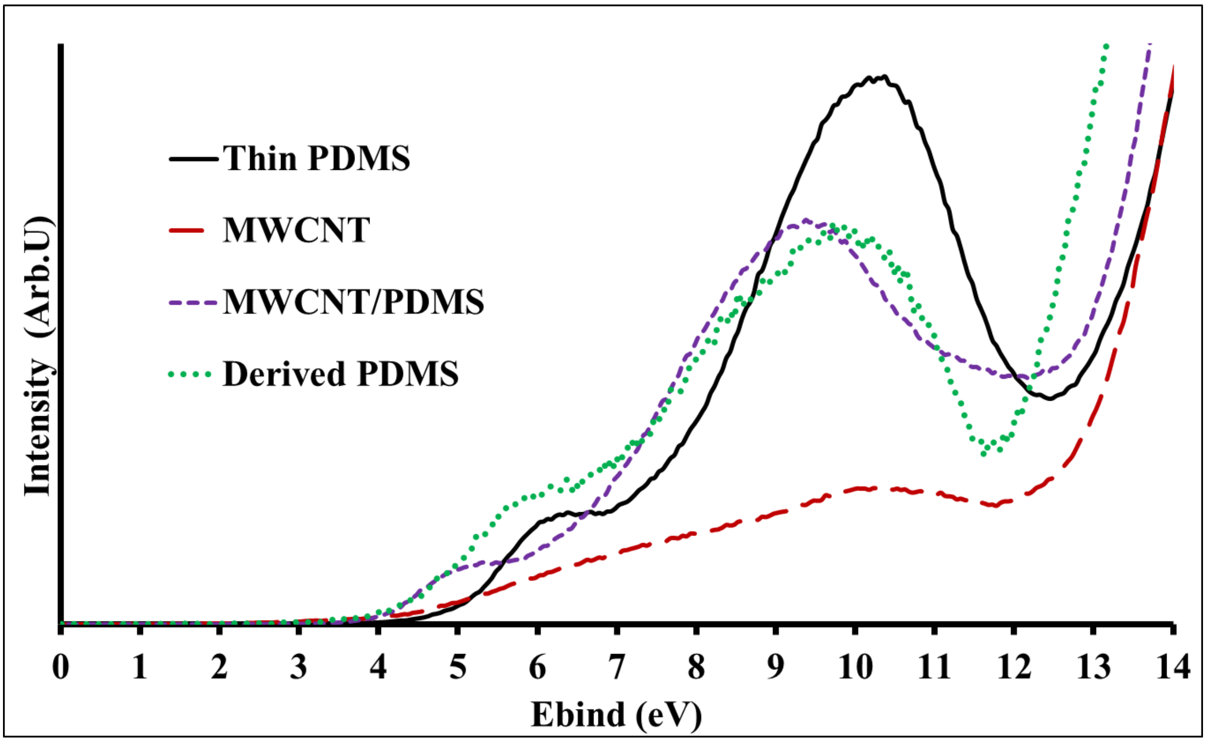

Figure 4.3: PDMS and MWCNT MIE spectral comparison. The derived PDMS spectrum is plotted on a separate Y axis to better show the DOS, the spectrum is plotted such that the intensity matches that of the MWCNT/PDMS sample at 10eV. Note that the MWCNT/PDMS sample has the same main spectral features of the thin PDMS but at a higher binding energy.

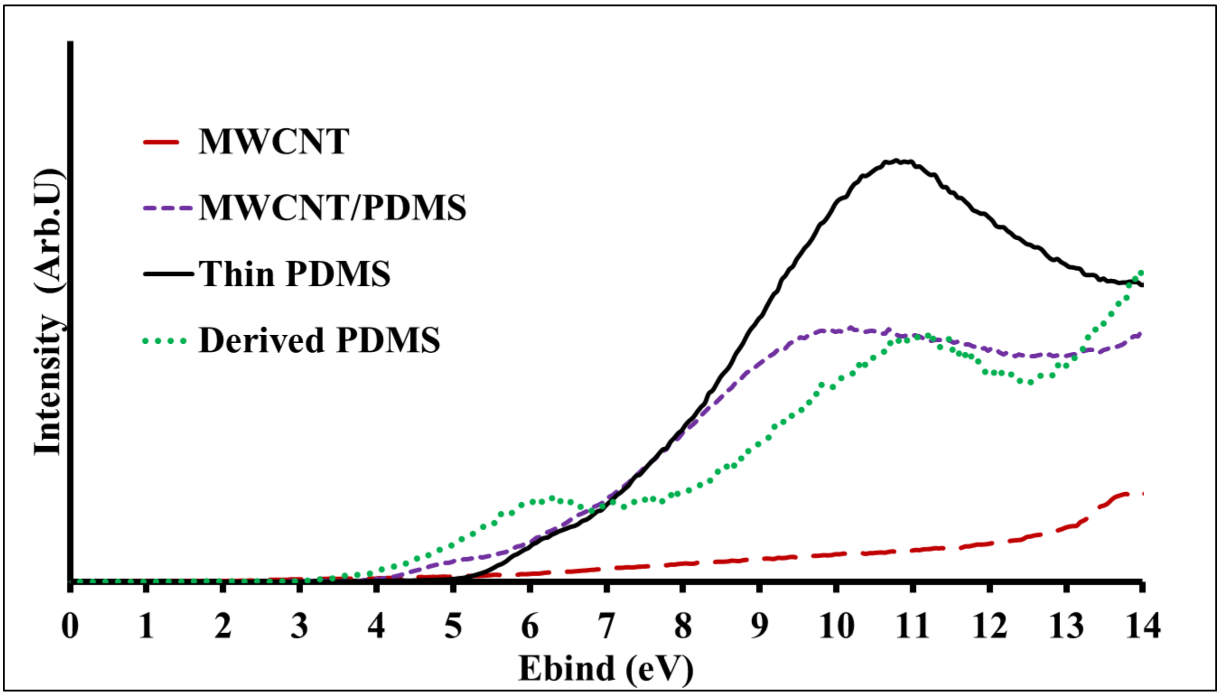

Figure 4.4: PDMS UP spectral comparison. The derived PDMS spectrum is plotted on a separate Y axis to better show the DOS, the spectrum is plotted such that the intensity matches that of the MWCNT/PDMS sample at 10eV. Note that the MWCNT/PDMS sample has the same main spectral features of the thin PDMS but at a higher binding energy.

The overall spectral features are similar for both sets of PDMS spectra. As stated, the derived spectra are qualitative in nature (with respect to intensity) and only used to verify the position of peaks in comparison to the other methods. For both UPS and MIES features at energies higher than around 12eV in the derived spectra cannot be discussed as the derivation process causes distortion from background subtraction this close to the secondary electron peak.

The spectral features of the thin PDMS and derived PDMS are shifted to a higher binding energy with respect to the MWCNT/PDMS sample. This can be easily seen by looking at the main features. The low binding energy feature shown at 5eV in the MWCNT/PDMS is shifted to 6eV in the thin film, and the high binding energy peak at 9.3eV for MWCNT/PDMS is shifted at 10.3eV in the thin film. This high level of similarity with an X-axis offset between the spectra indicates charging of the thin PDMS sample, which is still possible with a thin insulating film. Positive charging of a sample due to the emission of electrons from the sample shifts the features of a spectrum to a higher binding energy. Spectral broadening can also occur as the shifted features add to the DOS of the un-shifted features, effectively 'blurring' the spectrum, which is what is observed by looking at both the MIE and UP spectra of thin PDMS with respect to the MWCNT/PDMS composite. When comparing the position of the PDMS features relative to the energy scale of the derived spectrum it can thus be concluded that there was some charging present but to a lesser degree than the thin layer, as the features are shifted but to a lesser extent. This again can be more easily seen in MIES, and also most easily observed at the lower binding energy region as there are less features to overlap and also less background subtraction. Due to the charging the percentage of MWCNTs in the MIE spectrum was not able to be derived via the control spectra. The IP of the thin PDMS sample was found to be 7.8eV and the MWCNT/PDMS composite was 7.3eV. Both numbers have been stated here for completeness, but the value for the MWCNT/PDMS composite has been taken as the most accurate value.

As an interesting point of comparison, the VB of polydimethylsilane $[Si(CH_3)_2]_n$ has been measured and calculated by Seki *et.al*[30]. This is the conductive version of the polymer where the backbone is silane only. The features were very similar to those of the PDMS measured in this work. The IP was found to be 5.9eV.

4.4.2.2) Gaussian fitting

In order to compare the measured spectra with theoretically calculated DOS of PDMS by Ferenczy *et.al*[31] and also to their experimental data using XPS for the VB region, a Gaussian fit to the MIE and UP spectra were made to approximate the experimental peak positions for PDMS and can be seen in Figure 4. and Figure 1. A table summary of peak positions can be seen in Table 4.2. Peak positions were held as a constant between MIES and UPS so that only the spectral intensities were a fitting parameter. The MWCNT/PDMS composite was used for the peak fitting due to the lack of charging. The MWCNT control spectrum is broad and featureless in the binding energy region of interest (see Figures 4.3 & 4.4), so for the purposes of peak fitting does not need to be taken into account. An attempt was made to peak fit the thin layer PDMS, but the fit did not correlate well to the measured spectra as the charging distorts the spectral components away from a Gaussian shape.

Assigning the fitted peaks to the functional groups of PDMS is complicated by the fact that in the theoretically calculated work[31] the peak at the lowest binding energy is at a different binding energy than the peak at the lowest binding energy found in the UP and MIE spectra shown here. Measured and calculated binding energies usually differ thus need to be correlated. Correlating calculated binding energies to measured binding energies usually is achieved by offsetting the energy scales of the calculation such that the position of the peak with the lowest calculated binding energy aligns with the peak with the lowest binding energy in the experimentally measured spectrum[32]. Because the peak with the lowest binding energy in the XP spectrum in the theoretical calculations[31] is at about 1.5eV higher binding energy than the peak with the lowest binding energy in the UP spectrum shown here, we take the energy difference of 1.3eV into account in Table 4.2 for assigning the peaks in the UP spectra to specific functional groups.

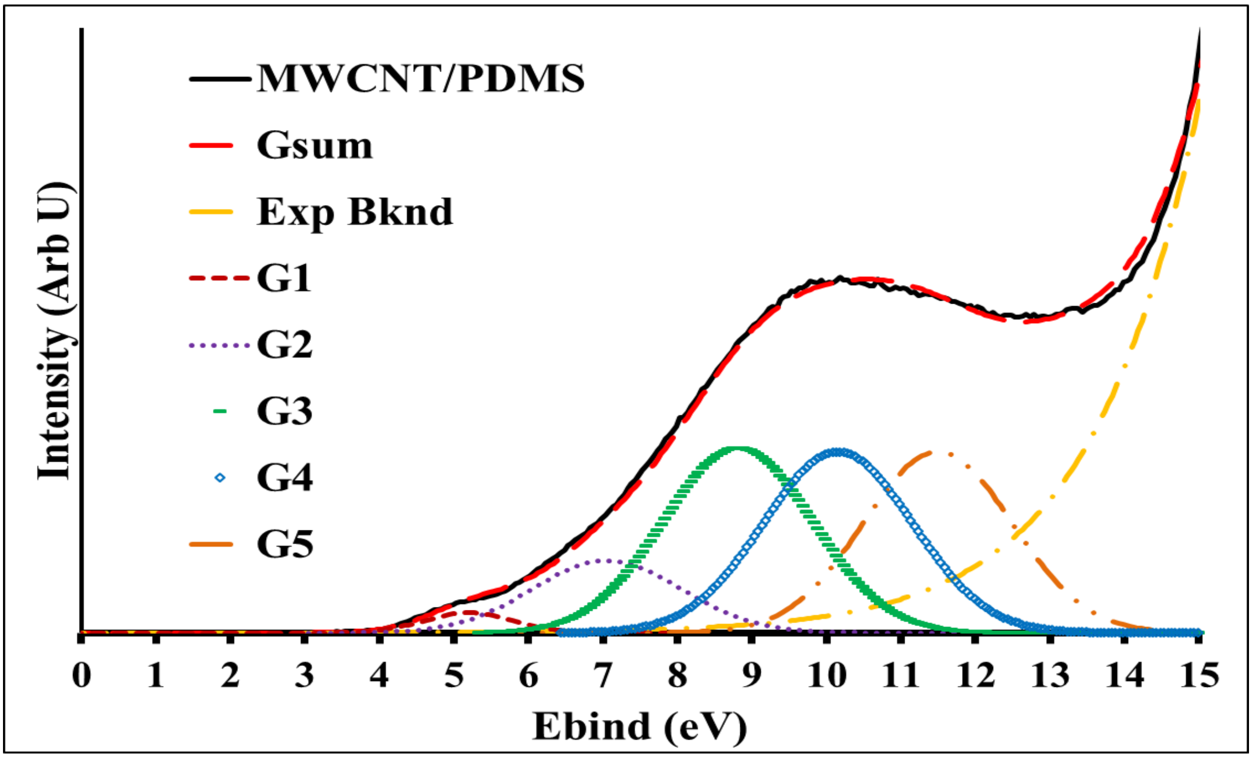

Figure 4.5: Gaussian peak fitting for the MIE spectrum of the MWCNT/PDMS composite, where Gsum is the sum of all Gaussians G1~G4, and Exp Bknd is the exponential background of the measurement. G1~G4 are optimized to best fit Gsum to the experimental data.

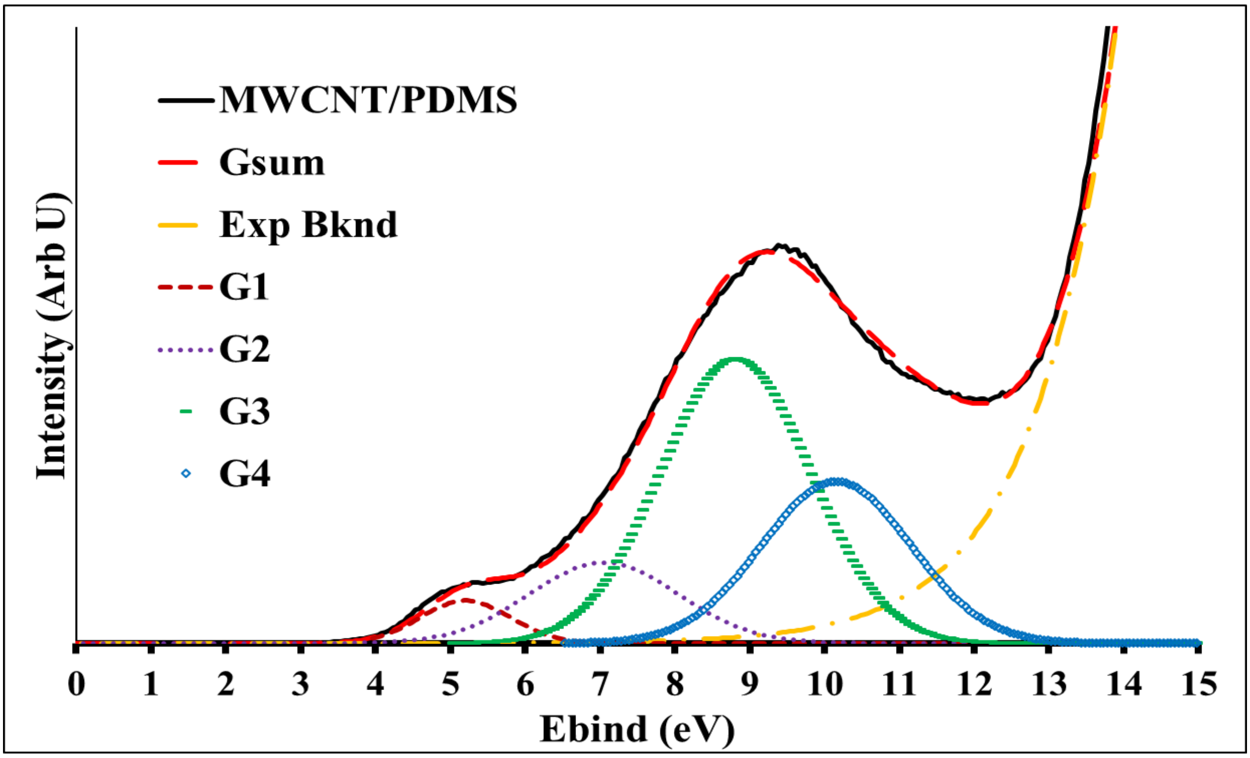

Figure 1.6: Gaussian peak fitting for the UP spectrum of the MWCNT/PDMS composite. where Gsum is the sum of all Gaussians G1~G5, and Exp Bknd is the exponential background of the measurement. The peak intensity of G1~G5 are optimized to best fit Gsum to the experimental data.

The MIE and UP spectra have very similar features but with different peak intensities. For the UP spectra the predominant features are G3, G4 and G5 and for the MIE spectra G3 and G4. G3 can be attributed to the O2p orbital and the siloxane backbone. G4 is spread across all components. Peak G5 in UPS can be attributed to the Si-O backbone (stated as broad peaks from 12~14eV in [31]) and is not present in the MIE spectrum. The presence of the low binding energy peak (G1) in MIES shows that there is oxygen present at the outermost layer as the states around 6 eV are attributed to lone pair oxygen[31]. This presence of G1 and absence of G5 in MIES indicates that any exposed areas of the polymeric backbone are primarily the O2p orbitals – which intuitively makes sense for two reasons. Firstly, the Si-O DOS would be physically shadowed by the methyl groups which are attached to the silicon. Secondly, the cross section between the O2p (lone pair) orbital and the He* is rather large. It cannot be concluded definitively to what extent alkyl chains cover the surface because the peak with a strong alkyl chain contribution – G4 – has also contributions from O2p. However, the absence of G5 in the MIE spectrum shows that the Si-O backbone does not cover the outermost layer. As a consequence it can be concluded, that the CH3 groups cover a substantial part of the surface due to the presence of the G4 peak in the MIE spectrum. Due to the low surface energy of PDMS adventitious hydrocarbons would be contributing a very low if any DOS to the MIE spectrum[1]. Also, if adventitious hydrocarbons were present in significant quantities on the surface then it is highly unlikely that the lone pair oxygen peak (G1) would be observed as the spectrum would be showing hydrocarbons instead.

Label	**MIES**	**XPS**	**UPS**	**Feature**
IP	-	-	7.3	-
G1	5.2	6.5 (5.2)	5.2	O2p, some CH*
G2	7.1	8.0 (6.7)	7.1	O2p
G3	8.8	9.5 (8.2)	8.8	SiO, O2p
G4	10.2	11 (9.7)	10.2	CH*, SiO, CH_3
G5	11.5	13 (11.7)	11.5	SiO, some O
G6	13.2	17 (15.7)	13.2	SiO
X	-	17	-	C2s

Table 4.2: Measured and calculated DOS for PDMS, all values are in eV. XPS features from [27], orbital specification (feature) from [31]. Hydrocarbon (*) features measured by [22]. The values in the XPS column are estimations from [31]. The values in brackets in the same column take into account the estimated shift of 1.3eV between the peaks in the XP spectra from [31] and the UP and MIE spectra from this work.

The previous experimental work using VBXPS[27-29, 31] show a similar overall spectral shape to that of this work, and all experimental spectra show occupied DOS below the theoretically calculated VB maximum of 7eV. There are some differences, however, and a few reasons for these are proposed in the following. Firstly, the increased sampling depth in VBXPS displays provides less surface sensitivity, thus displaying properties more akin to the bulk. The lowest surface energy arrangement for the polymer is to have the methyl chains sticking out from the surface rather than the Si-O backbone[33], so MIES in particular would be sampling DOS primarily from the methyl groups. UPS would penetrate through this and see the backbone, but still not necessarily as much as XPS, depending on the way the polymer is organised near the surface. Also, the non-monochromated source in Ferenczy's work[31] would have a small contribution of satellite peaks. The use of a flood gun in Haines' work[27] versus no charge compensation in Mundry's[29] versus thin layer film/ addition of MWCNTs or the Au mesh in this work could also cause discrepancies.

4.4.2.3) Spectra obtained for the derivation of the PDMS spectrum acquired using the Au mesh

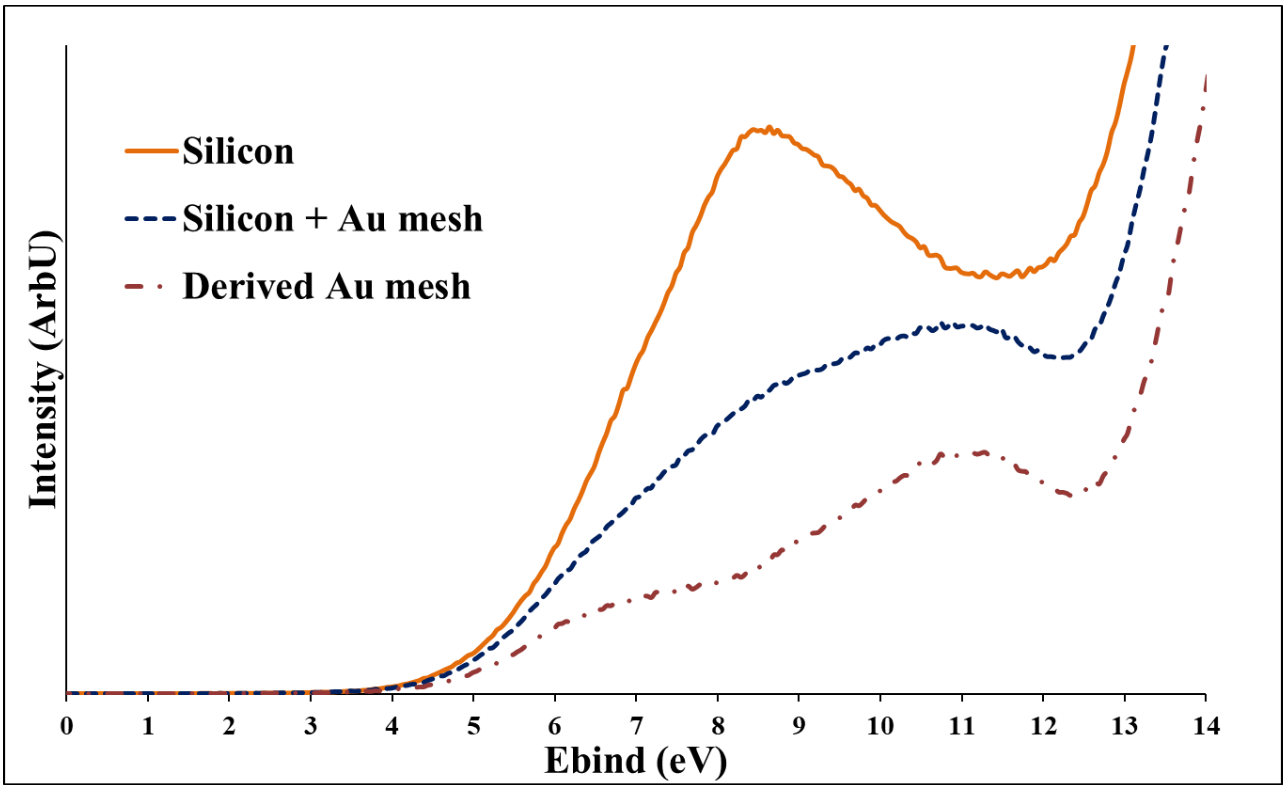

Figure 4.7: Spectra used for the derivation of the Au MIE spectrum, using Equation 4.4

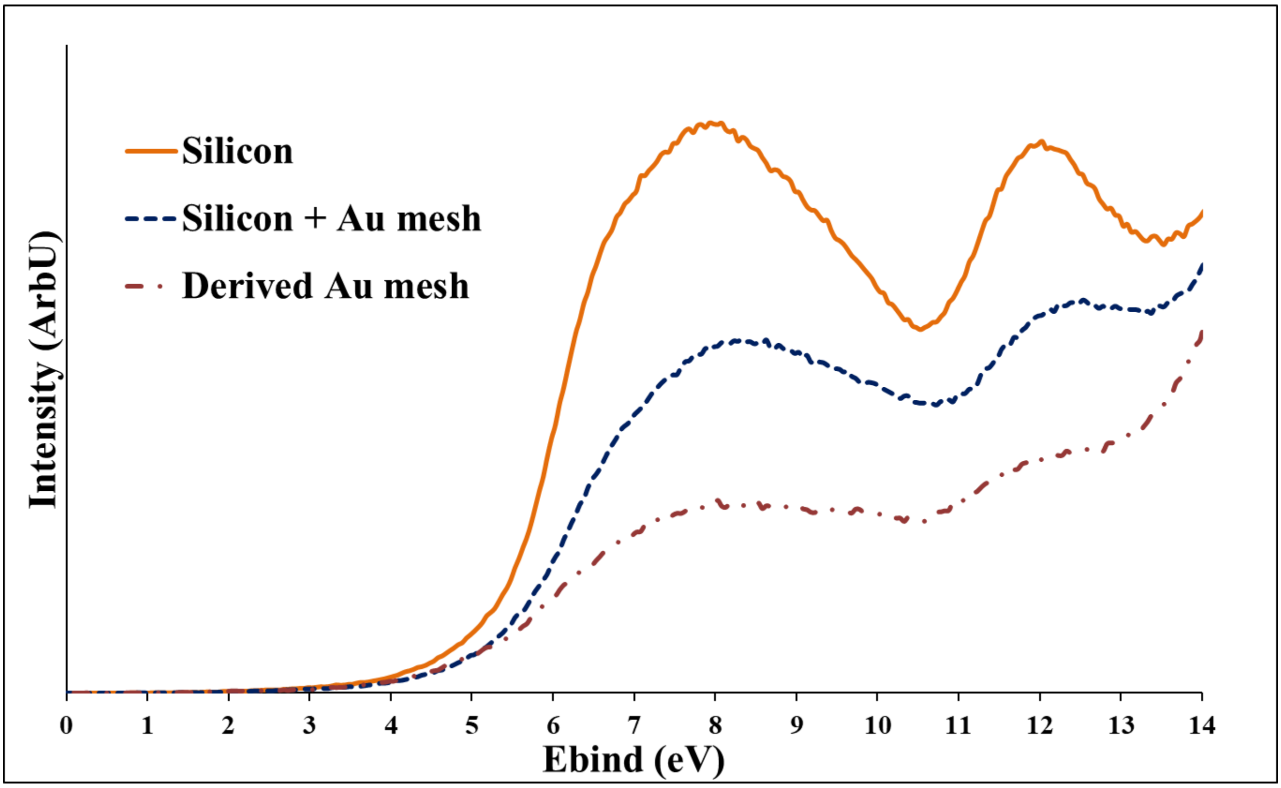

Figure 4.8: Spectra used for the derivation of the Au UP spectrum, using Equation 4.4

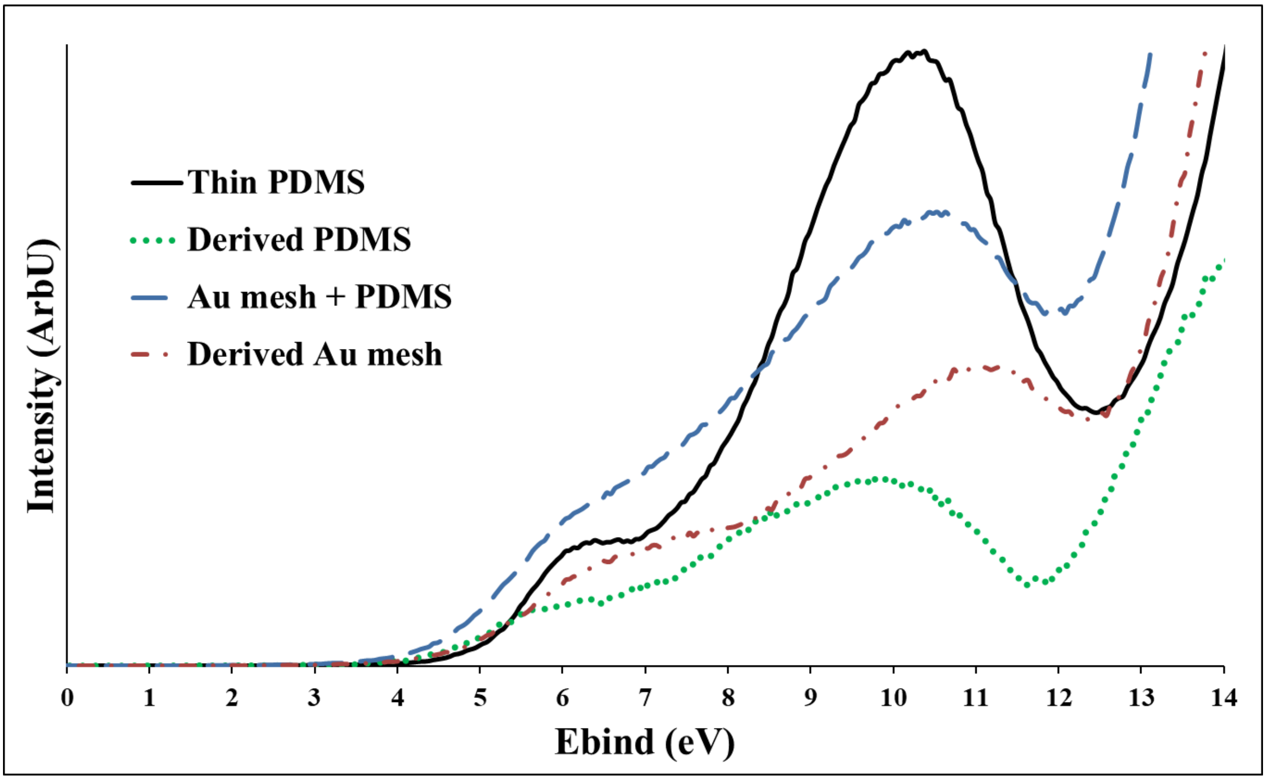

Figure 4.9: Spectra used for the derivation of the derived PDMS MIE spectrum, using Equation 4.5, thin PDMS also shown for comparison.

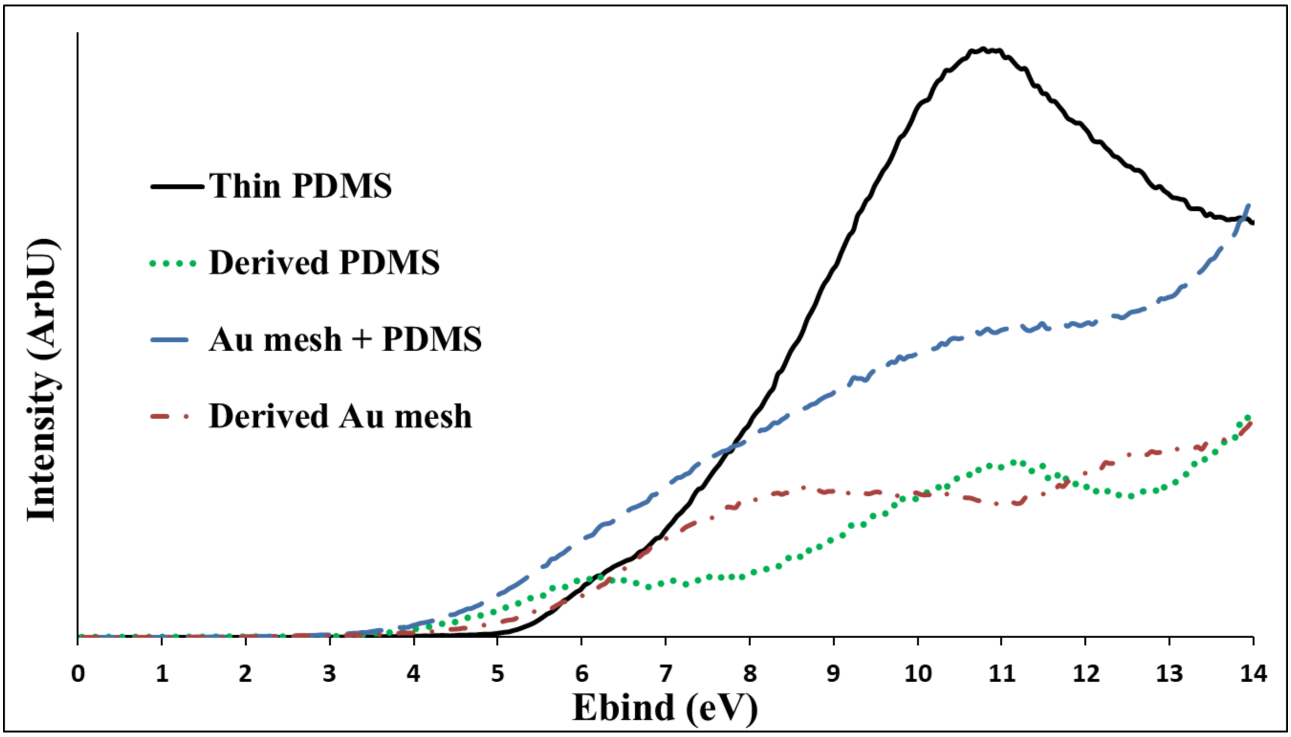

Figure 4.10: Spectra used for the derivation of the derived PDMS UP spectrum, using Equation 4.5, thin PDMS also shown for comparison.

4.4.3) NICISS

NICISS was performed on the MWCNT/PDMS composite in order to map the diffusion of the PDMS polymer. The results showed that silicon was present on the surface of the sample and that there was a uniform distribution throughout the near surface area. This may be seen in Figure by the constant concentration through the depth (fluctuations in concentration create minima and maxima in the concentration depth profile).

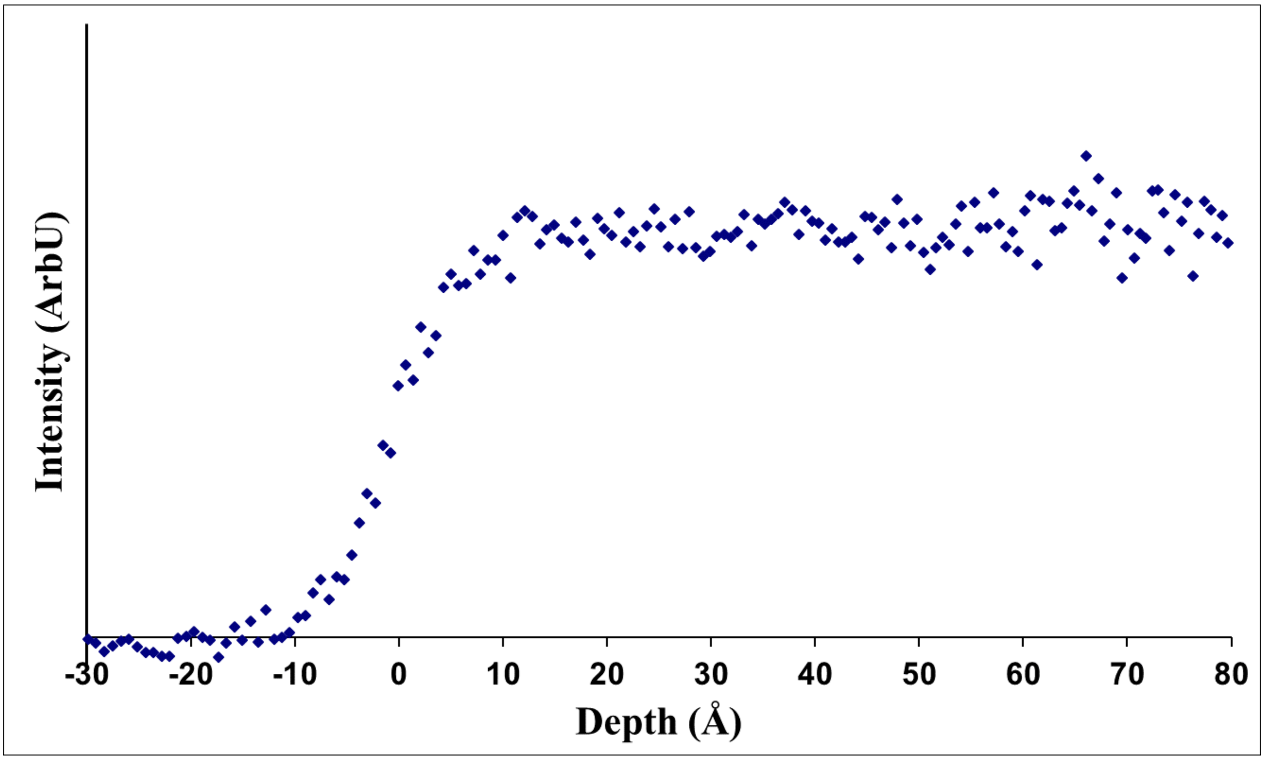

Figure 4.11: Depth profile (NICISS) for Si in the MWCNT/PDMS composite sample.

In this instance the spectrum has not been converted from intensity to concentration as the density of the MWCNTs is not known, nor is the chain length of the PDMS polymer. As such, converting to a concentration depth profile in this instance would have a large error associated with it, and for these purposes not necessary, as it is mainly the shape of the depth profile that is of interest. The exact concentration of MWCNTs at the surface of the sample is thus not calculated via NICISS. However, it is expected that there are MWCNTs present in the outermost layer, as the silicon spectrum shown in Figure 4.11 would show a slight decrease in intensity below the outermost (i.e. depth larger than 5 or 10Å) layer if there was a higher concentration of PDMS at the outermost layer compared to the rest of the measured depth. Equations 4.6 and 4.7 were utilized to calculate the maximum possible contribution of MWCNTs to the spectrum and was found to be 6.7%. This is slightly higher than that found in XPS. This has been attributed to the fitting of the carbon peak itself, which is difficult due to its position relative to the background. Carbon is positioned at the maximum of the hydrogen background, thus making the fitting process difficult. However, the calculated MWCNT contribution of the spectrum is still close to that shown with XPS.

4.5) Conclusion

The electronic energy levels for the outermost layer and near surface area of PDMS were measured for a thin layer film, a drop cast film with a gold mesh grid, and also with the use of MWCNTs as charge compensation. The MWCNT film was found to be the most reliable as it had no charging effects, and the full DOS was able to be seen as opposed to the slightly shifted and subtracted DOS of the mesh covered film. The observed PDMS DOS seen in UPS agreed with literature, and by comparing the UP spectra to the MIE spectra it was able to be seen that the outermost layer (MIES) is mainly comprised of the methyl side groups, along with a contribution of oxygen 2p orbitals from the backbone. UPS, however, also had features pertaining to silicon orbitals from the backbone.

The distribution of the MWCNTs was found to be uniform through the first 8 nm of sample, with a concentration of 5.2% as shown by XPS. The similar features observed in the MWCNT/PDMS spectra and mesh covered film and also the thin film spectra shows that MWCNT addition can be used as a method for measuring the MIE and UP spectra of some insulating materials. This is due to the low concentration of MWCNTs and featureless nature of the MWCNT VB spectra.

4.6) References

1. Salaneck, W. R., Photoelectron Spectroscopy of the Valence Electronic Structure of Polymers. *Critical Reviews in Solid State and Materials Sciences* **1984**, *12*, 267-296.

2. Naseh, N.; Mohseni, M.; Ramezanzadeh, B., Role of Surface Active Additives on Reduction of Surface Free Energy and Enhancing the Mechanical Attributes of Easy-to-Clean Automotive Clearcoats: Investigating Resistance against Simulated Tree Gum. *International Journal of Adhesion and Adhesives* **2013**, *44*, 209-219.

3. Sia, S. K.; Whitesides, G. M., Microfluidic Devices Fabricated in Poly(Dimethylsiloxane) for Biological Studies. *Electrophoresis* **2003**, *24*, 3563-3576.

4. Choi, J. Y., Seo, T.S, An Integrated Microdevice for High Performance Short Tandem Repeat Genotyping. *Biotechnology Journal* **2009**, *4*, 1530-1541.

5. Yi, C.; Li, C.-W.; Ji, S.; Yang, M., Microfluidics Technology for Manipulation and Analysis of Biological Cells. *Analytica Chimica Acta* **2006**, *560*, 1-23.

6. Yamanaka, K.; Saito, M.; Kondoh, K.; Hossain, M. M.; Koketsu, R.; Sasaki, T.; Nagatani, N.; Ikuta, K.; Tamiya, E., Rapid Detection for Primary Screening of Influenza a Virus: Microfluidic RT-PCR Chip and Electrochemical DNA Sensor. *Analyst* **2011**, *136*, 2064-2068.

7. Sheng, Y.; Bowser, M. T., Size Selective DNA Transport through a Nanoporous Membrane in a PDMS Microfluidic Device. *Analyst* **2012**, *137*, 1144-1151.

8. Fukuba, T.; Miyaji, A.; Okamoto, T.; Yamamoto, T.; Kaneda, S.; Fujii, T., Integrated in Situ Genetic Analyzer for Microbiology in Extreme Environments. *RSC Advances* **2011**, *1*, 1567-1573.

9. Fan, Z., et al., Three-Dimensional Nanopillar-Array Photovoltaics on Low-Cost and Flexible Substrates. *Nature Materials* **2009**, *8*, 648.

10. Lipomi, D. J.; Tee, B. C. K.; Vosgueritchian, M.; Bao, Z., Stretchable Organic Solar Cells. *Advanced Materials* **2011**, *23*, 1771-1775.

11. Liu, Y.; Chen, C.-C.; Hong, Z.; Gao, J.; Yang, Y.; Zhou, H.; Dou, L.; Li, G.; Yang, Y., Solution-Processed Small-Molecule Solar Cells: Breaking the 10% Power Conversion Efficiency. *Scientific Reports* **2013**, *3*, 3356.

12. Yamakawa, S.; Tajima, K.; Hashimoto, K., Buffer Layer Formation in Organic Photovoltaic Cells by Self-Organization of Poly(Dimethylsiloxane)S. *Organic Electronics* **2009**, *10*, 511-514.

13. Bodas, D.; Khan-Malek, C., Formation of More Stable Hydrophilic Surfaces of PDMS by Plasma and Chemical Treatments. *Microelectronic Engineering* **2006**, *83*, 1277-1279.

14. Szleifer, I.; Yerushalmi-Rozen, R., Polymers and Carbon Nanotubes—Dimensionality, Interactions and Nanotechnology. *Polymer* **2005**, *46*, 7803-7818.

15. Kohlmeyer, R. R.; Javadi, A.; Pradhan, B.; Pilla, S.; Setyowati, K.; Chen, J.; Gong, S., Electrical and Dielectric Properties of Hydroxylated Carbon Nanotube−Elastomer Composites. *The Journal of Physical Chemistry C* **2009**, *113*, 17626-17629.

16. Juwan, K.; Joohyung, L.; Tae Hyun, K.; June, P.; Maeng-Je, S.; Seunghun, H., Large-Scale Assembly of Carbon Nanotube-Based Flexible Circuits for DNA sensors. *Nanotechnology* **2008**, *19*, 135305.

17. Pasquardini, L.; Potrich, C.; Quaglio, M.; Lamberti, A.; Guastella, S.; Lunelli, L.; Cocuzza, M.; Vanzetti, L.; Pirri, C. F.; Pederzolli, C., Solid Phase DNA Extraction on PDMS and Direct Amplification. *Lab on a Chip* **2011**, *11*, 4029-4035.

18. Miao, L.; Jianren, S.; Ying, S.; Christopher, B.; Quanfang, C., Thickness-Dependent Mechanical Properties of Polydimethylsiloxane Membranes. *Journal of Micromechanics and Microengineering* **2009**, *19*, 035028.

19. Thangawng, A. L.; Swartz, M. A.; Glucksberg, M. R.; Ruoff, R. S., Bond–Detach Lithography: A Method for Micro/Nanolithography by Precision PDMS Patterning. *Small* **2007**, *3*, 132-138.

20. Oberbrodhage, J., Determination of a Solute Electron Energy Spectrum Not Accessible Experimentally by Means of Singular Value Decomposition. *Journal of Electron Spectroscopy and Related Phenomena* **2000**, *107*, 231-238.

21. Kirmse, K.; Morgner, H., Binary Liquid Mixtures. The Relation between Surface Tension and Surface Composition as Studied by MIES (Metastable Induced Electron Spectroscopy). *Langmuir* **2006**, *22*, 2193-2199.

22. Heinz, B.; Morgner, H., Surface Characterization by Means of Quantitative Evaluation of MIES Data. *Journal of Electron Spectroscopy and Related Phenomena* **1998**, *96*, 83-95.

23. Schmerl, N.; Andersson, G., A Layered Structure at the Surface of P3HT/PCBM Blends. *Physical Chemistry Chemical Physics* **2011**, *13*, 14993-15002.

24. Wendt, S.; Kim, Y. D.; Goodman, D. W., Identification of Defect Sites on Oxide Surfaces by Metastable Impact Electron Spectroscopy. *Progress in Surface Science* **2003**, *74*, 141-159.

25. Erbil, H. Y.; Yaşar, B.; Süzer, Ş.; Baysal, B. M., Surface Characterization of the Hydroxy-Terminated Poly(E-Caprolactone)/Poly(Dimethylsiloxane) Triblock Copolymers by Electron Spectroscopy for Chemical Analysis and Contact Angle Measurements. *Langmuir* **1997**, *13,* 5484-5493.

26. Schnyder, B.; Lippert, T.; Kötz, R.; Wokaun, A.; Graubner, V.-M.; Nuyken, O., UV-Irradiation Induced Modification of PDMS Films Investigated by XPS and Spectroscopic Ellipsometry. *Surface Science* **2003**, *532-535*, 1067-1071.

27. Haines, S. R.; Beamson, G.; Williams, R. L.; Weightman, P., Changes in the Electronic Structure of Silicone Rubber Surfaces Induced by Oxygen Plasma Treatment. *Surface and Interface Analysis* **2007**, *39*, 942-947.

28. Berjoan, R., XPS and XPS Valence Band Characterizations of Amorphous or Polymeric Silicon Based Thin Films Prepared by PACVD from Organosilicon Monomers. *Le Journal de Physique IV* **1999**, *9*, 1059-1068.

29. Mundry, T., Surface Characterization of Polydimethylsiloxane Treated Pharmaceutical Glass Containers by X-Ray Excited Photo- and Auger Electron Spectroscopy. *Fresenius J Anal Chem* **2000**, *368*, 820-831.

30. Seki, K., UV Photoelectron Spectroscopy of Conducting Polymers and Their Model Compounds. *Synth. Met.* **1987**, *17,* 629-634.

31. Ferenczy György, G.; András, T.; Imre, B.; Sándor, S., Valence Electronic Structure of Selected Polyorganosiloxanes; X-Ray Photoelectron Spectroscopy and Quantum Chemical Studies. *Journal of Physics: Condensed Matter* **1997**, *9*, 4781.

32. Acres, R. G.; Ellis, A. V.; Alvino, J.; Lenahan, C. E.; Khodakov, D. A.; Metha, G. F.; Andersson, G. G., Molecular Structure of 3-Aminopropyltriethoxysilane Layers Formed on Silanol-Terminated Silicon Surfaces. *The Journal of Physical Chemistry C* **2012**, *116*, 6289-6297.

33. Michalkova, A.; Tulyani, S.; Beals, J.; Leszczynski, J., Theoretical Study of the Surface Properties of Poly(Dimethylsiloxane) and Poly(Tetrafluoroethylene). *J Mol Model* **2012**, *18*, 239-250.

5. Surface and Near Surface Area Density of States for Magnetron Sputtered ZnO and Al-ZnO: A MIES, UPS and VBXPS Study Investigating UHV Sputter Cleaning and UV Oxygen Plasma

Natalya M Schmerl[1], Angus R Gentle[2], Jamie S Quinton[1], Geoff B Smith[2], Gunther G Andersson[1*]

[1]Flinders Centre for Nanoscale Science and Technology, School of Chemistry and Physical Sciences, Flinders University of South Australia, Bedford Park, SA 5042, Australia

[2]School of Mathematical and Physical Sciences, University of Technology Sydney, PO Box 123, Broadway, NSW, 2007

*Corresponding author: Email gunther.andersson@flinders.edu.au

This work has been published and listed in the publications arising from this work section, alterations have been performed only in that any experimental methods and analysis procedures previously described in Chapter 2 have been removed, and supplementary information from the publication has been included in the text.

Author Contribution:

Natalya Schmerl: Designed and performed experiments, data analysis and interpretation, and prepared the manuscript for publication.

Gunther Andersson: Intellectual contribution in conceptualising experiments, data interpretation & revision of manuscript.

Angus Gentle: Sample preparation, wrote sample preparation section of manuscript, revision of manuscript.

Jamie Quinton and Geoff Smith: Intellectual contribution in revision of manuscript.

5.1) Abstract

The impact of non-solvent based cleaning methods on zinc oxide and aluminium doped zinc oxide was investigated across a range of doping concentrations up to 22% aluminium. A combination of electron spectroscopic techniques was utilised in order to characterise the electronic states present on the surface and to discern the differences between the near surface area and outermost layer VB states. Understanding the differences between the near surface area and outermost layer of an interface is crucial when optimising devices for charge transfer. The techniques were XPS, VBXPS, UPS and MIES. The band gap was also measured via UV-Vis.

5.2) Introduction

TCOs are materials with a large range of potential applications including organic light emitting diodes (OLEDs), OPVs, and flat or touch panel displays. The properties required for a TCO to be considered suitable for such applications is a minimum charge carrier concentration of 10^{20} cm^{-3}, and minimum band gap energy of 3eV[1]. Zinc oxide (ZnO) is one potential material to meet these criteria. ZnO is cheap, non-toxic and abundant[2-3]. ZnO has a direct band gap of 3.37eV, a large exciton binding energy of 60meV which allows for stable exciton emission at room temperature, and thin films have a high transparency in the visible spectrum[4]. The optical and electrical properties of ZnO are tunable, commonly via doping with group III metal elements, one of the most highly studied of these being aluminium doped zinc oxide (AZO)[5-6].

The choice of preparation, doping concentration and sample cleaning method has a significant effect upon the surface properties of the final material, and the charge transfer across the surface of the TCO to the subsequent layer is critical for device performance[7]. It is determined by the composition of the TCO surface, the band structure, and the workfunction of the material at the interface. TCO films also need to be uniform, pure (lacking in contaminants) and easily reproducible for industrial use. Magnetron sputter deposition is capable of preparing such films and as such has often been used in film preparation[3, 5, 8-11]. Film annealing has been found to improve ZnO film properties and crystallinity for magnetron sputtered films, which tend towards a wurzite lattice configuration[10, 12] and so is also common practice.

Much work has been done on the impact of doping on the properties of ZnO films. Changes to the band gap are commonly measured through optical techniques such as UV/Vis. Currently there are varying conclusions on the influence of aluminium concentration on the band gap. Much of this variation is seemingly due to differences in film preparation[1, 13-17] but further investigations are required to understand these differences. Optical methods are ideal for determining bulk film properties but are insensitive to the surface properties and only able to determine the band gap, not the position of the VB or CB. An understanding of the band structure of the doped surface is necessary in order to understand the more subtle changes that occur near interfaces and crucial for successful charge transport through devices.

The band structure at the surface is also influenced by the surface cleaning procedures. In fabricating devices there is a need for clean ZnO surfaces and doped ZnO surfaces, respectively, which is rather difficult to obtain without cleaving a single crystal in vacuum[2]. Surfaces can be cleaned with solvents. However, this procedure leaves residual hydrocarbons on the outermost layer affecting the workfunction which is often undesirable for device performance[9, 18-19]. As such, either sputter cleaning by ion bombardment, or plasma treatments have been used to clean the ZnO surface and tune the workfunction, sometimes using annealing under UHV to assist this process[2, 10, 17, 20].

Changes to the band structure are most commonly measured via electron spectroscopy. XPS is used to determine the aluminium content and near surface chemical composition. VBXPS has been used on some occasions to study the VB structure and DOS [11, 21-24]. UPS also maps the structure and DOS but does not probe as deep into the bulk as VBXPS. UPS can also be used to follow the changes in workfunction due to surface treatments[25-29]. Changes to the electronic structure at the outermost layer can then be observed via MIES. There are reports in literature which have utilized some of the aforementioned techniques to analyze changes in band structure with doping or surface treatment [2, 5, 9, 23, 25, 29-30], but at this stage none have systematically mapped the near surface area and outermost layer across a range of dopant concentrations and surface treatments.

The aim of the present work is investigating the influence of Al doping on the valence electronic structure of AZO. We also investigate how a range of surface cleaning methods influence the electronic properties of the surface. We utilize the aforementioned techniques to map changes to the VB across a range of aluminium doped ZnO films up to 22% Al composition.

UV/Vis and VBXPS was used to observe the changes in the band gap and VB with doping in the bulk of the film so that bulk properties can be compared to the near surface band structure. XPS was employed to map chemical composition. VBXPS and UPS were used to measure the VB at different depths into the surface; and MIES was used to measure the outermost layer/ interface VB DOS.

Samples were prepared via magnetron sputter deposition and all samples were annealed at 300°C. Sample cleaning was either argon sputtering followed by annealing in UHV or annealing under nitrogen followed by an oxygen plasma clean. These plasma cleaned samples were also reheated in

UHV and remeasured to show changes in the surface when adventitious carbon and plasma induced species were removed.

5.3) Experimental

5.3.1) Materials and sample preparation

Silicon wafer substrates (n-type (Sb Dopant), 110, 0.005-0.02 Ohm-cm) were used for the electron spectroscopy measured samples and were purchased from Wafer WORKS Corp. Glass was used for the samples measured with optical spectroscopy using G300 super white glass from Proscitech. Samples were prepared via DC co-sputtering of ZnO and AZO targets for the lower aluminium percentages and AZO and Al targets for the higher percentages. Sputter targets were purchased from Semiconductor Wafer Inc. (semiwafer.com), the AZO target being (by weight 2% Al_20_3 / 98% ZnO hot pressed). All sputter targets were 2” in diameter with 99.99% purity. The base pressure of the vacuum system prior to deposition was approximately 10^{-6}mbar. Samples were introduced via a load lock to minimise pump-down time between depositions. The sample stage was rotated at five revolutions per minute, to ensure uniformity of the deposited film.

The target to sample stage working height was 180mm, with the AZO target positioned 200mm laterally from the centre of the substrate, directed off axis by 100mm. The ZnO and Al targets used the same target position separated by an offset of 50mm directed 25mm from the centre of rotation of the substrate. Depositions were carried out in a 2.0x10^{-3}mbar Argon atmosphere (72Sccm Ar). Deposition rates of the AZO and ZnO were both set to be 0.3Å/s with deposition currents of 0.2A and 0.1A respectively. For the set deposited with the AZO and Al targets a small amount of oxygen (see Table 5.1 below) was introduced in addition to the Ar gas to allow reactive sputtering of the Al to occur with deposition currents of and 0.07A and 0.1A. For all depositions a 20W RF bias was applied to the 110mm square rotating sample stage. In the sections that follow, the label “sample type” will be used for convenience and denotes the following specific set of deposition conditions (doping concentration).

Sample	Atmosphere (mbar)	O_2 Flow (sccm)	Target(s) + Current (A)
ZnO	$2.0\text{x}10^{-3}$ Ar	0	ZnO 0.2
AZO1	$2.0\text{x}10^{-3}$Ar	0	AZO 0.2 / ZnO 0.1
AZO2	$2.0\text{x}10^{-3}$Ar	0	AZO 0.2
AZO3	$2.0\text{x}10^{-3}$Ar/$1.6\text{x}10^{-4}$ O_2	2	AZO 0.2 / Al 0.07
AZO4	$2.0\text{x}10^{-3}$Ar/$1.1\text{x}10^{-4}$ O_2	2	AZO 0.2 / Al 0.1

Table 5.1: Sample deposition parameters for ZnO and AZO.

5.3.2) Sample cleaning

5.3.2.1) *UHV sputter and heat*

Argon sputtering was performed for 20 minutes at a chamber pressure of ~$9\text{x}10^{-8}$mbar. The ion source used was a SPECS Lab PU-IQE 12/38. The accelerating voltage was set to 3kV with an ion current of about 0.25 µA resulting in a total ion dose of about $2\text{x}10^{15}$ ions/cm^{2}applied for sputtering. Samples were then heated to 300^{o}C for 10 minutes using a SPECS Sample heater power supply SH100 attached to the main sample stage. The temperature was monitored with both a Eurotherm 2208e and an Omega ir2 series temperature measurement control system. This sample set will be denoted as S/H in the text.

5.3.2.2) *Plasma cleaned samples*

Samples were annealed in nitrogen for 10 minutes at 300^{o}C in an Innovative Technology PureLab^{HE} glovebox. Sample heating was performed on an IKA-RCT Basic heat element. Samples were then oxygen plasma cleaned in a Harrick Plasma plasma cleaner for 15 minutes at a pressure of 0.3mbar on high power. Oxygen was high purity from BOC. Samples were immediately transferred after plasma treatment into the load lock chamber of the UHV electron spectroscopy equipment with less than one minute exposure to atmosphere. These samples will be denoted as N_2P.

5.3.2.3) *Plasma cleaned and heated under UHV*

Prior to removal from UHV, the N_2P sample set was heated in UHV with the method as described for heating of S/H samples and remeasured. This was to observe the changes in the surface with the removal of adventitious carbon and plasma induced species. These samples will be denoted as N_2P/H.

5.3.3) Methods

5.3.3.1) Electron Spectroscopy

XP spectra were obtained using the Al Kα X-ray source (XRC1000M), operated at 100 W, 12 kV. XPS UPS and MIES were performed in the standard manner with pass energies and resolution described in Chapter 2.

5.3.3.2) UV-Vis

Transmission for the UV-Vis was measured using a Perkin-Elmer LAMBDA 950 UV/Vis/NIR Spectrophotometer with integrating sphere for the wavelength range of 300nm to 1000nm. Samples were measured on glass, and a blank glass control was also measured.

5.3.4) Analysis

5.3.4.1) UV-Vis

For UV-Vis analysis the control glass spectrum was subtracted from each transmission measurement, thus showing the transmission as a function of wavelength of the thin films rather than that of the substrate. The band gap was then calculated via the relation of the absorption coefficient α to the transmittance seen in[31]. The band gap is extracted from a plot of $(\alpha h\nu)^2$ vs. hν, where hν is the measured wavelength converted to energy, and α is the absorption coefficient. The band gap is the x-axis energy value obtained when the linear section of the plot is extrapolated. The optical properties of the films on glass compared to the silicon wafers used for electron spectroscopy measurements were checked via ellipsometry and the optical constant was found to be the same for both sets of data.

5.3.4.2) XPS

All XP spectra were calibrated to the carbon peak at 285.0eV. CASA XPS software using the standard Shirley background model was used for most peak fitting. For fitting the aluminium peaks a different procedure had to be applied because the concentration of aluminium for most samples was low. Further, the presence of the Zn3p satellite peak overshadows the standard background surrounding the primary Al2p photoelectron peak. This has been seen before[32]. The low aluminium content also meant the Al1s peak was not prominent enough to use as a substitute and the background of this peak was altered by the Zn3p Plasmon resonance peak. Thus, analysis was performed on the Al2p peak manually using a polynomial background fit, and a single peak was used to fit the doublet state as the peak separation between $Al2p_{3/2}$ and $Al2p_{1/2}$ is small. An example of this is shown below in Figure 5.1.

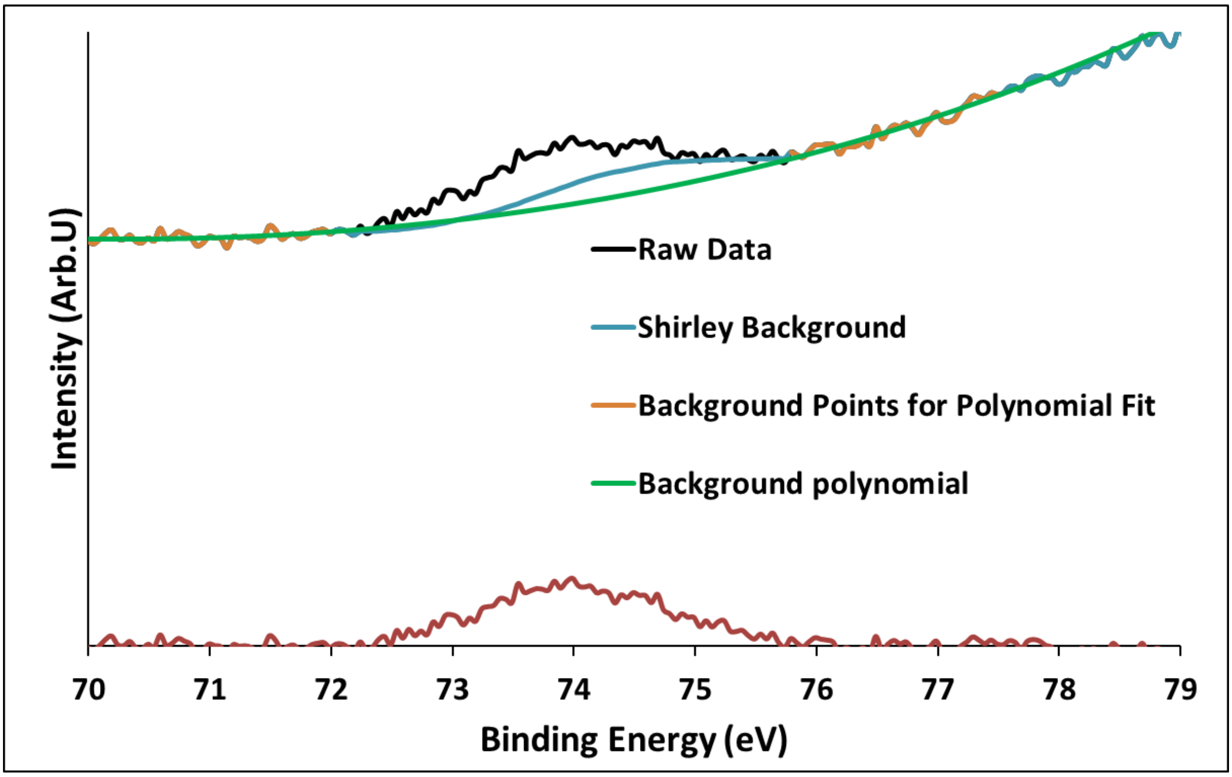

Figure 5.1: Example of the polynomial fit used to calculate Al2p peak area and comparison to the standard Shirley background fit. The example shown is for AZO3 with the N_2P treatment.

Data was entered into Microsoft Excel and a polynomial fit was made to the data points surrounding the Al peak. From here the area above the polynomial background was taken to be the Al2p peak intensity. Error for the aluminium content was found by creating the same polynomial fitting procedure for the neat ZnO and using the obtained area as the error for this procedure. Error in peak position of Al was found manually by determining the maximum viable peak position deviation for each spectrum. A check was made with one heavily doped sample (AZO4) to find the difference in aluminium content with the different fitting methods. The polynomial fit found the peak to be 20.5% of the measured depth content, Shirley fit found 21.1%. This method was used for all doped samples except for AZO4 which had sufficient aluminium content to fit in the standard method using a Shirley background.

5.3.4.3) VBXPS

XPS also measures the DOS of the VB, which yields information pertaining to the orbital arrangement (bonding) and subsequent conduction properties of the sample. VBXPS is the most accurate measure of the DOS as it only gives information pertaining to the bonding orbitals[11]. However, its lack of surface sensitivity makes it more useful for obtaining VB properties more akin to the bulk material rather than the sample/air interface. In this work VBXPS was performed for binding energies in the range of -5 to 30eV. The spectra were then offset so that the background intensity was equal between

0 to -3eV. Satellite peaks were also subtracted from each spectrum[33]. Satellite peaks are features which appear on the low binding energy side of all photoelectron peaks for spectra when spectra are recorded with a non-monochromated X-ray source[34]. These features are thus present in the VBXP spectra and need to be taken into account. This is an accurate procedure as the satellite energy offsets and intensities are well known for the anode used for data acquisition here. Details of this process are shown below in Table 5.2:

Satellite	$\alpha_{1,2}$	α_3	α_4	α_5	α_6
Intensity (%)	100	6.4	3.2	0.4	0.3
Offset (eV)	0	9.8	11.8	20.1	23.4

Table 5.2: Satellite peaks for non-monochromated AlKα, values taken from[34].

Only α_3 and α_4 need to be taken into account for VBXPS, as the contribution of α_5 and α_6 are insignificantly low. For the samples investigated in this study, the satellite intensity comes primarily from the Zn3d photoelectron peak located from 10.9~12.5eV depending upon aluminium content and surface treatment, but any small effects from the O2s peak ~25eV is also accounted for in the analysis. Analysis is performed by simply multiplying each spectrum by the relative intensity of each satellite peak, and then subtracting them from the original data. A comparison between raw data and the satellite removed data may be seen below in Figure 5.2.

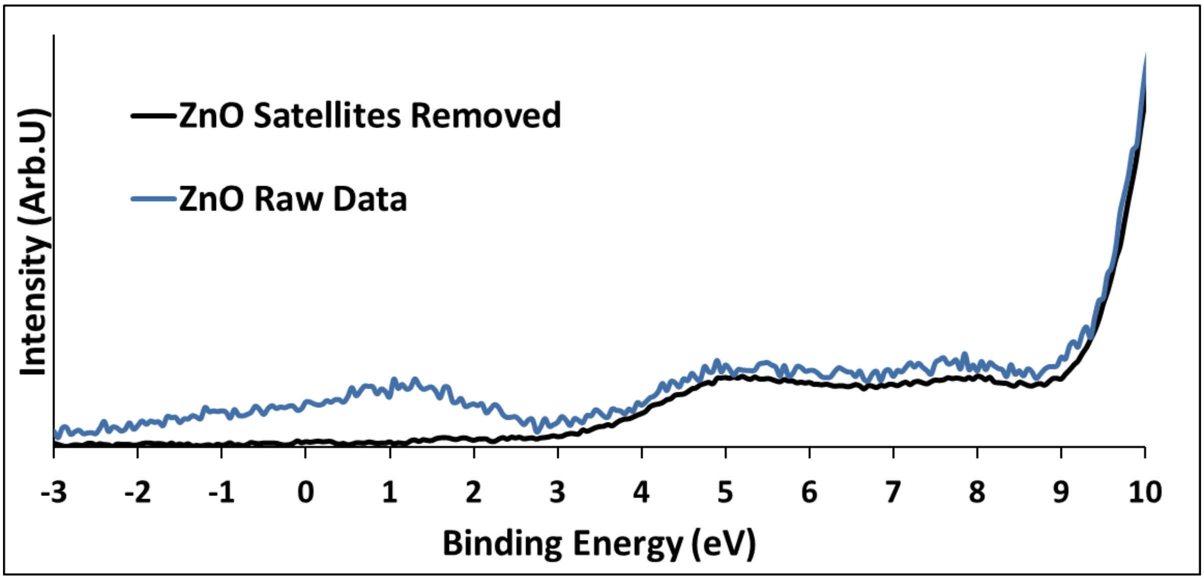

Figure 5.2: Example of the effects in the low binding energy region of satellites from low energy photoelectron peaks. Note the presence of DOS beyond the Fermi level prior to satellite subtraction. Example shown is for ZnO with the H/S treatment.

5.3.4.4) UPS

UPS measures DOS of the VB but to a shallower depth than XPS. This is due to the small electron mean free path when using the He I line. The electron mean free path for the materials used here is around 1nm for the He I line[35]. The intensities of the spectra were calibrated against a sputter cleaned gold sample. AZO4 had a large secondary electron background so was reweighted to 50% of the original intensity to allow for an easier comparison of relative DOS.

5.3.4.5) MIES

The relationship between kinetic energy, binding energy and excitation energy is more complicated in many MIES experiments than in a UPS experiment due to the de-excitation mechanisms which can occur. Thus for this chapter the MIES data are shown as function of the kinetic energy of the emitted electrons. MIE spectra required no modification for analysis, however the spectra were reweighted in order to align certain DOS regions to show similarities.

5.4) Results and Discussion

Results are discussed initially per technique in the order of UV/Vis (section 5.4.1), XPS (section 5.4.2), VBXPS (section 5.4.3), UPS (section 5.4.4), and MIES (section 5.4.5). In these sections there is a discussion of general results and the impact of doping and of cleaning at that particular depth into the surface. Data is displayed per sample set (S/H, N_2P, N_2P/H). A further discussion regarding the total outcome of the combined results follows in section 5.4.6.

5.4.1) Optical Band Gap – UV Vis Spectroscopy

All films had a transmittance greater than 85% in the visible range which is important for device function. The absorption edge of the films was seen to shift to shorter wavelengths with increasing aluminium content. Converting the spectra to $((\alpha h\nu)^2)$ vs. photon energy (hν) shows this to be an increase in optical band gap with doping (Figure 5.3). The increase in band gap has been attributed to the Burstein-Moss effect, and is the result of an increase of the charge carrier density in the ZnO lattice[13, 31, 36-37].

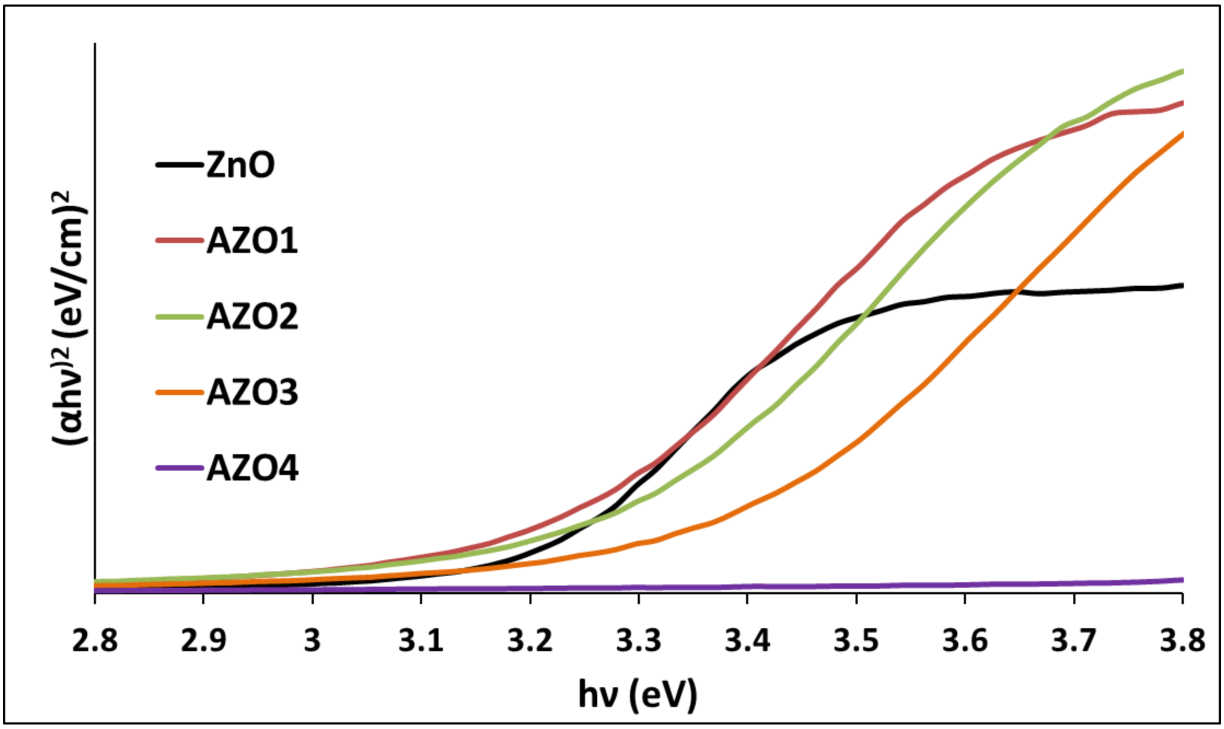

Figure 5.3: Plot of $(\alpha h\nu)^2$ vs. hν showing an increase in optical absorption cut-off energy with increasing aluminium content.

The optical band gap is the x-axis energy value obtained when the linear section of the plot is extrapolated. For ZnO and AZO1 it is 3.20eV. This increases to 3.25eV for AZO2, then to 3.36eV for AZO3. Similar values have been reported before for ZnO and 2% (Al) AZO in literature[13, 21, 38]. The band gap could not be extrapolated for AZO4. This is possibly due to the band gap being larger than that of the glass at around 3.50eV. However, as the primary aim of this work is to investigate changes in valence electron structure with Al doping and various cleaning methods the absence of this bandgap measurement is not a significant issue.

5.4.2) XPS

The aluminium content of the samples ranged from 0 to 21.2%. Although the deposition conditions for AZO3 and AZO4 were not that dissimilar, the Al concentration observed in AZO4 was significantly higher. This was not considered to be an issue in this work as the focus is on the impact of the Al presence rather than obtaining specific doping percentages. Argon was present in all samples at low concentration and was most likely incorporated via the deposition process. Small quantities (less than 2.0%) of nitrogen and chlorine were observed on some samples cleaned by plasma and were resulting from residues in the plasma cleaning apparatus. The concentration of these impurities was reduced to less than 1.0% with UHV heating. VB results indicated that the residual contamination did not impact upon the electrical properties as no changes in spectral shape were observed. Chemical compositions may be seen in Tables 5.3~5.5. The peak positions in Tables 5.3~5.5 are for the lowest binding energy peak for carbon and oxygen but the concentration is for the total element signal. Due to the amount of data, Tables 5.4 and 5.5 have been split into two sections: 5.4(a) and 5.5(a) showing the elements pertaining to the metal oxide films for the N_2P and N_2P/H samples respectively, and 5.4(b) and 5.5(b) showing the contaminant species for each respective film, all percentages shown are for the total film composition.

Only a single peak was observed for zinc and aluminium, both were in the oxidized state as seen by their binding energy positions. Oxygen and carbon had two or three peaks depending upon the cleaning method employed. A table of oxygen component ratios for all samples is present in Table 5.6 which has also been split into two sections due to the amount of data, 5.6(a) showing component ratios for the S/H samples, and 5.6(b) showing the component ratios for the N_2P and N_2P/H samples. Examples of the oxygen components are shown in Figure 5.4 and examples of $Zn2p_{3/2}$, Al2p and C1s peaks are shown in Figure 5.5.

S/H	$Zn2p_{3/2}$	Ebind (eV)	O1s	Ebind (eV)	Al2p	Ebind (eV)	C1s	Ebind (eV)	Ar2p	Ebind (eV)
ZnO	66.8 ±0.3	1022.2	29.3 ±0.3	530.8	-	-	2.9 ±0.2	285.0	1.0 ±0.03	242.0
AZO 1	64.4 ±0.3	1022.0	30.0 ±0.3	530.7	0.9 ±0.3	74.1	3.7 ±0.2	285.0	1.0 ±0.03	242.0
AZO 2	64.2 ±0.3	1022.4	31.0 ±0.3	531.0	1.5 ±0.3	74.4	2.6 ±0.2	285.0	0.7 ±0.05	242.1
AZO 3	59.6 ±0.3	1022.4	32.9 ±0.3	531.0	2.3 ±0.3	74.4	3.5 ±0.2	285.0	1.7 ±0.01	242.4
AZO 4	28.6 ±0.1	1022.5	45.1 ±0.4	531.1	21.1 ±0.6	74.4	1.0 ±0.1	285.0	4.2 ±0.1	242.5

Table 5.3: Chemical composition as a percentage for S/H samples.

N_2P	Zn2p$_{3/2}$	Ebind (eV)	O1s	Ebind (eV)	Al2p	Ebind (eV)
ZnO	48.3 ±0.3	1022.0	40.6 ±0.4	530.3	-	-
AZO 1	45.9 ±0.3	1021.9	39.2 ±0.4	530.2	0.5 ±0.3	73.2
AZO 2	46.9 ±0.3	1022.0	39.2 ±0.4	530.5	0.9 ±0.3	74.0
AZO 3	47.3 ±0.3	1022.2	39.8 ±0.4	530.6	2.0 ±0.3	74.0
AZO 4	20.2 ±0.2	1022.4	48.0 ±0.4	531.0	13.4 ±0.5	74.3

Table 5.4(a): Chemical composition as a percentage of total composition for N_2P samples showing elements pertaining to the metal oxide films.

N_2P	C1s	Ebind (eV)	Ar2p	Ebind (eV)	N1s	Ebind (eV)	Cl2p	Ebind (eV)
ZnO	8.9 ±0.3	285.0	0.9 ±0.06	242.8	1.3 ±0.1	399.8	-	-
AZO1	10.5 ±0.3	285.0	0.9 ±0.05	242.6	1.8 ±0.1	400.0	1.2 ±0.09	198.9
AZO2	9.5 ±0.2	285.0	0.9 ±0.05	242.7	1.6 ±0.1	399.9	1.0 ±0.09	199.3
AZO3	9.3 ±0.3	285.0	0.4 ±0.04	242.4	1.2 ±0.09	400.5	-	-
AZO4	15.7 ±0.4	285.0	1.5 ±0.06	242.4	1.2 ±0.09	401.2	-	-

Table 5.4(b): Chemical composition as a percentage of total composition for N_2P samples, contaminant species.

N_2P/H	$Zn2p_{3/2}$	Ebind (eV)	O1s	Ebind (eV)	Al2p	Ebind (eV)
ZnO	63.3 ±0.3	1022.0	31.8 ±0.3	530.6	-	-
AZO 1	61.3 ±0.3	1021.9	30.9 ±0.3	530.6	0.4 ±0.3	74.0
AZO 2	60.1 ±0.3	1022.1	31.5 ±0.3	530.8	1.3 ±0.3	74.1
AZO 3	60.5 ±0.3	1022.2	32.9 ±0.3	530.9	2.5 ±0.3	74.1
AZO 4	29.2 ±0.2	1022.2	43.9 ±0.4	531.0	18.3 ±0.5	74.2

Table 5.5(a): Chemical composition as a percentage of total composition for N_2P/H samples showing elements pertaining to the metal oxide films.

N_2P/H	C1s	Ebind (eV)	Ar2p	Ebind (eV)	N1s	Ebind (eV)	Cl2p	Ebind (eV)
ZnO	2.9 ±0.2	285.0	1.2 ±0.05	243.0	0.8 ±0.07	398.6	-	-
AZO 1	5.5 ±0.3	285.0	1.0 ±0.06	242.2	-	-	0.9 ±0.07	199.8
AZO 2	5.2 ±0.2	285.0	1.1 ±0.05	242.2	-	-	0.8 ±0.07	200.0
AZO 3	3.4 ±0.2	285.0	0.7 ±0.04	242.6	-	-	-	-
AZO 4	6.4 ±0.2	285.0	2.2 ±0.07	242.8	-	-	-	-

Table 5.5(b): Chemical composition as a percentage for N_2P/H samples, contaminant species.

S/H	**O1s(1) (eV)**	**%**	**O1s(2) (eV)**	**%**
ZnO	530.8	91.1	532.7	8.2
AZO1	530.7	89.9	532.4	10.1
AZO2	531.0	90.5	532.5	9.5
AZO3	531.0	88.3	532.6	11.7
AZO4	531.1	93.0	532.7	7.0

Table 5.6(a): Oxygen component ratios as a percentage of the total oxygen signal for S/H samples. Component errors were found to be a maximum of 0.3eV in each case.

	N_2P						**N_2P/H**			
	O1s(1) (eV)	**%**	**O1s(2) (eV)**	**%**	**O1s(3) (eV)**	**%**	**O1s(1) (eV)**	**%**	**O1s(2) (eV)**	**%**
ZnO	530.3	47.1	532.1	40.7	533.0	12.2	530.6	87.3	532.6	12.7
AZO1	530.2	44.3	531.9	42.3	532.8	13.4	530.6	86.0	532.4	14.0
AZO2	530.5	48.4	532.1	37.1	532.9	14.5	530.8	87.4	532.4	12.6
AZO3	530.6	50.1	532.2	38.1	533.1	11.8	530.9	85.8	532.3	14.2
AZO4	531.0	45.3	532.4	41.7	533.5	13.0	531.0	88.2	532.6	11.8

Table 5.6(b): Oxygen component ratios as a percentage of the total oxygen signal for N_2P and N_2P/H samples. Component errors were found to be a maximum of 0.3eV in each case.

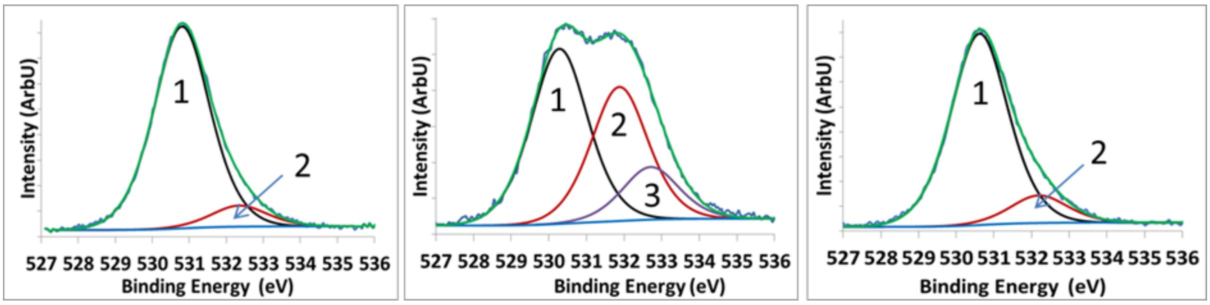

Figure 5.4: Example O1s peaks and oxygen components seen in all samples for different treatments. (left) S/H, (middle) N_2P, (right) N_2P/H. AZO2 used for the example.

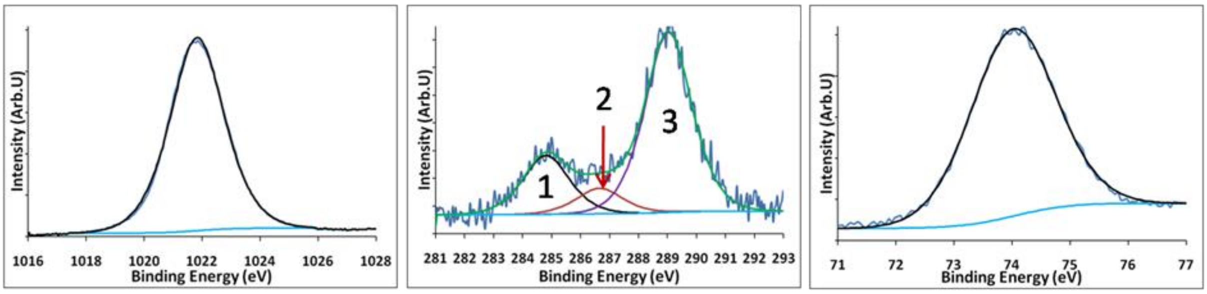

Figure 5.5: (left) $Zn2p_{3/2}$, (middle) C1s and, (right) Al2p example peaks. AZO2 N_2P samples shown for Zn and C, AZO4 N2P/H shown for Al as example for heavily doped samples. C1s peaks were assigned as 1) hydrocarbon, 2) C-O contaminant species, 3) C-O high binding energy contaminant species as a result of plasma treatments. Peak 3 was only present in N_2P samples and disappeared with heating.

Al2p and $Zn2p_{3/2}$ peaks could be fitted with a single component and attributed in both cases to oxidized species. Zinc was attributed to zinc in the ZnO lattice[32, 39-40]. Aluminium was attributed to oxidized species present either substitutionally in the ZnO lattice or as excess AlO_x[39-41]. These two states are within the same binding energy range for oxidized aluminium, so the exact chemical state could not be discerned. For oxygen there were two components for the UHV heated samples and a third present in the data set for plasma treatment prior to heating in UHV. Representative spectra are shown in Figure 5.4. The component at the lowest binding energy (peak 1) was attributed to metal oxide bonds either from the ZnO lattice or incorporated AlO_x[39-41]. The secondary peak (peak 2) has been attributed to various species in literature. An *in situ* investigation of magnetron sputtered ZnO revealed the presence of a secondary peak at 531.6eV and due to the lack of any contamination, attributed it to the presence of oxygen vacancies[30]. Secondary peaks have also been seen in investigations where there is a possibility of species such as hydroxyl groups or water, adsorbed oxygen, or adventitious carbon[19, 32, 42-43]. Based on the results here it is not possible to separate the contribution of oxygen vacancies and contaminant species in peak 2. Thus the changes in oxygen component ratios or oxygen vacancies will not be discussed in detail. The highest binding energy peak (peak 3) around 532.2eV is only present in the plasma treated samples prior to UHV heating and is attributed to various CO moieties adsorbed as a result of the oxygen plasma. These adsorbed contaminant species have also been seen before[29, 39]. This peak disappears with heating as shown in Table 5.6(b) and Figure 5.4, as does much of the carbon (compare Table 5.4(b) to Table 5.5(b)).

The changes in the zinc: oxygen: aluminium ratio with doping and cleaning is shown in Table 5.7. Zinc has been set to 1 for all samples. The Zn:O ratio is shown for both the total oxygen content and for that of the primary oxygen peak denoted O* (metal oxide component).

Element Ratios		**S/H**			**N$_2$P**			**N$_2$P/H**		
Sample	**Zn**	**O**	**O***	**Al**	**O**	**O***	**Al**	**O**	**O***	**Al**
ZnO	1	0.4	0.4	-	0.8	0.4	-	0.5	0.4	-
AZO 1	1	0.5	0.4	0.01	0.9	0.4	0.01	0.5	0.4	0.007
AZO 2	1	0.5	0.4	0.02	0.8	0.4	0.02	0.5	0.5	0.02
AZO 3	1	0.6	0.5	0.04	0.8	0.4	0.04	0.5	0.5	0.04
AZO 4	1	1.6	1.5	0.7	2.4	1.1	0.7	1.5	1.3	0.6

Table 5.7: Ratio of primary elements of interest for each sample set, Zn has been set to 1 in all cases**.**

Across all cleaning methods the oxygen content is seen to increase with increasing dopant concentration. Thus it can be concluded that the increasing presence of O* is due to an increasing presence of Al-O species that are incorporated in the lattice. The fraction of O* correlated to AlO_x does not match the stoichiometry of Al_2O_3 for AZO4 indicating that much of the excess AlO_x species are incorporated into the lattice rather than present as alumina grains in the AZO. The uncertainties for the XPS intensities of the Al species do not allow the same analysis for AZO1, AZO2, AZO3.

The cleaning method employed had a large impact on the carbon content, with sputter cleaning being the most effective method for removal. Plasma cleaned samples had the highest levels of carbon as well as oxygen due to plasma induced species (Figure 5.4(middle), peak 3) and hydrocarbon contamination. Plasma samples which had been heated in UHV showed a reduction in carbon and excess oxygen species, and an increase in metal oxide (Me:O*) bonds which becomes apparent with increasing aluminium concentration. Annealing in nitrogen did not incorporate nitrogen into the film and it was present only as a surface species which was able to be removed with annealing in UHV. Cleaning method had no significant impact on the Zn:O* ratio or observed aluminium concentrations for low doping, but for AZO4 sputter cleaning produced a slightly larger O*:Zn ratio and aluminium concentration than plasma cleaned samples. The proposed reason is that sputter cleaned samples have less surface contamination, thus a larger proportion of the observed depth in XPS will be from the metal oxide rather than contaminant species. This also accounts for the higher overall zinc and aluminium content observed in the S/H samples as compared to N_2P/H.

5.4.3) VBXPS

VBXP spectra from 0~15eV are shown in Figures 5.6 and 5.7. A table of relative peak intensities is given in Table 5.8 so that any background effects are removed for a direct comparison of occupied DOS. The occupancy of Zn3d is not believed to be influenced by doping[21], and as such, Table 5.8 shows the relative change in states with respect to Zn3d. The VBM cut-off values are shown at the end of this section in Table 5.9 along with the equivalent UPS data relevant to section 5.4.4.

The overall VB shape seen in Figure 5.6 and 5.7 has been noted previously in literature[21-22, 44] with three main features at ~5, 8 and 11eV. These pertain to O2p orbitals (lone pair), O2p hybridized (O_{hyb}) with Zn4s and Zn4p, and the Zn3d band respectively. Another feature at higher binding energy is seen at 23eV which is due to oxygen 2s states and can be seen in Figure 5.8.

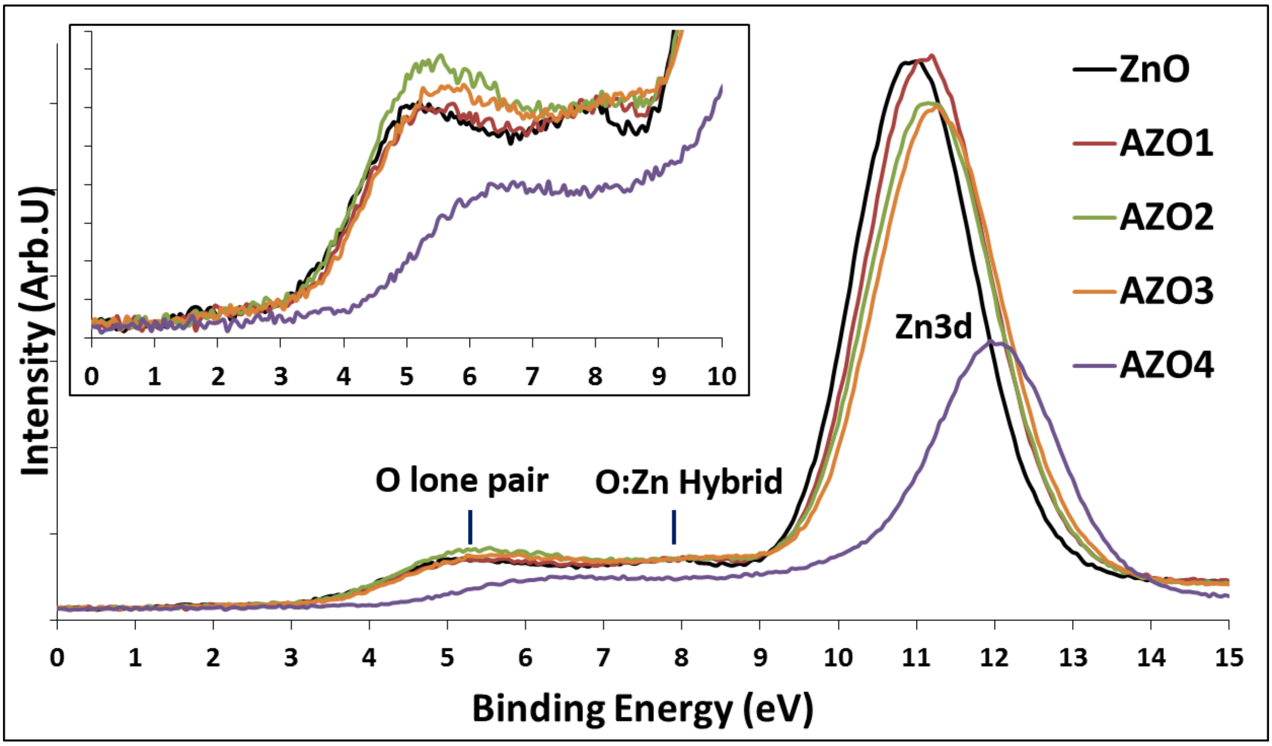

Figure 5.6: VBXPS for UHV sputtered then heated (S/H) ZnO and AZO.

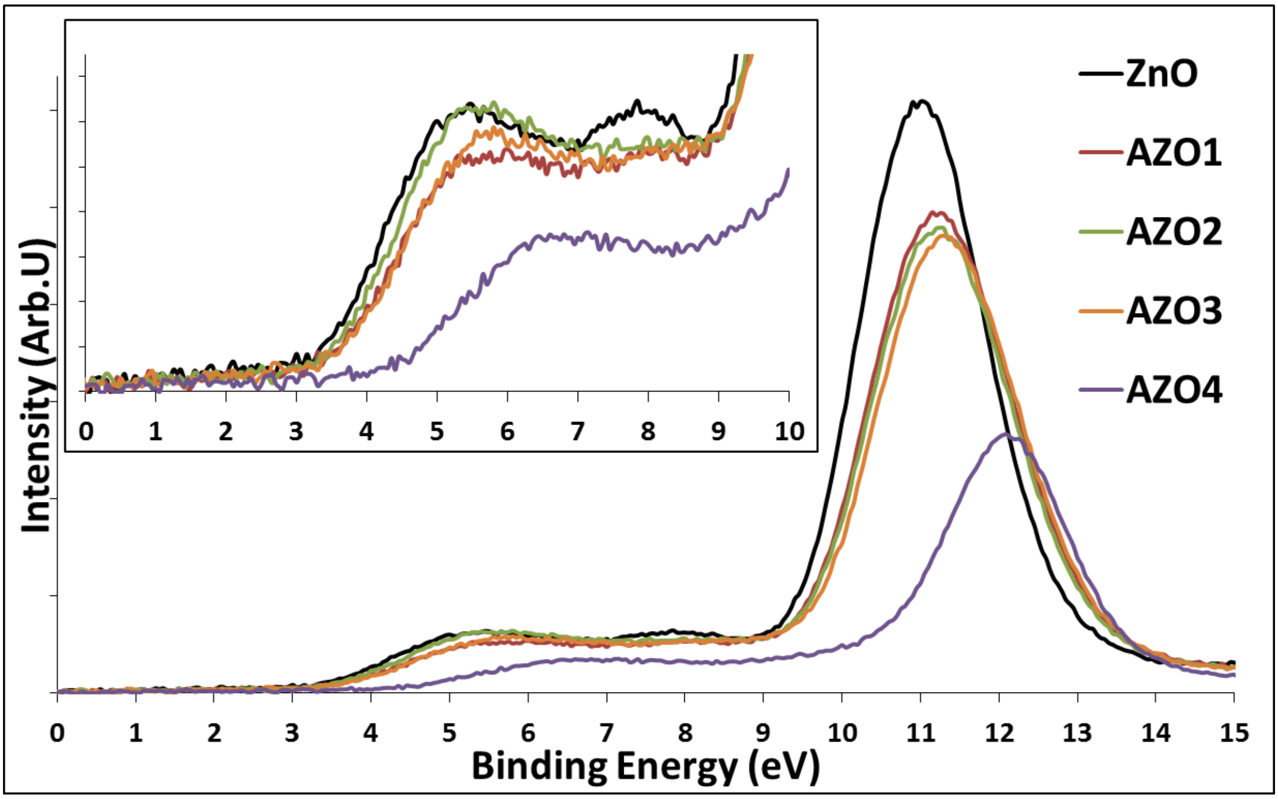

Figure 5.7: VBXPS for nitrogen annealed +oxygen plasma treated (N_2P) ZnO and AZO.

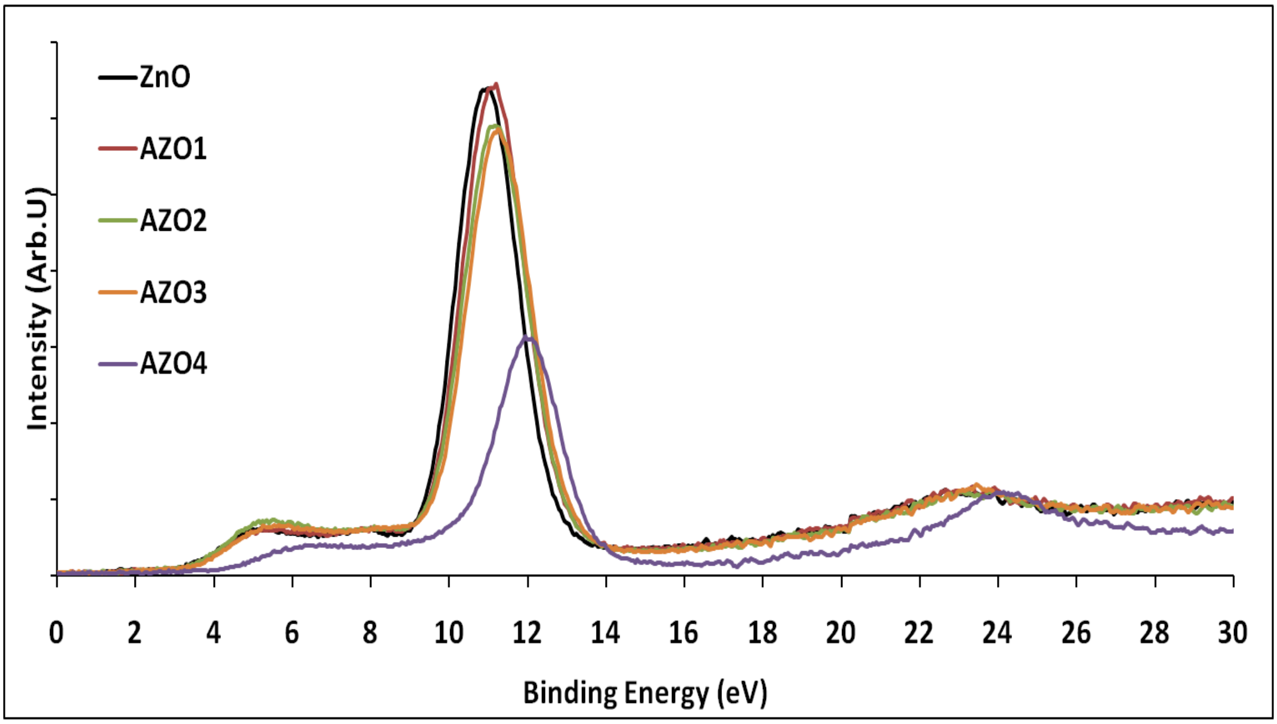

Figure 5.8: VBXPS example spectra to 30eV. Example is for sputter cleaned ZnO and AZO showing the O2s peak around 23eV. The same trend was observed for plasma treated samples.

S/H	**O2p**	**O$_{hyb}$**	**Zn3d**	**O2s**	**O2p:O$_{hyb}$**	**O$_{tot}$:Zn**
ZnO	0.09	0.09	1.00	0.06	0.99	0.24
AZO1	0.09	0.09	1.00	0.06	1.00	0.24
AZO2	0.12	0.10	1.00	0.07	1.14	0.29
AZO3	0.10	0.10	1.00	0.09	0.99	0.30
AZO4	0.11	0.13	1.00	0.21	0.85	0.46
N$_2$P						
ZnO	0.10	0.10	1.00	0.05	0.98	0.25
AZO1	0.10	0.11	1.00	0.06	0.97	0.27
AZO2	0.13	0.11	1.00	0.06	1.14	0.30
AZO3	0.12	0.11	1.00	0.06	1.06	0.29
AZO4	0.12	0.13	1.00	0.16	0.92	0.42

Table 5.8: Relative VBXPS peak intensities, Zn is set to 1. All peak intensities were measured from the peak maximum rather than from a set binding energy. Background values for Zn3d and O2s peaks were taken at the peak onset on the high binding energy edge. For Zn3d this is at 14eV, and for O2s this is at 27eV for ZnO, AZO1, AZO2 and AZO3, and at 28eV for AZO4.

Doping creates a shift of the VB which is observed as an upwards binding energy shift in VB features. This value is 1.0eV for both the S/H and N$_2$P data sets and is reflected in the VB cut-off values (Table 5.9). This upwards binding energy shift has been seen before and has been attributed to band bending[20, 24].

There is an overall increase in oxygen states with increasing Al content (Table 5.8) which has been seen before[21]. For low doping concentrations the increased oxygen is mostly from the lone pair or hybridized orbitals, and there is a clear change in spectral shape between 7~9eV (Figures 5.6, 5.7). The increase in states along with the shape change is attributed to band bending from the altered lattice energy and structure with high aluminium concentration, partially due to the difference in ionic radius between zinc and aluminium[6, 36] and also due to the addition of states belonging to AlO$_x$ as the aluminium content increases[45]. For AZO4 the O2s peak is the dominant oxygen peak in the VB (Figure 5.8). The extra O2s states are attributed to states belonging to AlO_x[46].

Differences between cleaning methods at this depth into the surface are not easily seen when visually comparing the S/H and N_2P spectra, but are apparent in the relative intensity of oxygen states in Table 5.8. Plasma treated samples have more occupied lone pair and hybridized orbital states, and sputter treating shows a higher occupation of O2s states deep in the VB. The VBM cut-off is higher for plasma treated samples (Table 5.9). This set of higher cut off energies for the plasma treated samples is attributed to the plasma induced surface states of ZnO with a possible small effect from the surface contamination as yet unremoved by the UHV anneal.

VBM (eV)	**VBXPS**		**UPS**		
Sample	**H/S**	**N_2P**	**H/S**	**N_2P**	**N_2P/H**
ZnO	3.1	3.2	3.2	4.1	3.1
AZO1	3.2	3.5	3.2	4.0	3.2
AZO2	3.4	3.4	3.4	4.0	3.3
AZO3	3.5	3.5	3.5	4.0	3.5
AZO4	4.1	4.2	4.5	4.7	4.4

Table 5.9: VBM binding energy cut off for VBXPS and UPS of all sample types and cleaning methods. The uncertainty for each cut off is 0.05eV.

VBXPS spectra were not recorded for the reheated plasma treated samples (N_2P/H) as the primary function of reheating is to remove surface contamination, thus the more surface sensitive methods of UPS and MIES are more suitable for observing these changes.

5.4.4) UPS

As received samples have almost identical occupied DOS in UPS due to the presence of hydrocarbons on the surface and shall not be shown as an example is shown later in the MIES data in Figure 5.15. Series of spectra for the three cleaning methods are shown in Figures 5.9-5.11. The same main features and peak assignments are observed in UPS as in VBXPS, but the relative peak intensities are different because cross sections for the electron excitations in the various orbitals depend on the excitation energy[22, 44]. Relative peak intensities are shown in Table 5.10, and workfunctions are shown in Table 5.11 and were obtained by extrapolating the line of the secondary electron cut off. Note that the UPS intensities in Table 5.10 cannot be directly compared to VBXPS intensities in Table 5.8 due to the difference in cross sections at different photon energies (Zn3d peaks not equivalent between the two tables). Only relative changes may be compared.

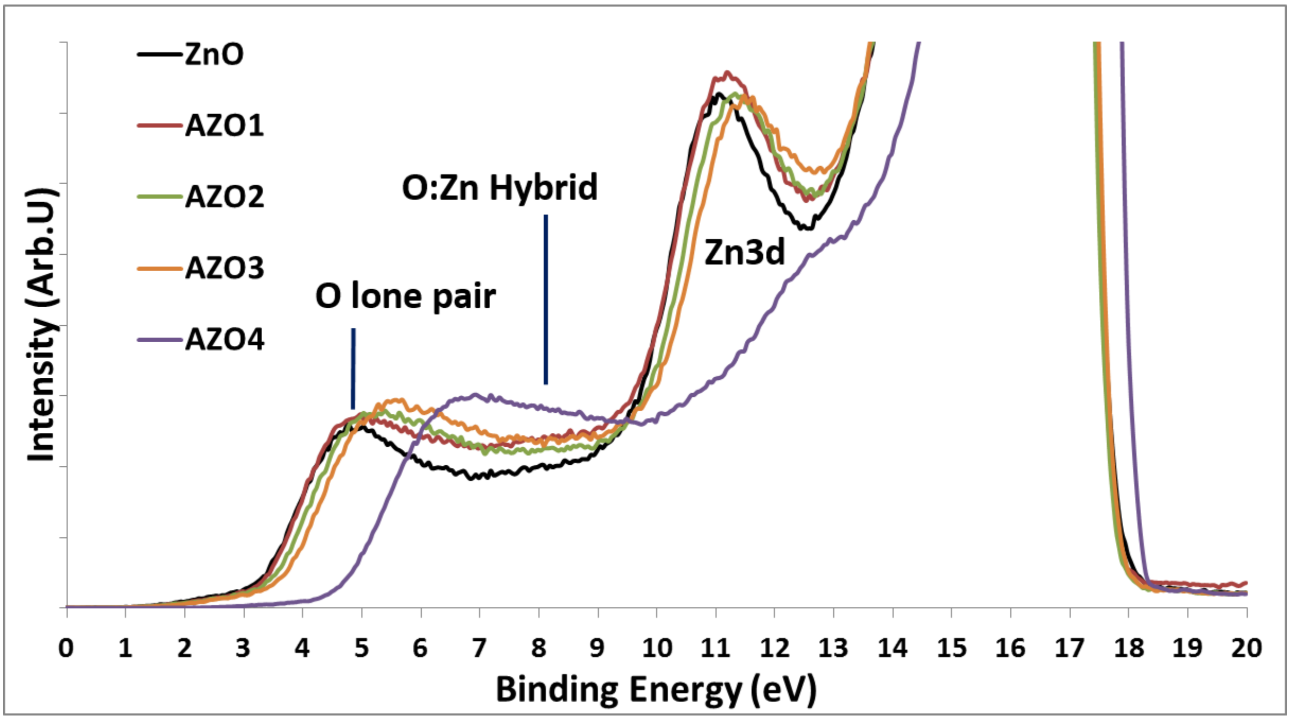

Figure 5.9: UPS of UHV sputtered and heated (S/H) ZnO and AZO.

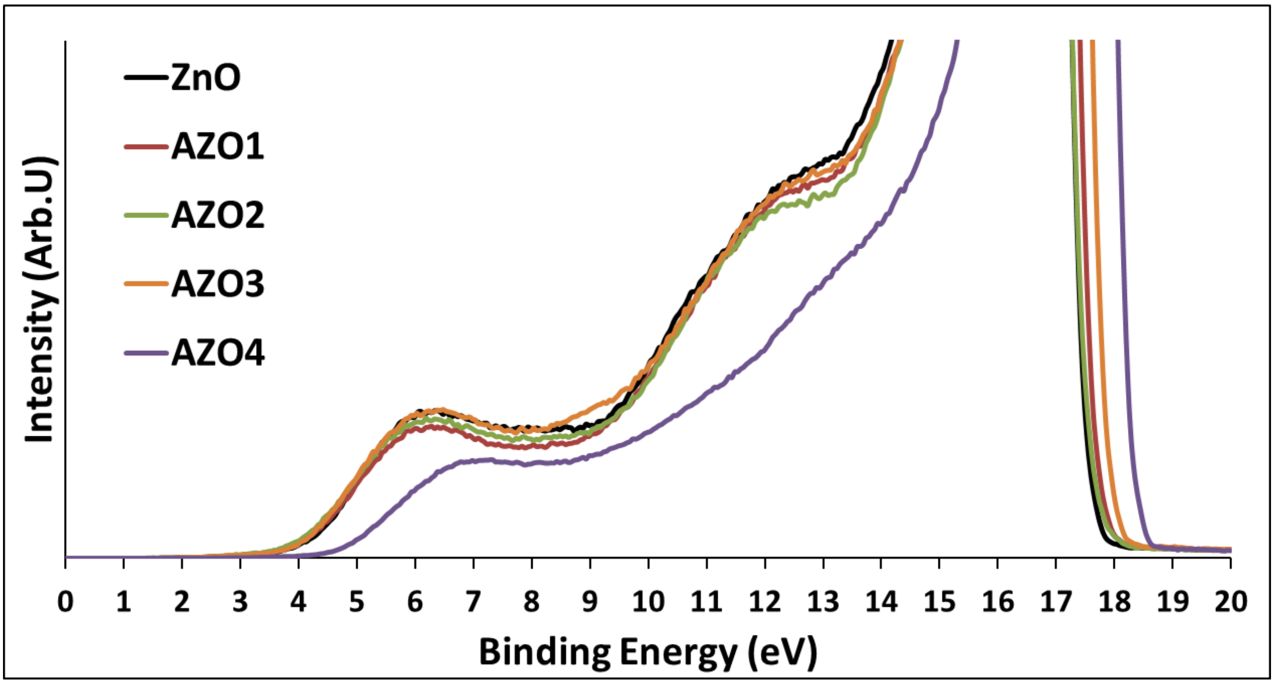

Figure 5.10: UPS of nitrogen annealed + oxygen plasma treated (N_2P) ZnO and AZO.

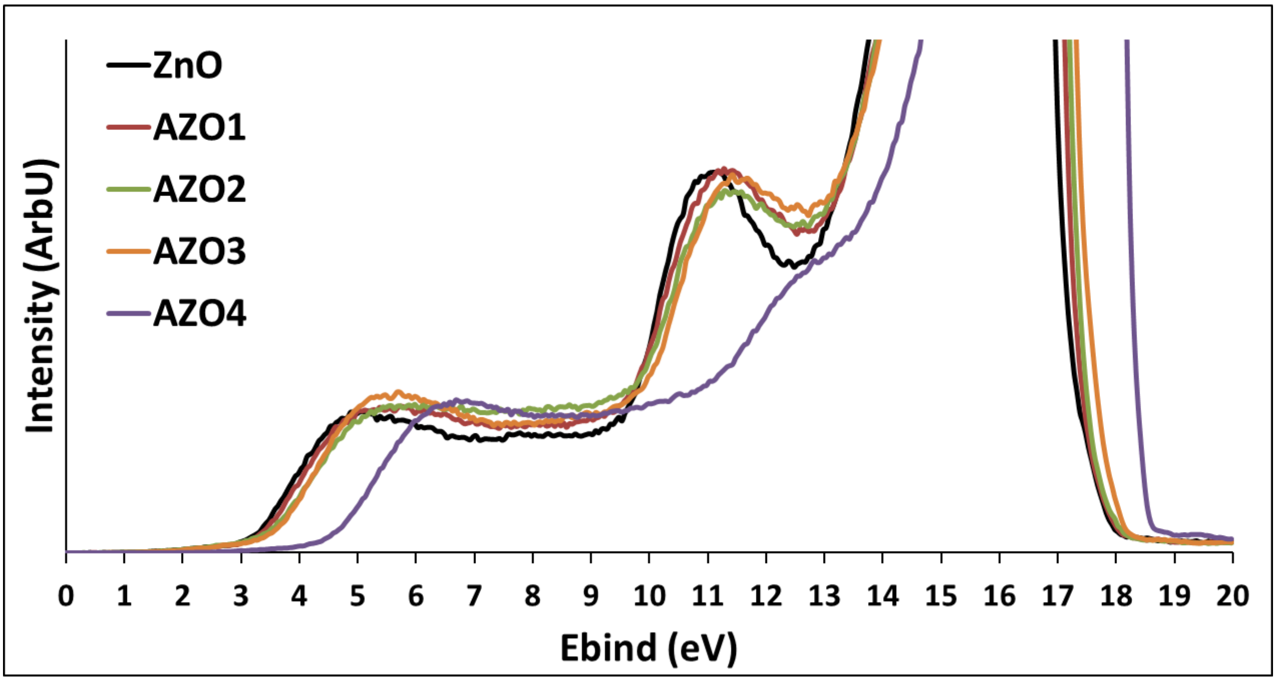

Figure 5.11: UPS of nitrogen annealed + oxygen plasma treated samples, post heating in UHV (N_2P/H) ZnO and AZO.

S/H	**O2p**	**O_{hyb}**	**Zn3d**	**O2p:O_{hyb}**	**O_{tot}:Zn**
ZnO	0.36	0.28	1.00	1.32	0.64
AZO1	0.37	0.31	1.00	1.21	0.68
AZO2	0.40	0.32	1.00	1.24	0.72
AZO3	0.41	0.33	1.00	1.24	0.75
AZO4	0.62	0.56	1.00	1.11	1.17
N_2P					
ZnO	0.41	0.36	1.00	1.11	0.77
AZO1	0.36	0.34	1.00	1.08	070
AZO2	0.39	0.37	1.00	1.05	0.76
AZO3	0.41	0.41	1.00	0.98	0.82
AZO4	-	-	-	-	-
N_2P/H					
ZnO	0.38	0.31	1.00	1.23	0.68
AZO1	0.37	0.33	1.00	1.11	0.71
AZO2	0.44	0.43	1.00	1.03	0.87
AZO3	0.42	0.37	1.00	1.15	0.79
AZO4	0.60	0.56	1.00	1.07	1.15

Table 5.10: Relative UPS peak intensities. Values for N_2P AZO4 are left out because the contribution of these states is small, and the differences in the band structure means there could be DOS at these energies which are not from these specific orbitals.

Sample	As Received (eV)	S/H (eV)	N_2P (eV)	N_2P/H (eV)
ZnO	3.3	3.7	3.8	4.2
AZO 1	3.5	3.7	3.7	4.0
AZO 2	3.4	3.8	3.8	3.9
AZO 3	3.3	3.7	3.5	3.8
AZO 4	2.7	3.3	3.0	3.0

Table 5.11: Workfunctions of ZnO and AZO for all cleaning methods.

As UPS is highly surface sensitive the surface needs to be very clean to properly observe all relevant changes in the VB of ZnO, as hydrocarbon contamination has an impact on the UP spectra and thus on the procedure of deriving surface band structure from measured UPS data[20, 47]. As such the plasma cleaned N_2P sample set is less representative of the ZnO surface and band structure changes due to the heavy carbon contamination. For the samples which had been heated in UHV (S/H, N_2P/H,) the states belonging to the Zn-d band can be easily identified.

The whole VB spectrum shifts to a higher binding energy upon doping, with an increasing shift as the aluminium concentration increases - similar to that observed in VBXPS. The shift is reflected in the VBM in Table 5.9. In the case of the doped samples, there is also a small increase in states at 12.5eV in both S/H and N_2P/H sample sets which could be attributed to the oxygen from AlO_x but the precise nature of the observed increase is difficult to confirm so close to the secondary electron background. It is important to note that the shift in VBM with increasing doping is larger than the increase in band gap for both S/H and N_2P/H samples. This means that the CB at the surface also shifts to lower energies.

There is an overall increase in oxygen relative to Zn3d occupation, and AZO4 shows a different spectral shape due to band bending as seen also in VBXPS. Due to the significantly large Al concentration in this sample it is also possible that another compound is present, however no indication of this was observed in the XPS data. The largest relative DOS increase in UPS is from the oxygen hybridized orbitals (Table 5.10) however, it needs to be noted that O2s states cannot be detected with UPS so it is a measure of the VB in the region < 10 eV only and changes to O2s cannot be taken into account at this depth. The workfunction was not significantly altered with low doping concentrations, which has been seen before[48], but AZO4 shows a significant decrease compared to ZnO (Table 5.11).

As stated above, the hydrocarbon contamination on the N_2P sample set has a significant impact on the VB. The spectra in Figure 5.10 are all offset to a higher binding energy relative to the other cleaning methods, and the VBM is largely unaffected by doping. The spectral shape from 9.5–14eV is also different, showing features mostly from the hydrocarbons[47]. The binding energy offset indicates the presence of a surface dipole[49], which in this instance is believed to be induced by the layer of hydrocarbons and also oxygen species present on the surface from the cleaning process and sample transfer to the vacuum chamber. This binding energy offset could also be due to the combination of hydrocarbon states convoluted with the features of ZnO, however it cannot be discerned whether it is the dipole or convolution of features causing this offset. Upon heating the plasma treated samples in UHV the dipole is removed, the features pertaining to Zn3d are more easily observed, and the VBM is seen to be impacted by changes in dopant concentration, becoming comparable to the values obtained from sputtering (Table 5.9). Sputter cleaning shows higher VBM cut-offs overall. The relative oxygen to zinc (O_{tot}:Zn) is lower for sputter cleaned samples, as is the relative intensity of hybridized orbitals to lone pairs (O_{hyb}:O2p). This could possibly be due to preferential sputtering of oxygen which has been seen before for ZnO films[20], but in this work is not sufficient to be detected by XPS.

All cleaning methods increased the workfunction with respect to the as received samples. This has been observed before for both sputter and plasma cleaning[19]. Plasma treating with a UHV anneal produced the highest workfunction per sample type in all but one instance. Plasma treatment producing a higher workfunction than sputter cleaning has been seen before for ZnO[9]. The sample cleaning creates a more negative ZnO surface which redistributes charge and reinforces the natural surface dipole moment, especially with the oxygen plasma, thus increasing the workfunction.

5.4.5) MIES

The MIE spectra taken from the as received samples were virtually identical with features attributed to hydrocarbons[47], an example is shown later in Figure 5.16. Relative peak intensity tables will not be given as the relative DOS are obvious upon inspection of the spectra in Figures 5.12-5.14 of the three cleaning methods. The features in MIES are much broader than in UP or VBXP spectra and thus RI and AN can be identified as the dominant He* de-excitation process for the samples investigated.

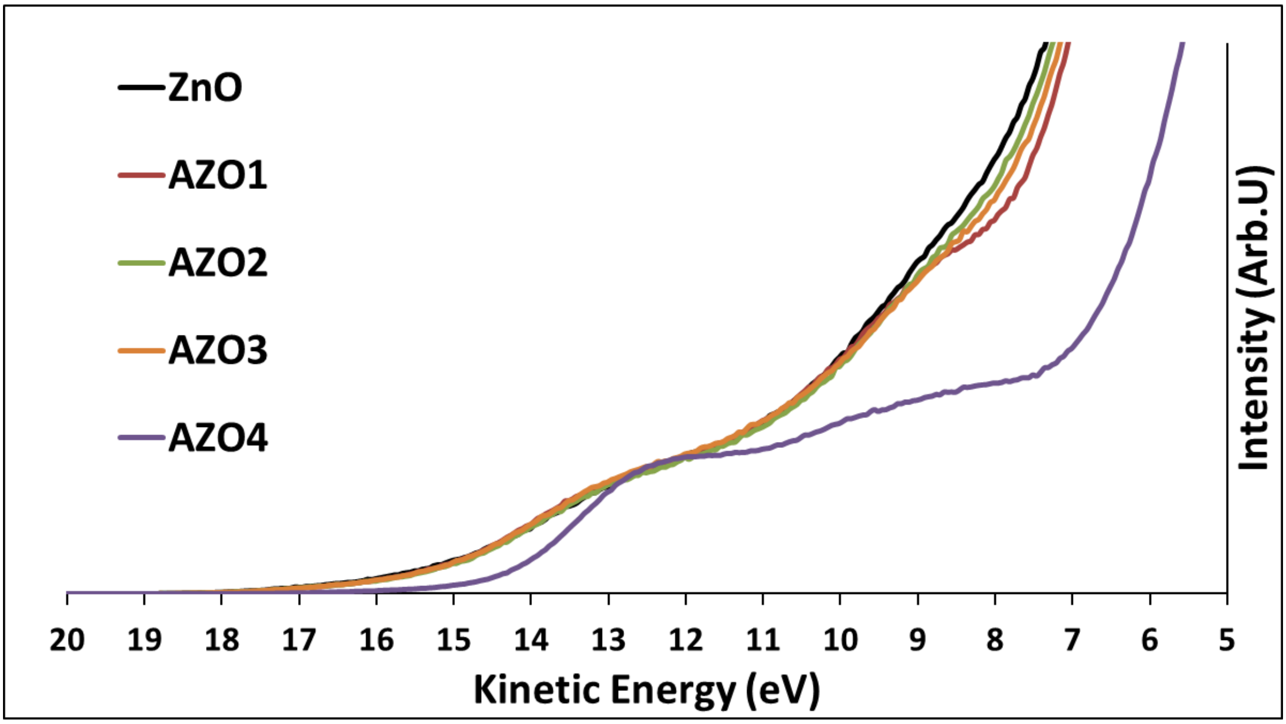

Figure 5.12: Weighted MIE spectra for UHV sputtered and heated (S/H) ZnO and AZO.

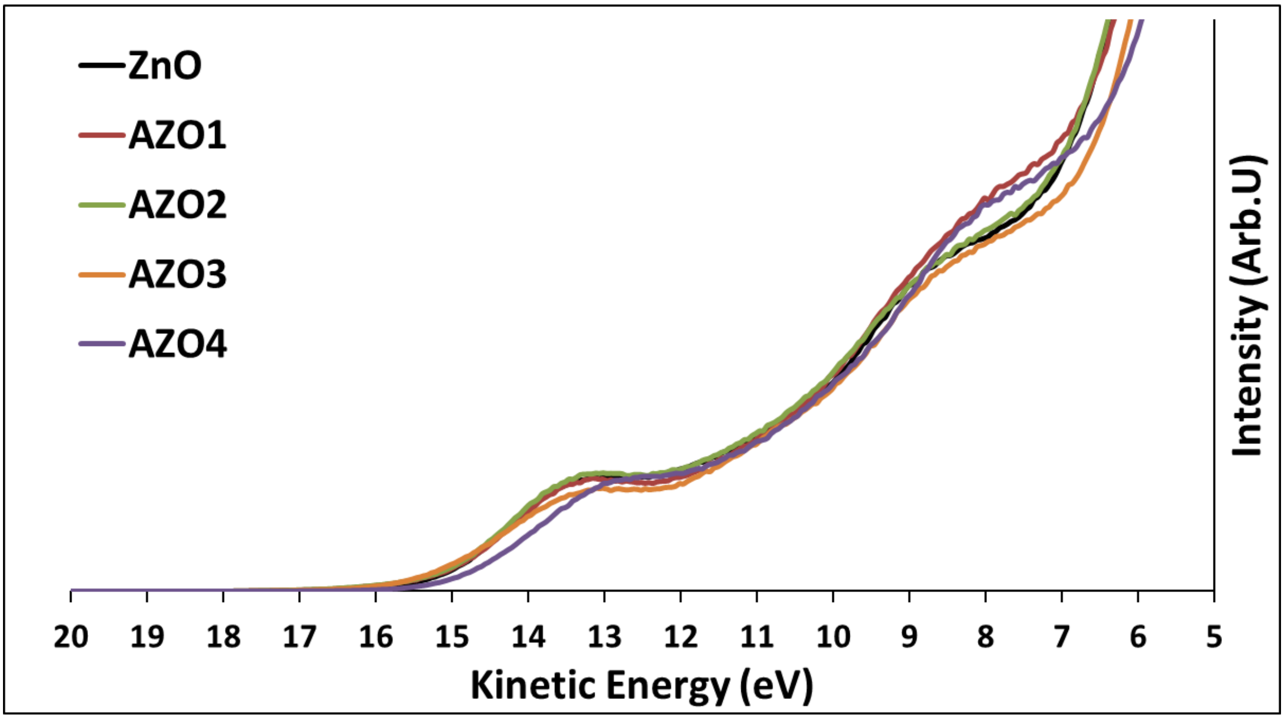

Figure 5.13: MIE spectra for nitrogen annealed + oxygen plasma treated (N_2P) ZnO and AZO. No spectra were reweighted in this instance.

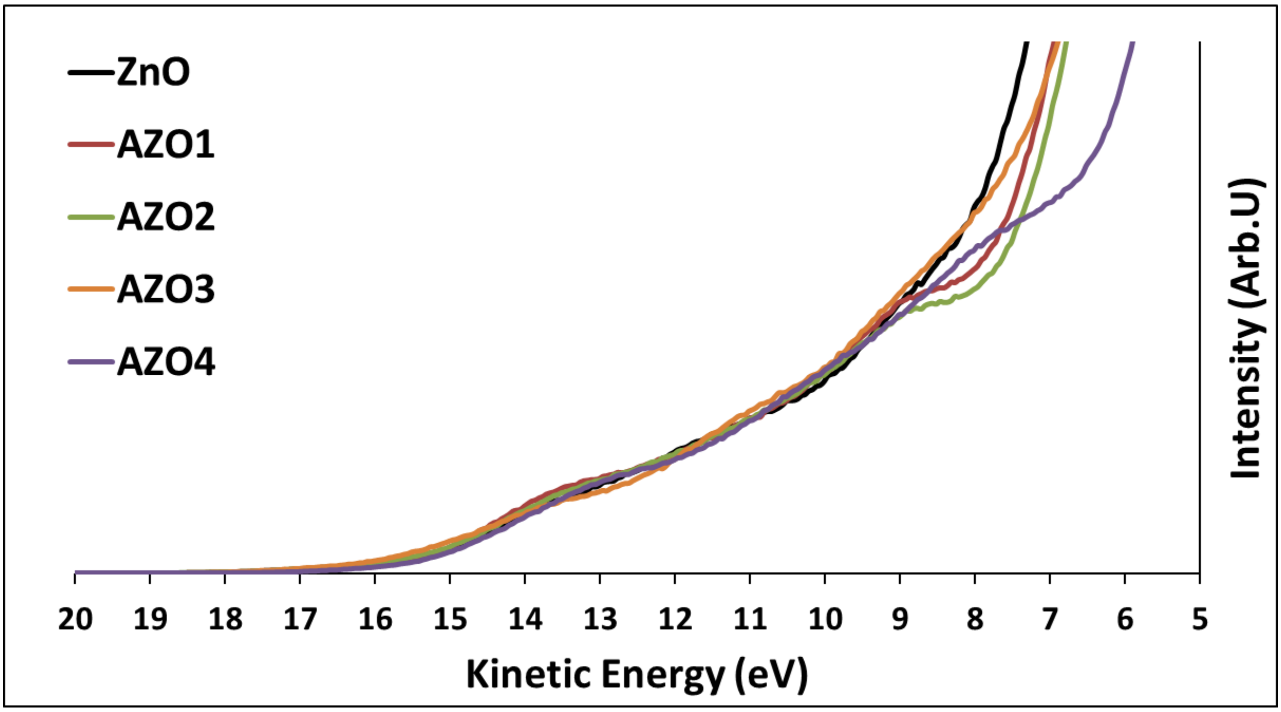

Figure 5.14: Weighted MIE spectra for nitrogen annealed + oxygen plasma treated ZnO and AZO, post heating in UHV (N_2P/H).

The outermost layer DOS do not significantly change for low doping concentrations. There is some variance at 8eV kinetic energy but features at these higher binding energies are hard to compare due to the influence of the secondary electron background. The absence of change in the MIE spectra with doping for N_2P spectra is due to the presence of remaining adventitious hydrocarbons on the sample surface. Note also that the He* de-excitation mechanism is still predominantly AD for this surface, revealing more defined features.

For the cleaner sample sets of S/H and N_2P/H however the fact that RI followed by AN is the dominant de-excitation mechanism indicates the presence of a surface conduction channel which can be seen on native ZnO surfaces once annealed in vacuum (to remove surface contamination), the presence of the channel is shown in Figure 5.15. It is an accumulation of electrons at low binding energy, i.e. in the band gap, in a potential well at the surface. This phenomenon has mainly been observed to date via Hall measurements[50-53], but states attributed to this quantum well have been observed in synchrotron PES by Piper *et.al*[54]. Band gap states leading to MIE spectra predominantly showing RI followed by AN has been seen before[55]. For ZnO the source of the charge carriers creating the channel is not known, but some works have attributed hydrogen species to be involved[51, 53, 56].

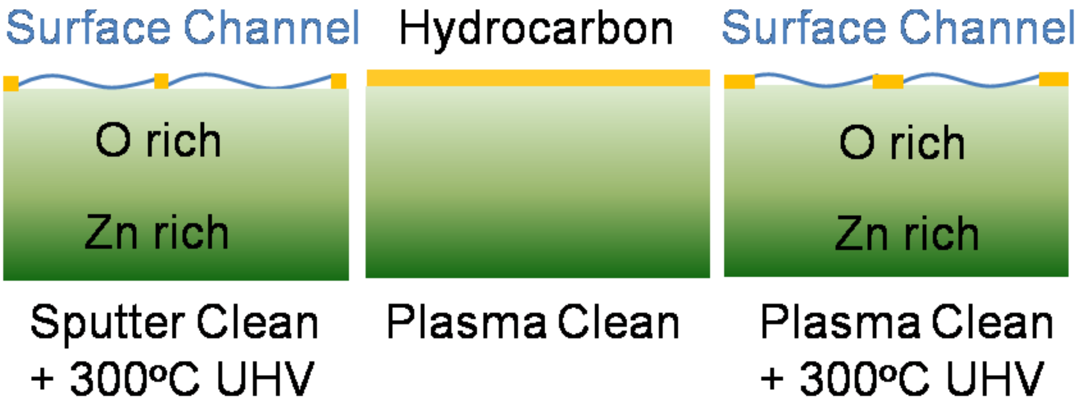

Figure 5.15: Comparison of the cleaned ZnO surfaces and presence of the conduction channel as seen with MIES. The same trend was observed across all sample types.

Previous work investigating doped and un-doped ZnO indicates that dopants do not destroy this channel and it was concluded the source of the surface charge carriers was independent of doping[57]. The MIE spectra in this work also suggests this to be the case, as the de-excitation mechanism is not altered at any doping concentration for the N_2P/H sample set, even with heavy doping. Sputter cleaned samples (S/H) do however show a very different spectrum for the heavily doped AZO4 sample. The features are still broad, showing that both de-excitation mechanisms (and thus the surface channel) are present, but to a lesser degree than the other samples, indicating that the channel is reduced in this instance.

Other than AZO4 in the sputtered samples, the MIE spectra are not seen to vary much or with any specific trend as the more subtle changes to the VB which can be observed in UPS or VBXPS would be blurred out with the change in de-excitation mechanism due to the enhanced metallicity of the surface. A comparison of the as received vs. cleaned samples can be seen in Figure 5.16.

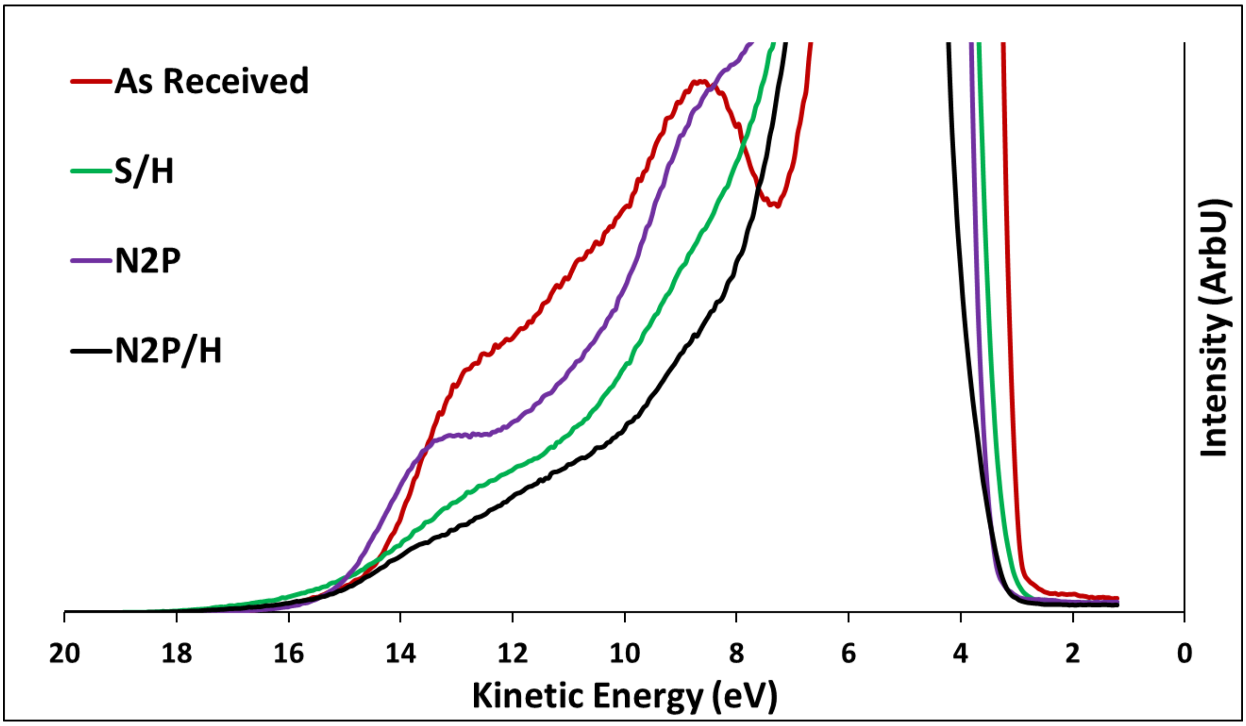

Figure 5.16: Comparison of as received and cleaned ZnO surfaces as seen with MIES. The as received spectrum is dominated by hydrocarbon. Plasma cleaning reveals a spectrum in which the O2p and Zn3d features can be identified, yet samples annealed in UHV (S/H, N_2P/H) show spectra which are almost identical. The same trend was observed across all sample types.

5.4.6) Further Discussion: Changes in the Valence Band with Depth

Measuring electron spectra with the three different methods VBXPS, UPS and MIES allows for a discussion on how the electronic structure of ZnO and AZO is changing with depth. The properties that can be discussed are the presence of the surface channel, the change in composition with depth, the impact of cleaning methods on the surface structure and corresponding changes in workfunction.

The presence of the conduction channel in MIES raises the question of the impact of this channel on the near surface area. The UP spectra in Figures 5.9 and 5.11 have intensities at binding energies below that of the VBM, most notably in the S/H samples (Figure 5.9) which clearly shows features down to ~1eV below the Fermi level, supporting the theory that there are states present in the band gap. XPS shows that sputter cleaning + UHV anneal is the most effective method for reducing contaminant species, so it follows that the states in the band gap and the conduction channel can be observed in this cleaner sample set.

Another main question that arises is how the DOS are changing with the depth when there is a different electrostatic potential at the surface, such as the difference between the vacuum annealed (surface channel) and non-vacuum annealed (no surface channel) samples in this work. A theoretical and experimental UPS study investigating electrostatic potentials on ZnO crystal surfaces found that the band separation between Zn3d and O2p changes between the surface and the bulk, arising from the different potentials inherent in lattice structure[58]. The O2p and Zn3d peak distance in both UPS and VBXPS was 6.1eV for both the S/H and N_2P/H samples indicating no change in potential over the first 10nm for either cleaning method (N_2P/H UPS was compared to N_2P VBXPS). Thus it appears that the selected cleaning methods do not affect the electrostatic potential of the ZnO or AZO surface.

The change in composition with depth is also apparent. XPS, VBXPS and UPS all show an overall increase in oxygen states with doping. However, the relative increase (with respect to undoped ZnO) observed in UPS is nearly double that seen in VBXPS (Tables 5.8 & 5.10). This cannot be explained by changes in cross section as only the relative changes are being compared, and it indicates that the doping and/ or annealing process enhances oxygen states near the outermost layer. Specifically, VBXPS indicates that the O2s states are enhanced toward the bulk, and UPS shows that the hybrid O:Zn orbitals are prominent toward the surface. This could possibly correlate to changes in structure observed with doping in microscopy and X-Ray diffraction studies[37, 59], or changes in the defects present in the lattice[2]. However, it is interesting to note that the extra oxygen states and doping does not impact on the DOS present in the band gap in UPS at low doping concentrations. This supports the hypothesis in the work by Piper *et.al*[54] that the source of the charge carriers in the conduction channel could be these band gap states, although in the work by Piper *et.al*[54] the states were observed at 0.5V below the Fermi level and in this work they are observed from 1~3eV. Heavily doped samples show a decrease in these states, indicating lattice disruption and band bending, but the surface is still metallic enough to allow for the RI and AN de-excitation mechanism in MIES.

As discussed, plasma cleaning alone (N_2P) clearly leaves significant residue on the surface which impacts the band structure of the near surface area and would affect device performance. The more pristine surfaces produced after UHV anneal reveal the surface conduction channel in MIES, and an increase in Me:O* in XPS. There are then also differences between S/H and N_2P/H. XPS shows that the S/H cleaning method shows the highest lattice related oxygen and aluminium overall, yet VBXPS reveals a lower overall oxygen related DOS relative to zinc in the VB compared to N_2P/H. The relative oxygen occupancy is also different, in that sputtering reveals more of the O2s states and less of the lower binding energy oxygen states in VBXPS, and UPS shows more of the lone pair states around 5eV compared to the O:Zn hybrid states around 8eV. This indicates that although the most effective way of removing carbon is via sputtering, the presence of extra oxygen species on the surface from plasma cleaning alters the surface when heated in UHV, allowing a higher occupancy of oxygen states in the VB, particularly the hybridized states. This could also account for the higher workfunction seen in plasma treated samples.

The surface oxygen provided by the oxygen plasma does not remove the conduction channel, provided the surface is annealed in UHV. This is an interesting point of note as there is currently debate on the impact of chemisorbed species such as oxygen on the channel and subsequent impact on devices such as ZnO field effect transistors and gas sensors. Some work indicating oxygen depletes the surface conduction[56], while other work suggests other species[60] or even the ZnO deposition conditions[61] are involved. The process of UHV annealing in this work removes most of the excess oxygen , but the remaining species do not destroy the conduction channel.

5.5) Conclusion

We have shown the impact of doping and non-solvent cleaning on the electronic states, workfunction and surface composition of ZnO. The presence of a surface conduction channel has been confirmed for the clean surfaces, the changes in composition with depth through the first 10nm has been shown, and the differences between cleaning methods has been discussed. Doping with an AZO or Al target clearly increases the metal oxide core level states in XPS and also the oxygen related DOS in the VB relative to zinc. It also shifts the VB and CB to higher binding energies and increases the band gap as seen by UV-Vis, thus indicating a Burstein-Moss shift and the incorporation of Al and extra O into the ZnO lattice. UHV annealing was shown to increase oxygen in the Me:O* lattice and reveal the surface conduction channel of ZnO, which was not affected with doping. Cleaning pre-treatments of sputtering or oxygen plasma showed different relative oxygen DOS in the near surface area. Although sputtering removes more surface contamination, the use of an oxygen plasma pre-treatment shows a greater increase in workfunction and overall higher occupancy of oxygen s and p states in the VB. This is believed to be due to the excess oxygen present from oxygen plasma on the surface which alters the band structure upon annealing.

5.6) Acknowledgment

This work was supported by the CSIRO Future Manufacturing Flagship: Flexible Transparent Electrodes for Plastic Electronics Cluster which includes The University of Queensland, University of Technology, Sydney and Flinders University.

5.7) References

1. Liu, Y.; Li, Y.; Zeng, H., ZnO-Based Transparent Conductive Thin Films: Doping, Performance, and Processing. *Journal of Nanomaterials* **2013**, *2013*, 9.

2. Brillson, L. J.; Lu, Y., ZnO Schottky Barriers and Ohmic Contacts. *Journal of Applied Physics* **2011**, *109*, 121301.

3. Anderson, J.; Chris, G. V. d. W., Fundamentals of Zinc Oxide as a Semiconductor. *Reports on Progress in Physics* **2009**, *72*, 126501.

4. Mallika, A. N.; RamachandraReddy, A.; SowriBabu, K.; Venugopal Reddy, K., Synthesis and Optical Characterization of Aluminium Doped ZnO Nanoparticles. *Ceramics International* **2014**, *40*, 12171-12177.

5. Jaramillo, R.; Ramanathan, S., Electronic Granularity and the Work Function of Transparent Conducting ZnO:Al Thin Films. *Advanced Functional Materials* **2011**, *21*, 4068-4072.

6. Kuo, S.-Y.; Chen, W.-C.; Lai, F.-I.; Cheng, C.-P.; Kuo, H.-C.; Wang, S.-C.; Hsieh, W.-F., Effects of Doping Concentration and Annealing Temperature on Properties of Highly-Oriented Al-Doped ZnO Films. *Journal of Crystal Growth* **2006**, *287*, 78-84.

7. Gao, Y., Surface Analytical Studies of Interfaces in Organic Semiconductor Devices. *Materials Science and Engineering: R: Reports* **2010**, *68*, 39-87.

8. Zhang, L.; Zhang, H.; Bai, Y.; Ma, J. W.; Cao, J.; Jiang, X.; Zhang, Z. L., Enhanced Performances of ZnO-TFT by Improving Surface Properties of Channel Layer. *Solid State Communications* **2008**, *146*, 387-390.

9. Fang-Ling, K.; Yun, L.; Marvin, S.; Jincheng, D.; Nigel, D. S., Workfunction Tuning of Zinc Oxide Films by Argon Sputtering and Oxygen Plasma: An Experimental and Computational Study. *Journal of Physics D: Applied Physics* **2012**, *45*, 065301.

10. Ding, J.; Chen, H.; Zhao, X.; Ma, S., Effect of Substrate and Annealing on the Structural and Optical Properties of ZnO:Al Films. *Journal of Physics and Chemistry of Solids* **2010**, *71*, 346-350.

11. Gabás, M.; Torelli, P.; Barrett, N. T.; Sacchi, M.; Ramos Barrado, J. R., Electronic Structure of Al- and Ga-Doped ZnO Films Studied by Hard X-Ray Photoelectron Spectroscopy. *APL Materials* **2014**, *2*, 012112.

12. Fang, G.; Li, D.; Yao, B.-L., Fabrication and Vacuum Annealing of Transparent Conductive AZO Thin Films Prepared by Dc Magnetron Sputtering. *Vacuum* **2002**, *68*, 363-372.

13. Maldonado, F.; Stashans, A., Al-Doped ZnO: Electronic, Electrical and Structural Properties. *Journal of Physics and Chemistry of Solids* **2010**, *71*, 784-787.

14. Huang, D.; Zeng, X.; Zheng, Y.; Wang, X.; Yang, Y., Influence of Process Parameters on Band Gap of Al-Doped ZnO Film. *Front. Optoelectron.* **2013**, *6*, 114-121.

15. Kim, Y.-S.; Tai, W.-P., Electrical and Optical Properties of Al-Doped ZnO Thin Films by Sol–Gel Process. *Applied Surface Science* **2007**, *253*, 4911-4916.

16. Rahmane, S.; Djouadi, M. A.; Aida, M. S.; Barreau, N.; Abdallah, B.; Hadj Zoubir, N., Power and Pressure Effects Upon Magnetron Sputtered Aluminum Doped ZnO Films Properties. *Thin Solid Films* **2010**, *519*, 5-10.

17. Yang, W.; Wu, Z.; Liu, Z.; Pang, A.; Tu, Y.-L.; Feng, Z. C., Room Temperature Deposition of Al-Doped ZnO Films on Quartz Substrates by Radio-Frequency Magnetron Sputtering and Effects of Thermal Annealing. *Thin Solid Films* **2010**, *519*, 31-36.

18. Sugiyama, K.; Ishii, H.; Ouchi, Y.; Seki, K., Dependence of Indium–Tin–Oxide Work Function on Surface Cleaning Method as Studied by Ultraviolet and X-Ray Photoemission Spectroscopies. *Journal of Applied Physics* **2000**, *87*, 295-298.

19. Wang, W.; Feng, Q.; Jiang, K.; Huang, J.; Zhang, X.; Song, W.; Tan, R., Dependence of Aluminum-Doped Zinc Oxide Work Function on Surface Cleaning Method as Studied by Ultraviolet and X-Ray Photoelectron Spectroscopies. *Applied Surface Science* **2011**, *257*, 3884-3887.

20. Park, S. H.; Kim, H. J.; Cho, M.-H.; Yi, Y.; Cho, S. W.; Yang, J.; Kim, H., The Effect of ZnO Surface Conditions on the Electronic Structure of the ZnO/CuPc Interface. *Applied Physics Letters* **2011**, *98*, 082111.

21. Gabas, M., Direct Observation of Al Doping Induced Electronic States in the Valence Band and Band Gap of ZnO Films. *Physical Review B* **2011**, *84*, 1533.3/1-153303/4.

22. Leontiev, S. A.; Koshcheev, S. V.; Devyatov, V. G.; Cherkashin, A. E.; Mikheeva, é. P., Detailed XPS and UPS Studies of the Band Structure of Zinc Oxide. *J Struct Chem* **1997**, *38*, 725-731.

23. Park, H.-W.; Chung, K.-B.; Park, J.-S.; Ji, S.; Song, K.; Lim, H.; Jang, M.-H., Electronic Structure of Conducting Al-Doped ZnO Films as a Function of Al Doping Concentration. *Ceramics International* **2015**, *41*, 1641-1645.

24. Cong, G. W., et al., Aluminium Doping Induced Enhancement of P–D Coupling in ZnO. *Journal of Physics: Condensed Matter* **2006**, *18*, 3081.

25. Sans, J. A., Chemical Effects on the Optical Band Gap of Heavily Doped ZnO:M(iii) (M=Al,Ga,In): An Investigation by Means of Photoelectron Spectroscopy, Optical Measurements and under Pressure, and Band Structure Calculations. *Physical Review B* **2009**, *79*, 195105.

26. Tseng, C.-A.; Lin, J.-C.; Chang, Y.-F.; Chyou, S.-D.; Peng, K.-C., Microstructure and Characterization of Al-Doped ZnO Films Prepared by RF Power Sputtering on Al and ZnO Targets. *Applied Surface Science* **2012**, *258*, 5996-6002.

27. Gabas, M.; Gota, S.; Ramos-Barrado, J. R.; Sanchez, M.; Barrett, N. T.; Avila, J.; Sacchi, M., Unraveling the Conduction Mechanism of Al-Doped ZnO Films by Valence Band Soft X-Ray Photoemission Spectroscopy. *Applied Physics Letters* **2005**, *86*, 042104-3.

28. Hofmann, D., The Pure Surface: Structure and Geometry, *Current Topics in Materials Science, Vol 7, Part 2, Subchapter 3.8;* North Holland Publishing Company, **1981**.

29. Tseng, C.-A., Photoelectron Spectroscopy and Optical Properties of Al Doped ZnO Films Prepared by Sputtering with Radio Frequency Power Applied to Al Target. *Japanese Journal of Applied Physics*, **2013**, *52*, 025801.

30. Kim, D., Effects of in Situ Annealing on the Properties of Al Doped ZnO Thin Films Deposited by RF Magnetron Sputtering. *J. Mater. Sci.* **2014**, *25*, 1589-1595.

31. Al-Ghamdi, A. A.; Al-Hartomy, O. A.; El Okr, M.; Nawar, A. M.; El-Gazzar, S.; El-Tantawy, F.; Yakuphanoglu, F., Semiconducting Properties of Al Doped ZnO Thin Films. *Spectrochimica Acta Part A: Molecular and Biomolecular Spectroscopy* **2014**, *131*, 512-517.

32. Jeong, S. H.; Boo, J. H., Influence of Target-to-Substrate Distance on the Properties of AZO Films Grown by RF Magnetron Sputtering. *Thin Solid Films* **2004**, *447–448*, 105-110.

33. Grant, J. T., Methods for Quantitative Analysis in XPS and AES. *Surface and Interface Analysis* **1989**, *14*, 271-283.

34. Moulder, J. F., Stickle, W., Sobol, W., Bomben, K., Handbook of X-Ray Photoelectron Spectroscopy; Physical Electronics Inc, **1992.**

35. Seah, M. P.; Dench, W. A., Quantitative Electron Spectroscopy of Surfaces: A Standard Data Base for Electron Inelastic Mean Free Paths in Solids. *Surface and Interface Analysis* **1979**, *1*, 2-11.

36. Zi-qiang, X.; Hong, D.; Yan, L.; Hang, C., Al-Doping Effects on Structure, Electrical and Optical Properties of C-Axis-Orientated ZnO:Al Thin Films. *Materials Science in Semiconductor Processing* **2006**, *9*, 132-135.

37. Bidmeshkipour, S.; Shahtahmasebi, N., Different Properties of Aluminum Doped Zinc Oxide Nanostructured Thin Films Prepared by Radio Frequency Magnetron Sputtering. *Semiconductors* **2013**, *47*, 787-790.

38. Lee, K. E.; Wang, M.; Kim, E. J.; Hahn, S. H., Structural, Electrical and Optical Properties of Sol–Gel AZO Thin Films. *Current Applied Physics* **2009**, *9*, 683-687.

39. Kim, D. K.; Kim, H. B., Room Temperature Deposition of Al-Doped ZnO Thin Films on Glass by RF Magnetron Sputtering under Different Ar Gas Pressure. *Journal of Alloys and Compounds* **2011**, *509*, 421-425.

40. Jeong, Y. S., Enhanced Electrical and Optical Properties of Atmospheric Plasma Treated Al Doped ZnO Thin Films with Hydrogen Gas. *Journal of The Korean Physical Society* **2009**, *54*, 944-949.

41. Nan, H.; Chao, S.; Mingwei, Z.; Bin, Z.; Jun, G.; Xin, J., Microstructure Evolution of Zinc Oxide Films Derived from Dip-Coating Sol–Gel Technique: Formation of Nanorods through Orientation Attachment. *Nanotechnology* **2011**, *22*, 265612.

42. Tong, H.; Deng, Z.; Liu, Z.; Huang, C.; Huang, J.; Lan, H.; Wang, C.; Cao, Y., Effects of Post-Annealing on Structural, Optical and Electrical Properties of Al-Doped ZnO Thin Films. *Applied Surface Science* **2011**, *257*, 4906-4911.

43. Coppa, B. J.; Fulton, C. C.; Hartlieb, P. J.; Davis, R. F.; Rodriguez, B. J.; Shields, B. J.; Nemanich, R. J., In Situ Cleaning and Characterization of Oxygen- and Zinc-Terminated, N-Type, ZnO{0001} Surfaces. *Journal of Applied Physics* **2004**, *95*, 5856-5864.

44. Ranke, W., Separation of the Partial S and P Densities of Valence States of ZnO from UPS Measurements. *Solid State Communications* **1976**, *19*, 685-688.

45. Imai, Y.; Watanabe, A., Comparison of Electronic Structures of Doped ZnO by Various Impurity Elements Calculated by a First-Principle Pseudopotential Method. *Journal of Materials Science: Materials in Electronics* **2004**, *15*, 743-749.

46. Jantrasee, S., Pinitsoontorn, S., Moontragoon, P., First Princicples Study of the Electronic Structure and Thermoelectric Properties of Al Doped ZnO. *Journal of Electronic Materials* **2014**, *43*.

47. Berlich, A.; Liu, Y. C.; Morgner, H., Evaporation of Ni and Carbon Containing Species onto NiO/Ni as Case Study for Metal Support Catalysts Investigated by Metastable Induced Electron Spectroscopy (MIES). *Radiation Physics and Chemistry* **2005**, *74*, 201-209.

48. Wei, M.; Li, C.-F.; Deng, X.-R.; Deng, H., Surface Work Function of Transparent Conductive ZnO Films. *Energy Procedia* **2012**, *16, Part A*, 76-80.

49. Habib, A.; Hosokai, T.; Mitsuo, N.; Nakagawa, R.; Nagamatsu, S.; Aoki, M.; Masuda, S.; Kera, S.; Ueno, N., Observation and Analysis of Small Inclination of Thymine Molecules on Graphite. *The Journal of Physical Chemistry C* **2011**, *115*, 511-515.

50. Chambers, S. A., Surface Science Opportunities in the Electronic Structure of ZnO (a Perspective on the Article, “Quantitative Analysis of Surface Donors in ZnO”, by D.C. Look). *Surface Science* **2007**, *601*, 5313-5314.

51. Look, D. C., Quantitative Analysis of Surface Donors in ZnO. *Surface Science* **2007**, *601*, 5315-5319.

52. Kassier, G. H.; Hayes, M.; Auret, F. D.; Mamor, M.; Bouziane, K., Electrical and Structural Characterization of as-Grown and Annealed Hydrothermal Bulk ZnO. *Journal of Applied Physics* **2007**, *102*, 014903.

53. Mtangi, W.; Nel, J. M.; Auret, F. D.; Chawanda, A.; Diale, M.; Nyamhere, C., Annealing and Surface Conduction on Hydrogen Peroxide Treated Bulk Melt-Grown, Single Crystal ZnO. *Physica B: Condensed Matter* **2012**, *407*, 1624-1627.

54. Piper, L., Preston, A., Fedorov, A., Cho, S., DeMasi, A., Smith, K., Direct Evidence of Metallicity at ZnO (0001^{-})-(1x1) Surfaces from Angle Resolved Photoemission Spectroscopy. *Phys. Rev. B* **2010**, *81*, 233305.

55. Krischok, S.; Günster, J.; Goodman, D. W.; Höfft, O.; Kempter, V., MIES and UPS(HeI) Studies on Reduced TiO2(110). *Surface and Interface Analysis* **2005**, *37*, 77-82.

56. Hu, Y.; Liu, Y.; Li, W.; Gao, M.; Liang, X.; Li, Q.; Peng, L.-M., Observation of a 2d Electron Gas and the Tuning of the Electrical Conductance of ZnO Nanowires by Controllable Surface Band-Bending. *Advanced Functional Materials* **2009**, *19*, 2380-2387.

57. Schmidt, O.; Kiesel, P.; Ehrentraut, D.; Fukuda, T.; Johnson, N. M., Electrical Characterization of ZnO, Including Analysis of Surface Conductivity. *Appl. Phys. A* **2007**, *88*, 71-75.

58. Matsunaga, K.; Oba, F.; Tanaka, I.; Adachi, H., Valence Band Structure of ZnO (1010) Surface by Cluster Calculation. *Journal of Electroceramics* **1999**, *4*, 69-80.

59. Li, L., Deng. H., Dai, L., Chen, J., Yuan, Q., Li, Y., Properties of Al Heavy Doped ZnO Thin Films by RF Magnetron Sputtering. *Mater. Res. Bull.* **2008**, *43*, 1456-1462.

60. Goldberger, J.; Sirbuly, D. J.; Law, M.; Yang, P., ZnO Nanowire Transistors. *The Journal of Physical Chemistry B* **2005**, *109*, 9-14.

61. Chaabouni, F.; Abaab, M.; Rezig, B., Metrological Characteristics of ZnO Oxygen Sensor at Room Temperature. *Sensors and Actuators B: Chemical* **2004**, *100*, 200-204.

6. On the Growth of Evaporated LiF on PCBM and P3HT

N.M Schmerl[1], J.S Quinton[1], G.G Andersson[1*]

[1]Flinders Centre for Nanoscale Science and Technology, School of Chemistry and Physical Sciences, Flinders University of South Australia, Bedford Park, SA 5042, Australia

*Corresponding author: Email gunther.andersson@flinders.edu.au

This work has been published since this dissertation was submitted for review. The published article is now listed in the publications arising from this work section. Alterations have been performed only in that the relevant experimental methods and analysis procedures described in Chapter 2 have been discussed in the text and some figures have been placed in supplementary information.

Author Contribution:

Natalya Schmerl: Designed and performed experiments, data analysis and interpretation, and prepared the manuscript for publication.

Gunther Andersson: Intellectual contribution in conceptualising experiments, data interpretation & revision of manuscript.

Jamie Quinton: Intellectual contribution in revision of manuscript.

6.1) Abstract

The electronic properties of thin layers of LiF evaporated onto PCBM and P3HT thin films have been examined to better understand how alkali halide salt layers between the metal electrode and photoactive layer materials improve device performance. The chemical state of LiF was observed for various layer thicknesses via XPS and also at different surface depths via ARXPS measurements. LiF was found to remain intact without dissociation for a very low deposition (~1Å) layer, a thick 30Å layer, and also for sequential depositions of the salt. The electronic properties of the VB were determined for a range of thicknesses with sequential depositions up to nominal value of 16Å LiF. Concentration depth profiles were obtained via ion scattering spectroscopy. An interfacial dipole forms on the organic surfaces, and a closed layer of salt was not formed with 16Å of salt deposition as shown via MIES. The combined results indicate that the salt layer forms as nano-scale islands with some diffusion.

6.2) Introduction

Conjugated polymers and modified fullerenes have shown to be promising for next generation flexible and lightweight electronic devices. An example is their use in BHJ OPVs, initially developed in 1995 by Heeger *et al* [1]. For developing efficiently functioning devices the electronic properties at the interfaces of the organic layer and electrodes need to be understood and then appropriately adjusted to facilitate efficient charge transfer. Various interlayers have been investigated to facilitate the charge transfer efficiently. For the case of the LWE, alkali halide salts have been deposited onto the active layer before a layer of metal, e.g. typically of aluminium or silver, is deposited as the electrode, with LiF being a prevalent alkali halide choice[2]. Typically, this ultra-thin interlayer has an equivalent thickness of only a few Å. While such layer thickness of alkali halide is insufficient to form a closed layer, the deposited layer significantly enhances device performance[3-7] and depending on the interlayer thickness and salt choice the efficiency can be doubled[8-12]. This interlayer is of particular interest as it is effective in both OPVs and OLEDs, yet the devices function in the exact opposite manner[13-14]. The role and function of the salt layer on a molecular level has not yet been agreed upon, but there are several proposals in the literature. These include: doping effects[3, 7, 11, 15-17], surface Plasmon resonance generation[5], electrode workfunction modification via dipole formation[18-22], and preservation of the electronic properties of the organic layer upon electrode deposition[2-3, 16, 23-24]. Ohmic contact formation has also been proposed for the case of LiF[20, 25-26 17]. It is known that component of the layers forming in these devices can inter-diffuse at elevated temperatures encountered in device manufacture and operation, but the molecular distribution occurring between the organic and inorganic layers has not been fully examined[27]. Such diffusion of components across interfaces will influence the function of the OPV, but it has not yet been taken into account for modelling PV device performance.

In order to understand the influence of the salt on the interfacial electronic properties of the organic layer, the chemical states and valence electronic structure in the area of the interface need to be investigated. Ideally, the concentration depth profiles of the components across the interface should also be determined to check for diffusion. There are many reports in literature which have determined changes of the electronic structure for the near surface area upon deposition of LiF onto organic interfaces materials[3, 21, 28-30 11, 31] and the LiF layer formation on various organic layers[15, 21, 29, 32-33] but none as yet have addressed the changes in electronic structure of the salt/organic layer interface upon salt deposition whilst monitoring the chemical changes with salt deposition and also determining the vertical distribution of the salt.

The aim of this work is to use the combination of ARXPS, UPS, MIES and NICISS to determine the vertical distribution of LiF deposited onto both P3HT and PCBM via vapour deposition and the valence electron structure of the surface and near surface region. P3HT and PCBM were selected due to the large number of literature reports regarding these as active materials in PV devices[13, 34-38]. Both organic materials were annealed prior to LiF deposition as the annealing process has been shown to enhance crystallinity of PCBM and overall device performance[39-43]. To understand the layer formation, the chemical states for a range of deposition thicknesses was measured with XPS. An ultrathin layer (denoted ~1Å in this work) and a thick 30Å layer were investigated via ARXPS to check for any chemical changes in the near surface area which may be facilitating the device efficiencies observed by Ahlswede[8]. The use of ARXPS in this work allows for the determination of qualitative, relative changes of the chemical states as function of the depth. A layer with an equivalent thickness of ~10Å of LiF was investigated with NICISS for determining the elemental concentration depth profile.

6.3) Experimental

6.3.1) Materials and sample preparation

Silicon wafer substrates (n-type (As Dopant), 111, 0.001-0.05 Ohm-cm) were used as a substrate and were purchased from Materials Tech International. Regioregular electronic grade (type 4002E) P3HT was obtained from Rieke Metals and PCBM (>99.9%) from Solenne BV. Reagent plus grade Orthodichlorobenzene (ODCB) was purchased from Sigma and used as the solvent for the organic material film preparation. LiF metals base >99.99% purity was obtained through Aldrich. Silicon wafers were first cleaned using Pyroneg solution obtained from Johnson Diversey, Australia. They were subsequently rinsed in deionized water, sonicated in pure ethanol, rinsed with pure ethanol and then dried with N_2. A thin Au film was sputtered onto the Si wafers used for one of the control samples. To prepare the Au samples a dual-target magnetron sputter coater (Quorumtech, Q300T-D) was used to first deposit a 2nm Cr layer onto a polished Si wafer, followed by a 50nm Au layer. Cr was used to improve adhesion between Si and Au. The thickness was monitored in situ with a quartz crystal microbalance. The sputter current for Cr it was 150mA, and for Au was 30mA.

P3HT and PCBM solutions were prepared at 1%wt and stirred for 12hrs under N_2 atmosphere prior to use. Samples were then prepared via drop casting the 1%wt solution onto the cleaned silicon wafers or Au films. These were allowed to dry in air at room temperature and then annealed on a hot plate at 140°C for 10 minutes.

LiF depositions were performed under vacuum with the Createch evaporator located in the load lock of the MIES apparatus. LiF was degassed prior to deposition, the load lock pressure during the evaporation process was in the order of 10^{-6}mbar. The evaporation temperature was set to 703°C for the single deposition measurements and set to 677°C for the sequential depositions in order to better control the layer thickness deposited. The LiF density programmed into the quartz crystal monitor (STM-100MF, Sycon Instruments) was 2.64g/cm^3. The deposition rate was found to be 1.6Å/s at 703°C and 0.8Å/s for 677$^{\circ C}$. The very low LiF exposure (~1Å) layer thickness was created by opening and closing the shutter separating the evaporator from the load lock in the shortest possible time (<1s exposure time). The two film thicknesses investigated via ARXPS (~1Å and 30Å) were deposited on separate samples, and the sequential depositions were performed on a single PCBM or P3HT sample. These LiF films deposited sequentially upon the same sample to display the evolution of the VB with increasing sequential layer thickness have been denoted (S)*. The XP spectra for the sequential depositions were obtained after the final deposition and measurement of MIES/UPS on each respective sample. 30Å of LiF was deposited onto a Si wafer and a sputtered Au film to provide control spectra for the electron spectroscopy measurements.

6.3.2) Methods

Experimental details for the *in situ* NICISS and electron spectroscopy apparatus (XPS, UPS, MIES) can be found in Chapter 2. For the ARXPS experiments in this work the photoemission angle was varied from 0 ~ 60^0 by rotating the sample stage with respect to the analyzer. The ARXPS experiments were performed in such a manner that changes in the interfaces with time would not be convoluted with changes in angle. Initially the standard 0^0 with respect to the analyzer was measured, followed by the most surface sensitive angle (60^0), then 45^0, 50^0 and 55^0 respectively.

6.3.3) Analysis

Standard analysis procedures as described in Chapter 2 were used for analysis of XPS, UPS, MIES and NICISS. For UPS and MIES the SVD algorithm also described in Chapter 2 was used for the analysis of the sequential VB spectral sets. The SVD was performed only up to 13eV in binding energy as higher energies include parts of the secondary electron peak in many of the spectra.

All XP spectra were calibrated to the primary C1s peak location of 285eV, which is that of the alkyl bonds present in both the thiophene and fullerene rings[41, 44-45]. For fitting the high resolution spectra of C1s, O1s and S2p$_{3/2}$ on the LiF modified samples, the component peak positions and the FWHM were locked to those corresponding to the polymer or fullerene control sample. All intensity errors which were found to be <0.1% of the photoelectron peak were rounded up to 0.1%. Intensity error for the components within the photoelectron peaks was estimated by maximizing the difference in plausible fit for each component and is given as a percentage of the component in question.

6.4) Results and Discussion

Results are discussed initially per technique in the order of XPS (section 6.4.1), ARXPS (section 6.4.2), UPS and MIES (section 6.4.3), and NICISS (section 6.4.4). In these sections there is a discussion of general results at that particular depth into the surface. A further discussion regarding the total outcome of the combined results follows in section 6.4.5.

6.4.1) XPS

The XPS results are presented initially for the pristine organic films (section 6.4.1.1), then followed by the LiF modified films (section 6.4.1.2).

6.4.1.1) Pristine film analysis

The chemical composition and binding energies for both pristine films are shown in Table 6.1(a) for PCBM and Table 6.1(b) for P3HT, along with the elemental component breakdown and references to the literature for peak assignment. Example peaks and component fits for the organic materials can be seen in Figures 6.1 and 6.2. The peak positions for the neat films were found to correspond to the literature.

PCBM			Total Element Intensity (%)		Component Intensity (%)	
Component	**Posn (eV)**	**Attribution**	**At 0^0**	**At 60^0**	**At 0^0**	**At 60^0**
		Richter[46] Belay[47]				
C1s (1)	285.0	Fullerene cage C=C	94.9 ± 0.5	93.7 ± 0.6	78.1 ± 0.4	73.3± 0.4
C1s (2)	285.8	Fullerene, side chain C-C	-	-	8.4 ± 0.2	13.0± 0.2
C1s (3)	286.9	Ester C-O	-	-	4.6 ± 0.2	5.7± 0.2
C1s (4)	289	Ester C(O)O	-	-	3.8 ± 0.2	3.7± 0.2
C1s (5)	290.9	π- π*	-	-	5.1 ± 0.4	4.3± 0.4
O1s (1)	532.3	Ester C-O-C	5.1 ± 0.1	6.3 ± 0.1	39.5 ± 0.5	42.6± 0.5
O1s (2)	533.5	Ester C=O	-	-	60.5 ± 0.5	57.4± 0.5

Table 6.1(a): Elemental component ratios for neat PCBM. The total element intensity is given as a percentage of the total measured composition. The component breakdown for each element is also given as a separate percentage which pertains only to the element in question (component intensity, where the component intensity sum for each element is 100%).

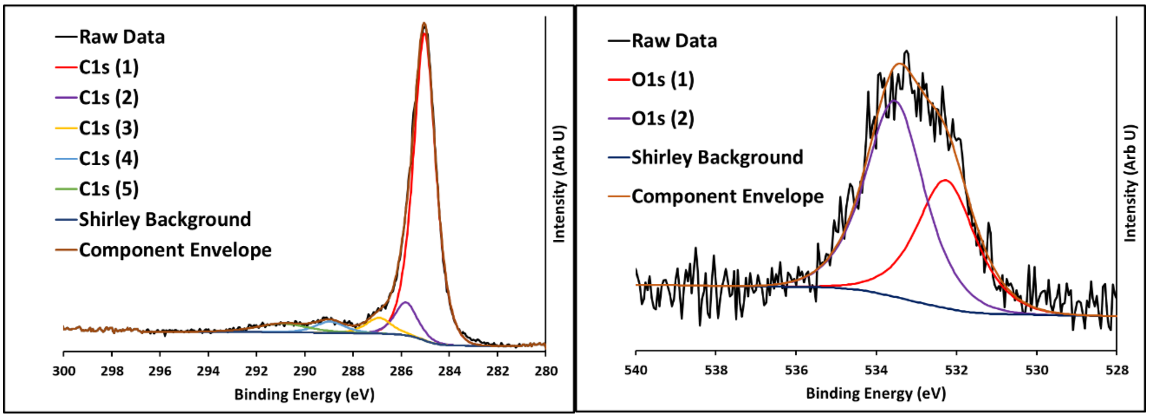

Figure 6.1: Example XP spectra from Table 6.1(a) showing components of PCBM in C1s (left) and O1s (right) spectra. The same components were observed at both measured angles.

P3HT			**Total Element Intensity (%)**		**Component Intensity (%)**	
Component	**Posn (eV)**	**Attribution**	**At 0^0**	**At 60^0**	**At 0^0**	**At 60^0**
		Jenkins[48]				
C1s (1)	285.0	Alkyl, neutral aromatic	86.0 ± 0.6	85.4 ± 0.7	95.5 ± 0.9	95.1 ± 0.9
C1s (2)	287.3	Oxidized Thiophene	-	-	2.8 ± 0.2	2.8 ±0.2
C1s (3)	288.3	Oxidized Thiophene	-	-	1.8 ± 0.2	2.1 ±0.2
$S2p_{3/2}$ (1)	164.0	Neutral aromatic	10.9 ± 0.2	10.4 ± 0.1	95.9 ± 1.3	94.8 ± 1.3
$S2p_{3/2}$ (2)	164.9	Oxidized Thiophene	-	-	4.1 ± 0.8	5.2 ± 0.8
O1s	532.5		3.1 ± 0.1	4.2 ± 0.1	-	-

Table 6.1(b): Elemental component ratios for neat P3HT. The total element intensity is given as a percentage of the total measured composition. The component breakdown for each element is also given as a separate percentage which pertains only to the element in question (component intensity, where the component intensity sum for each element is 100%).

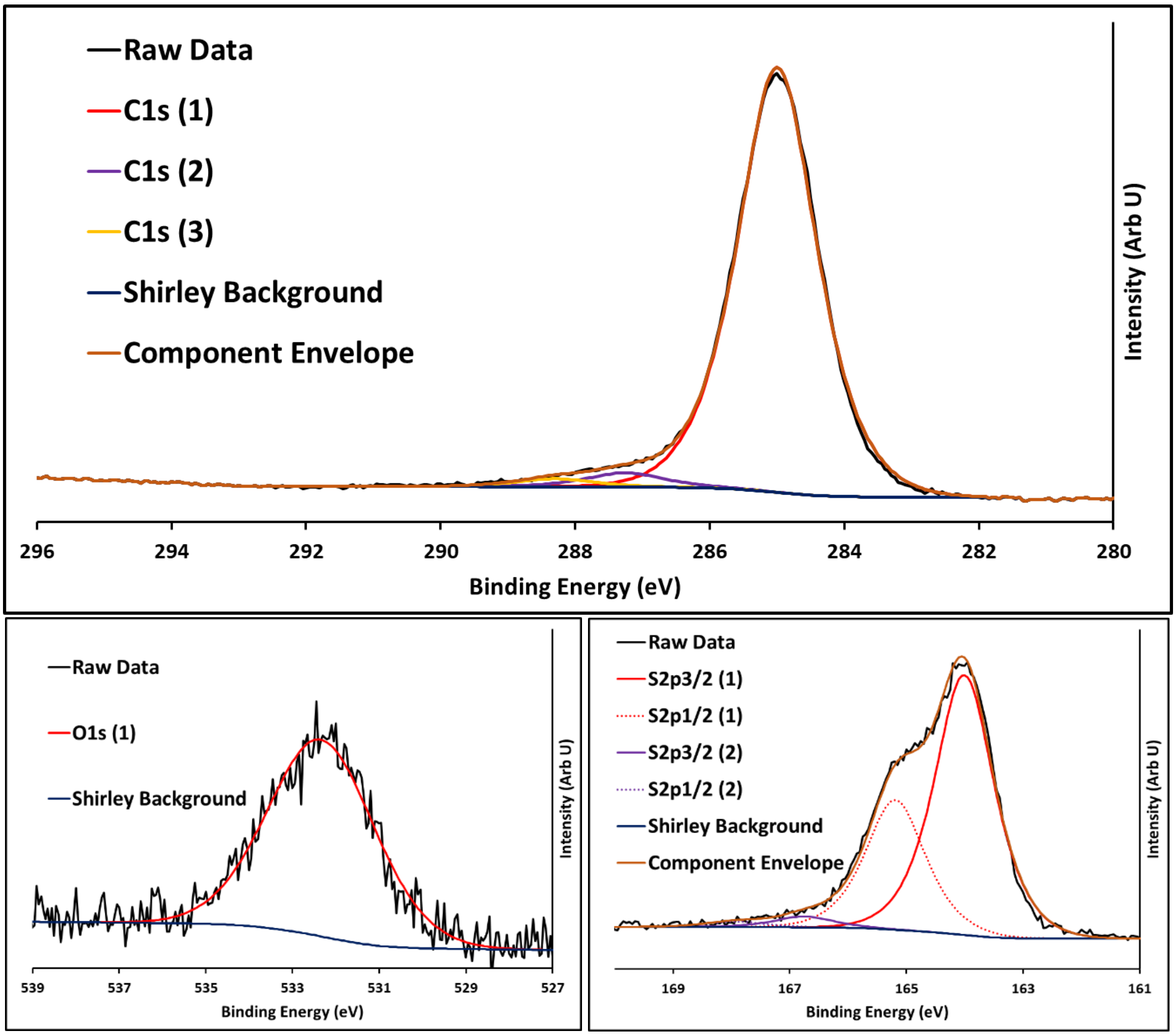

Figure 6.2: Example XP spectra from Table 6.1(b) showing components of P3HT in C1s (top) and O1s (bottom left) and S2p (bottom right) spectra. The S2p spectrum shows both the S2p3/2 and S2p1/2 states however only the S2p3/2 state is given in Table 6.1(b) such that a more accurate peak position could be described. Calculations of the intensity in Table 6.1(b) takes this into account. The same components were observed at both measured angles.

PCBM and P3HT films were both found to be oxidized. Excess oxygen was found in PCBM, with a C:O of 18:1, with the extra oxygen suspected as being present on the fullerene cage due to the reduced presence of the π shakeup peak as compared to unoxidized PCBM in the literature[46], oxidation of the fullerene cage is known to affect the π bonds[49]. Unoxidized PCBM (chemical formula $C_{72}H_{14}O_{2,}$) is 36:1. Unoxidized P3HT has no oxygen content (chemical formula $(C_{10}H_{14}S)_n$). Oxidation of films prepared in air has been seen previously[50-51]. No other contamination was observed. Oxidation of P3HT has been shown to induce the presence of polarons and bipolarons which appear as a high binding energy shoulder to the main S2p$_{3/2}$ peak[48, 52-53] with corresponding peaks in the C1s spectrum. The higher binding energy peaks were observed in this work (denoted C1s(3) and S2p$_{3/2}$(2) in Table 6.1(b)).

The pristine films were also analyzed at 60^0 with respect to the analyzer to check for any changes toward the surface (Table 6.1(a) and (b)). PCBM had an increase in oxygen content by 1.2% toward the surface. A 5% decrease in the primary C1s component and corresponding increase in the secondary component was also observed. This change in intensities is attributed to the more oxidized fullerene cage toward the surface of the film which increases the strain on the bonds in the near surface area. The slight reduction in conjugated π- π* states toward the surface also indicates this could be the case. P3HT had an overall increase in oxygen content toward the surface by 1.1%, and there was no difference within error observed for the C1s or $S2p_{3/2}$ components.

6.4.1.2) LiF modified film analysis for films investigated at 0^0 with respect to the analyzer

The LiF control samples revealed that no contaminant species (including water) were being deposited with the salt. This is critical as effects from contaminant species have been noted before in the literature and have a significant impact on the interfacial energy levels[54-55]. Analysis of LiF/Si revealed a single peak for both Li1s and F1s. Interestingly, the stoichiometry showed an Li:F of 0.6:1 rather than 1.1. This cannot be attributed to the differences in kinetic energy of the photoelectrons as Li1s is at the higher kinetic energy, thus sampling the greater film depth[56] and should show the opposite trend to that seen in this work. The stoichiometry was not able to be verified through other photoelectron peaks as there are no other peaks for lithium.

To verify the deposited salt was indeed LiF the peak to peak distance Δ(F1s – Li1s) was measured. Measuring the peak to peak distance of the core levels is a reliable method for chemical species identification[9, 57]. In literature Δ(F1s – Li1s) for bulk LiF is known to be 629.2eV[3, 9, 58]. On the Si control sample in this work it was found to be 629.3eV. As such, the issue with stoichiometry is attributed to the transmission function of the apparatus, and possibly due to differences in the inelastic mean free path. For the LiF/Au control an accurate peak position and intensity for Li1s was unable to be determined due to the presence of the Au5p3/2 peak at 57.0eV, the peak position for F1s was found to be 686.3eV.

Peak positions and binding energies for the LiF modified organic samples are shown in Table 6.2, and example spectra for Li1s and F1s are shown in Figure 6.3.

	C		Si		O		F		Li	
Sample	**Posn**	**%**	**Posn**	**%**	**Posn**	**%**	**Posn**	**%**	**Posn**	**%**
Si	286.3	1.9 ±0.1	(Si) 99.6	13.7 ±0.2	533.0	5.8 ±0.1	687.1	50.0 ±0.2	57.8	28.6 ±1.2
PCBM	285.0	94.9 ±0.5	-	-	532.3	5.1 ±0.1	-	-	-	-
~1Å	285.0	89.7 ±0.4	-	-	532.3	5.7 ±0.1	685.1	2.0 ±0.1	56.1	1.6 ±0.4
~3Å	285.0	87.8 ±0.5	-	-	532.3	7.0 ±0.1	685.0	3.0 ±0.1	56.0	2.2 ±0.4
16Å(S)*	285.0	40.3 ±0.3	-	-	532.3	2.0 ±0.1	686.1	37.4 ±0.2	56.8	20.3 ±1.1
30Å	285.0	22.3 ±0.2	-	-	532.3	1.1 ±0.1	686.2	48.9 ±0.2	57.0	27.7 ±1.0
P3HT	285.0	86.0 ±0.6	164.0	10.9 ±0.2	532.5	3.1 ±0.1	-	-	-	-
~1Å	285.0	84.8 ±0.7	164.0	10.6 ±0.2	532.5	1.8 ±0.1	685.3	2.0 ±0.1	56.3	0.8 ±0.3
~3Å	285.0	79.8 ±0.6	164.0	9.8 ±0.2	532.6	2.0 ±0.1	685.4	5.3 ±0.1	56.3	3.1 ±0.5
16Å(S)*	285.0	36.1 ±0.3	164.0	4.7 ±0.1	532.7	0.6 ±0.1	686.0	36.7 ±0.2	56.7	21.9 ±1.0
30Å	285.0	20.0 ±0.2	164.0	2.7 ±0.1	532.7	0.6 ±0.1	686.3	48.0 ±0.2	56.9	28.7 ±1.0

Table 6.2: Chemical composition as a percentage of the total composition, and primary peak positions for LiF on Si, PCBM and P3HT. Errors shown are for the peak intensity. Position in eV.

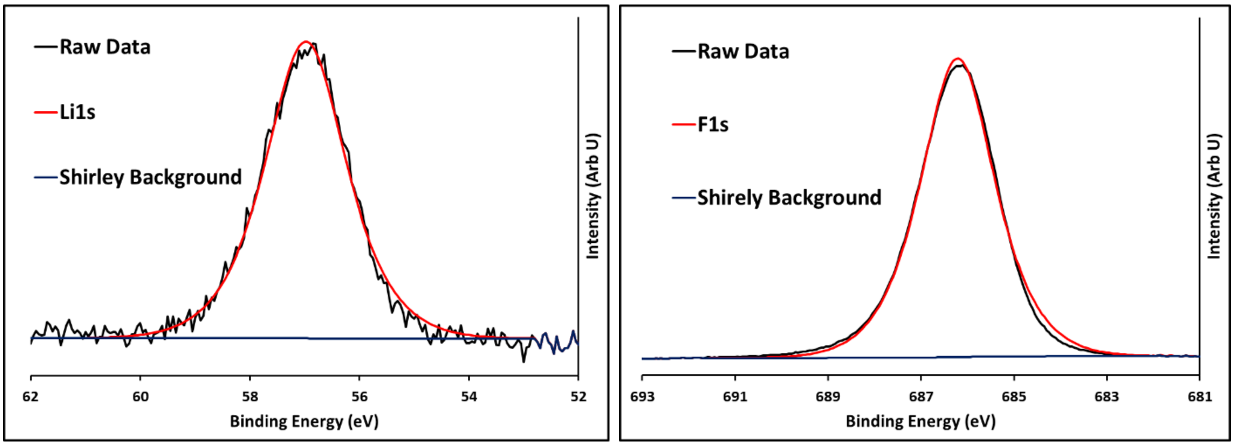

Figure 6.3: Example Li1s (left) and F1s (right) spectra for the deposited salt on the organic materials. All samples were found to have a single component for Li1s and F1s. Example shown is from 30Å LiF/PCBM.

LiF depositions on PCBM revealed a single component peak for Li1s and F1s (Table 6.2), with FWHM of 2.0eV for both elements for the thin layers and 1.8eV for the 30Å sample. No significant changes in C1s or O1s were observed at 0^0 with respect to the analyzer for the thin LiF layer samples, but for the 30Å sample the component intensity ratio was seen to change in a similar manner to that observed when investigating the pristine PCBM film at 60^0 with respect to the analyzer. This was attributed to two factors, the thick layer of LiF reducing the XPS probing depth of the PCBM and thus only measuring the more oxidized surface states, and also the presence of the salt inducing a charge distribution rearrangement within the oxidized PCBM. This will be further discussed in the ARXPS results. The π- states from the fullerene were preserved across the deposition range which has been seen previously for LiF on C_{60}[3]. Note that the increased oxygen observed for some of the LiF/PCBM samples (compared to the control PCBM spectrum) seen in Table 6.2 is due to variation in oxidation of each PCBM film prior to deposition, the total oxygen content for each PCBM sample decreased upon LiF deposition. The peak to peak distance Δ(F1s – Li1s) for all deposition thicknesses was seen to be the same within 0.3eV, indicating that the LiF was not dissociated. Likewise, the Li:F intensity ratio was consistent with both the deposition thickness and deposition method within error.

LiF depositions on P3HT also revealed a single peak for both Li1s and F1s with FWHM of 1.7eV and 1.8eV respectively. The O1s binding energy was seen to increase slightly with deposition thickness (Table 6.2), and an extra high binding energy shoulder was observed in $S2p_{3/2}$. This is again attributed to a charge distribution rearrangement like that seen for the oxygen in PCBM and will be further discussed in the ARXPS results. Peak to peak separations for Δ(F1s – Li1s) and Li:F were found to be consistent within error.

The Li1s and F1s peak positions were seen to increase in binding energy with increasing LiF layer thickness on both organic materials, and were at an even higher binding energy on the LiF/Si control sample. This can be attributed to an interfacial dipole occurring between the organic layer (or Si) and salt layer. Interfacial dipole formation on small organic molecules is not uncommon and has been documented previously with thin LiF layers[3, 20, 54]. The binding energy shift is positive with increasing layer thickness. This indicates that the side of this dipole pointing toward the outermost layer/vacuum interface is becoming more positive with thicker depositions. As the peak positions are higher on Si than the organics it can be deduced that this effect is more pronounced on the Si substrate than the organic layers. The Li1s peak on P3HT is slightly less shifted with increasing LiF thickness when compared to LiF/PCBM. This indicates that the dipole may be slightly less positive toward the outermost layer on P3HT. The Li1s and F1s peak positions for the sequential depositions follow the same trend as that for the increasing thickness single depositions. As such it can be concluded that the different deposition methods induce the same dipole orientation on the organic layers. It is worth noting at this point that the LiF dipole orientation or strength cannot be assumed to be equivalent on different organic materials. Reports in the literature observe the Li1s and F1s core level positions across a range of binding energies and as one example were reported at 55.6eV and 684.9eV respectively for 1.5nm LiF/Alq[9]. It is also worth noting that the lack of contamination observed in the XP spectra indicates that the dipole formation is indeed due to the LiF surface order (the separation of positive and negative charges in a specific way on the surface structure) on the substrates and not attributed to water which has been seen previously for LiF on metal substrates[54].

6.4.2) ARXPS: Chemical States with Depth

Angle resolved investigations of both the ~1Å and 30Å LiF/PCBM samples revealed the same chemical changes. As such, values will only be shown for the 30Å LiF/PCBM as no information is gained from the thin deposition other than to note that the changes do not differ with LiF thickness. For 30Å LiF/PCBM a single component was observed for both Li1s and F1s, each with a FWHM of 1.8eV and no change in FWHM with angle. New components in O1s pertaining to the organic film were observed at 531.1eV and 534.8eV. Details are shown in Table 6.3 and an example spectrum is shown in Figure 6.4.

30Å LiF/ PCBM			**Component Intensity with Angle (%)**					
Peak	**Component**	**Position (eV)**	**0^0**	**30^0**	**45^0**	**50^0**	**55^0**	**60^0**
O1s	**O1s(3)**	531.1	4.1 ±1.4	10.0 ±1.1	13.8 ±1.1	14.8 ±1.1	13.0 ±1.1	16.3 ±1.1
	O1s(1)	532.3	29.2 ±1.5	34.3 ±1.6	30.3 ±1.5	33.9 ±1.5	35.8 ±1.6	39.3 ±1.5
	O1s(2)	533.5	55.6 ±1.3	45.4 ±1.3	41.4 ±1.3	37.4 ±1.4	36.9 ±1.4	34.4 ±1.4
	O1s(4)	534.8	14.1 ±1.5	10.3 ±1.4	14.5 ±1.5	13.9 ±1.5	14.2 ±1.5	10.0 ±1.4
C1s	**C1s(1)**	285.0	73.4 ±0.5	74.9 ±0.5	70.5 ±0.5	71.3 ±0.5	67.7 ±0.5	71.1 ±0.5
	C1s(2)	285.8	14.1 ±0.2	14.0 ±0.2	17.7 ±0.2	19.4 ±0.2	22.3 ±0.3	18.4 ±0.2
	C1s(3)	286.9	4.9 ±0.2	2.7 ±0.2	4.0 ±0.2	3.1 ±0.2	3.8 ±0.2	3.9 ±0.2
	C1s(4)	289.0	3.1 ±0.3	3.6 ±0.3	3.1 ±0.3	2.9 ±0.3	2.6 ±0.3	2.9 ±0.3
	C1s(5)	290.9	4.5 ±0.4	4.7 ±0.4	4.7 ±0.4	3.3 ±0.3	3.6 ±0.4	3.6 ±0.4

Table 6.3: O1s and C1s component intensity ratios for 30Å LiF/PCBM, where the total component intensity per element is 100%.

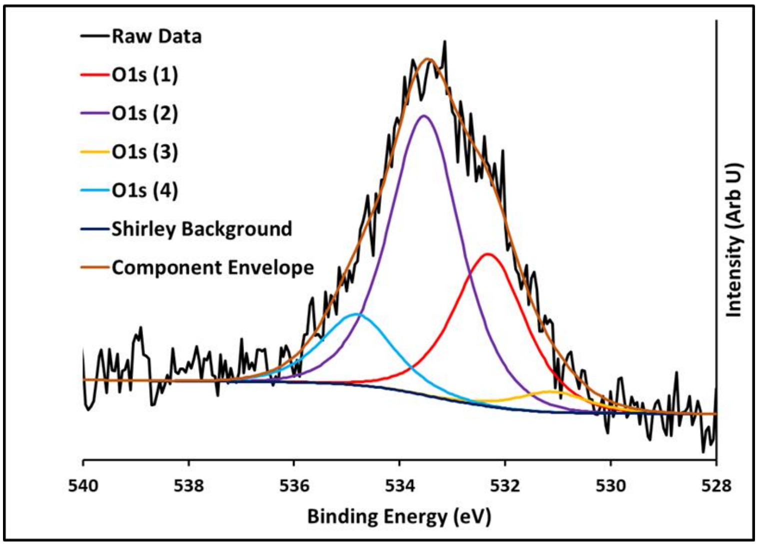

Figure 6.4: Example O1s spectrum for LiF on PCBM showing new oxygen components O1s(3) and O1s(4).

These new O1s components indicate some level of interaction between the PCBM and LiF. However, we do not attribute the observed changes in oxygen to bond formation between the PCBM and salt[59], as no new states were observed in Li1s or F1s. A high binding energy shoulder has been observed on PCBM when exposed to water[60], however, as no water has been detected in the control depositions the 534.8eV peak O1s(4) has been attributed to oxygen species from the PCBM protruding into the positive part of the organic/salt interfacial dipole. For the 531.1eV peak O1s(3), it is proposed that the presence and orientation of the LiF around the oxidized PCBM molecule is inducing a transfer of charge distribution across the functional groups within the organic material, primarily through the oxygen rather than the fullerene cage. No new components were observed in C1s however the component ratios were affected by the changes in oxygen as a secondary effect.

~1Å LiF/ P3HT			**Component Intensity with Angle (%)**					
Peak		**Posn (eV)**	**0^0**	**30^0**	**45^0**	**50^0**	**55^0**	**60^0**
C1s	**C1s(1)**	285.0	96.2 ±0.6	95.6 ±0.6	95.9 ±0.6	95.8 ±0.6	95.9 ±0.6	95.8 ±0.6
	C1s(2)	287.3	2.6 ±0.1	2.9 ±0.1	2.7 ±0.1	2.8 ±0.1	2.5 ±0.1	2.4 ±0.1
	C1s(3)	288.3	1.2 ±0.1	1.5 ±0.1	1.4 ±0.1	1.4 ±0.1	1.7 ±0.1	1.8 ±0.1
$S2p_{3/2}$	**$S2p_{3/2}$ (1)**	164.0	92.6 ±0.2	94.0 ±0.2	93.5 ±0.2	93.3 ±0.2	93.1 ±0.2	93.2 ±0.2
	$S2p_{3/2}$ (2)	164.9	4.0 ±0.1	4.9 ±0.1	5.5 ±0.1	5.0 ±0.1	5.2 ±0.1	5.2 ±0.1
	$S2p_{3/2}$ (3)	166.8	3.4 ±0.1	1.1 ±0.1	1.1 ± 0.1	1.7 ±0.1	1.7 ±0.1	1.6 ±0.1

Table 6.4(a): C1s and $S2p_{3/2}$ component intensity ratios angle for ~1Å LiF/P3HT. Total component intensity per element is 100%. Oxygen not included as it has only a single component which does not shift.

30Å LiF/ P3HT			**Component Intensity with Angle (%)**					
Peak		**Posn (eV)**	**0^0**	**30^0**	**45^0**	**50^0**	**55^0**	**60^0**
C1s	**C1s(1)**	285.0	95.7 ±0.6	95.1 ±0.6	95.1 ±0.6	95.3 ±0.6	94.8 ±0.6	96.0 ±0.6
	C1s(2)	287.3	3.4 ±0.1	4.0 ±0.1	4.9 ±0.2	4.7 ±0.2	5.2 ±0.2	4.0 ±0.1
	C1s(3)	288.3	0.9 ±0.1	0.9 ±0.1	0.0	0.0	0.0	0.0
S2p$_{3/2}$	**S2p$_{3/2}$ (1)**	164.0	93.1 ±0.2	92.4 ±0.2	88.7 ±0.2	97.9 ±0.2	98.2 ±0.2	99.1 ±0.2
	S2p$_{3/2}$ (2)	164.9	4.1 ±0.1	4.8 ±0.1	8.6 ±0.1	0.0	0.0	0.0
	S2p$_{3/2}$ (3)	166.8	2.9 ±0.1	2.7 ±0.1	2.7 ±0.1	2.1 ±0.1	1.8 ±0.1	0.9 ±0.1
O1s	**Single**	Shifts (eV)	532.7	532.6	532.5	532.4	532.3	531.9

Table 6.4(b): C1s and S2p$_{3/2}$ component intensity ratios, and O1s peak position with angle for 30Å LiF/P3HT. Total component intensity per element is 100%.

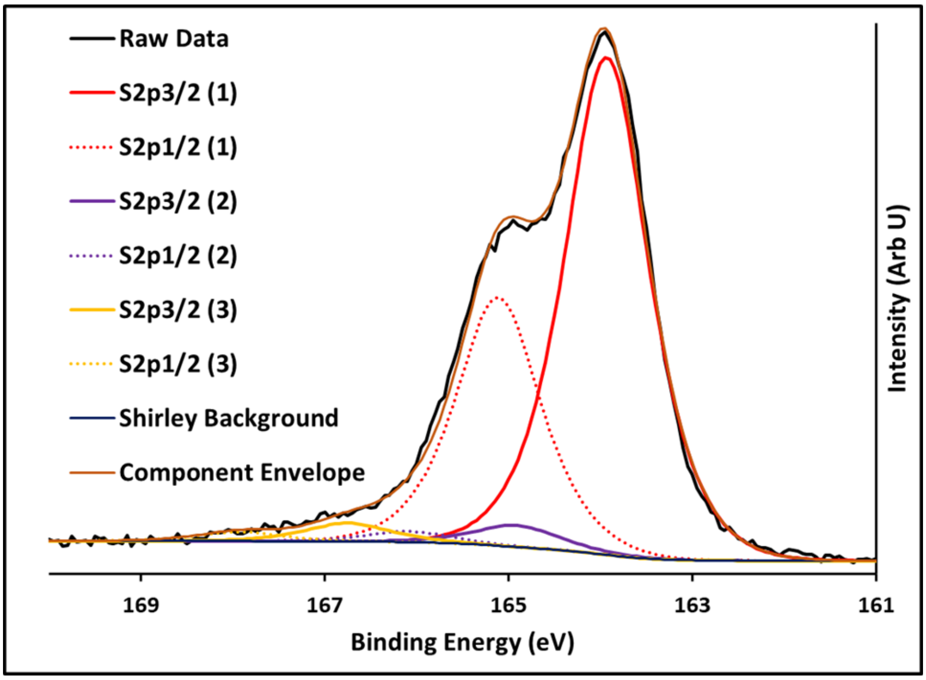

Figure 6.5: Example S2p spectrum for LiF on P3HT showing the new sulfur component S2p(3). Just like Figure 6.2, the S2p spectrum shows both the S2p3/2 and S2p1/2 states, however only the S2p3/2 state is given in the relevant tables such that a more accurate peak position could be described. Calculations of the element intensity takes this into account.

Angle resolved investigations of LiF/P3HT also revealed a single component for Li1s and F1s. There were some differences observed with different deposition thicknesses of LiF. An extra high binding energy component in $S2p_{3/2}$ was observed for all deposition thicknesses at 166.8eV and is denoted $S2p_{3/2}(3)$, see Table 6.4(a) and Table 6.4(b), and Figure 6.5. This component has been interpreted as some of the sulfur in the thiophene unit protruding into the positive region of the dipole. The C1s(3) and $S2p_{3/2}(2)$ components are both seen to slightly increase with increasing angle. This is attributed to the oxidation of the P3HT film which is higher toward the surface of the film.

For 30Å of LiF/P3HT the O1s state was shifted to a lower binding energy toward the surface although the total oxygen contribution did not change with angle. The change in peak position is shown in Table 6.4(b). This has been attributed to the LiF inducing a redistribution of charge through the functional groups through the oxygen which can then be observed once sufficient LiF is deposited. It was also seen that for this sample the high binding energy components of the organic film: C1s(3) and $S2p_{3/2}(2)$ decreased with increasing analysis angle and were not observed at the more surface sensitive angles of 50^0-60^0. These two states pertain to the oxidized thiophene unit so the changes in intensity here are related to the changes observed in the oxygen binding energy and believed to be nearest neighbor effects from the oxygen. The $S2p_{3/2}(3)$ component is still seen at 60^0 however although it is less than observed for the thin ~1Å LiF deposition. This indicates that some of the sulfur is still protruding into the positive region of the dipole with the thicker LiF deposition.

In summary the chemical information gained from the investigation of these films indicates that the pristine organic films are more oxidized toward the surface. When LiF is deposited it appears to remain intact as there is only a single component for both Li1s and F1s on all samples and the peak to peak distance Δ(F1s – Li1s) remains close to that of bulk LiF. An interfacial dipole between the organic layer and the salt has been proposed as the reason for the changes in the Li1s and F1s peak positions with different deposition thicknesses. High binding energy components were observed in the oxygen of PCBM and in the sulfur of P3HT. These states are attributed to the respective components of the organic film protruding into the positive region of the interfacial dipole. There also appears to be a redistribution of charge through the functional groups through the oxygen of both films, which has been induced by the presence and orientation of the salt on the surface. For PCBM the effects are observed for both LiF deposition thicknesses. For P3HT the redistribution of charge through the functional groups is only observed for the thicker LiF deposition.

6.4.3) MIES/ UPS

MIES/UPS results will begin with the pristine organic films and LiF control films (section 6.4.3.1). The LiF modified organic films will then be shown (section 6.4.3.2) beginning with the SVD results (section 6.4.3.2.1) then a comparison of the differences between the sequential vs. single LiF deposition method (section 6.4.3.2.2).

6.4.3.1) Pristine film analysis

The VB structure for P3HT and PCBM can be seen in Figures 6.8-6.11, with features in agreement to the literature[37, 51, 61-64]. The LiF control spectra may be seen along with the SVD results of the LiF/organic sequential depositions in Figures 6.6 and 6.7. The control LiF films on Au and Si revealed DOS which were found to agree with the literature for LiF. The VB of LiF has been studied experimentally and theoretically and it is known that the observed DOS pertain almost exclusively to the high cross section F2p orbitals[58, 65-66,67]. These F2p orbitals are located at 9.5eV for a LiF crystal[65, 67-69] but can vary in position depending on the nature of the surface. As an extra note it has been observed by Morgner *et.al* that the difference in peak position for MIES and UPS of the F2p states for a LiF crystal is 1.5eV[70]. For this work we observe a difference in peak position of 0.8~1.5eV depending on the substrate and nature of the deposition method. This is due to differences in the de-excitation mechanism of the metastable He* occurring on the various surfaces measured here.

6.4.3.2) LiF modified film analysis

The SVD algorithm was performed on each spectral set of the sequential depositions on the organic films. This was done to verify that there were no subtle changes in chemical states in the near surface area and outermost layer that were undetectable with XPS. Only two base spectra were found for the sequential depositions on both organic films. Naturally, one of these base spectra pertained to the organic film, thus the other clearly must be due to electronic states from the salt. The DOS of the reconstructed spectra pertaining to the salt are shown along with the LiF/Au and LiF/Si control depositions in Figures 6.6 and 6.7. The MIE and UP spectra for the full set of sequential depositions on each organic film are then shown in Figures 6.8-6.11. The 30Å LiF deposition thickness also shown in Figures 6.8-6.11 was deposited as a single thick layer and is physically the same sample as that analyzed in the XPS data.

6.4.3.2.1) SVD:

As well as deconvoluting the VB spectrum of LiF from each organic layer, the SVD algorithm reveals the surface coverage of LiF via the weighting factors for each base spectrum in MIES. Incomplete surface coverage was found for 16Å LiF deposition on both PCBM and P3HT. For LiF/PCBM, 27.5% of the spectrum was attributed to PCBM DOS, and for LiF/ P3HT it was 16.7% P3HT DOS. The weighting factors for the SVD of the UP spectra reveal the composition ratio of the near surface area. For LiF/PCBM the near surface area was 12.2% PCBM and for LiF/P3HT it was 7.6% P3HT. The full set of data for MIES and UPS SVD weighting factors for each layer thickness is given as a percentage of organic DOS present in the spectra in Table 6.5. As there are only two components in each spectrum the remaining quotient is comprised of LiF DOS.

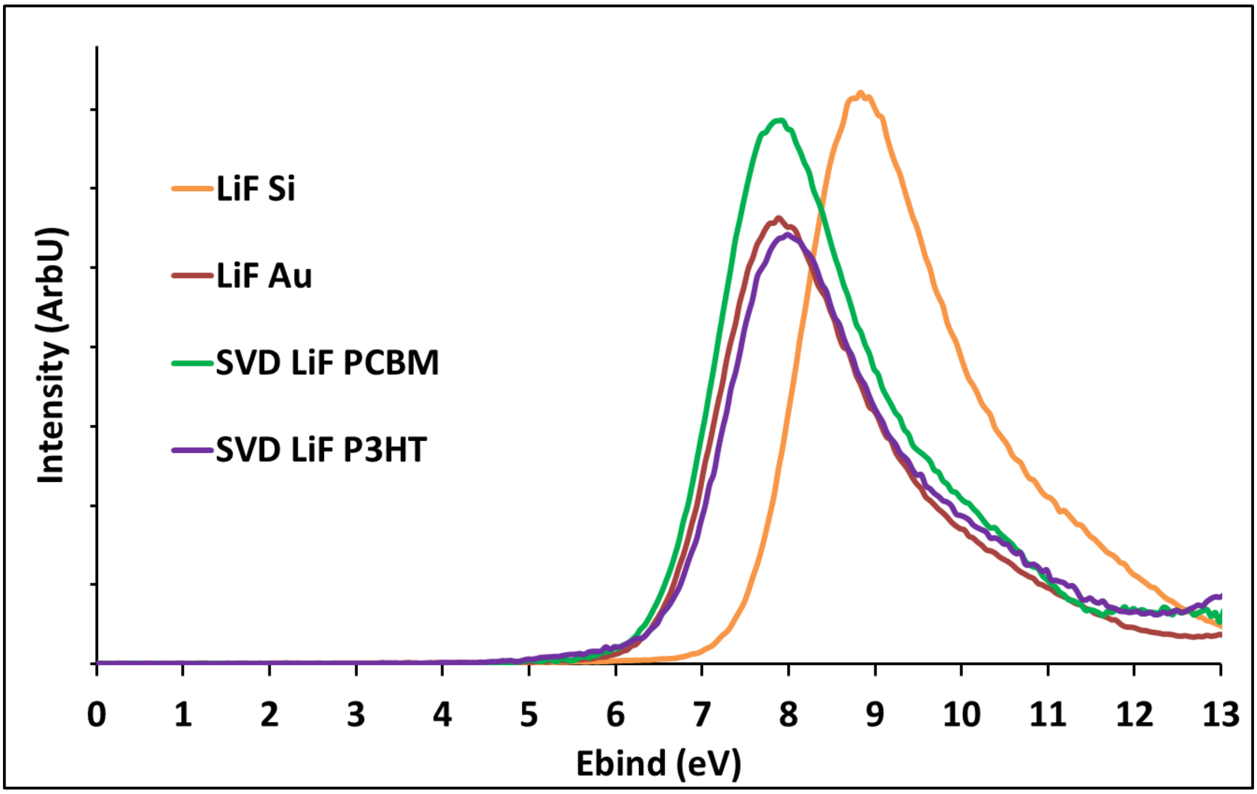

Figure 6.6: MIES of control samples: LiF/Au, LiF/Si, and the LiF reference spectra from the SVD analysis of the sequential depositions for LiF/PCBM and LiF/P3HT.

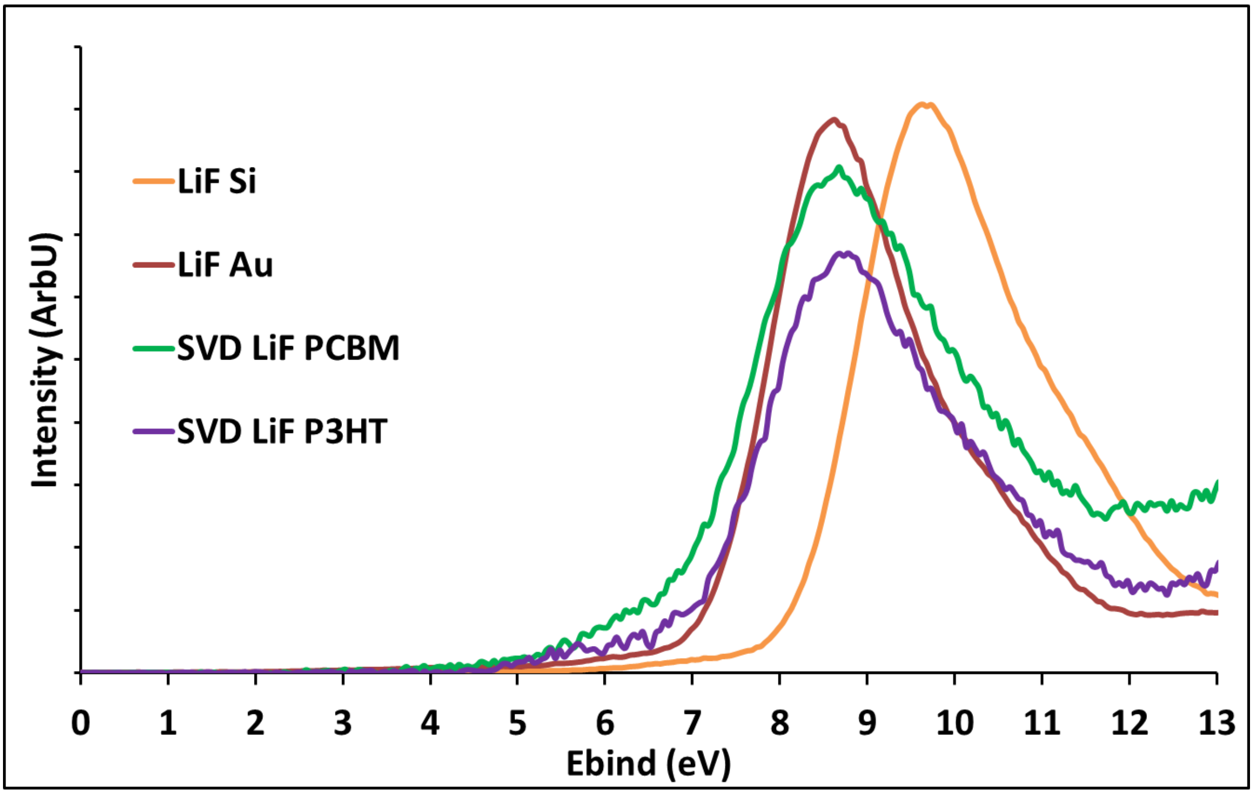

Figure 6.7: UPS of control samples LiF/Au, LiF/Si, and the LiF reference spectra from the SVD analysis of the sequential depositions for LiF/PCBM and LiF/P3HT.

% Organic layer DOS present in VB spectra with increasing thicknesses (Å) of LiF

MIES	**Neat**	**0.8Å**	**1.6Å**	**2.4Å**	**3.2Å**	**4.8Å**	**6.4Å**	**8.0Å**	**12Å**	**16Å**
PCBM	100	90.0	82.8	76.5	73.0	60.0	53.7	47.6	33.6	27.5
P3HT	100	90.3	83.2	77.9	74.5	61.7	54.2	46.3	29.7	16.7
UPS	**Neat**	**0.8Å**	**1.6Å**	**2.4Å**	**3.2Å**	**4.8Å**	**6.4Å**	**8.0Å**	**12Å**	**16**
PCBM	100	99.2	96.0	92.6	90.7	80.8	74.2	65.4	39.1	12.2
P3HT	100	96.9	94.5	91.4	88.6	78.6	70.7	60.9	34.8	7.6

Table 6.5: Weighting factor ratios for the SVD analysis of LiF on PCBM and P3HT, given as a percentage of organic DOS. Remaining percentage is LiF.

Jönnson *et.al* have claimed that ~10Å of LiF is sufficient to form roughly a monolayer on organic materials[3]. If this holds for PCBM and P3HT surfaces then the observation that an incomplete salt layer is observed via MIES for a 16Å LiF deposition indicates that either island type structures are formed on the surface, or that sections of the LiF have diffused into deeper layers leaving patches of the organic film at the outermost layer.

6.4.3.2.2) Sequential depositions compared to a single thick deposition

For the sequential depositions (Figures 6.8-6.11) a strong feature evolves with deposition at ~8eV in MIES and ~9eV in UPS. The DOS in both MIES and UPS are almost identical in structure to both of the LiF control spectra, and due to the results of the SVD the feature has been attributed to the F2p states. Upon inspection, the UP spectra have a larger range of occupied DOS (7~12eV) than the MIE spectra (6.5~10.5eV). This has been attributed in the literature to UPS probing DOS from all the F2p orbitals whereas MIES only sampled those facing the surface, claimed to be the F2pz[69]. It is worth noting that the metallic Li states ~2eV seen in other works[58, 69] are not present, verifying that no dissociation of the molecule is occurring, even at the outermost layer. There is no shift in the organic HOMO with LiF deposition on either organic material. Shifts in the HOMO are seen by changes in the low binding energy cutoff point. This is located at 1.4eV for UPS of LiF/PCBM and 0.5eV for UPS of LiF/P3HT. There is a gradual decrease in intensity at these binding energies with increasing deposition thickness, however the VB low binding energy cutoff does not shift. Thus it can be deduced that the decrease in intensity is due to the increasing presence of the salt and decreasing presence of the organic compound rather than the LiF altering the organic component.

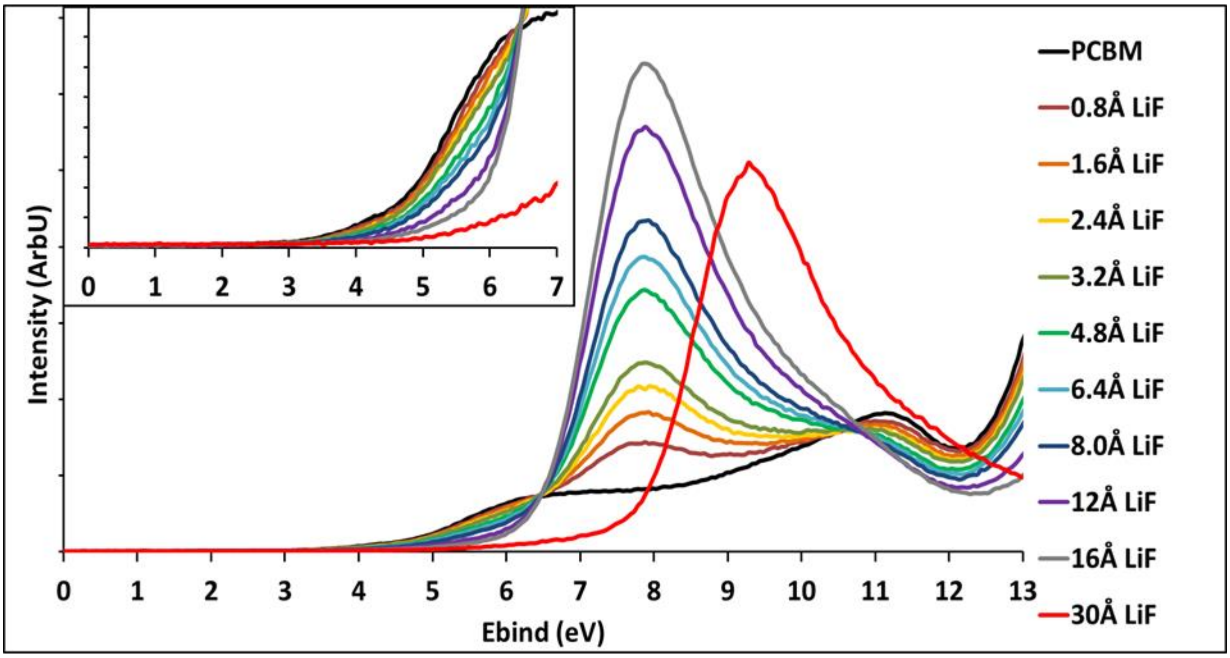

Figure 6.8: MIES of sequential LiF depositions on PCBM, with MIES of the single 30Å LiF/PCBM sample (in red) for comparison.

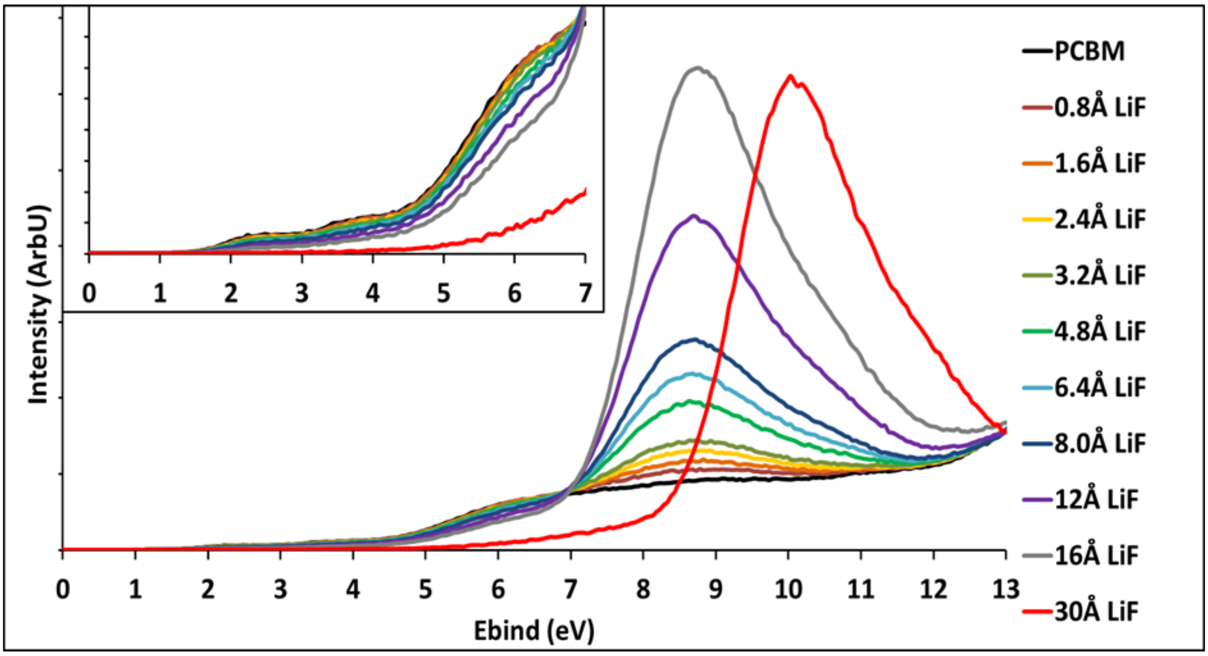

Figure 6.9: UPS of sequential LiF depositions on PCBM, with UPS of the single 30Å LiF/PCBM sample (in red) for comparison.

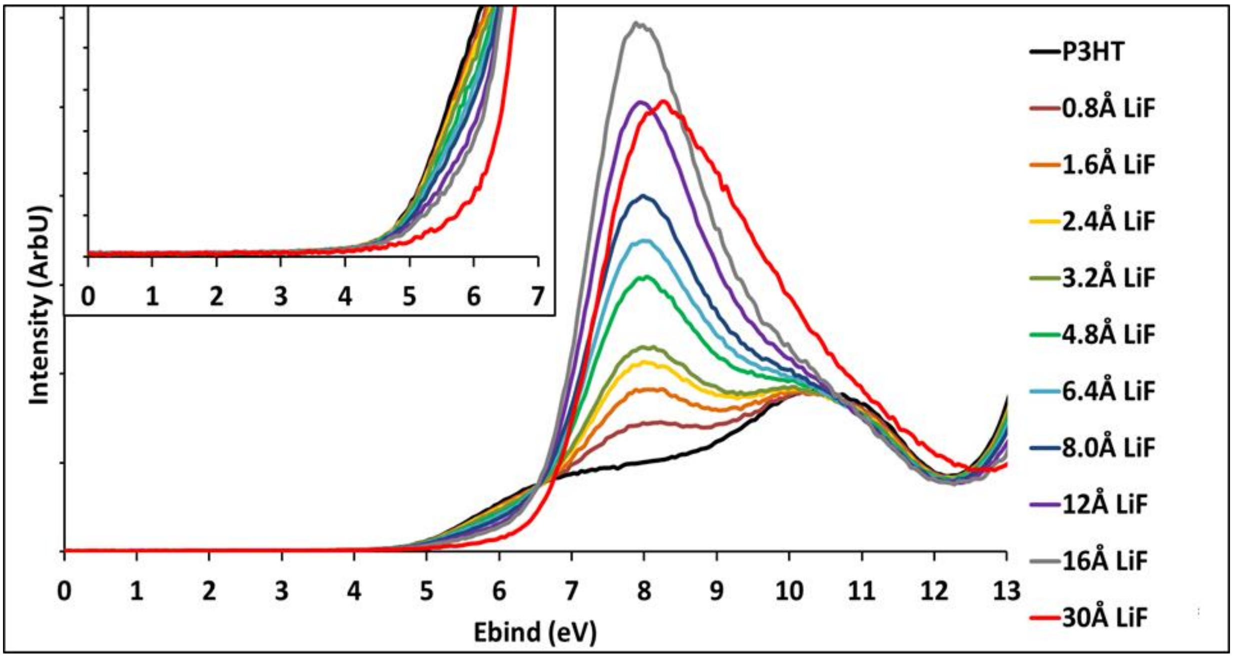

Figure 6.10: MIES of sequential LiF depositions on P3HT, with MIES of the single 30Å LiF/P3HT sample (in red) for comparison.

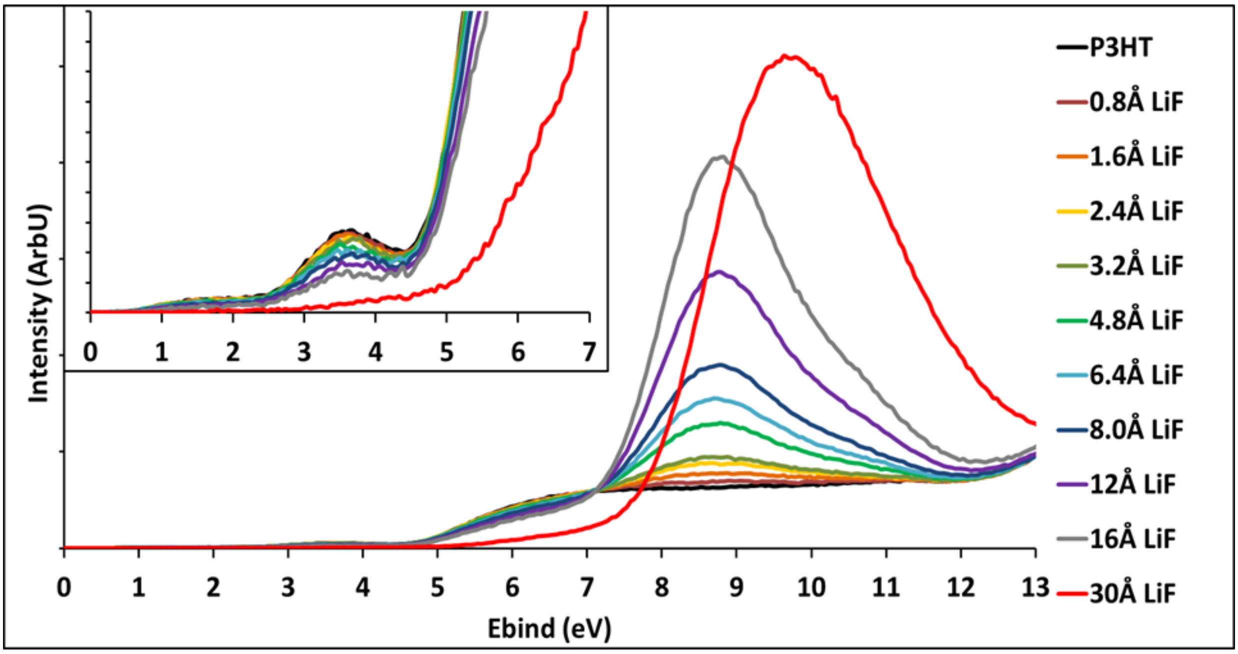

Figure 6.11: UPS of sequential LiF depositions on P3HT, with UPS of the single 30Å LiF/P3HT sample (in red) for comparison.

The position of the F2p DOS does not change with layer thickness during the sequential depositions on either organic material. This indicates that the salt/organic dipole does not change with sequentially increasing layer thicknesses on a single sample for LiF, There is also no significant difference in the F2p peak widths with sequential depositions when comparing LiF/PCBM to

LiF/P3HT which is most easily seen in the SVD results in Figures 6.6, 6.7. This is the case for both MIES and UPS respectively. Thus there is no significant difference with regard to the dipole strength between PCBM and P3HT as a substrate when sequential LiF depositions are performed. It is quite clear however that the F2p DOS for the single 30Å LiF deposition on both PCBM and P3HT are located at a higher binding energy to the sequential depositions (Figures 6.8-6.11). This is indicative of a change in the dipole between the salt and organic material with different deposition methods. Given we do not know the F2p peak position in MIES and UPS for zero dipole formation on the organic layers we cannot discuss the exact dipole strength and can only compare the relative positions.

On PCBM the DOS appear shifted by +1.5eV in both MIES and UPS for a single deposition of LiF compared to the sequential depositions. This indicates that the side of the dipole pointing to the outermost layer (i.e: parallel to the surface normal) is more positive for a single thick deposition by 1.5eV and that the outermost layer and near surface area are similarly influenced by the change. The binding energy width of the LiF DOS on PCBM are broader in both MIES and UPS for the sequential depositions compared to the single thick deposition (Figures 6.8, 6.9). This indicates that the distribution of orientations of the dipole is broader for the sequential depositions. Thus a single thick deposition of LiF on PCBM appears to have less of a range of dipole strengths on the surface than when LiF is deposited sequentially.

For P3HT the UPS of the single LiF deposition compared to the sequential depositions shows a binding energy increase of +1.0eV and for MIES it is +0.4eV. The smaller binding energy shift in UPS (compared to PCBM) indicates that the salt/organic dipole is less affected by the deposition method in the near surface area. The even smaller shift in MIES indicates that the impact of deposition method on the dipole strength at the outermost layer of LiF on P3HT is very little. For P3HT the single thick deposition of LiF reveals a wider range of binding energies as compared to the sequential depositions (Figures 6.10, 6.11). So in this instance it appears that there is a wider range of distributions of the dipole for a single thick deposition of LiF.

The position of the F2p DOS is seen to vary depending on the substrate upon which the LiF has been deposited. For the organic materials this has already been discussed, but there are also clear differences between the LiF layers on the Si and Au controls (Figures 6.6, 6.7). The differences in peak position are attributed to the differences in dipole between the salt and substrate, as also seen in the XPS results in Table 6.2. The features are seen to be shifted by +1eV in both MIES and UPS on Si compared to Au, thus the LiF/Si interfacial dipole is more positive than at the LiF/Au interface.

The workfunction of the surface is also altered by both deposition method and substrate for the LiF depositions, as shown in Table 6.6. The secondary cutoff for PCBM had an altered shape for 12Å and

16Å LiF in sequential depositions, so the workfunction for 8Å is given and denoted with a (*).One explanation is that there are two separate workfunctions present in the sample area under investigation due to non-uniformity of the LiF layer, but it is not conclusive[71]**.** The secondary cutoff region for spectra used for workfunction determination of LiF/PCBM surfaces can be seen in Figure 6.12.

Deposition method and thickness LiF (Å)	**Workfunction (eV)**	
	PCBM	**P3HT**
0 Å	3.9	3.9
Sequential deposition, 16Å	4.1*	4.2
Single deposition, 30 Å	2.6	3.8

Table 6.6: Workfunctions for pristine PCBM and P3HT, and deposited LiF. *Workfunction for sequential deposition on PCBM is from 8Å LiF thickness.

The choice of deposition method was shown to have an impact on the resulting workfunction, as shown in Table 6.6. For the case of LiF/PCBM there was a significant difference in workfunction between the deposition methods. The sequential depositions induced an 0.2eV increase in workfunction, but the single thick deposition induced a decrease of 1.3eV. Workfunction is affected by dipoles present at the vacuum interface (as well as chemical changes). Dipoles which are oriented with the positive component parallel to the surface normal toward the vacuum will decrease the observed workfunction of a material. This is due to the surface effectively having a negative charge which thus prevents electrons with the lowest kinetic energy from escaping the surface of the sample. Naturally, the opposite effect is observed for dipoles in the opposite orientation. The differences in workfunction with deposition method seen for LiF/PCBM thus indicates that the sample/vacuum dipole has opposing orientations depending on deposition method. For LiF/P3HT the effect is only small.

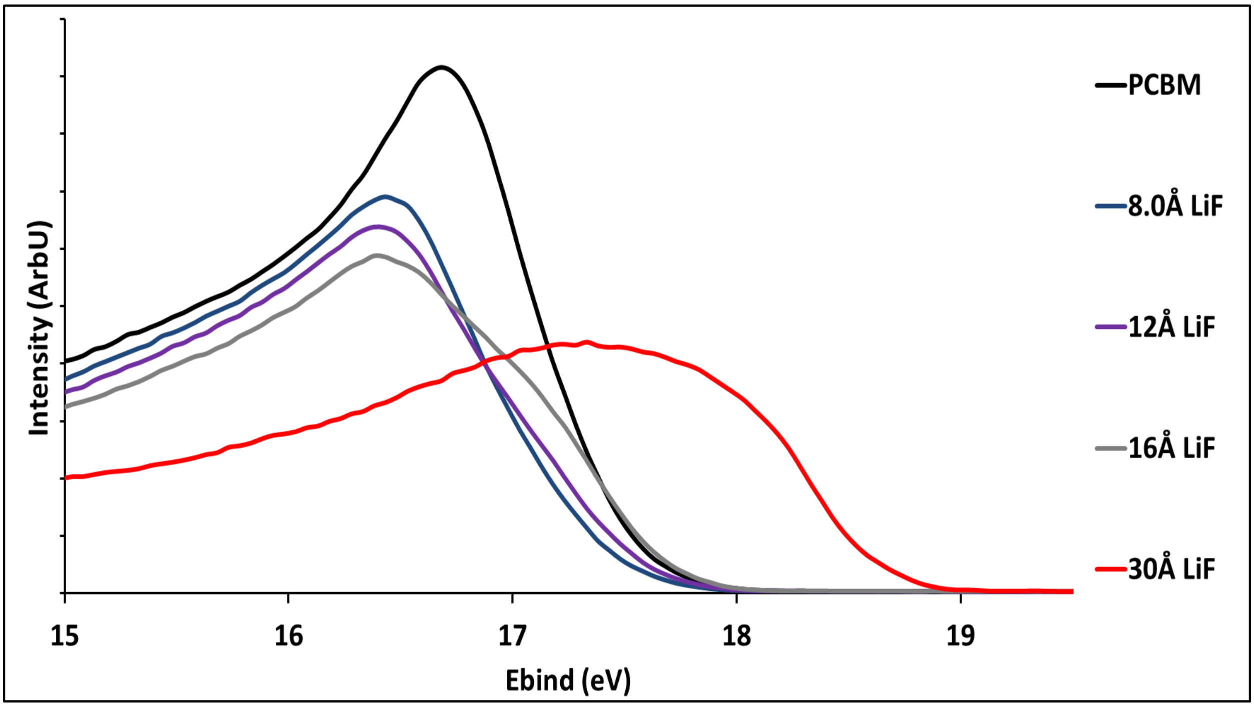

Figure 6.12: Secondary cut off region for UPS of LiF/PCBM for workfunction determination. Note the altered shape for both 12Å and 16Å.

6.4.4) NICISS

Fluorine depth profiles on PCBM and P3HT are shown in Figure 6.13. Li profiles cannot be detected with NICISS as its mass is too similar to that of the He^+ projectile. However, as the XPS results showed no dissociation of the LiF molecules it is acceptable to view the depth profile of F as that of the LiF molecule. The concentrations were calibrated from the carbon step for each sample.

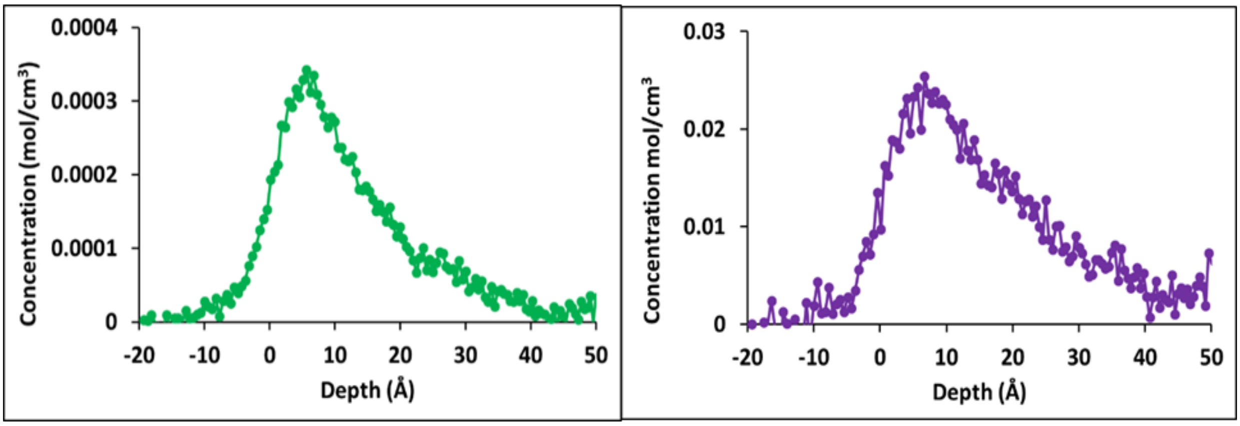

Figure 6.13: NICISS concentration depth profiles of F for 10Å LiF. Shown for depositions on PCBM (left) and P3HT (right).

Both fluorine profiles show a peak maximum between 5~10Å into the surface with a tail tapering off at around 40Å. In this instance the gauging of the zero mark for the depth has not been yet performed and thus the peak maximum below the surface is not indicative of diffusion. However, the peak shape still provides information regarding the surface. The profile for a layer of LiF present only on the surface would appear with a symmetrical peak and thus this observed concentration tapering off into the bulk indicates LiF molecules are present beneath the surface, so are either diffusing or growing as islands on the surface. The spectral intensity at a negative depth is due to the finite energy resolution of the apparatus and has been seen before[37].

6.4.5) Further Discussion

The results of this work clearly show that LiF is intact when deposited on PCBM or P3HT, regardless of layer thickness, and no new chemical states were observed in the core analysis for Li or F. Thus, in this instance, metallic doping effects and dissociation are not the mechanisms occurring at the salt/organic interface. The salt does not chemically react with the organic layer however a redistribution of electrons was observed on both PCBM and P3HT. For P3HT the redistribution of electrons seemed to be dependent upon the LiF thickness. For a thin layer of LiF the sulfur in the thiophene was affected, but for a thicker layer the oxygen was affected which lessened the effect observed in the sulfur. For PCBM changes in the electron distribution in the oxygen were observed similarly for all deposition thicknesses, especially toward the surface. These were observed at 1.2eV below and 1.3eV above the respective ester C=O and C-O-C peaks. As an interesting note, Turak *et.al* deposited LiF onto *in situ* evaporated C_{60} and observed a charge complex formation occurring via the F1s and C1s conjugated π states in the fullerene cage[28]**,** a high binding energy shoulder was present in the F1s XP spectrum and the conjugated π states were seen to increase in intensity. The air curing of the PCBM and consequential oxidation in the present work could possibly have had an impact on the observed differences in LiF upon deposition on the fullerene. The conjugated π structure of PCBM can be seen as satellite features in the C1s XP spectra and is the dominant feature in the VB structure[46]. This structure is shown to be preserved with LiF deposition which has been seen in other work on fullerenes[3] which is important as it is these states which are responsible for charge conduction in an OPV device.

The effects of an interfacial dipole between the LiF and substrate was observed on the various materials in both the XPS and VB data. The region of the dipole oriented toward the outermost layer was found to be most positive on the Si wafer and also when a thick (30Å) layer of LiF was deposited on PCBM. The dipole was found to change depending on deposition method on PCBM. For P3HT the different deposition methods only had a small impact on the observed position of the F2p states in the VB. The changes observed in workfunction on the different materials and deposition methods indicate there is dipole formation also occurring at the vacuum interface, which has the most pronounced effect for 30Å LiF on PCBM. The dipole is related to the strength of interaction between the salt and organic layer[3]. From the investigations in the present work it appears that there is a stronger interaction between LiF and PCBM compared to LiF and P3HT. The changes in interfacial dipole with deposition method could be of significance for OPV device function, the presence of a dipole induced by the interfacial layer is one of the commonly proposed mechanisms for enhanced charge injection to the electrode. As such, the ability to manipulate this dipole by altering the deposition method of LiF could change the resulting device efficiency.

The SVD of MIE spectra shows that 16Å of LiF is not enough to form a closed salt layer on either organic film, which indicates island-like growth or diffusion occurring. This also reflected in the NICISS data. The salt is clearly present up to 40Å into the surface when ~10Å LiF is deposited. Thus, the surface either has islands/grains up to 40Å in height sitting on the surface or has partial diffusion with some island-like structure at the surface. This correlates to the grain like structures observed by Brown et al via AFM studies of 40Å LiF deposited on polyfluorene[72]. We propose, however that there is possibly some diffusion occurring with deposition and not just islands of salt on top of the organic surface. The MIES data indicates that 30-40% of the organic layer is visible in the outermost layer for 10Å of LiF. Although possible, it is unlikely that islands 40Å high are forming on the surface for this level of coverage as more influence of the organic layer's electronic structure should be visible in the overall DOS if this were the case.

Although the salt may have diffused into the organic material upon deposition there was no evidence of doping. Doping becomes evident in VB data and can be observed by a shift in the HOMO[21, 73]. As discussed in the results no shift was observed, only a gradual decrease in intensity at the relevant binding energies of each organic material.

6.5) Conclusion

The evolution of electronic states on the surface and near surface area for LiF on air deposited and annealed PCBM and P3HT films has been investigated. An interfacial dipole between the salt and each substrate was observed, and the impact of the dipole changed with deposition method, especially for the case of PCBM. As such, trialing different deposition methods of the salt during device fabrication may influence the overall cell efficiency. The HOMO and conjugated π states of both organics were shown to be preserved with LiF deposition and there was no dissociation of the salt or evidence of doping. However, the presence of the salt did impact the oxygen on both films, inducing two new distinct oxygen states in PCBM, and when sufficient amounts were deposited there was a small shift in binding energy for the oxidized sites in P3HT. It is clear from the NICISS and MIES results that the salt is not growing mono-layer by mono-layer but in patches on the surface, and it appears that it is possibly diffusing into the organic surface as well as forming islands on the surface. It has been clearly shown in the literature that the alkali halide acts to preserve the charge transporting states of the organic material from the electrode upon deposition. Having it diffused into the near surface area of the organic film rather than segregated patches on and above the organic surface would enhance this protective mechanism.

6.6) Acknowledgement

We would like to thank Dr Cameron Shearer for depositing the Au films and Dr Anders Barlow for helpful discussions regarding the XPS results.

6.7) References

1. Yu, G.; Gao, J.; Hummelen, J. C.; Wudl, F.; Heeger, A. J., Polymer Photovoltaic Cells: Enhanced Efficiencies Via a Network of Internal Donor-Acceptor Heterojunctions. *Science* **1995**, *270*, 1789-1791.

2. Lai, T.-H.; Tsang, S.-W.; Manders, J. R.; Chen, S.; So, F., Properties of Interlayer for Organic Photovoltaics. *Materials Today* **2013**, *16*, 424-432.

3. Jönsson, S. K. M.; Carlegrim, E.; Zhang, F.; Salaneck, W. R.; Fahlman, M., Photoelectron Spectroscopy of the Contact between the Cathode and the Active Layers in Plastic Solar Cells: The Role of LiF. *Japanese Journal of Applied Physics* **2005**, *44*, 3695.

4. Armstrong, N. R.; Wang, W.; Alloway, D. M.; Placencia, D.; Ratcliff, E.; Brumbach, M., Organic/Organicprime Heterojunctions: Organic Light Emitting Diodes and Organic Photovoltaic Devices. *Macromolecular Rapid Communications* **2009**, *30*, 717-731.

5. Kim, Y.; Cook, S.; Choulis, S. A.; Nelson, J.; Durrant, J. R.; Bradley, D. D. C., Organic Photovoltaic Devices Based on Blends of Regioregular Poly(3-Hexylthiophene) and Poly(9,9-Dioctylfluorene-Co-Benzothiadiazole). *Chemistry of Materials* **2004**, *16*, 4812-4818.

6. Brown, T. M.; Friend, R. H.; Millard, I. S.; Lacey, D. J.; Burroughes, J. H.; Cacialli, F., LiF/Al Cathodes and the Effect of LiF Thickness on the Device Characteristics and Built-in Potential of Polymer Light-Emitting Diodes. *Applied Physics Letters* **2000**, *77*, 3096-3098.

7. Torabi, S.; Liu, J.; Gordiichuk, P.; Herrmann, A.; Qiu, L.; Jahani, F.; Hummelen, J. C.; Koster, L. J. A., Deposition of LiF onto Films of Fullerene Derivatives Leads to Bulk Doping. *ACS Applied Materials & Interfaces* **2016**, *8*, 22623-22628.

8. Ahlswede, E.; Hanisch, J.; Powalla, M., Comparative Study of the Influence of LiF, NaF, and KF on the Performance of Polymer Bulk Heterojunction Solar Cells. *Applied Physics Letters* **2007**, *90*, 163504-3.

9. Hung, L. S., Enhanced Electron Injection in Organic Electroluminescence Devices Using an Al/LiF Electrode. *Applied Physics Letters* **1997**, *70*.

10. Chen, X.; Zhao, C.; Rothberg, L.; Ng, M.-K., Plasmon Enhancement of Bulk Heterojunction Organic Photovoltaic Devices by Electrode Modification. *Applied Physics Letters* **2008**, *93*, 123302-3.

11. Ding, H., Irfan, So, F., Gao, Y., Interface Study of Insertion Layers in Organic Semiconductor Devices. *SPIE proceedings* **2009**, *7415*.

12. Lee, Y. J.; Li, X.; Kang, D.-Y.; Park, S.-S.; Kim, J.; Choi, J.-W.; Kim, H., Surface Morphology and Interdiffusion of LiF in Alq3-Based Organic Light-Emitting Devices. *Ultramicroscopy* **2008**, *108*, 1315-1318.

13. Eo, Y. S.; Rhee, H. W.; Chin, B. D.; Yu, J.-W., Influence of Metal Cathode for Organic Photovoltaic Device Performance. *Synthetic Metals* **2009**, *159*, 1910-1913.

14. Lee, T.-W.; Kim, M.-G.; Park, S. H.; Kim, S. Y.; Kwon, O.; Noh, T.; Park, J.-J.; Choi, T.-L.; Park, J. H.; Chin, B. D., Designing a Stable Cathode with Multiple Layers to Improve the Operational Lifetime of Polymer Light-Emitting Diodes. *Advanced Functional Materials* **2009**, *19*, 1863-1868.

15. D. Feng, X.; Grozea, D.; H. Lu, Z., Chemical Structure of MEH-PPV/LiF/Al Interface, *Mat. Res. Soc. Symp. Proc.*, **2011**; Vol. 734.

16. Steim, R.; Kogler, F. R.; Brabec, C. J., Interface Materials for Organic Solar Cells. *Journal of Materials Chemistry* **2010**, *20*, 2499-2512.

17. Helander, M. G.; Wang, Z. B.; Lu, Z. H., Contact Formation at the C60/Alkali-Metal Fluoride/Al Interface. *Applied Physics Letters* **2008**, *93*, 083311-3.

18. Wang, H.; Amsalem, P.; Heimel, G.; Salzmann, I.; Koch, N.; Oehzelt, M., Band-Bending in Organic Semiconductors: The Role of Alkali-Halide Interlayers. *Advanced Materials* **2014**, *26*, 925-930.

19. Matsumura, M.; Furukawa, K.; Jinde, Y., Effect of Al/LiF Cathodes on Emission Efficiency of Organic El Devices. *Thin Solid Films* **1998**, *331*, 96-100.

20. Brabec, C. J.; Cravino, A.; Meissner, D.; Sariciftci, N. S.; Rispens, M. T.; Sanchez, L.; Hummelen, J. C.; Fromherz, T., The Influence of Materials Work Function on the Open Circuit Voltage of Plastic Solar Cells. *Thin Solid Films* **2002**, *403*, 368-372.

21. Zhao, S.-H.; Chang, J.-K.; Fang, J.-J.; Tsai, H.-W.; Liu, I. H.; Tseng, W.-H.; Pi, T.-W.; Chen, M.-H., Efficiency Enhancement Caused by Using LiF to Change Electronic Structures in Polymer Photovoltaics. *Thin Solid Films* **2013**, *545,* 361-364.

22. Yang, X.; Mo, Y.; Yang, W.; Yu, G.; Cao, Y., Efficient Polymer Light Emitting Diodes with Metal Fluoride/Al Cathodes. *Applied Physics Letters* **2001**, *79*, 563-565.

23. van Gennip, W. J. H.; van Duren, J. K. J.; Thune, P. C.; Janssen, R. A. J.; Niemantsverdriet, J. W., The Interfaces of Poly(P-Phenylene Vinylene) and Fullerene Derivatives with Al, LiF, and Al/LiF Studied by Secondary Ion Mass Spectroscopy and X-Ray Photoelectron Spectroscopy: Formation of AlF_3 Disproved. *The Journal of Chemical Physics* **2002**, *117*, 5031-5035.

24. Greczynski, G.; Salaneck, W. R.; Fahlman, M., An Experimental Study of Poly(9,9-Dioctyl-Fluorene) and Its Interfaces with Al, LiF and CsF. *Applied Surface Science* **2001**, *175,* 319-325.

25. Limketkai, B. N.; Baldo, M. A., Charge Injection into Cathode-Doped Amorphous Organic Semiconductors. *Physical Review B* **2005**, *71,* 085207.

26. Kawano, K.; Adachi, C., Reduced Initial Degradation of Bulk Heterojunction Organic Solar Cells by Incorporation of Stacked Fullerene and Lithium Fluoride Interlayers. *Applied Physics Letters* **2010**, *96,* 053307.

27. Busby, Y.; List-Kratochvil, E. J. W.; Pireaux, J.-J., Chemical Analysis of the Interface in Bulk-Heterojunction Solar Cells by X-Ray Photoelectron Spectroscopy Depth Profiling. *ACS Applied Materials & Interfaces* **2017**, *9,* 3842-3848.

28. Turak, A., Zgierski, M.Z., Dharma-Wardana, M.W.C., LiF Doping of C60 Studied with X-ray Photoemission Shake up Analysis. *ECS Journal of Solid State Science and Technology* **2017**, *6*, M3116-M3121.

29. Soon Ok, J., Jun Yeob. L, Improved Lifetime in Organic Solar Cells Using a Bilayer Cathode of Organic Interlayer/ Al. *Sol. Energy Mater. Sol. Cells* **2012**, *101*, 160-165.

30. Kyuwook. I., T.-H. K., Ki-Jeong. K., Chan_Cuk. Hwang., Yong-Jun. P., Band Bending of LiF/Alq3 Interface in Organic Light Emitting Diodes. *Applied Physics Letters* **2003**, *83.*

31. Gao, Y., Surface Analytical Studies of Interfaces in Organic Semiconductor Devices. *Materials Science and Engineering: R: Reports* **2010**, *68,* 39-87.

32. Jin, Y. D.; Ding, X. B.; Reynaert, J.; Arkhipov, V. I.; Borghs, G.; Heremans, P. L.; Van der Auweraer, M., Role of LiF in Polymer Light-Emitting Diodes with LiF-Modified Cathodes. *Organic Electronics* **2004**, *5*, 271-281.

33. Lee, T.-W.; Lim, K.-G.; Kim, D.-H., Approaches toward Efficient and Stable Electron Extraction Contact in Organic Photovoltaic Cells: Inspiration from Organic Light-Emitting Diodes. *Electronic Materials Letters* **2010**, *6*, 41-50.

34. Clark, M. D.; Jespersen, M. L.; Patel, R. J.; Leever, B. J., Predicting Vertical Phase Segregation in Polymer-Fullerene Bulk Heterojunction Solar Cells by Free Energy Analysis. *ACS Applied Materials & Interfaces* **2013**, *5*, 4799-4807.

35. Reese, M. O.; Morfa, A. J.; White, M. S.; Kopidakis, N.; Shaheen, S. E.; Rumbles, G.; Ginley, D. S., Pathways for the Degradation of Organic Photovoltaic P3HT:PCBM Based Devices. *Solar Energy Materials and Solar Cells* **2008**, *92*, 746-752.

36. Dang, M. T.; Hirsch, L.; Wantz, G., P3HT:PCBM, Best Seller in Polymer Photovoltaic Research. *Advanced Materials* **2011**, *23*, 3597-3602.

37. Schmerl, N.; Andersson, G., A Layered Structure at the Surface of P3HT/PCBM Blends. *Physical Chemistry Chemical Physics* **2011**, *13*, 14993-15002.

38. Madogni, V. I.; Kounouhéwa, B.; Akpo, A.; Agbomahéna, M.; Hounkpatin, S. A.; Awanou, C. N., Comparison of Degradation Mechanisms in Organic Photovoltaic Devices Upon Exposure to a Temperate and a Subequatorial Climate. *Chemical Physics Letters* **2015**, *640*, 201-214.

39. Zhong, Y.; Izawa, S.; Hashimoto, K.; Tajima, K.; Koganezawa, T.; Yoshida, H., Crystallization-Induced Energy Level Change of [6,6]-Phenyl-C61-Butyric Acid Methyl Ester (PCBM) Film: Impact of Electronic Polarization Energy. *The Journal of Physical Chemistry C* **2015**, *119*, 23-28.

40. Rait, S.; Kashyap, S.; Bhatnagar, P. K.; Mathur, P. C.; Sengupta, S. K.; Kumar, J., Improving Power Conversion Efficiency in Polythiophene/Fullerene-Based Bulk Heterojunction Solar Cells. *Solar Energy Materials and Solar Cells* **2007**, *91*, 757-763.

41. Maibach, J., et al., Impact of Processing on the Chemical and Electronic Properties of Phenyl-C61-Butyric Acid Methyl Ester. *Journal of Materials Chemistry C* **2014**, *2*, 7934-7942.

42. Kanai, K.; Miyazaki, T.; Suzuki, H.; Inaba, M.; Ouchi, Y.; Seki, K., Effect of Annealing on the Electronic Structure of Poly(3-Hexylthiophene) Thin Film. *Physical Chemistry Chemical Physics* **2010**, *12*, 273-282.

43. Guralnick, B. W.; Kirby, B. J.; Majkrzak, C. F.; Mackay, M. E., Morphological Characterization of Plastic Solar Cells Using Polarized Neutron Reflectivity. *Applied Physics Letters* **2013**, *102*, 083305.

44. Heeg, J.; Kramer, C.; Wolter, M.; Michaelis, S.; Plieth, W.; Fischer, W. J., Polythiophene — O3 Surface Reactions Studied by XPS. *Applied Surface Science* **2001**, *180*, 36-41.

45. Leiro, J. A.; Heinonen, M. H.; Laiho, T.; Batirev, I. G., Core-Level XPS Spectra of Fullerene, Highly Oriented Pyrolitic Graphite, and Glassy Carbon. *Journal of Electron Spectroscopy and Related Phenomena* **2003**, *128*, 205-213.

46. Richter, M. H.; Friedrich, D.; Schmeißer, D., Valence and Conduction Band States of PCBM as Probed by Photoelectron Spectroscopy at Resonant Excitation. *BioNanoScience* **2012**, *2*, 59-65.

47. Belay, A. B.; Zhou, W.; Krueger, R.; Davis, K. O.; Ü, A.; Sorloaica-Hickman, N., Effect of UV-Ozone Exposure on PCBM. *IEEE Journal of Photovoltaics* **2012**, *2*, 148-153.

48. Jenkins, J. L.; Lee, P. A.; Nebesny, K. W.; Ratcliff, E. L., Systematic Electrochemical Oxidative Doping of P3HT to Probe Interfacial Charge Transfer across Polymer-Fullerene Interfaces. *Journal of Materials Chemistry A* **2014**, *2*, 19221-19231.

49. Brumboiu, I. E.; Ericsson, L.; Hansson, R.; Moons, E.; Eriksson, O.; Brena, B., The Influence of Oxygen Adsorption on the NEXAFS and Core-Level XPS Spectra of the C60 Derivative PCBM. *The Journal of Chemical Physics* **2015**, *142*, 054306.

50. Seo, H. O.; Jeong, M.-G.; Kim, K.-D.; Kim, D. H.; Kim, Y. D.; Lim, D. C., Studies of Degradation Behaviors of Poly (3-Hexylthiophene) Layers by X-Ray Photoelectron Spectroscopy. *Surface and Interface Analysis* **2014**, *46*, 544-549.

51. Guan, Z.-L.; Kim, J. B.; Wang, H.; Jaye, C.; Fischer, D. A.; Loo, Y.-L.; Kahn, A., Direct Determination of the Electronic Structure of the Poly(3-Hexylthiophene):Phenyl-[6,6]-C61 Butyric Acid Methyl Ester Blend. *Organic Electronics* **2010**, *11*, 1779-1785.

52. Shallcross, R. C.; Stubhan, T.; Ratcliff, E. L.; Kahn, A.; Brabec, C. J.; Armstrong, N. R., Quantifying the Extent of Contact Doping at the Interface between High Work Function Electrical

Contacts and Poly(3-Hexylthiophene) (P3HT). *The Journal of Physical Chemistry Letters* **2015**, *6*, 1303-1309.

53. Ratcliff, E. L.; Jenkins, J. L.; Nebesny, K.; Armstrong, N. R., Electrodeposited, "Textured" Poly(3-Hexyl-Thiophene) (E-P3HT) Films for Photovoltaic Applications. *Chemistry of Materials* **2008**, *20*, 5796-5806.

54. Schlaf, R.; Parkinson, B. A.; Lee, P. A.; Nebesny, K. W.; Jabbour, G.; Kippelen, B.; Peyghambarian, N.; Armstrong, N. R., Photoemission Spectroscopy of LiF Coated Al and Pt Electrodes. *Journal of Applied Physics* **1998**, *84*, 6729-6736.

55. Shaheen, S. E.; Jabbour, G. E.; Morrell, M. M.; Kawabe, Y.; Kippelen, B.; Peyghambarian, N.; Nabor, M. F.; Schlaf, R.; Mash, E. A.; Armstrong, N. R., Bright Blue Organic Light-Emitting Diode with Improved Color Purity Using a LiF/Al Cathode. *Journal of Applied Physics* **1998**, *84*, 2324-2327.

56. Wagner, C. D., Practical Surface Analysis, Auger and X-Ray Photoelectron Spectroscopy; John Wiley & Sons, **1990**; Vol. 1.

57. Ferraria, A. M.; Lopes da Silva, J. D.; Botelho do Rego, A. M., XPS Studies of Directly Fluorinated HDPE: Problems and Solutions. *Polymer* **2003**, *44*, 7241-7249.

58. Hamrin, K.; Johansson, G.; Gelius, U.; Nordling, C.; Siegbahn, K., Valence Bands and Core Levels of the Isoelectronic Series LiF, BeO, BN, and Graphite Studied by ESCA. *Physica Scripta* **1970**, *1*, 277.

59. Yuan, Y.; Grozea, D.; Han, S.; Lu, Z. H., Interaction between Organic Semiconductors and LiF Dopant. *Applied Physics Letters* **2004**, *85*, 4959-4961.

60. Bao, Q.; Liu, X.; Braun, S.; Fahlman, M., Oxygen- and Water-Based Degradation in [6,6]-Phenyl-C61-Butyric Acid Methyl Ester (PCBM) Films. *Advanced Energy Materials* **2014**, *4*, 1301272-n/a.

61. Chun-Qi, S.; Wang, P.; Ying, S.; Yan-Jun, L.; Wen-Hua, Z.; Xu, F.-Q.; Jun-Fa, Z.; Guo-Qiao, L.; Li, H.-N., Electronic Structure of PCBM, *Chin. Phys. B,* **2012**; Vol. 21, No 1.

62. Akaike, K.; Kanai, K.; Yoshida, H.; Tsutsumi, J. y.; Nishi, T.; Sato, N.; Ouchi, Y.; Seki, K., Ultraviolet Photoelectron Spectroscopy and Inverse Photoemission Spectroscopy of [6,6]-Phenyl-C61-Butyric Acid Methyl Ester in Gas and Solid Phases. *Journal of Applied Physics* **2008**, *104*, 023710-5.

63. Salaneck, W. R., Photoelectron Spectroscopy of Polyconjugated Polymer Surfaces and Interfaces. *Reports on Progress in Physics* **1991**, *54*, 1215.

64. Hao, X. T.; Hosokai, T.; Mitsuo, N.; Kera, S.; Okudaira, K. K.; Mase, K.; Ueno, N., Control of the Interchain Π−Π Interaction and Electron Density Distribution at the Surface of Conjugated Poly(3-Hexylthiophene) Thin Films. *The Journal of Physical Chemistry B* **2007**, *111*, 10365-10372.

65. Adams, J. M.; Evans, S.; Thomas, J. M., The Valence Band of Lithium Fluoride. *Journal of Physics C: Solid State Physics* **1973**, *6*, L382.

66. Gopikrishnan, C. R.; Jose, D.; Datta, A., Electronic Structure, Lattice Energies and Born Exponents for Alkali Halides from First Principles. *AIP Advances* **2012**, *2*, 012131.

67. Pong, W.; Inouye, C. S., Ultraviolet Photoemission Study of LiF. *Journal of Electron Spectroscopy and Related Phenomena* **1977**, *11*, 165-170.

68. Wiegershaus, F.; Krischok, S.; Ochs, D.; Maus-Friedrichs, W.; Kempter, V., Electron Emission in Slow Collisions of He Projectiles (He∗, He+, He++) with Li- and LiF-Surfaces. *Surface Science* **1996**, *345*, 91-100.

69. Ochs, D.; Brause, M.; Stracke, P.; Krischok, S.; Wiegershaus, F.; Maus-Friedrichs, W.; Kempter, V.; Puchin, V. E.; Shluger, A. L., The Surface Electronic Structure of Stoichiometric and Defective LiF Surfaces Studied with MIES and UPS in Combination with Ab-Initio Calculations. *Surface Science* **1997**, *383*, 162-172.

70. Morgner, H., Analysis of MIES and UPS Data of LiF and NaCl. *Surface Science* **1999**, *420*, 95-102.

71. Helander, M. G.; Greiner, M. T.; Wang, Z. B.; Lu, Z. H., Pitfalls in Measuring Work Function Using Photoelectron Spectroscopy. *Applied Surface Science* **2010**, *256*, 2602-2605.

72. Brown, T. M.; Friend, R. H.; Millard, I. S.; Lacey, D. J.; Butler, T.; Burroughes, J. H.; Cacialli, F., Electronic Line-up in Light-Emitting Diodes with Alkali-Halide/Metal Cathodes. *Journal of Applied Physics* **2003**, *93*, 6159-6172.

73. Kahn, A.; Koch, N.; Gao, W., Electronic Structure and Electrical Properties of Interfaces between Metals and Π-Conjugated Molecular Films. *Journal of Polymer Science Part B: Polymer Physics* **2003**, *41*, 2529-2548.

7. On the Growth of Evaporated NaF on PCBM and P3HT

N.M Schmerl[1], J.S Quinton[1], G.G Andersson[1*]

[1]Flinders Centre for Nanoscale Science and Technology, School of Chemistry and Physical Sciences, Flinders University of South Australia, Bedford Park, SA 5042, Australia

*Corresponding author: Email gunther.andersson@flinders.edu.au

Author Contribution:

Natalya Schmerl: Designed and performed experiments, data analysis and interpretation, and prepared the manuscript for publication.

Gunther Andersson: Intellectual contribution in conceptualising experiments, data interpretation & revision of manuscript.

Jamie Quinton: Intellectual contribution in revision of manuscript.

7.1) Abstract:

Thin layers of NaF were evaporated onto PCBM and P3HT thin films. The chemical state of NaF was observed for various layer thicknesses via XPS for a very low deposition (~1Å) layer, a thick 30Å layer, and also for sequential depositions of the salt. The chemical states were also mapped at different surface depths via ARXPS measurements. NaF was not found to dissociate, however an extra chemical state in fluorine was observed on all samples and it is suspected that incidental non-stoichiometric clusters were deposited along with the expected NaF monomer units. The electronic properties of the VB were determined via UPS and MIES for a range of thicknesses with the sequential depositions up to the nominal value of 30Å NaF. An interfacial dipole was observed and was seen to be affected by the deposition method of the salt and also by the salt layer thickness. Concentration depth profiles were obtained via NICISS and it is believed the salt layer is forming as islands with some diffusion.

7.2) Introduction:

The concept of using an interfacial layer between the active layer and LWE in an OPV device (or OLED) to enhance charge injection to the electrode has already been introduced in Chapter 1, and in Chapter 6 the electronic properties of various LiF layers on PCBM and P3HT were investigated in an attempt to gain insight into some of the mechanisms occurring at the salt/organic interface. Although LiF is a predominant choice for this interlayer there are many other salts which have been used in this manner. NaF is one of these alternative materials[1], although it has seen most of its use in OLEDs thus far[2-4,5]. A comparative study was performed by Ahlswede where various layer thicknesses of LiF, NaF and KF were used in P3HT/PCBM OPV devices and it was observed that for very thin layers of salt that NaF had the highest device efficiency[1]. When the salt layer thickness was increased LiF strongly outperformed the other salts. It was postulated that there were a combination of different effects occurring with the interlayer which included dipole formation, dissociation, diffusion and doping, and that these effects appeared to be thickness dependent. It was concluded that further research was required to understand the underlying mechanisms and why it was that NaF outperforms LiF when the layer is sufficiently thin, and there is potential for NaF as a LiF replacement due to the reduction in required materials for the interlayer enhancing effect.

The aim of this work is to use the combination of XPS, ARXPS, UPS, MIES and NICISS to determine the vertical distribution of NaF deposited onto both P3HT and PCBM via vapor deposition and the valence electron structure of the surface and surface near region, in a similar manner to that performed for LiF in Chapter 6. The chemical states for a range of deposition thicknesses were also determined with XPS. Deposited ultrathin (denoted ~1Å in this work) and thick (~30Å) layers were then investigated via ARXPS to check for any chemical changes in the near surface region which may facilitate the device efficiencies observed by Ahlswede[1]. A 30Å NaF layer was then investigated with NICISS for determining the elemental concentration depth profile.

7.3) Experimental

7.3.1) Materials and sample preparation

Materials and sample preparation are identical to that described in Chapter 6 section 6.3.1, except NaF was used in place of LiF. The NaF was metals base >99.99% purity and obtained through Aldrich. The NaF depositions were performed using an NaF density of 2.6g/cm^3. The deposition rate was found to be 1.5Å/s at 750°C and 0.7Å/s for 700℃.

7.3.2) Methods

Experimental details for the *in situ* NICISS and electron spectroscopy apparatus (XPS, UPS, MIES) can be found in Chapter 2. Spectral acquisition for ARXPS was also identical to that already described in Chapter 6, section 6.3.2.

7.3.3) Analysis

Data analysis was also performed in the same manner as described in Chapter 6, however for the XPS analysis the new high binding energy C1s peak observed at around 293eV was permitted a FWHM of 3eV and was not locked in position. For this work the SVD was performed only up to 12eV in binding energy as higher energies include parts of the secondary electron peak in many of the spectra.

7.4) Results and Discussion

Results are discussed initially per technique in the order of XPS (section 7.4.1), ARXPS (section 7.4.2), UPS and MIES (section 7.4.3), and NICISS (section 7.4.4). In these sections there is a discussion of general results at that particular depth into the surface. A further discussion regarding the total outcome of the combined results follows in section 7.4.5. Comparisons of LiF results (Chapter 6) and NaF results from this chapter are discussed in section 7.5.

7.4.1) XPS

The analysis of pristine PCBM and P3HT films has been previously shown in Chapter 6, section 6.4.1.1 so does not require further discussion here. The XPS results for the NaF control films were found to be non-trivial and as such the XPS results shall begin with a section dedicated to these films (section 7.4.1.1). The surface chemistry observed for the NaF depositions on the organic materials was also non-trivial. As such the results will be presented in the following manner: the chemical composition of the films will first be given (section 7.4.1.2). The chemical states of the salt will then be shown for the range of NaF deposition thicknesses (section 7.4.1.3). Then the chemical states of the organic materials and the influence of the salt on these states will follow (section 7.4.1.4).

7.4.1.1) Control NaF film analysis

The NaF/Au and NaF/Si control samples revealed that no contamination was deposited with the NaF, if any water was present in the salt during evaporation it was at levels below the detection limit of XPS. Chemical composition and peak positions for the Si control sample is shown in Table 7.1(a), and for the Au control sample in Table 7.1(b). The XP spectra of interest for the Si control sample prior and post NaF deposition are shown in Figures 7.1(a) and (b), respectively. No change was seen in the Au4f spectrum was seen so it has not been shown, and the Na1s and F1s spectra from the Au control showed the same components as that observed on Si (seen in Figure 7.1(b)).

Si Wafer		**Pristine Si**			**NaF/Si**		
Peak	**Attribution**	**Posn and (FWHM), (eV)**	**Component Intensity (%)**	**Total Element Intensity (%)**	**Posn and (FWHM), (eV)**	**Component Intensity (%)**	**Total Element Intensity (%)**
Si2p$_{3/2}$(1)	Si	99.4 (1.1)	83.0	67.3 ±0.5	99.4 (1.1)	73.0	19.5 ±0.1
Si2p$_{3/2}$(2)	SiO$_x$ native oxide layer	102.9 (2.0)	17.0		103.9 (2.0)	14.0	
Si2p$_{3/2}$(3)	Electron redistribution in Si or SiO$_x$	-			100.6 (1.1)	4.0	
Si2p$_{3/2}$(4)	Reacted oxide layer with NaF	-	-		106.1 (2.0)	8.0	
O1s(1)	SiO$_x$ native oxide layer	532.7 (2.0)	100	28.0 ±0.2	532.1 (2.0)	19.0	6.5 ±0.1
O1s(2)	Reacted oxide layer with NaF	-	-		533.8 (2.0)	81.0	
Na1s	NaF	-	-		1073.7 (2.0)	100	44.5 ±0.1
F1s(1)	NaF	-	-		686.2 (1.7)	58.0	28.7 ±0.1
F1s(2)	NaF	-	-		688.4 (1.7)	42.0	
C1s(1)	Adventitious C	285.4 (3.0)	100	4.7 ±0.2	286.2 (1.4)	100	0.8 ±0.1

Table 7.1(a): Chemical composition, component ratios within each element, peak positions and attributions for the NaF/Si control sample prior to and post NaF deposition. Note that compositional errors of <0.1% have been rounded up to 0.1%.

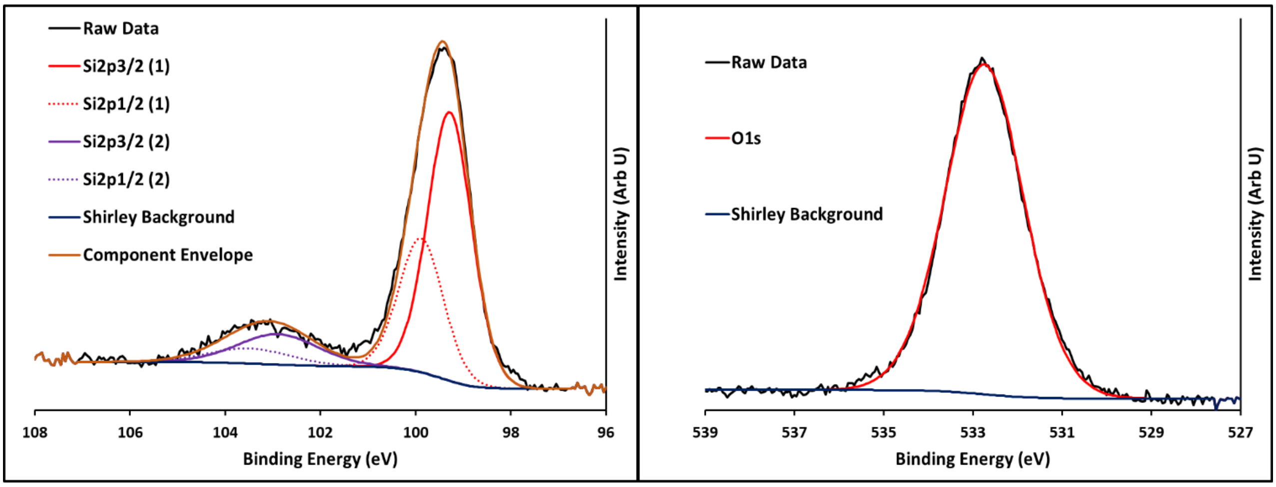

Figure 7.1(a): XP spectra of the Si2p (left) and O1s states (right) of the cleaned silicon wafer prior to NaF deposition.

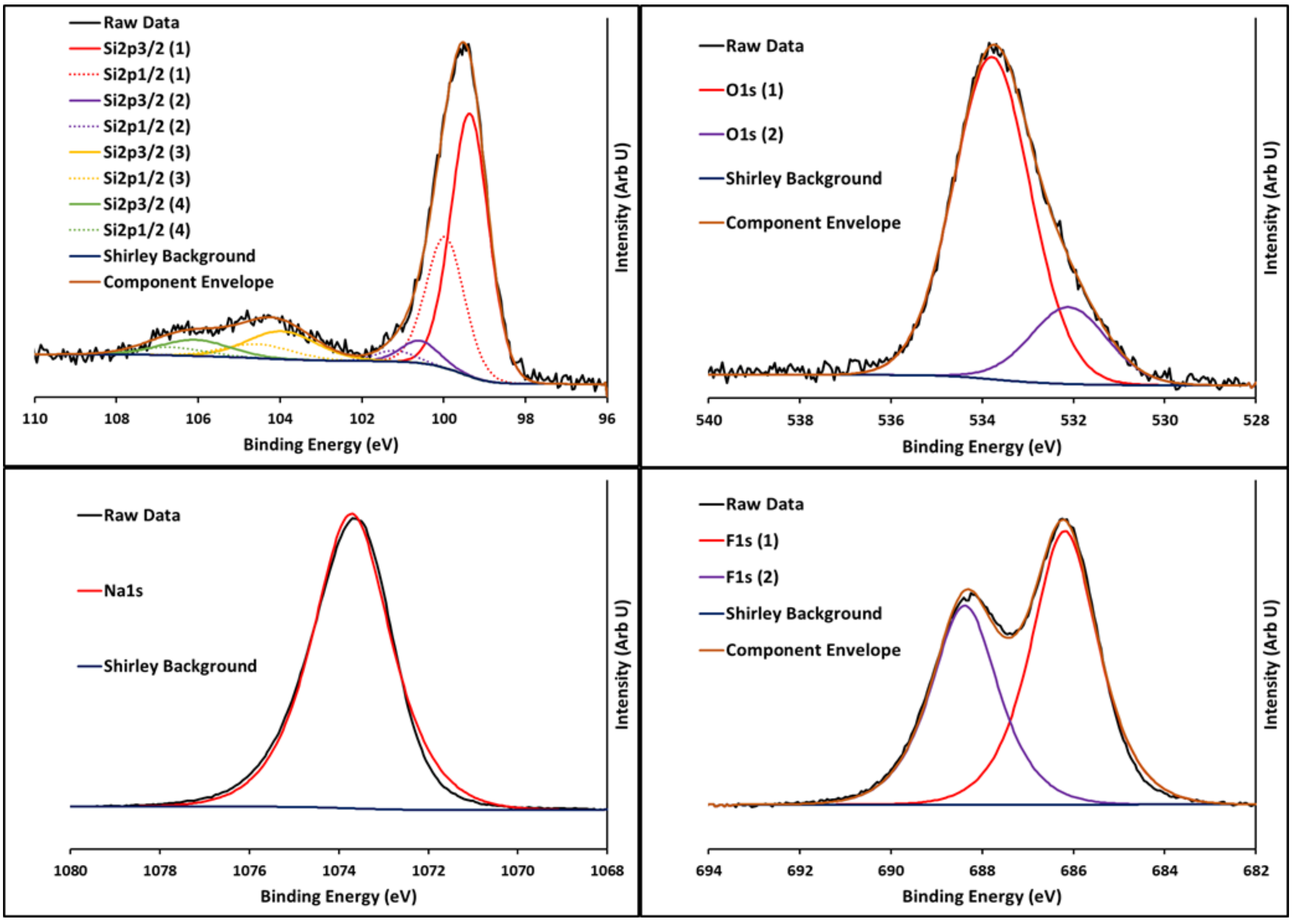

Figure 7.1(b): XP spectra of the Si2p (top left), O1s (top right), Na1s (bottom left) and F1s (bottom right) states of the cleaned silicon wafer after NaF deposition.

		Pristine Au			**NaF/Au**		
Au Film							
Peak	**Attribution**	**Posn and (FWHM), (eV)**	**Component Intensity (%)**	**Total Element Intensity (%)**	**Posn and (FWHM), (eV)**	**Component Intensity (%)**	**Total Element Intensity (%)**
Au4f$_{7/2}$	Au	84.0 (1.2)	100	92.8 ± 0.2	84.0 (1.2)	100	25.5 ± 0.1
Na1s	NaF	-	-		1073.1 (2.4)	100	42.6 ±0.1
F1s(1)	NaF	-	-		685.9 (2.0)	60.0	30.9 ±0.1
F1s(2)	NaF	-	-		688.2 (2.0)	40.0	-
C1s(1)	Adventitious C	284.7 (2.6)	73.0	7.2 ±0.2	-	-	-
C1s(2)	Adventitious C-O moiety	288.0 (2.6)	27.0		287.3 (3.5)	100.0	-

Table 7.1(b): Chemical composition, component ratios within each element, peak positions and attributions for the NaF/Au control sample prior to and post NaF deposition. Note that compositional errors of <0.1% have been rounded up to 0.1%.

The stoichiometry of the NaF on the control samples was observed to be Na:F ~1.4:1 rather than 1:1 as expected. This is not necessarily indicative of non-stoichiometric deposition as already mentioned in Chapter 6. The transmission function of the XPS apparatus and differences in the inelastic mean free path (IMFP) are believed to contribute to the observed ratio. It was observed that there was a tendency for the peak intensities to be over represented for high binding energy photoelectron peaks (Li:F from Chapter 6 was 0.6:1, and Na:F is 1.4:1), thus the transmission function is possibly incorrect. However as relative intensities and component analysis are the main point of focus in this work it is not considered to be problematic. For NaF the stoichiometry cannot be verified via other core level peaks as the Na2p binding energy overlaps that of F2s.

A single component was observed for Na1s, however two components were observed for F1s which have been denoted F1s(1) and F1s(2) for the primary and secondary peak respectively. It is also worth noting there are differences in the FWHM between the two control samples. This could be indicative of differences in the NaF bonds between the two substrates, but it is not definitive. To understand the nature of the secondary fluorine species a thorough discussion on the nature of the NaF deposited on the controls is thus required. For both controls the $F1s_2$ component was ~40% of the total fluorine intensity, which equates to ~12% of the overall sample composition.

If the NaF had dissociated by reacting with either of the substrates then it is to be expected that significant chemical changes would be observed in the core levels pertaining to the substrate in the control spectra. For NaF/Au there was no indication in the high resolution XP spectra that the NaF had interacted with the Au film other than with the adventitious carbon remaining on the surface after sputter cleaning. As the carbon contribution is only ~1% of the total composition it does not account for the observed phenomenon. For NaF/Si the NaF had reacted with the native oxide layer present on the silicon wafer. The native oxide peak $Si2p_{3/2}(2)$ was seen to be shifted by +1.0eV, and two new states appeared at 100.6eV ($Si2p_{3/2}(3)$) and 106.1eV ($Si2p_{3/2}(4)$). However, given that the F1s spectrum is so similar to that observed for NaF/Au it has been interpreted that the deposited NaF has not dissociated, but has had a partial reaction with the silicon oxide layer.

The lack of sufficient chemical reactions with the control surfaces to account for the presence of the F1s(2) peak is an immediate indication that the deposited salt is not NaF in the standard monomer form and there is possibly some form of Na_xF_y clusters being deposited, although with the techniques used in this work the nature of these possible clusters cannot be determined. Clusters could have a different electron distribution between the various Na and F species present depending on what the cluster conformation is[7], so could explain the secondary F component given that it is certainly not a covalent bond with the substrate.

As discussed in Chapter 6 an accurate measure for chemical species identification is via the binding energy difference in the core level positions. The core level Na1s and F1s peak positions for the control samples along with values from the literature are shown in Table 7.2. To determine the chemical species present the Δ(Na1s – F1s) was measured, also shown in Table 7.2. This distance Δ(Na1s – F1s) for NaF has been shown in the literature with a range of values, depending on the form of the salt.

Method	Substrate	Na1s (eV)	F1s (eV)	Δ(Na1s – F1s), (eV)	Reference
Evaporated HV conditions	Si wafer	1073.7	686.2, 688.4	387.5 (for $F1s_1$), 385.3 (for $F1s_2$)	This work
Evaporated HV conditions	Au film	1073.1	685.9, 688.2	387.2 (for $F1s_1$), 384.9 (for $F1s_2$)	This work
Evaporated HV conditions	Al	1072.0	686.0	386.0	Kemeny[6]
Evaporated HV conditions,	Stainless steel	1076.7	689.6	387.1	Kikas[8]
Evaporated, annealed at 400C, 30min*	Mo film on Si	1074.0, 1073.6*	687.2, 686.8*	386.8	Granath[9]
Not described **values obtained via different spectrometers.	Not described	1071.4 – 1072.8**	684.5 - 686.0**	386.8	Nefedov[10]
Rock salt	Dry salt	1071.4	684.6	386.8	Shimizu[11]
Rock salt	Dry salt	1071.0	683.9	387.1	Morgan[12]
Theoretical Calculation	Koopman's Theorum	1071.1	683.7	387.4	Morgan[12]
Cryo frozen from hematite solution	Dried paste onto sample holder	1071.4	683.9	387.5	Shimizu[11]

Table 7.2: Core level binding energy values for NaF. Note: Works which have utilized XPS for analysis of NaF films that do not mention either the peak to peak distance or peak positions of both Na1s and F1s are not discussed here.

When comparing the peak to peak values observed in this work to that in the literature it is apparent that the values measured in this work for the primary Fs(1) peak is within the extremes already documented for NaF and correlate well to the theoretical values obtained via Koopman's theorem.

The primary peak F1s(1) can thus be attributed to a standard NaF conformation. The Δ(Na1s – F1s(2)) shows the presence of a less ionic bond than standard NaF, which appears to be slightly more covalent in nature (by 0.4eV) on the Au film compared to the Si wafer.

As such it is suspected that there are clusters of NaF being deposited along with the expected monomer units. The presence of the secondary F1s peak indicates that the clusters have an excess of F, as this would change the electron distribution from the standard ionic NaF bond to a more covalent one. Thus we conclude that the electron distribution through these clusters is the source of the partially covalent Na-F bond observed in the core levels, which can be influenced by the surface upon which the salt is deposited. The production of clusters without using a specific cluster source has been seen before[13-14] via heating in an oven and utilizing adiabatic expansion, and it was noted that clusters were formed independently of the discharge conditions used to generate the evaporation. Thus it is entirely possible that clusters could also be produced when evaporating in HV vacuum conditions. As an extra note the F1s(2) phenomenon was observed independently of evaporation temperature. A range of evaporation temperatures were selected between 500^0C-750^0C to test the nature of the secondary F species and for each temperature the same phenomenon was observed.

The peak positions of both Na1s and F1s on the controls also provides further information regarding the nature of the NaF/Si interface. The binding energy for Na1s is up at 1073.7eV is above the accepted range of binding energies possible for chemical interactions involving the Na1s core level. The high binding energy observed for the NaF/Si in this work has thus been interpreted as a dipole formation at the NaF/Si interface. The presence of an interfacial dipole would also have an effect upon the observed FWHM of the photoelectron peaks as there is generally a range of dipole strengths on a surface. Thus the broader nature of the FWHM for NaF/Au could be attributed to reduced surface order at the interface compared to NaF/Si.

7.4.1.2) NaF modified organic films at standard XPS takeoff angle

The range of NaF depositions on PCBM and P3HT is shown in Table 7.3, shown as a percentage of the total composition. No contamination was observed.

	C1s		**S2p$_{3/2}$**		**O1s**		**F1s**		**Na1s**	
Sample	**Posn (eV)**	**%**	**Posn (eV)**	**%**	**Posn (eV)**	**%**	**Posn (eV)**	**%**	**Posn (eV)**	**%**
P3HT	285.0	87.0 ±0.4	164.0	11.3 ±0.1	532.5	1.7 ±0.1	-	-	-	-
~1Å	285.0	84.0 ±0.5	164.0	10.9 ±0.1	532.4	1.5 ±0.1	684.3	0.9 ±0.1	1072.0	2.7 ±0.1
~3Å	285.0	81.9 ±0.4	164.0	10.8 ±0.1	532.5	1.4 ±0.1	684.4	1.6 ±0.1	1072.0	4.3 ±0.1
30Å	285.0	27.8 ±0.2	164.0	3.0 ±0.1	532.6	1.0 ± 0.1	685.5	29.1 ±0.1	1073.0	39.1 ±0.1
30Å(S)*	285.0	22.4 ±0.2	164.0	1.7 ±0.1	532.7	0.3 ±0.1	685.5	36.6 ±0.1	1073.2	38.9 ±0.1
PCBM	285.0	93.8 ±0.4	-	-	532.3	6.2 ±0.1	-	-		-
~1Å	285.0	89.4 ±0.4	-	-	532.3	6.0 ±0.1	683.8	0.5 ± 0.1	1072.0	1.8 ±0.1
~3Å	285.0	86.9 ±0.4	-	-	532.3	6.1 ±0.1	684.1	1.8 ± 0.1	1072.0	5.3 ±0.1
30Å	285.0	29.4 ±0.2	-	-	532.3	1.4 ±0.1	685.3	26.6 ±0.1	1072.6	42.7 ±0.1
30Å(S)*	285.0	26.2 ±0.2	-	-	532.3	1.1 ±0.1	685.2	34.3 ±0.1	1072.8	38.4 ±0.1

Table 7.3: Chemical composition and primary peak positions for all elements in the NaF/organic depositions.

Deposition of NaF layers on the organic materials revealed that the chemical composition of the salt showed a stoichiometry that was not 1:1. Also, the results showed that the stoichiometry varied with deposition thickness. As this data was all collected from the same analyzer these changes cannot be attributed to the transmission function of the apparatus and are therefore a representation of changes in the salt layer with thickness. Thin layers reveal an apparent excess of Na in the salt layer whereas the thick layers reveal a composition of ~1:1. This further indicates that there is some form of NaF cluster being deposited, and that these clusters are non-stoichiometric, non- stoichiometric clusters were also observed in the work performed by Teodorescu[13]. As the error in the transmission function is not known and there are possible IMFP effects also occurring with the changes in thickness the exact material excess cannot be discerned.

The peak positions of both Na1s and F1s were seen to increase with increasing deposition thickness. This indicates the presence of an interfacial dipole between the salt and organic layer similar to that which was observed in the NaF/Si control spectrum, although for the NaF/Si control the effect was more pronounced as seen by the higher Na1s and F1a binding energies.

7.4.1.3) Influence of NaF thickness and organic film on observed NaF composition

The Na1s and F1s spectra observed on the organic samples were very similar to those seen on the Si and Au controls (example Na1s and F1s spectra shown in Figure 7.1(b)). A single component was observed for Na1s across all deposition thicknesses. The secondary F1s(2) peak seen in the NaF/Si and NaF/Au controls was also observed for the NaF depositions on the organic films. As such, the range of salt thicknesses and influences on the observed salt composition (with respect to fluorine) is shown in Table 7.4. It was found that the F1s(2) peak was altered in intensity with thickness on the organic layers.

Sample	Position F1s(1) (eV)	Component Intensity F1s(1) (%)	Position F1s(2) (eV)	Component Intensity F1s(2) (%)	Δ(Na1s - F1s(1)) (eV)	Δ(Na1s - F1s(2)) (eV)	Δ(F1s(2) - F1s(1)) (eV)
P3HT							
~1Å	684.3	100.0	-	-	387.7	-	-
~3Å	684.4	96.0	686.4	4.0	387.6	385.6	2.0
30Å	685.5	73.0	687.6	27.0	387.5	385.4	2.1
30Å(S)*	685.5	53.4	687.7	46.6	387.7	385.5	2.2
PCBM							
~1Å	683.8	82.0	686.2	18.0	388.2	385.8	2.4
~3Å	684.1	88.0	686.3	12.0	387.9	385.7	2.2
30Å	685.3	74.0	687.4	26.0	387.3	385.2	2.1
30Å(S)*	685.2	41.8	687.4	58.2	387.6	385.4	2.2

Table 7.4: Peak positions and relative intensities of the two fluorine components F1s(1) (primary peak) and F1s(2) (secondary peak), where the total fluorine component intensity is 100%. Peak to peak distances between Na1s-F1s(1), Na1s-F1s(2) and F1s(1)-F1s(2) are also shown. Component errors of F1s were a maximum of 0.4% in all instances.

The secondary F1s(2) peak increases in intensity with increasing thickness on the organic materials. This indicates that increasing the deposition thickness increases the proportion of the total salt deposited in a cluster formation. The 30Å NaF deposition on both organic materials revealed that ~26% of the total fluorine intensity was from the F1s(2) component, indicating that for this thickness the salt layers are somewhat equivalent in composition. However, for the very thin ~1Å NaF deposition on P3HT only a single F1s component was seen, and for the ~3Å NaF/P3HT the F1s(2) component was only 4% of the total fluorine intensity. For NaF/PCBM the F1s(2) component was 18% of the total fluorine intensity for the ~1Å NaF deposition and was 12% for the ~3Å NaF deposition. Given that the deposition conditions in the chamber were equivalent for both organic materials this indicates that the organic layer has an influence on the adsorbed salt when the salt layer is sufficiently thin.

The peak to peak energy ‘distances’ Δ(Na1s - F1s) for single depositions of NaF on PCBM are seen to decrease with increasing deposition thickness by 0.9eV for Na1s - F1s(1) and by 0.5eV for Na1s - F1s(2). However for the various deposition thicknesses on P3HT these values do not vary beyond the position error of 0.4eV (0.2eV per photoelectron peak). This is another indication that the organic film has an influence on the adsorbed salt when the deposited salt layer is sufficiently thin.

There is also a clear difference in the fluorine component ratios between the different deposition methods of the salt. For the single 30Å NaF deposition the F1s(2) component is around 27% of the total fluorine intensity on the organic materials. This is less than what is observed for a single 30Å deposition of NaF on the Si and Au controls. However, when the salt is deposited as sequential thin depositions (30Å(S)*) the F1s(2) component is 46.6% of the total fluorine intensity on P3HT, and is 58.2% of the total fluorine intensity on PCBM.

7.4.1.4) Influence of NaF depositions on the organic films

The influence of NaF on the observed chemical states of PCBM is shown in Table 7.5 and Figure 7.2. For NaF/P3HT it is shown in Table 7.6 and Figure 7.3.

Peak	Component	Position (eV)	~1Å	~3Å	30Å	30Å(S)*
O1s	O1s(1)	532.3	40.8	38.8	36.3	46.7
	O1s(2)	533.5	59.2	57.5	53.0	53.3
	O1s(3)	530.6	0.0	3.7	10.7	0.0
C1s	C1s(1)	285.0	80.0	80.4	57.5	45.8
	C1s(2)	285.8	7.1	6.9	6.7	8.5
	C1s(3)	286.9	4.4	4.1	3.0	3.6
	C1s(4)	289.0	3.9	3.9	4.7	4.1
	C1s(5)	290.9	4.7	4.7	0.0	0.0
	C1s(6)	292.8	0.0	0.0	28.2	38.0

Table 7.5: Changes in component ratios of PCBM films with various NaF deposition thicknesses. Error in component analysis of C1s was a maximum of 0.5% in all instances.

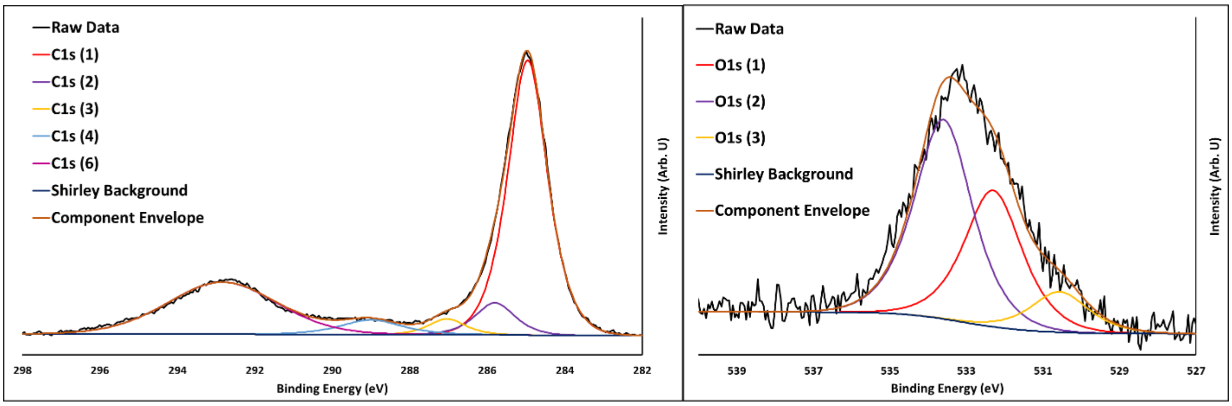

Figure 7.2: Example XP spectra of C1s (left) and O1s (right) from PCBM post NaF deposition, example shown is for the 30Å NaF/PCBM sample. Note the lack of peak C1s (5) for this thick NaF layer (see Figure 6.1 for pristine PCBM example).

Peak	**Component**	**Position (eV)**	**~1Å**	**~3Å**	**30Å**	**30Å(S)***
S2p$_{3/2}$	S2p$_{3/2}$ (1)	164.0	92.9	92.6	90.0	94.4
	S2p$_{3/2}$ (2)	164.9	2.6	2.9	5.0	3.1
	S2p$_{3/2}$ (3)	166.3	4.5	4.5	4.9	2.5
C1s	C1s(1)	285.0	95.8	95.9	70.9	54.8
	C1s(2)	287.2	2.6	2.7	0.7	0.3
	C1s(3)	288.1	1.6	1.4	0.2	2.0
	C1s(4)	293.3	0.0	0.0	28.2	42.9
O1s	O1s(1)	532.5	100.0	89.1	64.0	100.0
	O1s(2)	530.4	0.0	10.1	36.0	0.0

Table 7.6: Changes in component ratios of P3HT films with various NaF deposition thicknesses. Error in component analysis of C1s was a maximum of 0.5% in all instances.

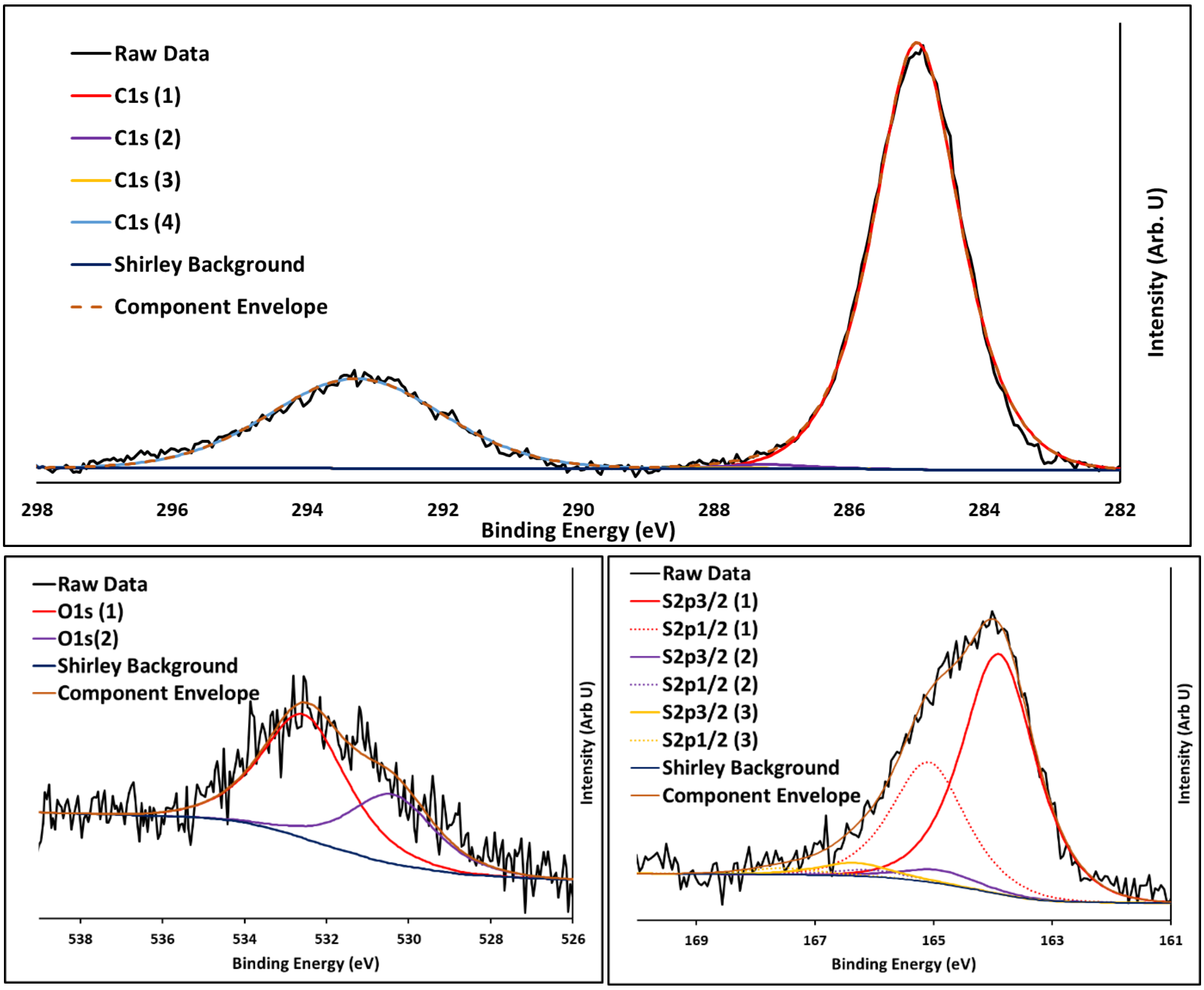

Figure 7.3: Example XP spectra of C1s (top), O1s (bottom left), S2p (bottom right) from P3HT post NaF deposition, example shown is for the 30Å NaF/P3HT sample. (see Figure 6.2 for pristine P3HT example). In this example the S2p (3) component is small, another example of this component can be seen in Figure 7.4.

The ~1Å NaF deposition on PCBM did not reveal any significant changes in the PCBM chemical components. On P3HT however a new high binding energy component was observed for sulfur and is denoted $S2p_{3/2}$ (3). A similar phenomenon was observed in Chapter 6 and attributed to some of the sulfur units in the thiophene protruding into the positive part of the interfacial dipole between the salt and P3HT. It has thus been attributed to the same phenomenon here.

For all other deposition thicknesses an extra O1s component was observed on both organic films. For PCBM this component is located at 530.6eV and for P3HT it is at 530.4eV. A similar phenomenon was observed in Chapter 6 and attributed to the presence and orientation of the salt inducing a redistribution of electrons in the organic materials. Thus it has also been attributed to this for the NaF depositions.

For the 30Å deposition thicknesses (single deposition and sequential depositions) a new component was observed in the C1s spectra of both organic materials. This phenomenon shall now be discussed for the single deposition on both organic materials. On PCBM this state is located at 292.8eV and denoted C1s(6) (Figure 7.2) and on P3HT at 293.3eV, denoted C1s(4) (Figure 7.3). On both materials this component was 28.2% of the total C1s peak intensity, which indicates that a significant chemical change has occurred. Carbon peaks located at these binding energies are generally attributed to CF_x bond formation[15-18]. However, when observing the respective fluorine peaks for these samples (Table 7.4) there are no separate chemical states observed which correspond to the component observed in the C1s spectra. Given that 28.2% of the C1s spectra reflected chemical changes it would be expected that changes could also be easily observed in the F1s peaks. However, the secondary fluorine component F1s(2) is located around the binding energy position for F-C bond formation. It was shown via the NaF/Si and NaF/Au control depositions that the F1s(2) component is present independently of any chemical bonds formed with either Si or Au, and on these control samples this F1s(2) component comprised around 40% of the total F1s intensity, so as such the F1s(2) component on the organic materials cannot be attributed only to CF_x bonds, especially given that the total intensity of the F1s(2) peak on the organic materials is actually less than observed on the control samples. We propose that the new peaks observed in the C1s spectra are indeed due to chemical bond formation with F, but are possibly bonds forming with the clusters rather than monomers of NaF which would explain both the presence of the peak in the C1s spectra, and also why the peak to peak distances in Table 7.4 do not change significantly to indicate dissociation of the salt.

For this deposition thickness on PCBM it was observed that the C1s(5) peak attributed to the conjugated π states in the fullerene is no longer present, which shows that the fullerene structure has been disrupted. There is also an increase in the O1s(3) component attributed to the redistribution of electrons in the organic layer. This increase in the O1s(3) component was also seen at this deposition thickness on P3HT.

For the sequential depositions on PCBM and P3HT (30Å(S)*) the high binding energy C1s component (C1s(6) for PCBM, C1s(4) for P3HT) comprised a larger percentage of the total C1s intensity compared to the single 30Å deposition. Another difference between the sequential and single depositions was also observed, which is that the low binding energy oxygen component attributed to the redistribution of electrons in the organic materials (O1s(3) for PCBM, O1s(2) for P3HT) was not present. This indicates that performing sequential depositions of NaF as opposed to a single thick layer alters the surface chemistry occurring upon deposition. It appears that the sequential depositions are facilitating more CF bond formation as opposed to electronic redistributions in the organic layers.

7.4.2) ARXPS: Chemical States with Depth

Angle resolved investigations of the NaF modified organic films revealed further complexities in the surface chemistry when the more surface sensitive angles were measured.

The salt itself showed no significant changes on either organic material with the various analysis angles measured so requires no further discussion. For depositions on PCBM there were no significant changes with angle for the thin NaF deposition. For the thick 30Å NaF deposition the most significant change observed with angle was that the new C1s component observed (C1s(6) seen in Figure 7.2) increased toward the surface, and there was also a decrease in the primary C1s peak C1s(1) pertaining to the fullerene cage see Table 7.7. This correlates also to the lack of C1s(5) at this deposition thickness and is further indication that the fullerene cage is disrupted for the thick deposition of NaF. Angle resolved investigations on P3HT revealed other new components in carbon and sulfur toward the surface, see Figure 7.4 and Table 7.8(a) for ~1Å NaF/P3HT and 7.8(b) for 30Å NaF/P3HT.

30Å NaF/ PCBM			**Component Intensity with Angle (%)**					
Peak	**Component**	**Posn (eV)**	**0^0**	**30^0**	**45^0**	**50^0**	**55^0**	**60^0**
O1s	O1s(3)	530.6	10.7	12.0	12.5	8.2	10.0	7.9
	O1s(1)	532.3	36.3	41.2	44.7	52.3	54.4	64.0
	O1s(2)	533.5	53.0	46.8	42.8	39.5	35.6	28.1
C1s	C1s(1)	285.0	57.5	51.1	43.0	39.9	37.4	35.2
	C1s(2)	285.8	6.7	8.5	9.2	11.0	12.1	12.8
	C1s(3)	286.9	3.0	2.5	2.5	2.7	2.6	2.6
	C1s(4)	289.0	4.7	4.6	5.3	4.5	4.3	4.4
	C1s(5)	290.9	0.0	0.0	0.0	0.0	0.0	0.0
	C1s(6)	292.8	28.2	33.3	40.1	41.9	43.6	45.1

Table 7.7: O1s and C1s component intensity ratios with various analysis angles for 30Å NaF/PCBM, where the total component intensity per element is 100%. Component errors for oxygen were a maximum of 0.3%, for carbon error was a maximum of 0.5%.

~1Å NaF/ P3HT			Component Intensity with Angle (%)					
Peak	**Component**	**Posn (eV)**	**0^0**	**30^0**	**45^0**	**50^0**	**55^0**	**60^0**
C1s	C1s(1)	285.0	95.8	95.4	95.6	95.2	94.0	81.8
	C1s(2)	287.3	2.6	2.8	2.5	2.1	1.9	1.8
	C1s(3)	288.2	1.6	1.8	1.9	1.7	2.0	2.0
	C1s(4)	293.3	0.0	0.0	0.0	0.0	0.0	0.0
	C1s(5)	282.4	0.0	0.0	0.0	1.0	2.0	5.9
	C1s(6)	284.1	0.0	0.0	0.0	0.0	0.0	8.5
S2p$_{3/2}$	S2p$_{3/2}$ (1)	164.0	92.9	94.0	94.6	98.4	91.3	88.5
	S2p$_{3/2}$ (2)	164.9	2.6	1.9	0.0	0.0	0.0	0.0
	S2p$_{3/2}$ (3)	166.3	4.5	4.1	5.4	1.6	5.4	6.7
	S2p$_{3/2}$ (4)	167.9	0.0	0.0	0.0	0.0	3.4	4.7
O1s	O1s(1)	532.5	100.0	100.0	100.0	100.0	95.5	88.1
	O1s(2)	529.8	0.0	0.0	0.0	0.0	4.5	11.9

Table 7.8(a): O1s, S2p$_{3/2}$ and C1s component intensity ratios with various analysis angles for ~1Å NaF/P3HT, where the total component intensity per element for each film is 100%. Component error for sulfur was a maximum of 0.3%, for carbon the error was a maximum of 0.5%.

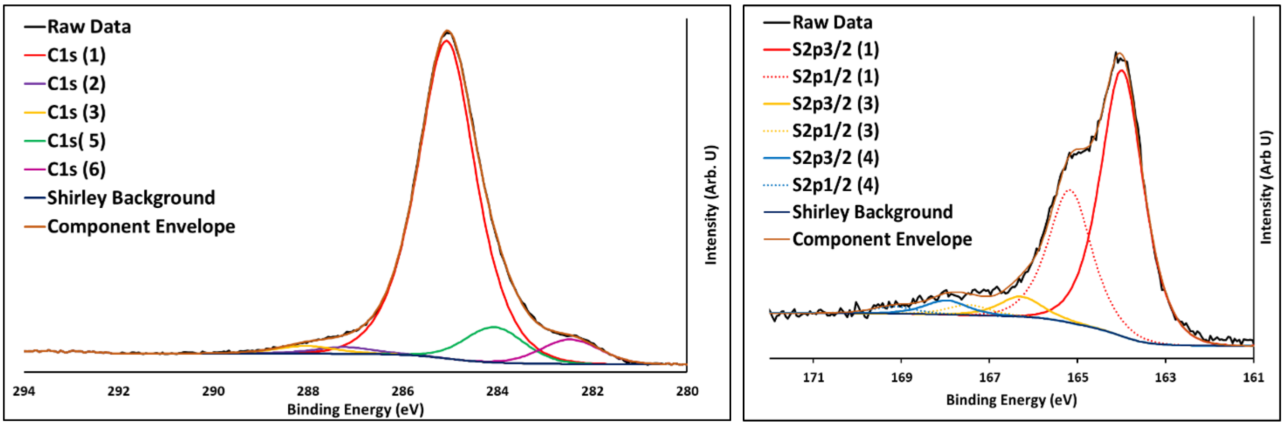

Figure 7.4: Example XP spectra of C1s (top) and S2p (bottom) from P3HT post NaF deposition, example shown is for the thin ~1Å NaF/P3HT measured at 60^0 angle with respect to the analyzer. For C1s note the clear absence of the high binding energy C1s (4) state for this thin deposition and presence of peaks C1s (5) and C1s (6). For S2p note the absence of the S2p (2) state, a larger S2p (3) component and new component S2p (4).

30Å NaF/ P3HT			Component Intensity with Angle (%)					
Peak	**Component**	**Posn (eV)**	**0^0**	**30^0**	**45^0**	**50^0**	**55^0**	**60^0**
C1s	C1s(1)	285.0	70.9	66.0	45.4	56.3	55.6	46.5
	C1s(2)	287.3	0.7	1.5	0.8	1.1	0.1	0.0
	C1s(3)	288.2	0.2	1.6	0.5	1.8	0.6	1.1
	C1s(4)	293.3	28.2	31.0	25.8	38.5	39.4	43.9
	C1s(5)	282.8	0.0	0.0	27.5	2.3	4.3	8.5
S2p$_{3/2}$	S2p$_{3/2}$ (1)	164.0	90.0	95.6	93.5	90.2	91.1	88.9
	S2p$_{3/2}$ (2)	164.9	5.0	0.1	1.5	0.0	0.0	3.7
	S2p$_{3/2}$ (3)	166.3	4.9	4.3	5.0	9.8	8.9	7.3
O1s	O1s(1)	532.5	64.0	75.5	56.8	33.8	22.8	7.9

Table 7.8(b): O1s, S2p3/2 and C1s component intensity ratios with various analysis angles for 30Å NaF/P3HT, where the total component intensity per element for each film is 100%. Component error for sulfur was a maximum of 0.3%, for carbon the error was a maximum of 0.5%.

For the ~1Å NaF/P3HT there were multiple new components observed in the organic film toward the surface (see Figure 7.4). For sulfur there was another high binding energy component, denoted $S2p_{3/2}$ (4) at 167.9eV. For carbon there were two states denoted C1s(5) and C1s(6) located at 282.4eV and 284.1eV respectively. The secondary oxygen component (see Figure 7.3) was also observed in this sample toward the surface but at a lower binding energy of 529.8eV. This combination of changes in the near surface region could be interpreted as damage to some of the thiophene structure, however, this would be due to the NaF dissociating and breaking bonds, and the Na1s and F1s bonds are clearly intact from the binding energy separation between them (Table 7.4). Thus these changes in the organic film are attributed to redistributions of electrons through the thiophene unit toward the surface, and possibly different sections of the polymer structure protruding into the positive and negative regions of the interfacial dipole. A similar observation is made for the 30Å NaF/P3HT sample with the C1s(5) low binding energy peak, but the other components in this instance follow the same trend observed with the standard analysis angle. If the NaF had indeed broken bonds in the thiophene unit on the ~1Å NaF deposition it would be expected that this would also occur for a thicker salt deposition. The fact that this is not the case indicates that indeed the changes in states are due to electron redistributions occurring in the organic layer which change with thickness of NaF. The fact that it changes with different salt thicknesses is an indication that the NaF orientation on the polymer is different with different layer thicknesses.

7.4.3) MIES/UPS

The MIES/UPS results for the NaF control films were found to be non-trivial and as such the MIES/UPS results shall begin with a section dedicated to these films (section 7.4.3.1). The NaF modified organic film spectra will then be shown (section 7.4.3.2), first discussing the SVD results (section 7.4.3.2.1), and then a discussion on impact of the sequential vs. single deposition method ono the VB (section 7.4.3.2.2).

7.4.3.1) Control NaF film analysis

The VB structure of the PCBM and P3HT films can be seen in Figures 7.11-7.14 but do not require further discussion. The VB for NaF in the literature is not dissimilar to LiF in that the DOS pertain only to the F2p states[8, 19-22]. The MIE spectra for the 30Å NaF/Si and 30Å NaF/Au control spectra did not reflect this however as can be seen in Figure 7.5. The MIE spectra clearly show a range of DOS between 7-15eV on both substrates, indicating that whatever is occurring at the outermost layer on these samples is not a straightforward case of F2p states like that in the aforementioned literature.

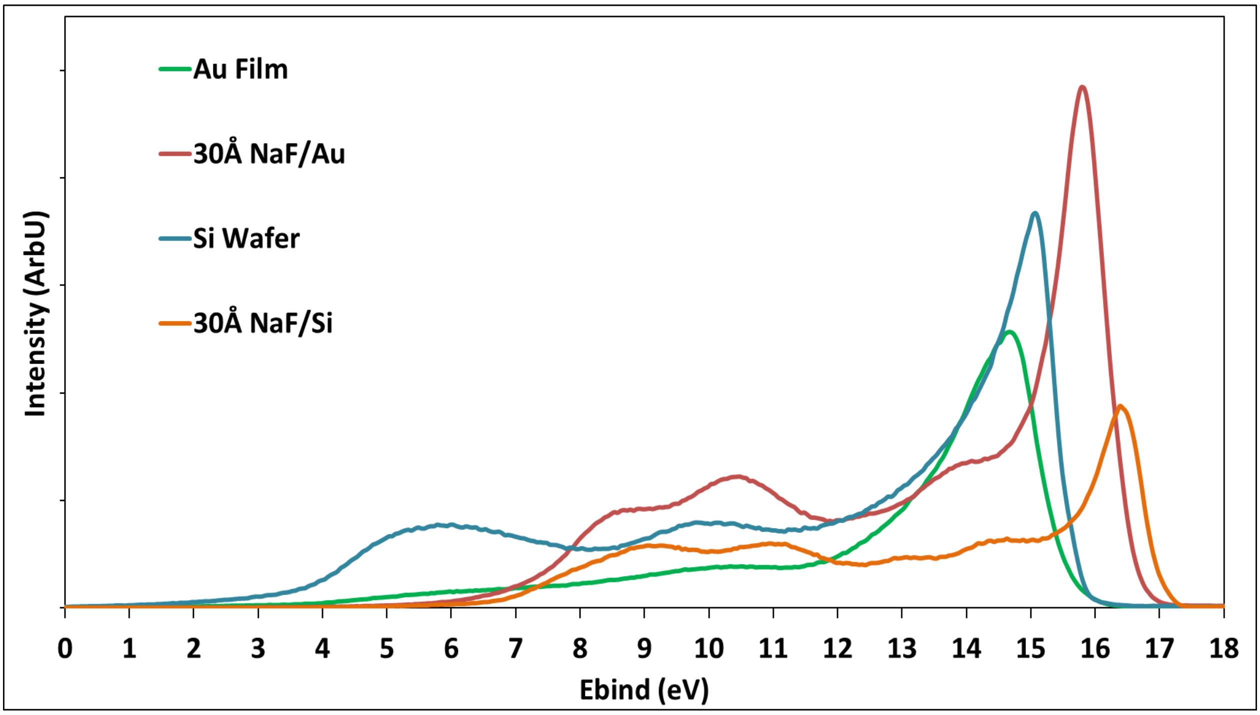

Figure 7.5: MIES of Au and Si controls, and with 30Å NaF deposited.

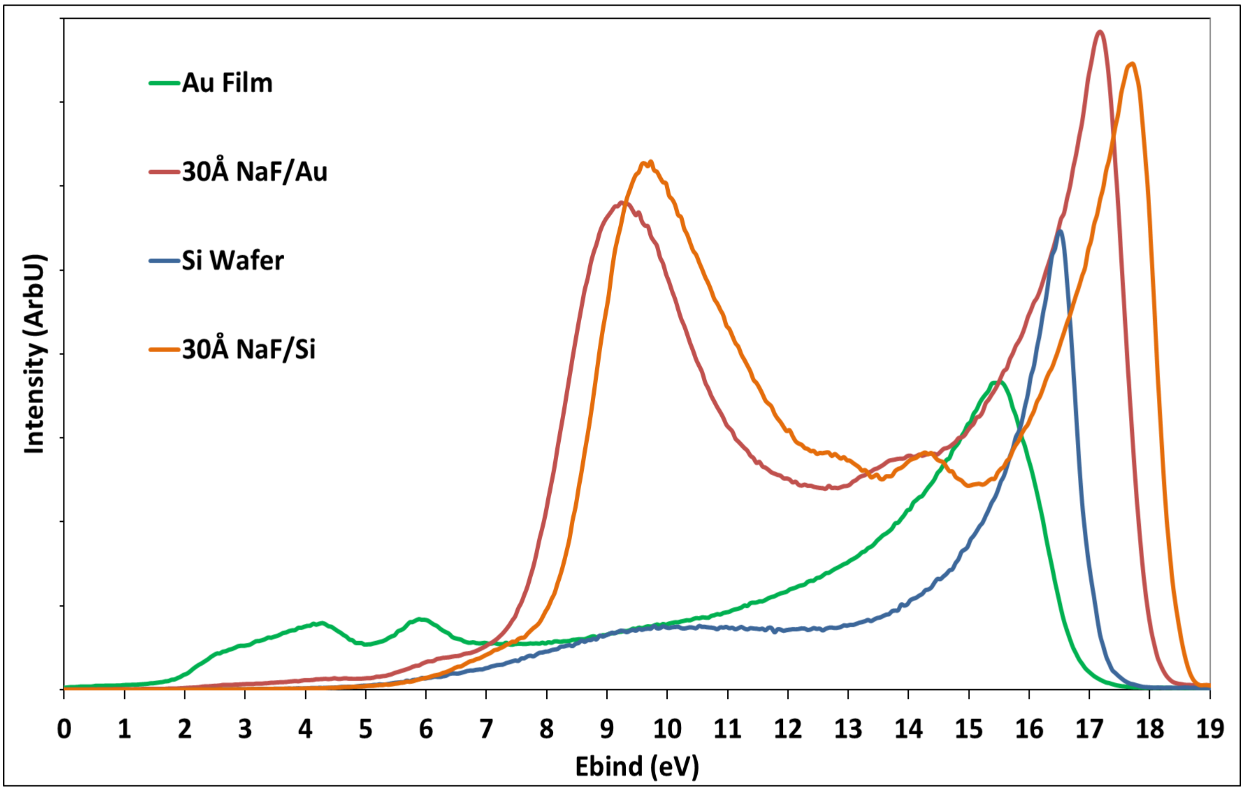

Figure 7.6: UPS of Au and Si controls, and with 30Å NaF deposited.

The respective UP spectra shown in Figure 7.6 appeared far more like that described in other works noted above with a strong feature at 9.3eV for NaF/Au and at 9.7eV for NaF/Si, this is believed to be the F2p states. There were however states at 13.6eV for NaF/Au and at 12.9eV and 14.3eV for NaF/Si which could not be explained. Given the lack of chemical interaction observed in XPS for the NaF/Au sample it appears that the respective MIE and UP spectra are representative of the NaF, however this is not conclusive without further investigation. Given the focus of this work is NaF depositions on organic materials these spectra were not used conclusively. It was however noted that low binding energy states pertaining to Na3s between 1.2-4eV[23] were not observed which is further indication that the NaF did not dissociate upon deposition.

7.4.3.2) NaF Modified Organic Spectra

For the VB analysis the SVD described in Chapter 2 was again used, each set of reference spectra along with the weighting factors for each sequential deposition are shown in Figures 7.7-7.10. The unmodified spectra for the sequential depositions are then shown in Figures 7.11-7.14 along with a single 30Å thick deposition for comparison. This single deposition sample is physically the same sample as that analyzed in the XPS data.

7.4.3.2.1) SVD

In this instance the SVD resulted in a three component system for each analyzed spectral set. The organic film was used as one base spectrum, and the thickest NaF deposition for each sequential deposition run was used as the second base spectrum so that the third component could be deconvoluted in the algorithm as intermediate states. This used the assumption of full surface coverage for the thickest deposition as the second base spectrum. For the SVD of the UP spectra of NaF/PCBM the fitting parameters needed to allow for a binding energy shift of the third base spectrum to obtain a feasible solution, this method was developed by Berlich *et.al*[24] and is indicative of a dipole change at the interface.

The presence of the third spectrum indicates some form of surface interaction or phenomenon occurring with the different deposition thicknesses. This third reference spectrum is thus the spectrum of interest from this analysis.

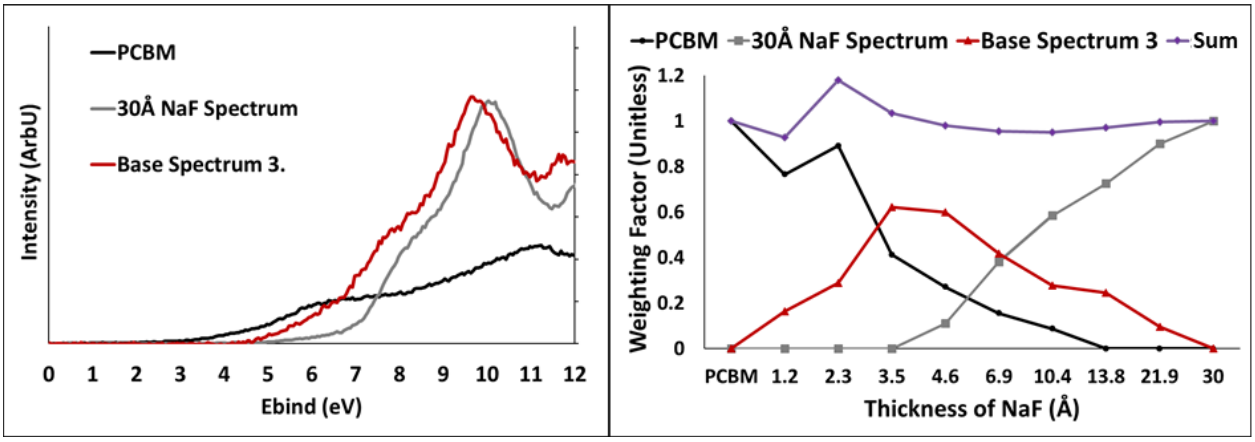

Figure 7.7: MIES SVD base spectra (left) and weighting factors (right) for each of the sequential depositions for NaF/PCBM.

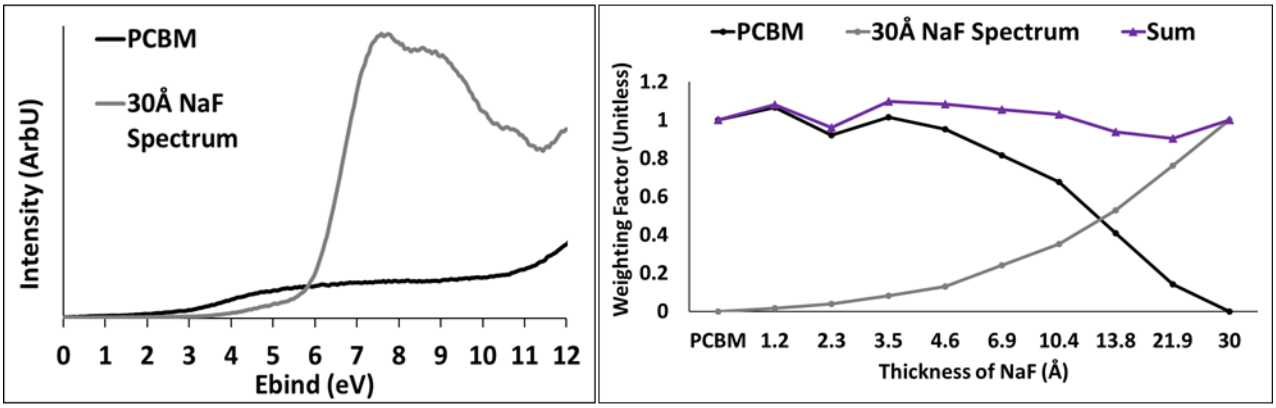

Figure 7.8: UPS SVD base spectra (left) and weighting factors (right) for each of the sequential depositions for NaF/PCBM.

NaF Thickness (Å)	PCBM	1.2	2.3	3.5	4.6	6.9	10.4	13.8	21.9	30
Ebind shift (eV)	-	-0.6	-0.6	-0.5	-0.4	-0.3	-0.3	-0.2	-0.1	-

Table 7.9: Binding energy shift of the NaF reference spectrum for the SVD of UPS of NaF PCBM.

For MIES of NaF/PCBM (Figure 7.7) the reconstructed third reference spectrum looks very similar in shape to the NaF reference spectrum but shifted in binding energy. As such, the third reference spectrum is believed to be caused by a change in the NaF/PCBM interfacial dipole strength with layer thickness rather than intermediate chemical states. The weighting factors indicate that for layers up to 4.6Å thickness the side of the dipole pointing to the outermost layer has become slightly less positive and that this gradually changes with thickness up to 30Å NaF. The difference in binding energy between the second and third base spectra is not large however (~0.4eV at the maximum intensity of 9.7 and 10.1eV), which suggests that the difference in dipole strength at the outermost layer is not large.

For UPS of NaF/PCBM (Figure 7.8) the third base spectrum found in the SVD was actually the NaF reference spectrum but shifted in binding energy, thus appearing as a different base spectrum in the deconvolution procedure. Thus only the organic and NaF reference spectra are shown in Figure 7.8. The binding energy shift of the NaF reference spectrum is shown in Table 7.9.

The data shows that for the initial depositions (1.2Å and 2.3Å) of NaF the NaF spectrum is in a position 0.6eV lower in binding energy than the 30Å NaF thickness. This then shifts to more positive binding energies with increasing thickness, to then become what is measured as the final NaF deposition thickness spectrum. The fact that this reference spectrum is shifting almost constantly with thickness indicates that the outwards facing component of the dipole parallel to the surface normal is continually becoming more positive with increasing NaF thickness. Comparing this to the MIES results (Figure 7.7) shows that the effect of this changing interfacial dipole strength is not as pronounced at the outermost layer and that the shift between the thin and thicker depositions is marginal as shown by the very small difference in binding energy between the third reference spectrum and that of NaF in Figure 7.7 (left).

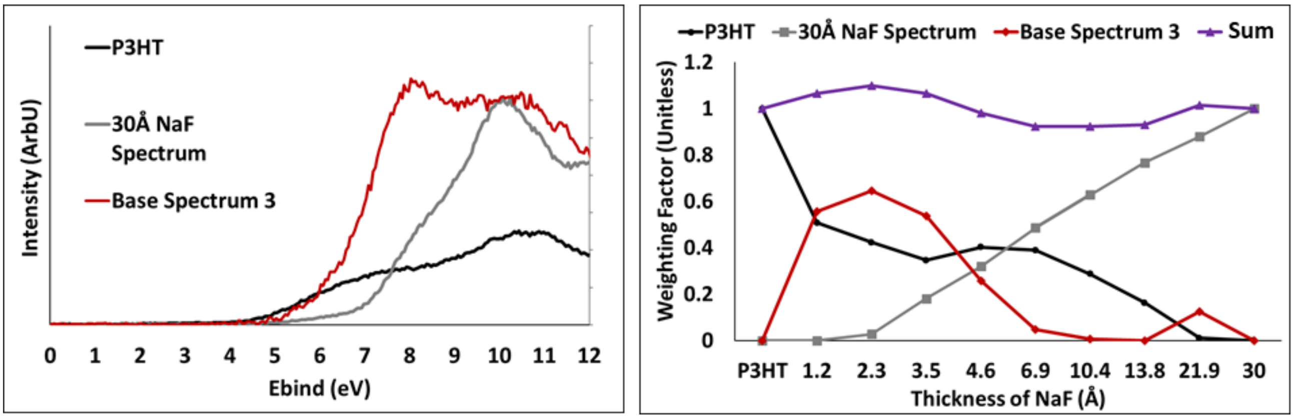

Figure 7.9: MIES SVD base spectra (left) and weighting factors (right) for each of the sequential depositions for NaF/P3HT.

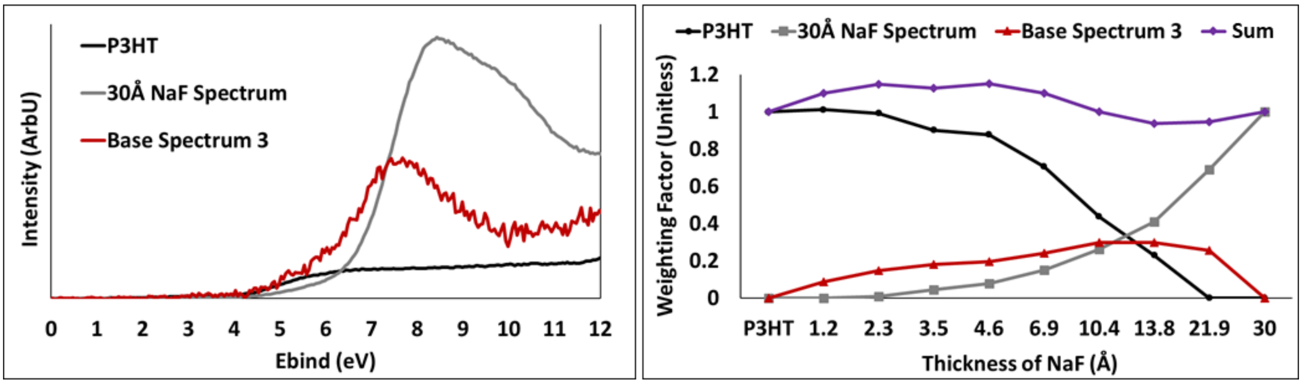

Figure 7.10: UPS SVD reference spectra (left) and weighting factors (right) for each of the sequential depositions for NaF/P3HT.

For NaF/P3HT the MIES SVD results (Figure 7.9) also revealed a third reference spectrum which was very similar in shape to that of the final NaF base spectrum but shifted in binding energy, so was attributed to changes in the interfacial dipole. The weighting factors show that the third reference spectrum has a sharp increase in contribution up to 2.3Å, but by 6.9 Å the contribution becomes almost zero, indicating that there is no further shift induced by the interfacial dipole for thicker layers. The difference in binding energy (and thus dipole changes) between reference spectrum two and three was much greater in this instance, having a difference of ~2eV between the maximum intensity points of each spectrum.

For UPS of NaF/P3HT (Figure 7.10) the SVD showed the third reference spectrum again appearing to be the NaF reference spectrum but shifted in binding energy. In this instance the weighting factors (Figure 7.10 right) reveal that for thin depositions of NaF (<10.4Å) there are similar contributions of the measured spectra coming from both the NaF reference spectrum and the third reference spectrum. Thicker depositions are then predominantly the final NaF reference spectrum. The difference in binding energy between base spectra 2 and 3 is 1eV in this instance.

7.4.3.2.2) Sequential vs. Single deposition method:

Comparing the sequential depositions to a single thick deposition reveals differences in the VB on both organic films, see Figures 7.11-7.14.

The MIE spectra for both deposition methods and organic materials (Figures 7.11 and 7.13) appear to be dissimilar to the NaF DOS stated in the literature[8, 19-21] in that there are far more states present than just the F2p states. This difference would be partially related to the changing interfacial dipole, but it is suspected that the features ~12eV and 13.5eV could also be indicating that a small amount of water is present at the outermost layer for both deposition methods. Features pertaining to water have been observed previously at around these binding energies, with the position varying upon which state the water was in[25]. This could also be the reason for the MIE spectral shape observed for the NaF/Au and NaF/Si controls (Figure 7.5).

The UP spectra for the single thick deposition on both organics have features which appear to be like that of the NaF F2p states[8, 19-21], albeit shifted in binding energy (caused by the dipole), for NaF/PCBM this is seen at 8.9eV (Figure 7.12) and for NaF/P3HT at 11.9eV (Figure 7.14). The sequential depositions however, particularly for NaF/PCBM (Figure 7.12) has more features in similar positions to the extra features observed in MIES. It is suspected that a little water is embedded within the salt upon deposition, and that by performing sequential depositions the water is trapped in the near surface area, however when a single thicker layer is deposited this is not the case. Thus the UPS single depositions appear to be the F2p NaF states observed in the literature[8, 19-21], and the sequential depositions do not. Although the evaporator was run for over an hour prior to depositions the water could still be present in the salt[26]. A very small concentration of water particularly only near the outermost layer could quite possibly escape detection in XPS.

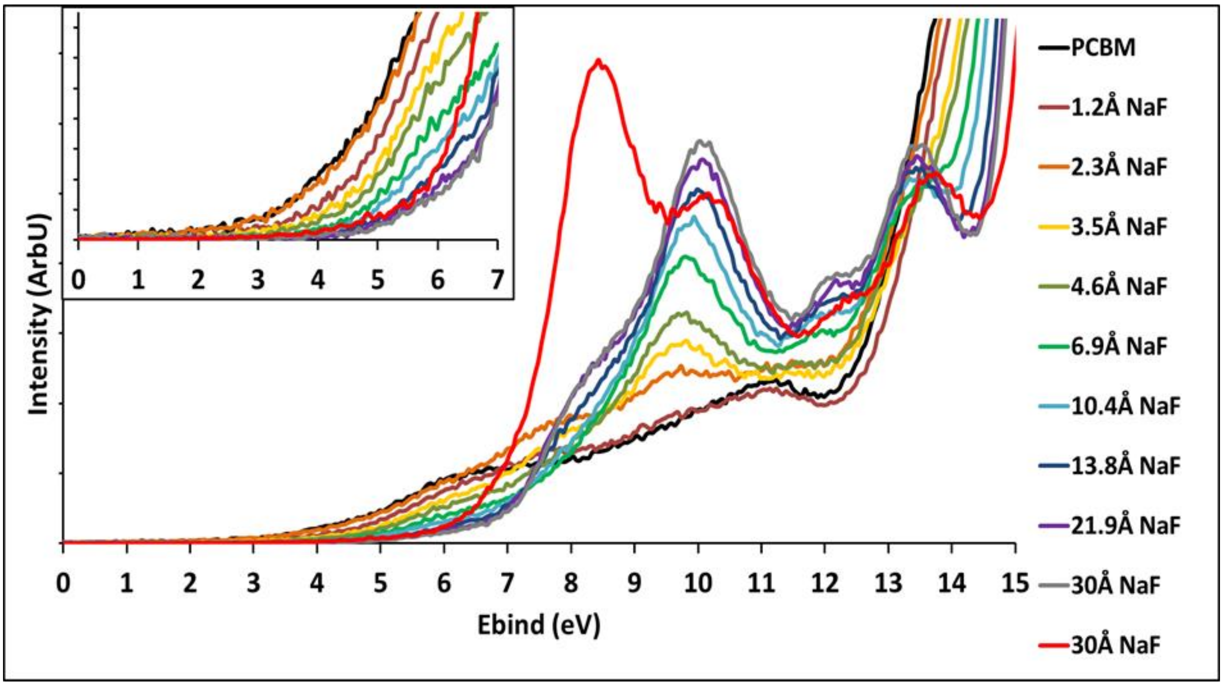

Figure 7.11: MIES of sequential NaF depositions on PCBM, with MIES of the single 30Å NaF/PCBM sample (in red) for comparison.

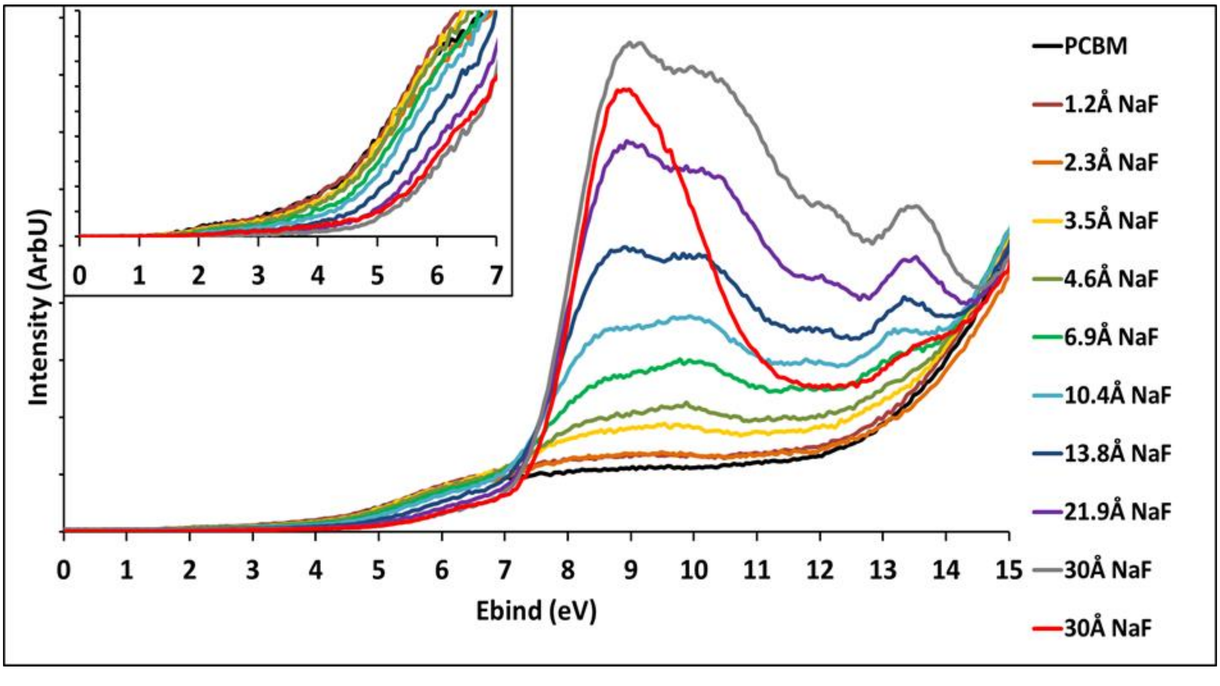

Figure 7.12: UPS of sequential NaF depositions on PCBM, with UPS of the single 30Å NaF/PCBM sample (in red) for comparison.

For MIES of NaF/PCBM (Figure 7.11) most of the spectral features between the single and sequential depositions are the same. The difference is in the 7~9eV region, where the single deposition shows a strong peak which is only small in the sequential depositions. This is an indication that the interfacial NaF/PCBM dipole is affected by the deposition method. Given we do not know the F2p peak position for zero dipole formation on the organic layers we cannot discuss the exact dipole strength and can only compare the relative positions. The strong presence of the DOS in the 7~9eV region in MIES for the single deposition (Figure 7.11) indicates that in some regions of the measured surface the side of the dipole pointing to the outermost layer (i.e.: parallel to the surface normal) is less positive for a single thick deposition than sequential depositions.

When comparing the UPS of the two deposition methods (Figure 7.12) a much larger difference in the DOS is observed. The DOS in the 7~11eV region of the single deposition sample appear as more of a single peak than for the sequential depositions and the DOS at 11~15eV have a reduced intensity compared to the thicker sequential depositions. As stated above it is believed this could possibly be indicative of water present in the near surface area for the sequential depositions, but it is also likely that there are differences in the interfacial dipole between the two deposition methods as well. The single and more narrow main peak observed at 8.9eV for the single deposition suggests that the interfacial dipole is a more uniform strength in the near surface area for the single deposition compared to the sequential depositions. Thus the sequential depositions may have regions where the component of the dipole parallel to the surface normal are more positive compared to the single deposition.

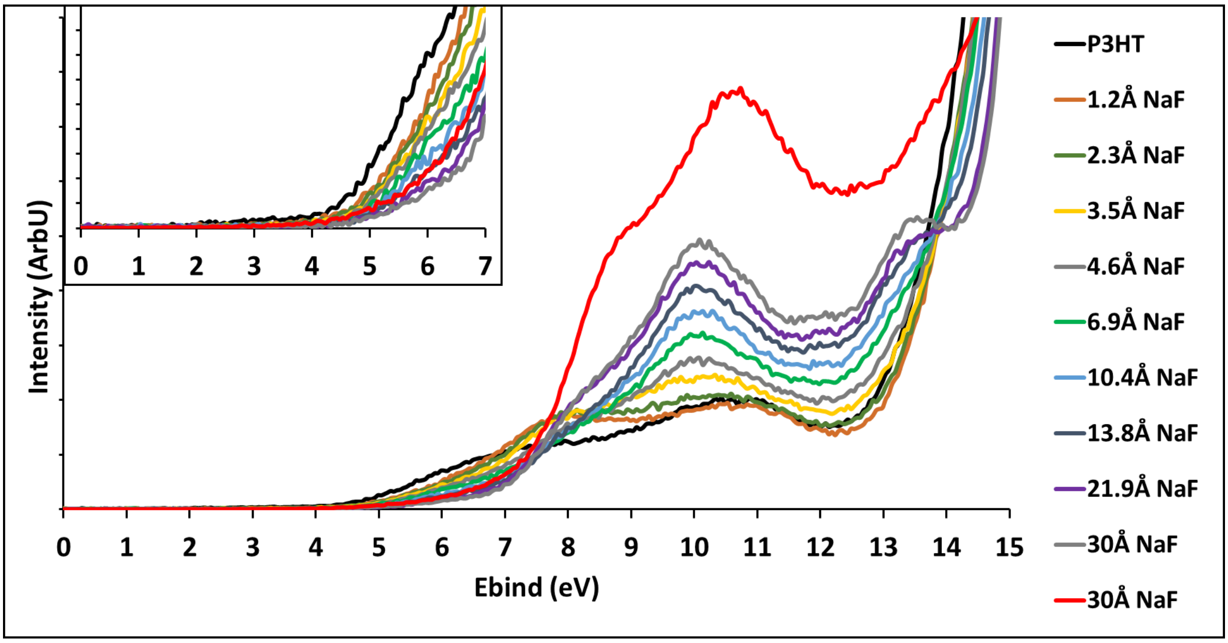

Figure 7.13: MIES of sequential NaF depositions on P3HT, with MIES of the single 30Å NaF/P3HT sample (in red) for comparison.

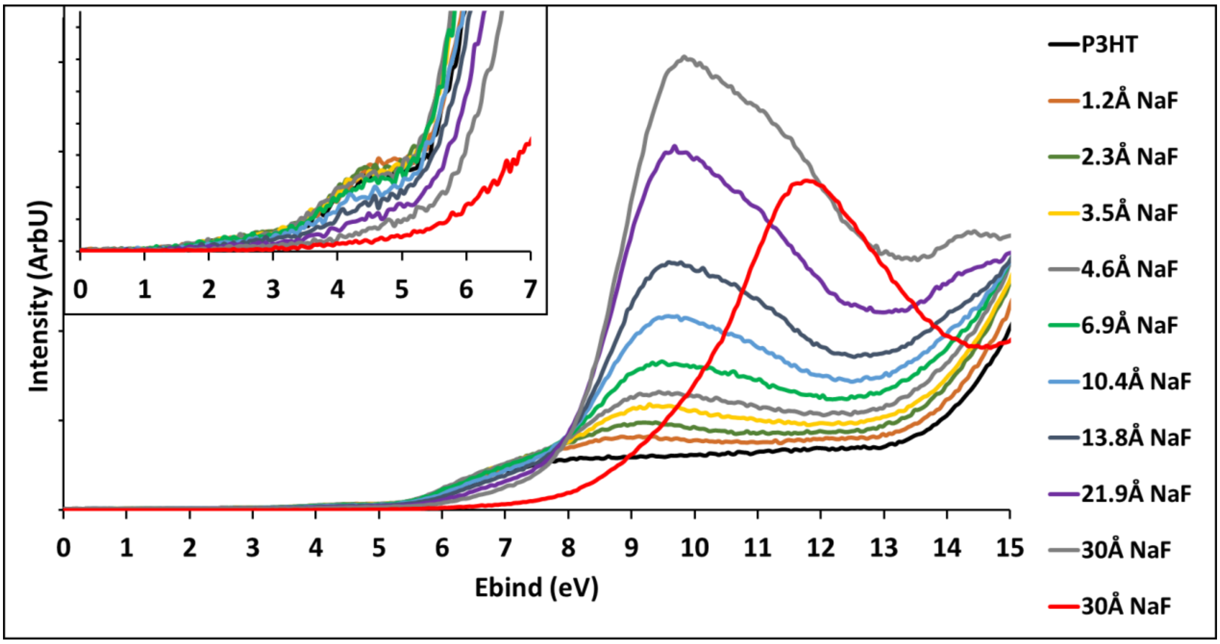

Figure 7.14: UPS of sequential NaF depositions on P3HT, with UPS of the single 30Å NaF/P3HT sample (in red) for comparison.

When comparing the sequential depositions to the single deposition for NaF/P3HT the MIE spectra do not show much of a difference in spectral shape (Figure 7.13). There is a small positive binding energy shift for the DOS of the single deposition which is most easily observed with the most prominent feature, located at 10.6eV for the single deposition and 10.1eV for the sequential depositions. This indicates that the effect of the interfacial dipole at the outermost layer is 0.5eV more positive for the single deposition. For UPS however (Figure 7.14) there is a larger positive shift observed for the single deposition, with the most prominent feature located at 11.8eV for the single deposition and 9.9eV for the thickest of the sequential depositions. A comparison to the features located above 13eV for the sequential depositions cannot be made as these features would be within the secondary electron peak region in the single deposition spectrum. From the observable information it appears that the effect of the interfacial dipole in the near surface area is 1.9eV more positive for the single deposition.

The workfunction is also affected by the deposition method, see Table 7.10. For NaF/PCBM the workfunction decreases with both deposition methods, but the sequential deposition induces a 0.4eV larger shift. For NaF/P3HT the workfunction increases for the single deposition by 0.3eV but for the sequential depositions it is downshifted by 0.7eV. The difference in workfunction shift for NaF/PCBM could be induced by a different dipole strength at the vacuum interface. For NaF/P3HT the differences in workfunction with deposition method indicates that the sample/vacuum dipole has opposing orientations depending on deposition method.

Sample	Pristine Organic Layer	Single 30Å Deposition	Sequential Depositions
PCBM	4.2	4.0	3.6
P3HT	3.4	3.7	2.7

Table 7.10: Workfunctions for pristine PCBM and P3HT and deposited NaF**.**

7.4.4) NICISS

Sodium and fluorine depth profiles on PCBM and P3HT are shown in Figure 7.15. The concentrations were calibrated from the carbon step for each sample.

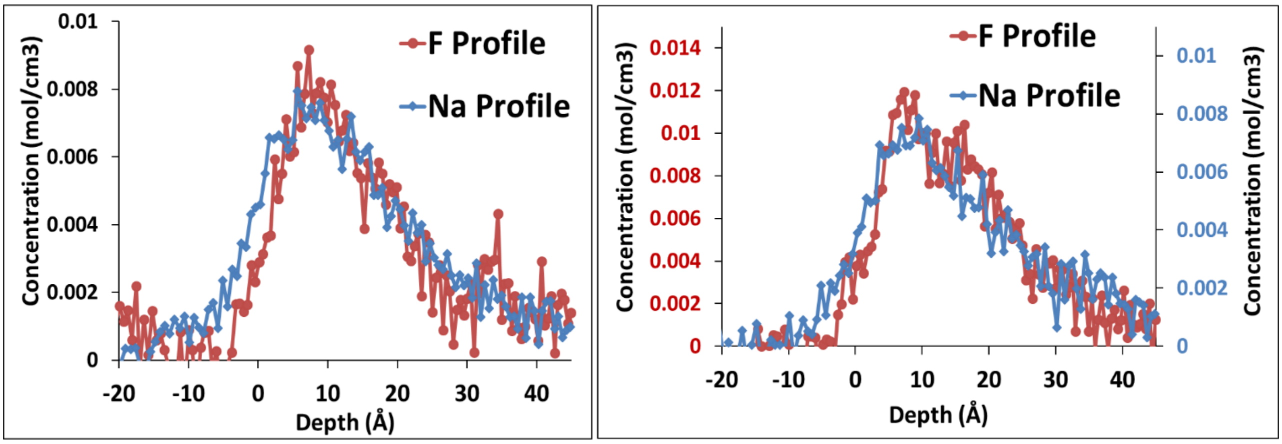

Figure 7.15: Na and F profiles for 10Å NaF/PCBM (left) and 10Å NaF/P3HT (right).

The sodium and fluorine profiles on each organic film show a peak maximum between 5~10Å into the surface with a tail tapering off at around 40Å. In this instance the gauging of the zero mark for the depth has not been yet performed and thus the peak maximum below the surface is not indicative of diffusion. However, the peak shape still provides information regarding the surface. Just as discussed in Chapter 6, the profile for an element present only on the surface would appear with a symmetrical peak and thus this observed concentration tapering off into the bulk indicates NaF molecules are present beneath the surface, so are either diffusing or growing as islands on the surface. The spectral intensity at a negative depth is due to the finite energy resolution of the apparatus and has been seen before[27].

7.4.5) Further Discussion

The results of this work shows that the NaF depositions are not just monomer units of NaF, this was seen on all substrates. An extra fluorine component was observed in XPS on all substrates and was present even when no chemical reactions were observed with the surface as seen by the NaF/Au control sample. This secondary peak changes in intensity depending upon the thickness of NaF deposited on the organic materials, it was seen to increase as thicker NaF layers were deposited. It was also observed that the stoichiometry of the NaF changed with thickness on the organic materials, with thicker depositions showing increasing amounts of fluorine. The interpretation of these results is that the deposited salt incidentally contains non-stoichiometric clusters of Na_xF_y, and it is suspected that the excess is fluorine, which would explain the less ionic peak to peak distance Δ(Na1s – F1s(2)).

The peak to peak distances of NaF (Table 7.4) were seen to decrease with increasing NaF thickness on PCBM, yet for P3HT no significant change was observed. The relative intensity of the fluorine components was also different for PCBM and P3HT for equivalent thin (~1 Å and ~3Å) single NaF depositions, with PCBM showing a larger percentage of the secondary F1s peak. When the thick 30Å NaF layer was deposited as a single layer there was no difference in the F1s component ratios between the two organic materials. When the NaF was deposited sequentially however the depositions on PCBM again showed a much larger portion of the fluorine at the higher binding energy secondary component region. These results combined indicate that the material upon which the salt is deposited has an influence on the electron distribution within the salt when a thin layer of NaF is deposited, and that this electron distribution is also affected by deposition method.

The electron distribution in the organic materials was also affected by the NaF deposition thickness and deposition method (Tables 7.5 and 7.6) and were observed more toward the surface on both organic materials (Tables 7.7 and 7.8(a) and 7.8(b)). An extra low binding energy component was observed in the O1s XP spectrum for both organic materials when ~3Å and 30Å were deposited as a single deposition which is attributed to a redistribution of electrons, in a similar manner to what was observed for LiF in Chapter 6, however this component was not observed with sequential depositions. When 30Å NaF was deposited a new high binding energy carbon component was observed, and it was larger for the sequential depositions. The peak to peak distance between the high binding energy fluorine component and high binding energy carbon component was ~394.5eV for both organic materials. This lies between values recorded for OCF_3 and OCF_2O in the literature[15]. In a dissertation released in 2012[16] Barlow noted that the presence of oxygen on CNTs facilitated fluorination. It could be that the oxidation of the organic films in the present work has performed a similar role. With respect to OPVs this fluorination is undesirable as it clearly affects the conjugated π states of PCBM responsible for charge conduction in the device.

Evidence of an interfacial dipole was seen in XPS with the increase in peak position of both Na1s and F1s with increasing thickness of single NaF depositions on both organic materials (Table 7.3). The increase in binding energy with thickness indicates that the outwards facing component of the dipole parallel to the surface normal became more positive with increasing NaF thickness.

The SVD analysis of the sequential depositions revealed further effects of the interfacial dipole. The MIES and UPS SVD for both organic materials revealed three base spectra (Figures 7.7-7.10). One of these was the organic film, the second was the thickest deposition of NaF, and the third in each instance revealed a spectrum which appeared to be the same as the second base spectrum only shifted to a lower binding energy and has thus been interpreted as changes in the interfacial dipole with sequential deposition thickness and not to intermediate chemical states. The relative contribution and position of this third base spectrum changed differently with thickness of NaF for each case. It appears that there is a greater range of dipole strengths for NaF/P3HT at the outermost layer and near surface area compared to NaF/PCBM, as the difference in binding energy between base spectrum two and three are larger for NaF/P3HT in both MIES and UPS (Figures 7.7-7.10). No evidence of doping of either organic material was observed, if it were present it would have appeared as a shift in the low binding energy edge (VBM) of the VB[4].

Differences between the deposition methods were quite apparent in MIES and UPS (Figures 7.11-7.14). There was a significant difference in spectral shape between single and sequential depositions for the near surface area of both films but similar shape observed for the outermost layer. We believe this could quite possibly be indicating the presence of trace amounts of water absorbed within the NaF which is trapped in the near surface area when the salt is deposited sequentially. Other differences were also observed for the depositions which were attributed to changes in the interfacial dipole. For NaF/PCBM (Figure 7.11), there was a different ratio of the observed DOS which has been interpreted as some regions of the side of the interfacial dipole pointing toward the outermost layer being more positive. This positive difference in the dipole for sequential depositions was also observed in the near surface area (Figure 7.12). For NaF/P3HT there was an offset between the single or sequential deposition spectra despite having the same overall spectral shape, which is also indicative of changes in the dipole. The sequential depositions appeared to induce a shift of the spectrum to a lower binding energy compared to the single thick deposition for both the outermost layer (Figure 7.13) by 0.5eV, and the near surface area (Figure 7.14) by 1.9eV.

When comparing deposition methods in XPS on each organic material (30Å vs. 30Å(S)*) there was no significant difference in Na1s and F1s peak positions, which indicates that deposition method does not have an impact on the interfacial dipole at this probing depth (~10nm).

The depth profiles of the salt on the two organic materials were very similar (Figure 7.15). Both profiles indicated that the Na and F were present to ~30Å into the surface. Although it is possible that 30Å high islands were forming on the surface it is unlikely, as the MIE spectra for this deposition thickness did not indicate that there was a significant amount of the organic substance present at the outermost layer (Figures 7.11 and 7.13). If a significant portion of the organic DOS were present at the outermost layer this would be evident in the low binding energy region <6eV as the DOS pertaining to the salt do not contribute to this region. Thus it appears that the salt is diffusing into the organic surface.

7.5) Comparisons between LiF and NaF

When comparing the depositions between LiF (from Chapter 6) and NaF a brief comparison of the salts must first be made. The LiF molecule is more tightly bound and has a bond strength of 137.5kcal/mol, which is higher than that of NaF which is 114kcal/mol[28]. LiF is also more ionic in nature than NaF[29]. In the crystal form both are reported to have the NaCl lattice structure[29], and both salts are capable of forming clusters and several investigations have been made into various cluster formations[7, 13, 28, 30-31].

The first difference to be observed between the two salts was shown via XPS. The LiF depositions revealed a single chemical state for Li and F that had a peak to peak binding energy difference of that expected for the undissociated salt. For NaF there were clearly two states observed for fluorine, and the stoichiometry was seen to change when the deposition thickness was varied. It is suspected that the NaF depositions were, in part incidental non-stoichiometric clusters.

An interfacial dipole between the deposited salt and organic material was observed in all instances. For the probing depth of XPS the effect of increasing the salt thickness on the dipole was similar, the peaks for both salts increased in binding energy by around 1eV between the thinnest and thickest deposition. The effects of the dipole in the near surface area were quite different. For LiF it appeared that a single deposition induced the outwards facing component of the dipole parallel to the surface normal to become more positive compared to sequential depositions. For NaF on P3HT this was also the case. The opposite seemed to occur for single depositions on PCBM however, the single deposition appeared to induce the outwards facing component of the dipole to become less positive.

There were several chemical changes in the organic materials observed upon depositing the salts. For either salt on PCBM a low binding energy component in the oxygen was observed and attributed to electronic redistributions within the organic material. Depositing NaF induced this component at a binding energy 0.5eV lower than that seen for LiF. For P3HT there were several states attributed to electron redistributions observed toward the surface for NaF depositions that were not present for LiF depositions. This indicates that NaF has a stronger influence on the electron distribution in the organic materials compared to LiF. Although it is not conclusive, it is possible that this enhanced electron redistribution induced by NaF in even the thinnest layers could in part be why the use of NaF in OPV devices compared to LiF was found to be more beneficial for cell efficiency when a sufficiently thin alkali halide layer was deposited[1].

There was a high binding energy component in sulfur of P3HT which was observed for both NaF and LiF depositions. This was denoted S2p$_{3/2}$(3) and attributed to thiophene chains protruding into the positive region of the interfacial dipole. This state was observed at a 0.5eV higher binding energy for the LiF depositions which gives an indication that there is a difference in either surface ordering or dipole strength between the two salts. The conjugated π states in carbon of PCBM responsible for charge conduction were preserved for thin depositions of either salt. For NaF this was seen to change when a thicker layer was deposited. The π states were no longer present and a clear peak indicating fluorination of the organic layer appeared at around 293eV. This fluorinated carbon peak was also seen on P3HT for thick NaF layers. Thus it appears than when a sufficient amount of NaF is deposited it fluorinates both PCBM and P3HT. This did not occur when films of LiF were deposited.

The concentration depth profiles (from NICISS) of the two salts revealed very similar profiles, both salts appeared to be growing as islands on the organic surface with suspected diffusion into the organic materials.

7.6) Conclusion:

The evolution of electronic states on the surface and in the near surface area for NaF on air deposited and annealed PCBM and P3HT films has been investigated and a concentration depth profile for a thick layer of NaF on both organic materials was obtained. The salt did not appear to be dissociating or inducing doping in the organic materials. An interfacial dipole between the salt and organic layer was observed for both PCBM and P3HT and for the probing depth of XPS it appears that the effect of this dipole is similar to that observed for LiF in Chapter 6. No contaminants were observed in XPS, however it is suspected that trace amounts of water was present in the salt upon deposition as indicated by the MIES results. This appeared at the outermost layer for both deposition methods. There was a significant difference occurring in the near surface area when sequential depositions were performed as compared to a single thick NaF deposition as indicated by UPS. The single thick deposition of NaF revealed DOS similar to that seen in the literature, whereas the sequential depositions appeared to be more complex and attributed to a convolution of changes in the interfacial dipole along with possible water trapped by this deposition method. The interfacial dipole appeared to be affected by deposition method at the outermost layer as well, with the sequential depositions inducing the outwards facing component of the dipole parallel to the surface normal to become more positive for NaF/P3HT, and less positive for NaF/PCBM. Although the possible water content is clearly undesirable for OPV devices the changes in interfacial dipole induced by deposition method could have an effect on charge injection in OPV devices as the dipole is one of the proposed and accepted mechanisms enhancing electron injection into the electrode[5]. We believe further experiments with testing devices would only be appropriate for thin NaF layers, as the thick layers were seen to induce fluorination of the organic materials and damage the conjugated π states of PCBM. This fluorination of the organic materials and lacking conjugated structure in the fullerene with thick layers of NaF could possibly be part of the reason for the drastic differences in device efficiency noted in Ahlswede's work[1] for thick layers of LiF vs. NaF, with LiF being clearly superior for device function when a thicker interlayer was used. The enhanced ability of NaF (compared to LiF) to induce an electron redistribution within the organic materials could possibly be related to the enhanced performance of devices for thin layers of salt, however further experiments involving electrode deposition are required to observe how the electronic redistributions change once the electrode material is present.

The growth mechanism of the NaF appeared to be similar to that observed for LiF in Chapter 6 as shown in the NICISS results, and it is concluded that films of the salt grow in an island-like manner but diffusion also possibly occurs.

7.7) Acknowledgements

We would like to thank Dr Cameron Shearer for depositing the Au films and Dr Anders Barlow for helpful discussions regarding the XPS results.

7.8) References

1. Ahlswede, E.; Hanisch, J.; Powalla, M., Comparative Study of the Influence of LiF, NaF, and KF on the Performance of Polymer Bulk Heterojunction Solar Cells. *Applied Physics Letters* **2007**, *90*, 163504-3.

2. Helander, M. G.; Wang, Z. B.; Lu, Z. H., Contact Formation at the C60/Alkali-Metal Fluoride/Al Interface. *Applied Physics Letters* **2008**, *93*, 083311-3.

3. Helander, M. G.; Wang, Z. B.; Mordoukhovski, L.; Lu, Z. H., Comparison of Alq3/Alkali-Metal Fluoride/Al Cathodes for Organic Electroluminescent Devices. *Journal of Applied Physics* **2008**, *104*, 094510.

4. Lee, J.; Park, Y.; Kim, D. Y.; Chu, H. Y.; Lee, H.; Do, L.-M., High Efficiency Organic Light-Emitting Devices with Al/NaF Cathode. *Applied Physics Letters* **2003**, *82*, 173-175.

5. Liu, J.; Duggal, A. R.; Shiang, J. J.; Heller, C. M., Efficient Bottom Cathodes for Organic Light-Emitting Devices. *Applied Physics Letters* **2004**, *85*, 837-839.

6. Kemeny, P. C.; Jenkin, J. G.; Liesegang, J.; Leckey, R. C. G., Measurement of Relative Subshell-Photoionization Cross Sections in Sodium Chloride and Sodium Fluoride by X-Ray-Photoelectron Spectroscopy. *Physical Review B* **1974**, *9*, 5307-5315.

7. Rajagopal, G.; Barnett, R. N.; Landman, U., Metallization of Ionic Clusters. *Physical Review Letters* **1991**, *67*, 727-730.

8. Kikas, A.; Nõmmiste, E.; Ruus, R.; Saar, A.; Martinson, I., Core Excitons in Na K Photoabsorption of NaF: Resonant Auger Spectroscopy, *Phys. Rev. B*, **2001**; Vol. 64, 235120.

9. Granath, K.; Bodegård, M.; Stolt, L., The Effect of NaF on Cu(In,Ga)Se2 Thin Film Solar Cells. *Solar Energy Materials and Solar Cells* **2000**, *60*, 279-293.

10. Nefedov, V. I.; Salyn, Y. V.; Leonhardt, G.; Scheibe, R., A Comparison of Different Spectrometers and Charge Corrections Used in X-Ray Photoelectron Spectroscopy. *Journal of Electron Spectroscopy and Related Phenomena* **1977**, *10*, 121-124.

11. Shimizu, K.; Shchukarev, A.; Kozin, P. A.; Boily, J.-F., X-Ray Photoelectron Spectroscopy of Fast-Frozen Hematite Colloids in Aqueous Solutions. 5. Halide Ion (F–, Cl–, Br–, I–) Adsorption. *Langmuir* **2013**, *29*, 2623-2630.

12. Morgan, W. E.; Van Wazer, J. R.; Stec, W. J., Inner-Orbital Photoelectron Spectroscopy of the Alkali Metal Halides, Perchlorates, Phosphates, and Pyrophosphates. *Journal of the American Chemical Society* **1973**, *95*, 751-755.

13. Teodorescu, C. M.; Esteva, J. M.; Womes, M.; El Afif, A.; Karnatak, R. C.; Flank, A. M.; Lagarde, P., Sodium 1s Photoabsorption Spectra of Na and NaF Clusters Deposited in Rare Gas Matrices. *Journal of Electron Spectroscopy and Related Phenomena* **2000**, *106*, 233-245.

14. Castleman, A. W.; Keesee, R. G., Ionic Clusters. *Chemical Reviews* **1986**, *86*, 589-618.

15. Ferraria, A. M.; Lopes da Silva, J. D.; Botelho do Rego, A. M., XPS Studies of Directly Fluorinated HDPE: Problems and Solutions. *Polymer* **2003**, *44*, 7241-7249.

16. Barlow, A. J. Plasma Processing Studies with Application to Carbon Nanotube Fluorination. PhD dissertation, Flinders University, **2012**.

17. Claves, D.; Giraudet, J.; Hamwi, A.; Benoit, R., Structural, Bonding, and Electrochemical Properties of Perfluorinated Fullerene C70. *The Journal of Physical Chemistry B* **2001**, *105*, 1739-1742.

18. Cox, D. M.; Cameron, S. D.; Tuinman, A.; Gakh, A.; Adcock, J. L.; Compton, R. N.; Hagaman, E. W.; Kniaz, K.; Fischer, J. E., X-Ray Photoelectron and NMR Studies of Polyfluorinated C60: Evidence That C-C Bonds Are Broken. *Journal of the American Chemical Society* **1994**, *116*, 1115-1120.

19. Hessabi, R.; Urch, D. S., Chemical Effects in the X-Ray Emission (F Kα) and X-Ray Photoelectron Spectra of Alkali-Metal and Alkaline-Earth-Metal Fluorides. *Journal of the Chemical Society, Faraday Transactions* **1990**, *86*, 247-252.

20. Baumeier, B.; Krüger, P.; Pollmann, J.; Vajenine, G. V., Electronic Structure of Alkali-Metal Fluorides, Oxides, and Nitrides: Density-Functional Calculations Including Self-Interaction Corrections. *Physical Review B* **2008**, *78*, 125111.

21. Wertheim, G. K.; Rowe, J. E.; Buchanan, D. N. E.; Citrin, P. H., Valence-Band Structure of Alkali Halides Determined from Photoemission Data. *Physical Review B* **1995**, *51*, 13675-13680.

22. Kowalczyk, S. P.; McFeely, F. R.; Ley, L.; Pollak, R. A.; Shirley, D. A., X-Ray Photoemission Studies of the Alkali Halides. *Physical Review B* **1974**, *9*, 3573-3581.

23. Krischok, S.; Höfft, O.; Günster, J.; Souda, R.; Kempter, V., The Chemistry of Alkali Atoms on Solid Water: A Study with MIES and UPS. *Nuclear Instruments and Methods in Physics Research Section B: Beam Interactions with Materials and Atoms* **2003**, *203*, 124-129.

24. Berlich, A.; Liu, Y.-C.; Morgner, H., Growth of Nickel Nanoparticles on NiO/Ni(001): Evidence of Adsorbed Oxygen on Metal Particles by Metastable Induced Electron Spectroscopy (MIES). *Surface Science* **2008**, *602*, 3737-3744.

25. Partanen, L.; Mikkelä, M.-H.; Huttula, M.; Tchaplyguine, M.; Zhang, C.; Andersson, T.; Björneholm, O., Solvation at Nanoscale: Alkali-Halides in Water Clusters. *The Journal of Chemical Physics* **2013**, *138*, 044301.

26. Schlaf, R.; Parkinson, B. A.; Lee, P. A.; Nebesny, K. W.; Jabbour, G.; Kippelen, B.; Peyghambarian, N.; Armstrong, N. R., Photoemission Spectroscopy of LiF Coated Al and Pt Electrodes. *Journal of Applied Physics* **1998**, *84*, 6729-6736.

27. Schmerl, N.; Andersson, G., A Layered Structure at the Surface of P3HT/PCBM Blends. *Physical Chemistry Chemical Physics* **2011**, *13*, 14993-15002.

28. Cox, X. B.; Linton, R. W.; Bursey, M. M., Formation of Small Cluster Ions from Alkali Halides in SIMS. *International Journal of Mass Spectrometry and Ion Processes* **1984**, *55*, 281-290.

29. Khan, D. C.; Khowash, P. K., Theoretical Study of the Electronic Structure of Covalent Solids. *Canadian Journal of Physics* **1991**, *69*, 720-725.

30. Aguado, A.; Ayuela, A.; López, J.; Alonso, J., Structure and Bonding in Small Neutral Alkali-Halide Clusters, *Phys. Rev. B,* **1997**; Vol. 56.

31. Bréchignac, C.; Cahuzac, P.; Calvo, F.; Durand, G.; Feiden, P.; Leygnier, J., Evidence for Entropic Effects in the Dissociation of Cationic Sodium Fluoride Clusters. *Chemical Physics Letters* **2005**, *405*, 26-31.

8. Conclusions

This dissertation has focused on utilizing the unique combination of ion scattering and electron spectroscopic techniques at Flinders University to investigate the electronic properties of a selection of thin films and modifications which have potential applications in OPV technology. This combination of techniques has facilitated the ability to map the electronic properties of the selected films in the near surface region but particularly at the outermost layer so that any differences between these regions of the surface could be quantified. Despite the obvious potential advantages which come with mapping the electronic properties of the outermost layer in interfacial studies this is not yet a commonly employed methodology in OPV related research, which is naturally in part due to the availability of this combination of techniques. As well as mapping electronic properties, the concentration depth profiles of the constituent elements in the samples were also obtained for most of the investigations in this work such that the vertical composition could be understood. This was not performed for the work in Chapter 5 on the sputter deposited metal oxide films as the deposition method is known to produce rather uniform films and as such the concentration depth profile was not required. The selected materials and modification methods were varied such that the project as a whole investigated across a range of interfaces and surfaces rather than focusing only on one particular material or interface. As such, and as per the aims section of this dissertation the conclusions shall be discussed separately below with respect to the initial research aims outlined in Chapter 3.

8.1) Obtaining Valence Band Data for Insulating Materials

Given the rising interest in the use of insulating materials in composite films a comparison of various methods for obtaining VB spectra for electrical insulators was performed in Chapter 4, using the polymer PDMS as the insulator. This involved the use of multiple charge compensation mechanisms which were: the use of an ultra-thin PDMS film such that electrons could tunnel through from the substrate to the surface, a gold mesh grid on the sample surface, and embedding CNTs into the polymer prior to curing. Both the thin film method and use of the gold mesh were found to still produce spectra which were slightly charged, however they both still had some success. The thin film was found to be slightly more oxidized than the other films, but had similar features in the VB to the other measured PDMS spectra which is interesting to note given that PDMS is known to undergo a critical transition when the film is sufficiently thin. For the case of the gold mesh grid the VB spectrum of PDMS had to be derived by subtracting the DOS of the grid from the obtained spectrum. This was found to be successful for a qualitative assessment of the overall spectral shape, and was shown to produce a spectrum with a similar set of features to that obtained with the other methods, however this method clearly holds the disadvantage of induced error from the possibility of subtracting DOS at binding energies common to both the mesh and the polymer. The use of embedded CNTs in the polymer film was certainly the most successful method for charge compensation, and for this case the measured DOS were able to be fitted with Gaussian components and compared to theoretical calculations. The use of an embedded nanotube matrix could also be a possibility for a flexible electrode if the CNTs were appropriately functionalized and a sufficient portion of them were present at the outermost layer to receive charge carriers, although in this work the exact concentration at the surface was not able to be calculated.

8.2) Assessing the Impact of Doping and Surface Preparation/ Cleaning Methods on Transparent Conductive Oxides

Surface preparation treatments are a common modification performed on metal oxide films serving as transparent electrodes to prepare the surface for subsequent material deposition. As such, in Chapter 5 several surface treatment methods were performed on ZnO with a range of Al doping concentrations up to 21.2% Al to assess their impact on the electronic properties of the surface and near surface, whilst simultaneously assessing the effect of dopant concentration. UV-Vis was also employed to measure the changes in band gap with doping. The treatments were UHV sputter cleaning with heating, oxygen plasma cleaning, and oxygen plasma cleaning with UHV heating.

Doping was seen to increase the band gap and also shift the VB to higher binding energies which were larger than the changes observed in the band gap. Thus the doping process appears to have induced band bending in the VB as well as lowering the CB in the near surface area. The doping process was also shown to incorporate extra oxygen into the metal oxide lattice. Sputter cleaning with heating was found to be the most effective method for removing surface contaminants. The use of the oxygen plasma without UHV heating was found to have a high surface contaminant concentration as shown by XPS and MIES, which was due to the brief exposure to atmosphere. It also had a significant impact on the VB in the near surface area, obscuring changes induced by doping as well as induce a surface dipole. UHV heating the plasma treated sample was shown to remove both the contamination and dipole as well as induce the greatest increases in workfunction seen in the samples for all investigated cleaning methods. The process of UHV heating for both the sputter and plasma cleaned samples was shown to reveal a surface conduction channel on both the ZnO and doped surfaces, the charge carriers for the channel were not affected by doping. For the purposes of an HWE electrode the use of oxygen plasma cleaning with UHV heating creates the most favourable workfunction shifts as well as a surface conduction channel for charge transfer. Assessing the exact impact of any cleaning procedure on the surface is not a trivial process however, as it is difficult to discern the difference between purely removing contamination as compared to also changing the metal oxide surface. As such, it is necessary to fabricate devices to fully assess the changes the observed phenomena have on the charge transfer at the interface.

8.3) Assessing the Impact of Alkali Fluoride Layer Thickness and Deposition Method on the Electronic Structure of PCBM and P3HT

It is clear when looking at the literature that the mechanisms behind OPV device improvements when introducing an interlayer between the active layer and LWE are not concluded, and the use of different materials induces a variety of effects at the interface. LiF is a popular salt chosen for this interlayer in OPV devices, and for the active layer the blend of PCBM and P3HT is commonplace, so in Chapter 6 a study of the electronic structure and vertical distribution of LiF on both PCBM and P3HT as separate materials was conducted. The effect of deposition method on the electronic structure was also investigated. A comparative study using NaF was then performed and was the subject of Chapter 7. In both cases the organic materials were air cured and annealed, so oxidation was present in the films prior to salt deposition.

For LiF depositions the salt was found to remain intact and was not seen to form chemical bonds with either organic material, although it was shown to induce a redistribution of electrons in PCBM as seen through changes in the O1s spectrum. When the LiF layer was sufficiently thick the oxygen in P3HT was affected and was shifted to a lower binding energy. This was only observed in XPS at more surface sensitive angles via the ARXPS measurements. An interfacial dipole was observed on both organic materials upon depositing the salt. Effects of this were observed in XPS as well as MIES and UPS. Depositing the salt as a single deposition as opposed to a series of thinner depositions was shown to shift the VB features to a higher binding energy, indicating that the side of the dipole pointing to the outermost layer is more positive for the single deposition method on both organic materials. The salt was not seen to dissociate as shown by both XPS and the results of the SVD performed on the VB data. Doping of either organic material did not occur as shown by the lack of a shift in the VBM. The combination of NICISS and MIES results indicated that the salt was growing as islands, and that diffusion of the salt into both organic materials was also occurring. Thus, for LiF on PCBM the effect at this interface appears to be an electron redistribution within the PCBM along with interfacial dipole formation and some LiF diffusion. For LiF on P3HT the effect is the interfacial dipole formation and diffusion, with an added effect on the electron distribution at oxidized sites when a sufficiently thick layer was deposited

For the case of NaF depositions the results were more complex. An extra chemical state was observed for fluorine in XPS, even on the gold control sample where there were no chemical interactions with the substrate, and the stoichiometry of the salt was seen to change with deposition thickness on the organic materials. It is believed that the salt was therefore being deposited in part as non-stoichiometric clusters, and from the MIES data it is suspected that trace amounts of water are possibly also deposited, although this was not observed below the outermost layer for single thick depositions. For thin depositions of NaF the salt was seen to induce electron redistributions in both organic materials, with a stronger effect than observed for LiF. For thick NaF depositions chemical bonding between carbon and fluorine was seen on both PCBM and P3HT and the conjugated π states responsible for conduction in PCBM were no longer observed in XPS. An interfacial dipole was observed for NaF depositions on both organic materials, and like the LiF evidence of this dipole was seen in XPS as well as MIES and UPS. The effect of deposition method for NaF was different to LiF. Changes in the interfacial dipole strength were observed when performing sequential depositions as shown by the SVD results. The single deposition method on P3HT induced the side of the dipole pointing to the outermost layer to become more positive than sequential depositions. The opposite was observed on PCBM. It is believed that depositing the NaF sequentially trapped some water within the salt layer. The NICISS results appeared very similar to those seen for LiF, so the same growth and diffusion is believed to be occurring for NaF as LiF. So for NaF, the effects of deposition on the interface with regard to diffusion is similar to LiF, but the effect of electron redistribution is enhanced and effects of the interfacial dipole more variable. It is also clearly more reactive with the organic materials and fluorinates them when a sufficient amount is deposited. These results are a potentially important finding for OPV devices in that the strength of the interfacial dipole can be tuned not only by salt layer thickness but also by the deposition method, and for future work it would be worth experimenting with deposition methods of the salt prior to electrode material deposition and measuring the effects on the electronic states.